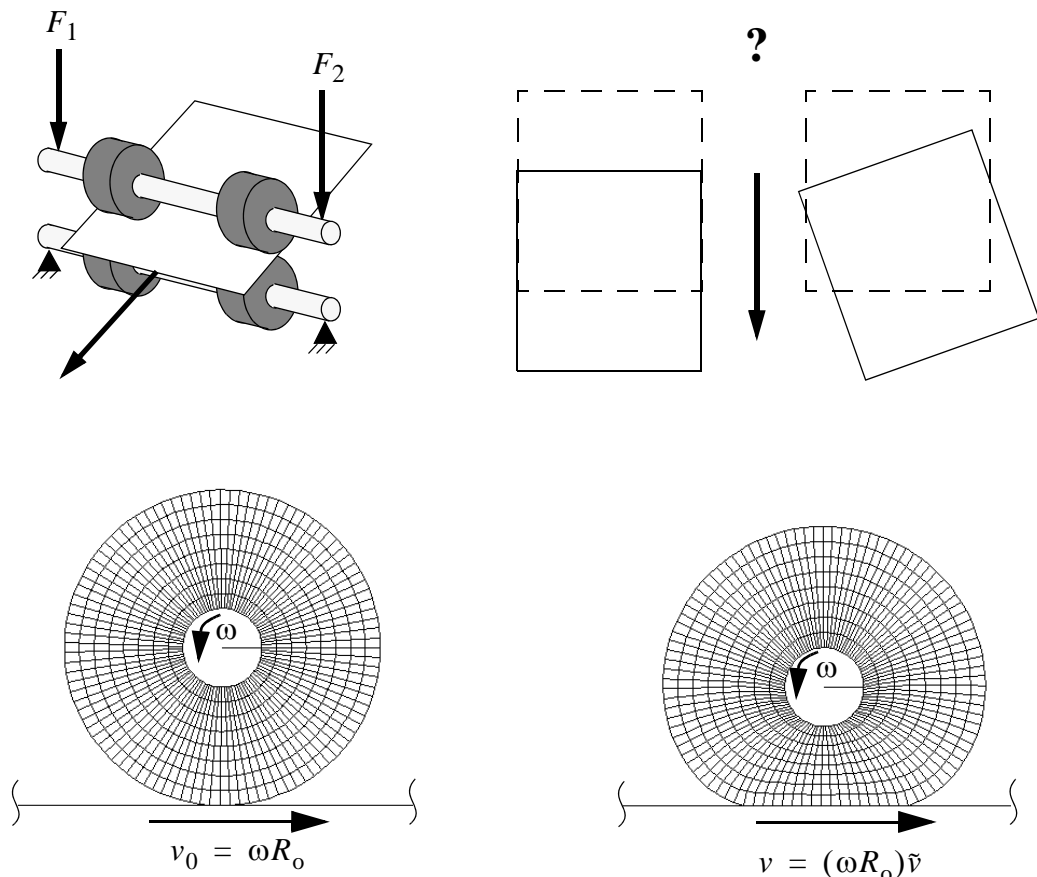


Two-Dimensional and Three-Dimensional Analysis of Nonlinear Nip Mechanics with Hyperelastic Material Formulations

Ted Diehl

Department of Mechanical Engineering
College of Engineering and Applied Science
University of Rochester
1995



Two-Dimensional and Three-Dimensional Analysis of Nonlinear Nip Mechanics with Hyperelastic Material Formulations

by

Ted Diehl

Submitted in Partial Fulfillment
of the
Requirements for the Degree
Doctor of Philosophy

Supervised by

Dr. Richard C. Benson

Department of Mechanical Engineering
College of Engineering and Applied Science

University of Rochester
Rochester, New York

1995

Copyright © 2010, 1993 by Ted Diehl

All rights reserved.

Revised printing, August 2010, to correct typographical errors in equations 2.10, C.21, and C.61.

This is dedicated to my parents and grandparents for teaching me the values of responsibility, hard work, and persistence.

Curriculum Vitae

The author was born on March 5, 1965, in Syracuse, New York. He earned the degrees of Bachelor of Science and Master of Science from the Mechanical Engineering Department at the Rochester Institute of Technology in 1988. His thesis work, under the supervision of Professor Hany Ghoneim, was on the finite element modeling of elastic/viscoplastic behavior. While a student at RIT, the author was awarded Society of Die Casting Engineers, NCAA Post-Graduate, RIT Graduate, and Kodak scholarships. He also received the Ellingston Award (recognizing RIT's best student athlete) and was named to the GTE Academic All-American and NCAA Lacrosse All-American teams. Following graduation, he accepted an engineering position with Eastman Kodak Company. His work at Kodak has concentrated on the analysis of a variety of structural mechanics problems. In the fall of 1989, he entered the Department of Mechanical Engineering of the University of Rochester to begin his doctoral studies on a part-time basis. His work, under the supervision of Professor Richard Benson, has concentrated on nonlinear mechanics related to flexible structures.

Acknowledgments

I wish to express my sincere gratitude to my advisor, Richard Benson, for his insight, guidance, and encouragement. Thanks are extended to the thesis committee: Victor Genberg, Renato Perucchio, Brian Stone, and Larry Taber. I would also like to thank fellow graduate students Ken Stack and John Lafleche for their informative discussions and assistance.

The author gratefully acknowledges the financial support of Eastman Kodak Company; particularly Woody Noxon, Ken Schwenker, Bill Hunt, Steve French, John Derimiggio, Charles Hura, and Richard Gammons. Special thanks are owed to several Kodak engineers for their assistance during various stages of this project: John Coval, Dave Fuest, Chip Hewitt, Bob Huot, Mike Moscato, Steve North, Bill Pelligra, Dwight Petrushik, Dan Rehberg, Tim Young, and Bob Zeman. The valuable technical discussions with Gary Bisson, Kevin Cole, and Eric Shih are acknowledged.

I would like to recognize Joop Nagtegaal for his generous support and valued advice regarding many theoretical aspects of ABAQUS and hyperelasticity. Special thanks are also owed to the HKS development and support-staff engineers.

The assistance of Michael McMindes and Daniel Rockafellow of illbruck, incorporated is acknowledged.

On a personal note, I would like to express my deepest appreciation and gratitude to my family. To my mother and father: your guidance gave me the foundation to make this possible. To my wife Kim: your understanding, support, and love gave me the strength to endure. To my daughter Krista: your entrance into the world gave me the inspiration to finish.

Abstract

Elastomer-covered rollers are commonly used in nip systems. This dissertation is built upon purely elastic constitutive relationships to model three elastomers: an open-cell polyurethane foam, a closed-cell ethylene propylene diene methylene (EPDM) expanded rubber, and a nearly incompressible urethane rubber. The first two materials are categorized as compressible and analyzed in the large strain region ($> 15\%$ compressive nominal strain) using hyperelastic strain-energy functions. Evaluation of urethane rubber is limited to small strains and Hooke's law because of its large stiffness. The compressible materials are experimentally tested under uniaxial compression and simple-shear deformation modes. Measurements of compressive stress, transverse strain, shear stress, and Poynting stress are utilized to evaluate two strain-energy functions: the "Blatz-Ko law for polyurethane foam" and the general "Ogden-Hill" form. The material data demonstrates that the Blatz-Ko form lacks sufficient generality to model, even qualitatively, these compressible materials for this range of deformation. Results establish that the highly nonlinear nature of the Ogden-Hill form allows for good quantitative predictions with two-term models. Experimental measurements of the urethane rubber using an ultrasound technique yield a Poisson's ratio of 0.4997.

Based on the constitutive laws, nip parameters of load/deflection, nip width, media speed ratio, and media skew are studied. Comparisons between implicit static and explicit dynamic finite element methods demonstrate the superior robustness of the latter in solving large-deformation frictional rolling problems. Experimental results on nip systems demonstrate that the analytical models yield good qualitative and reasonable quantitative predictions. These results establish that purely elastic material formulations capture the dominant behavior, but that material hysteresis, especially for the compressible materials, is needed for improved accuracy. In particular, non-rolling indentation-type predictions are more accurate than analyses which involve rolling (cyclic loading). Analysis of tire-like nip systems made of nearly incompressible urethane shows that the commonly used plane strain assumption causes significant overprediction of the media speed ratio. Assessment of nip parameter sensitivity to elastomer type and loading conditions indicates that media speed ratio is the most sensitive variable and nip width is the least.

Contents

1	Introduction	1
1.1	Overview	1
1.1.1	General Problem Description	1
1.1.2	Influence of Nonlinear Materials: Elastomers	3
1.1.3	Axial Variations	5
1.2	Literature Review	5
1.2.1	Nip Mechanics and Contact	6
1.2.2	Hyperelastic Material Formulations	11
1.3	Methods of Analysis	18
1.3.1	ABAQUS/Standard: Implicit Algorithms	18
1.3.2	ABAQUS/Explicit: Explicit Algorithms	20
1.4	Scope of Present Work	22
2	Theoretical Background of Hyperelastic Material Modeling	25
2.1	Compressible Elastomers	25
2.1.1	Evaluation of Non-Ideal Boundary Conditions	33
2.1.2	Drucker Stability	38
2.2	Nearly/Fully Incompressible Elastomers	39
2.2.1	Determination of Poisson's Ratio	43
3	Experimental Material Testing of Three Elastomers	46
3.1	Material Testing of SE410	47
3.1.1	Uniaxial Compression Test Results	47
3.1.2	Simple-Shear Test Results	52
3.1.3	Computing Constitutive Coefficients	54
3.2	Material Testing of R600U	60
3.2.1	Uniaxial Compression Test Results	64
3.2.2	Simple-Shear Test Results	66

3.2.3	Computing Constitutive Coefficients.....	69
3.3	Material Testing of Urethane.....	76
3.3.1	Uniaxial Tension Test Results.....	76
3.3.2	Poisson's Ratio Measurement Test Results.....	77
3.3.3	Evaluation of Neo-Hookean Material Representation.....	77
4	Nip Mechanics: Analyses and Experiments	81
4.1	Simplified Analysis of Media Speed Ratio.....	83
4.2	Non-Rolling Nip Problems.....	88
4.2.1	SE410.....	88
4.2.2	R600U.....	94
4.2.3	Urethane.....	101
4.3	Rolling Nip Problems.....	106
4.3.1	SE410.....	108
4.3.2	R600U.....	118
4.3.3	Urethane.....	122
4.3.4	Comparisons between SE410, R600U, and Urethane.....	127
4.4	Axial Variations.....	127
4.4.1	Skew in a R600U Tire-Based Nip System.....	127
4.4.2	Axial Variations in Continuous Nip Systems.....	132
5	Conclusions	139
5.1	Material Modeling.....	139
5.1.1	Theoretical Background.....	140
5.1.2	Experimental Results.....	142
5.2	Nip Mechanics.....	144
5.2.1	Non-Rolling Nip Results.....	144
5.2.2	Rolling Nip Results.....	145
5.2.3	Axial Variations.....	146
5.3	Summary.....	147
5.4	Suggestions For Future Work.....	148

References	149
Appendices	
A Large Deformation Mechanics	157
A.1 Kinematics of Deformation in 1-D.....	157
A.2 Kinematics of Deformation for General Motions	160
A.2.1 Common Measures of Strain for General Motions	166
A.2.2 Principal Measures of Strain	168
A.2.3 Stretch Invariants.....	168
A.3 Measures of Stress.....	170
A.4 Using Conjugate Pairs to Compute Stresses from a Strain-Energy Density Function.....	172
A.4.1 Compressible Materials.....	173
A.4.2 Nearly and Fully Incompressible Materials	176
B Comparison of Implicit and Explicit Finite Element Methods	180
B.1 Standard Algorithm: Implicit, Static	180
B.2 Explicit Algorithm: Central-Difference, Dynamic.....	187
C Further Details on Ogden-Hill Hyperelasticity	193
C.1 Compressible Ogden-Hill.....	193
C.1.1 Uniaxial Deformation.....	195
C.1.2 Simple-Shear Deformation.....	196
C.1.3 Volumetric Deformation.....	202
C.2 Nearly/Fully Incompressible Ogden-Hill.....	203
C.2.1 Volumetric Deformation.....	205
C.3 Drucker Stability	205
C.3.1 Drucker Stability for Compressible Ogden-Hill	208

List of Tables

3.1	Material constants for various laws to characterize SE410.....	57
3.2	Material constants for various laws to characterize R600U.....	69

List of Figures

1.1	Schematics of generic 3-D nip mechanics problems.	2
2.1	Schematics of primitive deformation modes.....	28
2.2	Schematic of uniaxial compression test set-up.	29
2.3	Schematic of simple-shear test set-up.	30
2.4	Applied stresses for simple-shear.....	31
2.5	Linear finite element model used to study end effects in uniaxial compression. Model uses 1/8 symmetry.....	34
2.6	Effective values of Young's modulus for a block constrained between two rigid plates. Solution based on Hooke's law.	35
2.7	Effective values of Poisson's ratio for a block constrained between two rigid plates. Solution based on Hooke's law.	37
3.1	Hysteresis in SE410 as measured by uniaxial compression.....	48
3.2	Experimental results for SE410 in compression. Specimen dimension ratio, B/L = 1.	49
3.3	Experimental results for SE410 in compression. Evaluation of different dimension ratios.	50
3.4	Measured value of initial tangent Poisson's ratio for SE410 correlates well with effective Poisson's ratio variation based on Hooke's law.	51
3.5	Experimental results for SE410 in simple-shear. Evaluation for different maximum shear strains.	53
3.6	Neither Blatz-Ko nor Brockman's law adequately models SE410.	55
3.7	One-term and two-term Ogden-Hill fits to SE410.	56
3.8	Calculated stress measures from two-term Ogden-Hill representation of SE410 for several compressive deformation modes.....	58
3.9	Calculated Drucker stability checks from two-term Ogden-Hill representation of SE410 for several compressive deformation modes.	59
3.10	Comparison of actual experimental results from uniaxial compression of SE410 and a nonlinear finite element model of the experiment using a two-term Ogden-Hill law. FEA model includes non-ideal boundary conditions.....	61
3.11	Hysteresis in R600U as measured by uniaxial compression.....	62
3.12	Anisotropic behavior of R600U in uniaxial compression.....	63
3.13	Influence of maximum applied strain on compression behavior of R600U.	64

3.14	Experimental results for R600U in compression. Specimen dimension ratio, $B/L = 1$.	65
3.15	Experimental results for R600U in compression. Evaluation of different dimension ratios.	67
3.16	Experimental results for R600U in simple-shear. Evaluation for different maximum shear strains.	68
3.17	One-term and two-term Ogden-Hill fits to R600U data.	70
3.18	Calculated stress measures from two-term Ogden-Hill representation of R600U for several compressive deformation modes.	72
3.19	Calculated Drucker stability checks from two-term Ogden-Hill representation of R600U for several compressive deformation modes.	73
3.20	Demonstration that using data from only one deformation mode yields poor results. Fits calculated for R600U.	75
3.21	Comparison between Hooke's law and neo-Hookean material representations for an uniaxial deformation mode.	78
3.22	Evaluation of simple-shear stress predictions for urethane using Hooke's law and neo-Hookean material representations.	79
3.23	Calculated Cauchy stresses from Hooke's law and neo-Hookean representations of urethane for several compressive deformation modes.	80
4.1	Schematic of nip systems evaluated.	82
4.2	Schematic of Y-symmetric plane strain elastomer-covered roller.	84
4.3	Simplified evaluation of speed ratio.	85
4.4	Standard finite element model for compression test of a SE410 roller.	89
4.5	Several Explicit finite element solutions for compression test of a SE410 roller.	91
4.6	Comparing different nip measures to evaluate Explicit solutions of SE410 roller compression.	92
4.7	Comparing approximate measures of speed ratio to evaluate Explicit solutions for SE410 roller compression.	93
4.8	Finite element prediction correlates well with experimental data from the non-rolling SE410 roller compression test.	95
4.9	Geometric approximation of nip width.	96
4.10	Influence of friction on approximate measures of speed ratio. Solutions from Explicit models of SE410 roller compression.	97
4.11	Finite element prediction compared to experimental data: non-rolling R600U roller compression test.	99

4.12	Strain contours in a R600U roller under 56% nominal compressive effective radial strain. Predictions from nonlinear finite element model.	100
4.13	Standard 2-D finite element model for compression of a urethane roller.	102
4.14	Finite element predictions compared to experimental data: non-rolling urethane roller compression test.	103
4.15	Evaluating the influence of Poisson's ratio on nip behavior and stable time increment.	105
4.16	Schematic of physical testing apparatus to measure media speed ratio and media skew.	107
4.17	Explicit finite element model of feeding a rigid sheet with a SE410 tire.	110
4.18	Evaluation of nip pressure and interfacial shear stress from Explicit rolling solution of SE410 roller. $\epsilon^{\text{eff}} = -33.3\%$	111
4.19	Predictions of media speed ratio of sheet from Explicit rolling solution of SE410 roller. $\epsilon^{\text{eff}} = -33.3\%$	113
4.20	Comparing estimates of media speed ratio for a SE410 roller based on nonrolling models to predictions based on a rolling model.	114
4.21	Experimental measurements of speed ratio for a stiff sheet fed by SE410 rollers.	117
4.22	Comparison of adjusted experimental data and analytical prediction of speed ratio for a SE410 roller feeding a sheet.	118
4.23	Comparing estimates of media speed ratio for a R600U roller based on nonrolling models to predictions based on a rolling model.	120
4.24	Comparison of experimental data and analytical prediction of speed ratio for a R600U roller feeding a sheet.	121
4.25	Plane strain Explicit finite element model of feeding a rigid sheet with a urethane tire.	123
4.26	Comparing estimates of media speed ratio for a urethane roller based on nonrolling models to predictions based on a rolling model. All solutions are plane strain.	124
4.27	Comparison of experimental data and analytical predictions of speed ratio for a urethane roller feeding a sheet.	126
4.28	Final assessment of the analytical modeling capability to predict media speed ratio for three elastomers: SE410, R600U, and urethane.	128
4.29	3-D Explicit rolling model used to analyze sheet skew in a R600U nip system.	129
4.30	Results from R600U nip system sheet skew evaluation.	131
4.31	Finite element models used to evaluate the continuous hollow-drum design. Meshes shown for hard-rubber case.	133
4.32	Primary cause of axial variation in nip parameters: drum deflections.	135

4.33	Comparison of shell and beam model predictions of axial variation in nip pressure for hollow-drum designs.	136
4.34	Comparing predictions of the axial variation in average speed ratio evaluated at nip edge for beam and shell models.	137
A.1	One-dimensional stretching of a bar.....	158
A.2	Schematic of relationship between strain and stretch ratio.	159
A.3	Comparison of several strain measures.....	160
A.4	Kinematics of deformation for general motions	161
A.5	Influence of rigid body rotation on unrotated and rotated configuration measures.	163
C.1	Schematic of simple-shear.....	197

List of Symbols

a	half nip width.
\mathbf{B}	left Cauchy-Green tensor.
\mathbf{C}	right Cauchy-Green tensor.
C_1, C_2	Mooney-Rivlin material constants.
c_d	dilatational wave speed of a bulk material about its undeformed state.
D_n	volumetric material constant for nearly incompressible Ogden-Hill form.
E, E^{eff}	Young's modulus, effective Young's modulus.
\mathbf{E}	tangent elasticity matrix.
f_μ	static coefficient of friction
F	applied load.
\mathbf{F}	deformation gradient tensor.
\mathbf{I}	identity tensor.
I_1, I_2, I_3	1st, 2nd, and 3rd invariants.
J	volume ratio.
K, K_0	bulk modulus, initial tangent bulk modulus.
$\tilde{\mathbf{n}}_{\text{I}}, \tilde{\mathbf{n}}_{\text{II}}, \tilde{\mathbf{n}}_{\text{III}}$	three principal directions of stretch in the unrotated configuration.
$\tilde{\mathbf{N}}_{\text{I}}, \tilde{\mathbf{N}}_{\text{II}}, \tilde{\mathbf{N}}_{\text{III}}$	three principal directions of stretch in the rotated configuration.
N	number of terms in an Ogden-Hill strain-energy function.
p	hydrostatic pressure.
P	nip contact pressure.
q	nip contact shear stress.
\mathbf{R}	rigid body rotation matrix.
R_o	outer radius of roller.
\mathbf{S}	second Piola-Kirchhoff stress tensor.
S, s	distance measure inside nip for undeformed and deformed states.

t	time.
$\Delta t, \tilde{\Delta t}$	time increment, nondimensional time increment.
\mathbf{t}	surface traction vector.
\mathbf{T}	Piola-Kirchhoff stress tensor.
\mathbf{T}^P	first Piola-Kirchhoff stress tensor.
T_i^{nom}	principal nominal stress.
t_{norm}	normal stress on inclined surface for simple-shear deformation mode.
t_{Poynt}	applied Poynting stress.
t_{shear}	applied shear stress.
t_{tang}	tangential stress on inclined surface for simple-shear deformation mode.
\mathbf{U}	right stretch tensor.
\mathbf{V}	left stretch tensor.
v	actual transport speed of sheet.
v_0	reference speed of sheet computed from the undeformed roller outer radius.
\tilde{v}	media speed ratio.
W	material strain-energy density function.
W^{dev}	deviatoric part of the material strain-energy density function.
W^{vol}	volumetric part of the material strain-energy density function.
X, Y, Z	Cartesian coordinates.
α_n	power constants for Ogden-Hill form.
β_n	material parameter for compressible Ogden-Hill form.
γ	shear stress from simple-shear deformation mode.
$\Gamma, \Gamma^{\text{ave}}$	instantaneous and average estimates of speed ratio.
δ_{ij}	Kronecker delta.
$\varepsilon, \varepsilon^{\text{con}}$	strain, conjugate strain.
ε^{a}	Almansi's measure of strain.
$\varepsilon^{\text{b}}, \varepsilon^{\text{biot}}$	Biot's measure of strain.
ε^{eff}	nominal effective radial strain.

ε^g	Green's measure of strain.
ε^{\ln}	logarithmic measure of strain.
θ	sheet skew.
t	time increment counter.
κ	material constant for Brockman law.
λ	stretch ratio.
Λ	Lamé constant for Hooke's law.
μ, μ_0	shear modulus, initial tangent shear modulus.
μ_n	shear moduli coefficients for Ogden-Hill form.
ν, ν^{eff}	Poisson's ratio, effective Poisson's ratio
ν_n	generalized Poisson's ratio.
ξ	fraction of critical damping.
ρ	material density.
σ	Cauchy stress.
σ^m	hydrostatic (mean) stress.
τ	Kirchhoff stress.
τ^{con}	conjugate stress.
${}_n\Psi$	shape functions for n nodes.

Notations

\bar{A}	deviatoric part of A .
A^T	transpose of A .

Chapter 1

Introduction

Study of the transportation and processing of a thin sheet by elastomer-covered rollers is known as *nonlinear nip mechanics*. *Nip* denotes the area of contact between the elastomer-covered rollers and the thin sheet. The description *nonlinear* refers to the nonlinear stress-strain behavior of elastomers, the nonlinear effects of large strains and large rotations, and the initially unknown contact boundary conditions that exist in the nip. The term *elastomer* denotes materials that can endure large amounts of elastic (recoverable) deformation without incurring significant permanent (nonrecoverable) deformation.

1.1 Overview

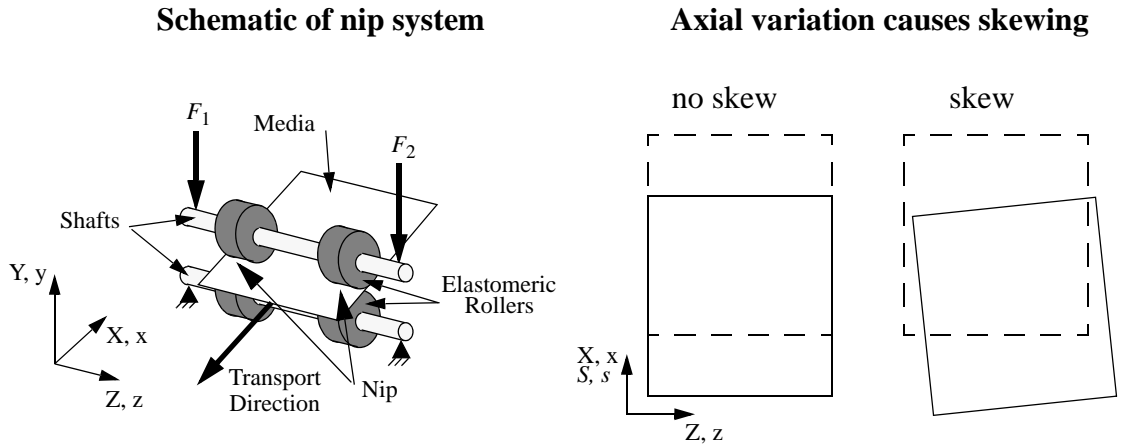
The technology of nip mechanics is vital to systems that handle and process thin media. Many devices such as web manufacturing equipment, photocopiers, printers, and facsimile machines process thin sheets of media. In office imaging equipment, behavior such as media skew, nonuniform image density generation, timing problems, and registration inconsistencies can all be caused by the unacceptable interaction between the elastomer-covered rollers and the media. These effects are frequently sensitive to changes in roller geometry, elastomer type, and external loading. Analytical models¹ that can reliably simulate these interactions will enable the development of improved, reliable, and robust technology.

1.1.1 General Problem Description

Figure 1.1 depicts two generic nip mechanics problems. The first design (Figure 1.1a) shows a nip system in which elastomeric tires are used to transport a sheet. The roller/sheet system is forced together creating two nips, one at each pair of tires. Rotation

1. Analytical models refer to classical “closed-form” or series-type solutions as well as numerical techniques such as finite elements or finite differences.

(a) Tire-based nip system



(b) Continuous nip system

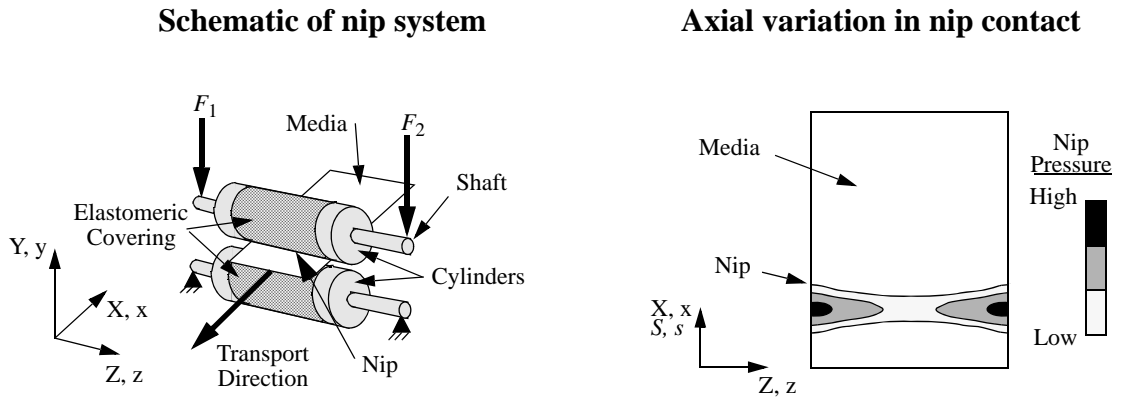


Figure 1.1: Schematics of generic 3-D nip mechanics problems.

of one of the shafts by an external torque along with frictional forces in the nip will cause both shafts to rotate, moving the sheet through the nip. This type of set-up is very common in situations where the sheet is only transported and not processed by the nip system. The second design (Figure 1.1b) consists of two continuous elastomer-covered cylinders which are compressing and feeding a sheet. This type of nip is frequently used to transport and process the sheet in subsystems such as a fuser station in a copier or printer. Variations of the continuous nip design depicted in Figure 1.1b are often found in nip mechanics problems. The classic calendering design, for example, has one elastomer-covered cylinder and one noncovered, relatively rigid, cylinder.

For elastomeric nip systems, sheets transporting through the nip travel at speeds which are different than would be predicted based on simple tangential-speed calculations using the undeformed outer radius of the feed rollers (or covered cylinders). The ratio of the actual transport speed, v , to the nominal (undeformed) calculated speed, v_0 , is termed the *speed ratio*, denoted as \tilde{v} . If the speed ratio is greater than one, the media is said to *overdrive* the feed rollers. When the speed ratio is less than one, the media is said to *underdrive* the feed rollers. Whether the media overdrives or underdrives the feed rollers is strongly dependent on the mechanical properties of the elastomers and the amount of external load applied to the nip system. Axial variations in speed ratio may exist if there is any nonsymmetric loadings or any axial variation in effective roller stiffness.

1.1.2 Influence of Nonlinear Materials: Elastomers

Many nip systems use elastomeric rollers to achieve both compliance and traction in the nip. In general, elastomeric materials can endure large amounts of elastic (recoverable) deformation without incurring significant permanent (nonrecoverable) deformation. Elastomers may be grouped into three categories: (1) nearly or fully incompressible elastomers such as rubber, (2) moderately compressible elastomers such as foam rubber, and (3) highly compressible elastomers such as resilient foam. Unfortunately, the inclusion of elastomers often leads to many unexpected results in terms of media transport and nip response.

The media speed ratio is governed by the local radial compression and the local hoop strain of the elastomer in the nip. The amount of compressibility of a given elastomer will determine the coupling between radial compression and hoop strain. For nearly (or fully) incompressible elastomers, this coupling will be very strong. As the compressibility of an elastomer increases, this coupling will decrease.

Another complicating factor in the analysis is the nonlinear material characteristics of many elastomers. In designs with highly compressible or moderately compressible elastomers, these materials may undergo deformations greater than 10% nominal effective radial strain and can be as large as 30% nominal effective radial strain.¹ This causes two problems: (1) simple linear strain measures may not be sufficient and (2) Hooke's law may not be appropriate to model a given elastomer. At large deformations, more advanced measures based on the deformation gradient and stretch ratios are frequently used (see Appendix A for further details). An improved material model for the elastomeric coverings requires the use of hyperelastic material formulations. A hyperelastic material formulation is built on the concept of a material strain-energy-density function which can be used to describe very general elastic stress/strain behavior. A material whose stress state is derivable from a strain-energy potential that is solely a function of the deformation gradient tensor is a hyperelastic material.

To be applicable to the variety of elastomeric materials used in industry, these hyperelastic constitutive laws must be capable of modelling the range of elastomer compressibility from nearly incompressible to highly compressible.² Elastomers can also be anisotropic and exhibit viscoelastic, time-dependent, hysteretic behavior. For this research, the material laws utilized will be limited to isotropic, time-independent behavior.

1. Nominal refers to a Biot measure of strain (see Appendix A for further details). Effective radial strain means that the radial strain is measured based on the net change in thickness of the elastomer due to deformation. The actual radial strain will vary through the thickness of the elastomer and will, in some locations, be greater than the effective radial strain.

2. A highly compressible material has a Poisson's ratio that is near zero.

1.1.3 Axial Variations

In general, axial variation in nip parameters such as media speed ratio, nip pressure, and nip width can significantly degrade the performance of nip systems. For imaging applications, these variations cause many image defects and transport problems due to induced image skew, media wrinkling, nonuniform image density transfer, and localized media/elastomer wear.

Figures 1.1a and 1.1b depict two common axial variations in nip systems. In Figure 1.1a, axial variations in the media speed ratio generate sheet skew. These axial variations can be caused by uneven external loading, nonuniform roller geometry, or other nonsymmetries in the system. The example in Figure 1.1b depicts axial variation in nip parameters such as nip contact pressure and nip width which are caused by deflections of the cylinders. Although not explicitly shown in this case, the axial variation in nip pressure will also cause axial variation in the media speed ratio which may induce media wrinkling. Since it is impossible to completely eliminate variations in these quantities, the system should be designed such that the sensitivity of nip parameters to these variations is minimized.

1.2 Literature Review

The literature for this research is divided into two main sections. The first section contains papers related to nip mechanics and contact in general. The second section discusses research focused strictly on hyperelastic material laws. The papers in the second section are not restricted to nip mechanics applications. A few papers that are reviewed in the first section have some references to hyperelasticity but do not concentrate on it.

For brevity of description, contact analyses that assume linear-elastic material laws and small strains will be referred to as “small-deformation” analyses. Analyses that include large strains and/or hyperelastic material laws will be referred to as “large-deformation” analyses.

1.2.1 Nip Mechanics and Contact

The fields of nip mechanics and contact have been studied by numerous researchers over the past one hundred years. These researchers have employed both experimental methods and analytical methods to evaluate these problems. Due to the complexity required for thorough experimental investigation, most of the published literature contains analytical studies. The books by K. L. Johnson [64] and by Kikuchi and Oden [71] provide excellent overviews of analytical techniques applied to nip mechanics and contact. The review by Raous [93] contains nineteen articles on numerical methods used for analyzing frictional contact.

The vast majority of the past analytical work in nip mechanics has focused on classical elasticity theories in which almost all solutions were limited to two-dimensional planar analysis. These planar analyses were usually plane strain models where axial variation in the nip was neglected. The solutions were based on some form of Hertzian contact where friction, if included, was typically limited to small relative sliding between bodies.

With the rapid advancement of numerical techniques in the last quarter century, numerous researchers have studied these problems with approximate numerical methods such as finite element techniques. As with many of the classical studies, a majority of the numerical investigations were restricted to planar analysis.

1.2.1.1 Experimental Investigations

In the late 1800's, Osborne Reynolds [92] published a very astute account of rolling friction. In his studies, Reynolds experimentally observed the phenomena of overdrive and underdrive for two systems: a soft rubber roller rolling on a flat, relatively rigid surface and a relatively rigid roller rolling on a flat rubber surface. Although he did not have a method (or modern computational tools) for a thorough mathematical treatment of the problem, he qualitatively explained that differences in elastic constants and/or geometry between the two bodies in contact would cause such observations. Reynolds described how the history-dependent nature of friction would cause asymmetric tangential surface tractions which, along with material and geometric differences, would create

microslipping¹ in the contact interface. He concluded that both microslipping in the contact zone and material hysteresis would cause energy dissipation which in turn would lead to rolling resistance.

Other researchers performing similar experimental investigations include Tabor [110], Parish [90], Borchardt [13], Greenwood, Minshall, and Tabor [38], Spengos [105], and Augenblick [4]. Tabor's experiments in 1955 evaluated a metal cylinder rolling over a rubber surface from which he concluded that the primary cause of rolling resistance was hysteresis losses in the rubber. Tabor determined that interfacial microslip added minimally to rolling resistance. Parish [90] measured pressures and nip widths for calendering designs: one metal roller and one rubber-covered roller. He compared his experimental results to small deformation plane strain equations developed by Hannah [43]. Parish found that, as the nip deformation increased, Hannah's formulae diverged from the experimental data. Parish suggested that the assumptions of small linear deformations utilized in Hannah's theoretical calculations caused the discrepancies. Borchardt [13] evaluated overdrive and underdrive for several calendering designs and demonstrated that, as cylinder length increases, global nip behavior approaches a state of plane strain. In 1965, Spengos [105] performed experimental investigations on a steel cylinder driving a rubber-covered cylinder. Spengos made numerous measurements of normal and tangential stresses at the nip interface and was able to quantitatively determine stick and slip regions.

In the early 1980's, Cole and Piarulli [21] made numerous experimental investigations of overdrive and other nip parameters related to the transport of thin media. Their studies considered systems with elastomeric rollers on shafts. Recently, Zeman [119] has experimentally studied pressure profiles and nip widths for media processing systems comprised of short hollow drums. Zeman's experiments show that nip parameters are extremely sensitive to both the drum and elastomer geometry as well as the types of media and elastomer in the nip.

1. *Microslipping* describes a phenomenon in which small zones of relative slipping occur in the nip. This is different from *gross slip* in which the nip is in a state of slip everywhere.

1.2.1.2 Analytical Investigations

The first satisfactory treatment of the contact of two elastic bodies was performed by Hertz [44] and is summarized in Johnson [64] and Kikuchi and Oden [71]. The analysis of Hertz assumes (1) the contact zone between the two bodies is elliptical, (2) the contact region is small relative to both the overall body dimensions and the radii of curvature for the bodies, (3) frictional forces are negligible, and (4) small-deformation theory is valid. This allowed Hertz to utilize elastic half-space formulations to solve the boundary-value problem of contact. Although the Hertzian-type formulations are limited to small-deformation mechanics, many important studies in nip mechanics have been performed with this type of analysis. A vast majority of these analyses are summarized in the books by Johnson [64] and by Kikuchi and Oden [71]. Only a select few are reviewed here.

In 1961 Parish [91] used Hertzian equations along with empirical relationships to analytically calculate nip width and nip pressures for rubber-covered pressure rollers. The study included axial variation in nip pressure and nip width caused by beam-bending effects of the rollers. The model consisted of a beam on a nonlinear Winkler foundation where the foundation stiffness was determined from independent plane-strain Hertzian-based analyses. The models quantitatively predicted only stiff systems in which rubber deformations were small. During the late 1960's, Bentall and Johnson [10] produced a detailed study of rolling contact using small deformation, plane strain, elastic half-space models. The analyses of [10] showed that microslip only had a small influence on overall rolling friction. Kalker [66,67,68,69] performed several analyses (both 2-D and 3-D) of rolling contact using small deformation half-space models. Studies of both steady state and transient (history dependent but with no inertial effects) rolling friction were presented. Steady state solutions of Kalker were in good agreement with those of Bentall and Johnson [10]. Hahn and Levinson [40,41] studied the indentation of elastic layers bonded to a rigid cylinder. Their solutions used closed-form series solutions based on a stress function and were restricted to two-dimensional small-deformation theory. For small Coulomb friction coefficients (< 0.3), friction did not significantly affect contact stresses.

The analytical investigations surveyed up to this point have not included any effects of media that may exist between the rolling bodies. In 1968 Bentall and Johnson [11] analyzed an elastic strip in plane rolling contact using a modified Hertzian solution. The models, including frictional stick and slip, computed the strip's overdrive and underdrive behavior. In the early 1980's Soong and Li [102,103,104] used two-dimensional small-deformation theory with series-type solutions to study various rolling contact problems with elastic-layered cylinders nipping a sheet. Evaluations of sheet overdrive were performed for sheets with and without external loads. The studies found that significant slip did not occur when high-traction rollers (Coulomb friction coefficient > 0.8) were driving a sheet of paper.

Cole and Piarulli [19,20,21,22,23] performed numerous small-deformation analyses of systems similar to Soong and Li [102,103,104]. Axial variations due to roller beam-bending were included by Cole and Piarulli using methods similar to that of Parish [91]. The analysis used the amount of hoop strain in the elastomeric coverings inside the contact zone to determine the resulting overdrive of the media. Retarding sheet forces and incompressible covers were studied. The small-deformation analyses of Cole and Piarulli provided excellent insight relative to the causes of various nip phenomena. Unfortunately, because of the linear assumptions used in the analyses, their analytical models had a difficult time predicting accurate quantitative nip parameter results when nip deformations became large.

In 1988, Keene [70] used linear finite element methods with point-gap contact algorithms (see [81] for an explanation of point-gap contact) to study the axial pressure variation of a hollow metal drum and a solid metal cylinder compressing a sheet of paper. Keene's model consisted of a shell loaded through gap contacts by a two-dimensional field of discrete linear springs representing the effective stiffness of the paper and solid cylinder.¹ Keene concluded that shell effects were the primary cause of axial variation in nip pressure. Unfortunately, this form of elastic foundation was incapable of evaluating media overdrive and underdrive because hoop strains in the media (or elastomer, if one had been included in the field of springs) were not part of the formulation.

1. Keene's model is a two-dimensional version of a Winkler foundation.

All of the analytical studies discussed up to now have assumed small-deformation theory; linear-elastic material laws, small strains, etc. Recently several researchers have used a variety of nonlinear analyses to model large-deformation nip mechanics. In 1980, Batra [7] studied a plane strain, thick rubber-covered, rigid cylinder being indented by a frictionless, noncovered, rigid cylinder. Batra employed nonlinear finite element methods and modeled the elastomer as a Mooney-Rivlin material (see Section 1.2.2.1 for a description of a Mooney-Rivlin material). Batra compared his solutions to the experimental work of Spengos [105] and found reasonable agreement. In 1986, Oden and Lin [85] extended some nonlinear finite element methods used by Campos, Oden and Kikuchi [16] to model steady state large-deformation rolling contact of a viscoelastic cylinder including inertial dynamic effects. The analysis was developed to simulate a tire rolling on a flat surface at high speeds. The problem formulation was specifically designed for cylindrical spinning bodies, similar to earlier small-deformation analyses by Zeid and Padovan [120,121]. All analysis was plane strain and the elastomer was modelled with Mooney-Rivlin hyperelastic laws. To model viscoelastic behavior, a linear strain-history term was appended to the original Mooney-Rivlin formulation. Frictional contact was modelled with a smoothed Coulomb friction law (a form of penalty method). Oden later investigated several forms of friction laws [78]. In 1987, Bass [5] extended previous work by Oden, Bass, and Lin [84] to analyze 3-D rolling contact of an incompressible Mooney-Rivlin tire subjected to loads typical of those experienced during the driving of an automobile.

In 1992, Diehl [26,27,28], using nonlinear finite element methods, expanded the basic work of Keene [70] to include multiple layers of different media in the nip using surface contact algorithms and a variety of stiffened shell designs. The two-dimensional field of linear springs used by Keene [70] was replaced by continuum elements whose material behavior was based on simple nonlinear hypoelastic material laws with no Poisson effect. Diehl showed by analysis that adding hoop-ribs inside the drums dramatically reduced the axial pressure variation. He also found that designs with low nip compliance (no elastomeric covering in the nip) were extremely sensitive to drum concavities as small as 0.0005 inch. These findings were verified informally in experiments by Zeman [119]. Diehl noted that the simple hypoelastic material laws used to model the elastomeric

materials in the nip were not sufficient (because of the omission of Poisson's effect) for proper evaluation of the media overdrive that was prevalent in the system.

In 1993, Diehl, Stack, and Benson [29] studied axial variations in nip pressure, nip width, and media overdrive using three-dimensional nonlinear finite element methods. The study investigated two different designs: an identical-short-hollow-drum design and a classic calendering design. Both cases included effects of elastomeric coverings modelled with hyperelastic material laws. The analysis evaluated axial variations in nip pressure and media overdrive. For the short-hollow-drum design, the axial variation in nip quantities was dominated by local shell effects and not by global beam-bending behavior. In the classic calendering design, the transition from plane strain near the axial middle of the roller to plane stress at the free edge of the roller was found to cause significant axial variation in nip quantities. Axial variations in overdrive were then used to compute approximate boundary conditions for the study of web wrinkling which were used in the analysis of Benson, et al. [9].

In 1993, Stack and Benson [9] analyzed the axial variations in contact loads for an elastomer-covered rigid cylinder slowly rotating (inertial dynamics negligible) against a flat rigid surface with Coulomb friction. Both right-circular cylinders and conical cylinders were studied. Nonlinear finite element methods were used for the three-dimensional solutions and the elastomers were modeled with the same Mooney-Rivlin hyperelastic law used by Oden and Lin [85]. Strong edge effects were found which further demonstrated the limitations of plane strain models.

1.2.2 Hyperelastic Material Formulations

The books by Treloar [112], Atkin and Fox [3], Ogden [89], Green and Zerna [37], and Ward [116] and the papers by Treloar [113], Hopkins [61], and Beatty [8] provide an excellent overview of both the theoretical and experimental study of hyperelastic materials. In particular, the book by Treloar [112] contains numerous test data and hyperelastic formulations that have been used by many researchers.

The constitutive behaviors in the current study will utilize phenomenologically based strain-energy functions and will be limited to isotropic, time-independent materials under isothermal conditions. Statistical, molecular-based material models for rubbers are discussed in Treloar [112] but will not be used in this work. The research of Srinivasan and Perucchio [106] and Morman [80] address hyperelastic issues of material orthotropy and viscoelasticity, respectively. The work of Ashby [2], Gent and Thomas [34], Gibson and Ashby [35,36], and Warren and Kraynik [117] evaluates basic deformation mechanisms to describe the mechanical behavior of highly compressible foams in various deformation regions. While this work develops equations to describe the basic mechanisms that govern a foam's mechanical behavior, these simple relationships are not applicable to analyzing general stress states.

Much of the literature in the area of hyperelasticity is divided into two basic forms: (1) strain-energy functions written as functions of stretch invariants¹ (see Equations A.53 - A.55 for stretch-invariant definitions) and (2) strain-energy functions written as functions of the principal stretch ratios (which are themselves invariant). In the following subsections, several equations will be shown describing various forms of strain-energy functions. The reader is directed to Appendix A for further details on the variables used in the equations and a detailed discussion of large-deformation mechanics.

1.2.2.1 Stretch-Invariant Forms

In 1940, Mooney [79] published one of the earliest phenomenological models used for the analysis of rubbers undergoing large deformations. Mooney's model assumed that the material was isotropic and incompressible, and that shear stress was proportional to shear strain in simple-shear. Mooney proposed a strain-energy function, W , of the form

$$W(\lambda_1, \lambda_2, \lambda_3) = C_1(\lambda_1^2 + \lambda_2^2 + \lambda_3^2 - 3) + C_2(\lambda_1^{-2} + \lambda_2^{-2} + \lambda_3^{-2} - 3) \quad (1.1)$$

1. I use here the term *stretch* invariants to describe what is commonly called *strain* invariants. The use of the word *strain* can be misleading because the invariants are not computed as invariants of a strain tensor but rather as invariants of the left or right Cauchy-Green tensors (which are measures of stretch). Strictly speaking, computing invariants of a strain tensor would produce different values for the invariants depending on the strain definition chosen.

where λ_1 , λ_2 , and λ_3 are the three principal stretch ratios computed from the deformation gradient tensor. The material constants C_1 and C_2 are related to the shear modulus, μ , by

$$\mu = 2(C_1 + C_2) \quad (1.2)$$

and the three stretch ratios are related by the incompressibility constraint as

$$\lambda_1 \lambda_2 \lambda_3 = 1. \quad (1.3)$$

Based on experimental evidence for soft rubber, Mooney reported that the linear shear stress-strain relation was valid up to at least 200% shear strain.

As published by Mooney, his strain-energy function is written as a function of the principal stretch ratios. Combining the incompressibility assumption of Equation 1.3 with the definitions of the stretch invariants, Equations A.53 - A.55, Mooney's strain-energy function, Equation 1.1, can be written as

$$W(I_1, I_2) = C_1(I_1 - 3) + C_2(I_2 - 3) \quad (1.4)$$

where I_1 and I_2 are the first and second stretch invariants, respectively. This form, Equation 1.4, is commonly referred to as the Mooney-Rivlin strain-energy function.

In the late 1940's and early 1950's, Rivlin et al. [94 - 99] performed extensive theoretical and experimental analyses of rubbers undergoing large deformations. Similar to Mooney, Rivlin et al. assumed that the materials were elastic, incompressible, and isotropic. However, Rivlin chose a rather abstract approach to model the strain-energy functions; he allowed for the possibility of negative values of principal stretch ratios (see [97] p. 384).¹ This required that the strain-energy function be a function of λ_1^2 , λ_2^2 , and λ_3^2 and was therefore expressed in terms of the stretch invariants (I_1, I_2, I_3). Applying the *assumed* incompressibility constraint, Rivlin expressed the strain-energy function as a function of the first two stretch invariants;

$$W = W(I_1, I_2). \quad (1.5)$$

1. A negative principal stretch ratio implies that the material has turned inside-out. The modern definition of principal stretch ratios is that they must all be positive.

Rivlin's experimental work concentrated on finding functional forms of $\partial W / \partial I_1$ and $\partial W / \partial I_2$. This was based on the fact that, for incompressible materials, the principal Cauchy stresses, σ_i , can be expressed as functions of the partial derivatives of W with respect to I_1 and I_2 plus an arbitrary hydrostatic pressure, p ; namely

$$\sigma_i = 2 \left(\lambda_i^2 \frac{\partial W}{\partial I_1} - \frac{1}{\lambda_i^2} \frac{\partial W}{\partial I_2} \right) + p \quad i = 1, 2, 3. \quad (1.6)$$

Numerous investigators have used Rivlin's foundation as a basis for further study regarding hyperelastic material laws.

In 1962, Blatz and Ko [12] developed constitutive models for compressible elastomers (foam rubbers). Their strain-energy function was based on experimental observations from polyurethane foamed rubber and an assumption that Poisson's ratio is valid to relate true logarithmic strains to each other, even for large strains.¹ The "Blatz-Ko form for foamed polyurethane" is

$$W = \frac{\mu}{2} \left(\frac{I_2}{I_3} + 2J - 5 \right) \quad (1.7)$$

where I_2 and I_3 are the second and third stretch invariants, J is the volume ratio, and μ is the shear modulus. This form yields an effective Poisson's ratio, ν , of 1/4. Several closed-form solutions for a variety of finite strain problems with Blatz-Ko materials have been presented by Carroll and Horgan [17] and Chung and Horgan [18]. Beatty [8] presents detailed theoretical analysis of the Blatz-Ko law in his overview of hyperelasticity.

Brockman [14] used a modified version of the general Blatz-Ko form (see [12] for the general form) to model compressible rubbers. Brockman's form is

$$W = \frac{\mu}{2} \left[I_1 - 3 + \frac{2}{\kappa} (J^{-\kappa} - 1) \right] \quad (1.8)$$

1. This assumption is only valid for the logarithmic measure of strain, $\ln(\lambda)$. For measures of strain such as Green's strain, $(1/2)(\lambda^2 - 1)$, this assumption is not valid. This is easy to show using a uniaxial tension deformation with Poisson's ratio, ν , equal to 0.5. The volume ratio, J , should be computed as unity.

where I_1 is the first stretch invariant, μ and J have the same meanings as above, and κ is related to Poisson's ratio by

$$\kappa = \frac{2\nu}{1-2\nu}. \quad (1.9)$$

Brockman used a value of $\kappa = 13.3$ ($\nu = 0.465$) in his analysis. In Brockman's paper he notes that the generalized Blatz-Ko theory and the Mooney-Rivlin models suffer from the fact that their limited (and constrained) material parameters typically allow only qualitative predictions over a wide range of deformations.

Alexander [1] reviewed strain-energy functions for his work in analyzing neoprene films used in balloons. Alexander shows that the Mooney-Rivlin strain-energy function, Equation 1.4, does provide good correlation with uniaxial tension and simple-shear test data of Treloar [112]. However, the Mooney-Rivlin form provided poor correlation with biaxial tension and pure shear experiments. The final form of the strain-energy function adopted by Alexander is quite complex and was reported to work well for neoprene. Other prominent work with stretch-invariant based strain-energy functions includes James, Green, and Simpson [63], Haines and Wilson [42], and Ling, et al. [74].

1.2.2.2 Principal Stretch-Ratio Forms

In 1967, Valanis and Landel [115] moved away from Rivlin's stretch-invariant-based formulations and proposed that the strain-energy function, W , could be expressed as separable symmetric functions of the principal stretch ratios, $w(\lambda)$, as

$$W(\lambda_1, \lambda_2, \lambda_3) = w(\lambda_1) + w(\lambda_2) + w(\lambda_3) \quad . \quad (1.10)$$

Valanis and Landel noted that their separability assumption was in accordance with similar separability assumptions used in statistical network theory (see Treloar [112] for details of the statistical network theory). Moreover, experimental data from James, Green, and Simpson [63], supported the Valanis-Landel assumption.

In the early 1970's, Ogden [86,87,88] proposed that the strain-energy could be written in the form

$$W = \sum_n^N \frac{\tilde{\mu}_n}{\alpha_n} (\lambda_1^{\alpha_n} + \lambda_2^{\alpha_n} + \lambda_3^{\alpha_n} - 3) \quad (1.11)$$

where N is the number of terms used in the series defined by material parameters $\tilde{\mu}_n$ and α_n (both of which are real and not restricted to being integers). This form assumes material isotropy and was initially developed for incompressible materials. Ogden based this form on the initial work by Hill [57,58] (plus some unpublished work of Hill) and on the work of Valanis and Landel [115].

For this thesis, I will be using several variations of the basic function proposed by Ogden, Equation 1.11, written in a slightly more physical form; namely

$$W = \sum_n^N \frac{2\mu_n}{\alpha_n} (\lambda_1^{\alpha_n} + \lambda_2^{\alpha_n} + \lambda_3^{\alpha_n} - 3) \quad (1.12)$$

where the summation of the coefficients μ_n equals the initial tangent shear modulus. Ogden's modified formulation, Equation 1.12, is a special form the Valanis-Landel model, Equation 1.10, with

$$w(\lambda_i) = \sum_n^N \frac{2\mu_n}{\alpha_n} (\lambda_i^{\alpha_n} - 1) . \quad (1.13)$$

In developing his model, Ogden has utilized the fact that the principal stretch ratios are always positive. Thus, Ogden has removed Rivlin's non-physical restriction that the strain-energy be functions only of *even* powers of the principal stretch ratios. Ogden [87,88], as well as Treloar [112,113], Twizell and Ogden [114], Storakers [109], and Hibbitt et al. [54] have demonstrated that the basic form of Equation 1.12 is capable of simulating both incompressible and compressible hyperelastic materials.¹

In 1978, Hill [59] proposed the general form of a strain-energy function suitable for materials with large amounts of compressibility (such as foams). Hill's function augments

1. There are slight modifications applied to Equation 1.12 for various compressibility conditions. This is discussed in more detail in Chapter 2 and Appendix C.

the basic Ogden form by adding an extra function of the volume ratio, J . Hibbitt et al. [49,50,51,54] formalized Hill's basic equation, which had been further developed by Storakers [109], as

$$W = \sum_{n=1}^N \frac{2\mu_n}{\alpha_n} \left[(\lambda_1^{\alpha_n} + \lambda_2^{\alpha_n} + \lambda_3^{\alpha_n} - 3) + \frac{1}{\beta_n} (J^{(-\alpha_n\beta_n)} - 1) \right] \quad (1.14)$$

where the material parameters β_n are related to a generalized Poisson's ratio measure;

$$\beta_n = \frac{\nu_n}{1 - 2\nu_n}. \quad (1.15)$$

We note that the strain-energy functions developed by Ogden, which were based in part by the work of Hill, and the strain-energy functions proposed by Hill, which were modifications of Ogden's formulation, are very similar. For the rest of this thesis, strain-energy functions of the form

$$W = \sum_{n=1}^N \frac{2\mu_n}{\alpha_n} \left[(\lambda_1^{\alpha_n} + \lambda_2^{\alpha_n} + \lambda_3^{\alpha_n} - 3) + f(J) \right] \quad (1.16)$$

where f denotes a function, will be referred to as Ogden-Hill formulations.

In a discussion of Treloar's review article on hyperelasticity [113], Hopkins [61] notes "... that there is generally, relatively much greater ease fitting finite representations of the stored-energy [strain-energy] function to experimental data when it is expressed in terms of the principal stretches, λ_i , rather than in terms of (say) the invariants, I_1, I_2, I_3, \dots . Moreover, the λ_i 's are intrinsically of a similar nature, whereas, in contrast, the invariants, I_1, I_2, I_3 are dissimilar quantities and further they lack a direct kinematical interpretation." Hopkins further points out that one *disadvantage* of stretch-ratio-based strain-energy functions is that for general boundary value problems (other than simple deformation modes in which principal *directions* do not vary throughout the body), the principal stretch directions must be included as unknowns. Recent work by Li [73], Saleeb, Chang, and Arnold [100], and Hibbitt et al. [51] have addressed this issue in the context of finite element implementations.

1.3 Methods of Analysis

Finite strain theory must be utilized to analyze elastomeric nip configurations that endure large amounts of deformation. In addition, geometry and stiffness characteristics of the shafts and cylinders may need to be considered by idealizing them as beams, shells, solids, or any combination thereof. Considering these requirements, we chose nonlinear finite element methods to perform the bulk of the analysis.

The solution algorithms must include the following features: nonlinear geometric and material capabilities, surface contact algorithms with friction capabilities, and multipoint constraint (MPC) capabilities to correctly and efficiently include additional required constraints (such as rigid *bars* or beam offsets for rib-stiffened shells). Since the development of an entirely new nonlinear finite element program that includes all these formulations is not practical for a single thesis research project, the use of existing commercial codes is pursued.

Two nonlinear finite element programs with many of these capabilities are ABAQUS and MARC. This research will utilize the numerous solution algorithms available in ABAQUS because of its implementation of Ogden-Hill hyperelasticity and the explicit dynamics algorithms which will be used to study rolling frictional behavior in 2-D and 3-D analyses. ABAQUS uses nonlinear Lagrangian-based finite element methods and is actually two distinct programs: ABAQUS/Standard and ABAQUS/Explicit (see [47,49,50,51,52] for detailed documentation). The following two subsections provide a brief description of these programs. More detailed descriptions of these programs and their methods of solution are found in Appendix B.

1.3.1 ABAQUS/Standard: Implicit Algorithms

ABAQUS/Standard (or simply Standard) contains static and dynamic algorithms plus several user-definable utilities which make the program very useful for research. The Standard program uses traditional implicit algorithms with Newton-Raphson methods to solve the resulting nonlinear equations of equilibrium. The algorithms are implicit because, in general, an explicit solution of the unknown variables is not possible. This is

due to the nonlinear nature of the equations plus the use of Newton-Raphson (or modified Newton-Raphson) algorithms. For a given *step*, the magnitude of each boundary condition (forces, displacements, etc.) is subdivided into *increments*. The general solution of any increment usually involves a few iterations through a Newton-Raphson solver to obtain a converged answer.¹ The solver uses a banded Jacobian matrix (often called a tangent stiffness matrix) to find the corrections to the most recent approximations of the unknown variables. Because hundreds of equations (or more) are solved in any iteration, inversion is expensive. However, for many problems, relatively large increments can be taken which makes the solution to many problems feasible.

One of the most difficult nonlinear structural problems to solve with Newton-Raphson techniques is that of large deformation with frictional contact. This is because (1) contact with large deformation requires complex and expensive contact algorithms and (2) frictional contact is a nonconservative discontinuous phenomenon. Standard offers several algorithms to evaluate many types of large deformation contact.² The discontinuous nature of friction, however, can cause serious convergence difficulties. This is especially true when solving 2-D or 3-D rolling nip mechanics problems with friction. The primary reason for difficulty is a behavior known as chatter: during the Newton iterations of a given increment, certain locations in the mesh oscillate between either stick and slip or between contact and no contact. The likelihood of this chatter tends to increase with the size of the model. When chatter occurs, the Newton-Raphson quasi-time discretization (solution incrementation) decreases in size in an attempt to obtain convergence. If chatter persists, the increment size will continue to decrease until, for all practice purposes, the solution dies. Standard offers several numerical algorithms (typically applying a variety of penalty methods) to minimize this problem by lessening the discontinuous nature of friction. Unfortunately, experience has shown that excessive and frequent chatter is likely for 2-D or 3-D rolling frictional contact.

1. Newton's method is quadratically convergent and therefore will typically converge in less than 10 iterations given a sufficiently close initial approximation to the solution.

2. Algorithms to model completely general three-dimensional flexible-flexible contact with large relative sliding in any direction are not currently available in ABAQUS/Standard but such algorithms are available in ABAQUS/Explicit. Several algorithms are available in ABAQUS/Standard for three-dimensional flexible-flexible contact with certain restrictions. See [49] for a complete description.

1.3.2 ABAQUS/Explicit: Explicit Algorithms

ABAQUS/Explicit (or simply Explicit)¹ uses an explicit dynamics approach to solve the nonlinear equations of *dynamic* equilibrium. An explicit central-difference integration operator is used to *march* the equations of dynamic equilibrium forward in time. The solution of equilibrium at any given point in time is very efficient because the solution is based on the inversion of a diagonal (lumped) mass matrix. The inversion of a diagonal matrix is trivial compared to the very expensive computations required to invert the banded Jacobian matrix with the implicit method (Standard program). The essence of the explicit solution is that, at any time, the accelerations are *explicitly* computed by “dividing” the difference between external and internal forces by the mass matrix. The newly found accelerations are then integrated by the central-difference formulae to obtain velocities and displacements. These new values of velocity and displacement at the new (later) time are then used to update internal and external forces and the algorithm is repeated for the next time increment.

Two advantages of this method are seen immediately: no inversion of a banded matrix and no repeated iterations for convergence. Two disadvantages of the explicit method are that only dynamic solutions are computed and that the solution stability is limited by the highest natural frequency in the system.² This stability limit requires that the time increment be extremely small (less than twice that of the smallest natural period in the system). Since the explicit method is based on time marching, computational effort is directly related to the number of time increments required for solution. Due to the small time-increment constraint, explicit techniques are only feasible for short-duration events (typically much less than one second).

The greatest advantage of the explicit technique is realized when solving large deformation problems with frictional contact. The contact algorithms in Explicit are capable of handling very general 2-D and 3-D flexible-flexible contact with large relative

1. Generic references to *implicit* or *explicit* finite element methods use no capitalization. References specifically related to ABAQUS' implicit and explicit codes are denoted as Standard and Explicit, respectively.

2. The reasons for this stability limit are discussed in Appendix B.2.

sliding in any direction. The algorithms are based on kinematic enforcement of contact between faceted surfaces. The essence of the method is as follows:

1. During any given increment in the solution, the kinematic state (accelerations, velocities, and displacements) of all nodes in the model are advanced one time increment into a *predicted* state *without* regard to contact constraints;
2. The contact conditions of two surfaces, **A** and **B**, are evaluated. Are nodes penetrating surfaces and/or sliding along surfaces?
3. If any node is found to violate contact, nodal accelerations are modified and distributed loads¹ applied to the node and contacting surface such that contact constraints are kinematically satisfied. If friction is present, appropriate frictional forces are also included.

The general algorithm uses a weighted *master-slave* formulation:

1. The contact calculation is performed for the nodes of surface **A** penetrating surface **B**
2. The contact calculation is performed for the nodes of surface **B** penetrating surface **A**
3. The two solutions are combined by a user-defined weighted average.

The algorithm is extremely robust and does not suffer from chatter because no iterations are necessary.

Originally, explicit dynamic techniques were used for very high speed, dynamic events like a car crash or a missile impacting a tank (“event time” much less than one second). Recent research [46,82] has demonstrated that explicit dynamic techniques are capable of solving many other problems where *inertial dynamic effects are not important* and whose actual event-time may be greater than one second. These quasi-static solutions are computed by artificially speeding up the time of the event to a point that an efficient dynamic solution is obtained while inertial effects remain negligible.

1. Distributed loads are the corresponding inertial body forces to decelerate the nodes to avoid penetration.

Many metal-forming problems have recently been solved in this manner [46,82]¹. Two characteristics of metal-forming problems are large deformations and rolling frictional contact. These are the same characteristics that occur in nonlinear nip mechanics.

The current study of nip mechanics is only applied to problems where inertial effects are not significant and not of interest. Hence, the same method of artificially increasing the event speed will be used to investigate the nip problem. To verify that valid artificial values of the event speed have been chosen, several 2-D quasi-static Explicit computations will be compared against Standard implicit (static) solutions.

1.4 Scope of Present Work

The primary thrust of this research is to improve our understanding of elastomeric nip systems. This study will enhance our capabilities in analyzing and simulating these nip systems as they process and transport thin media. This thesis will utilize finite element models with large deformation, large strain, large rotation, and hyperelastic material formulation capability. The specific objectives are to

1. thoroughly evaluate the capability of representing elastomeric materials with the general family of Ogden-Hill strain-energy density functions,
2. obtain Ogden-Hill material constants for three particular elastomers classified as highly compressible, moderately compressible, and nearly incompressible,
3. verify the qualitative and quantitative capability of modeling non-inertial 2-D and 3-D elastomeric rolling nip problems by comparing models with experiments,
4. assess sensitivity of various nip-system parameters to elastomer type and loading conditions.

Because the Ogden-Hill forms of hyperelasticity are very general functions of the primary stretch ratios, they have the ability to describe a wide variety of elastomeric materials

1. Previous attempts at solving realistic metal-forming problems with implicit-based solution techniques have had only limited success; primarily due to frictional contact chatter and extreme computational expense.

ranging from highly compressible foams to nearly incompressible (and fully incompressible¹) rubbers. The Rivlin-style polynomial invariant hyperelastic formulations discussed in Section 1.2.2.1 are more traditional hyperelastic constitutive relationships based on the material's stretch invariants. These forms are less general than the Ogden-Hill formulations because they are constrained to even functions of the principal stretch ratios.

To better understand the capabilities, limitations, and applications of the Ogden-Hill strain-energy functions, several experiments with three different types of elastomers will be performed. The materials used will be

1. R600U² - a highly compressible polyester-based open-cell polyurethane foam,
2. SE410² - a moderately compressible closed-cell EPDM³ expanded rubber,
3. urethane - a nearly incompressible polyether-based polyurethane rubber.

Material experiments will concentrate on obtaining stress-strain information needed to compute the required material coefficients. More will be said about this in Chapters 2 and 3.

To further quantify the adequacy of these material laws, several nip-related experiments will be undertaken. The first set of nip experiments will be non-rolling tests where an elastomeric roller (with a solid steel hub) is compressed between two flat plates. Measurements of applied load and nip width as a function of roller compression will be compared against finite element models using the hyperelastic constants obtained from the material experiments. The final set of experiments will involve the assessment of media speed ratio as a function of roller deformation and roller material. These nip experiments and analyses will be discussed completely in Chapter 4.

1. More will be said about fully incompressible materials later.

2. This material was manufactured by illbruck, incorporated, Rochester NY.

3. EPDM stands for ethylene propylene diene methylene.

The analyses that are performed in Chapter 4 utilize 2-D and 3-D models. The 2-D plane strain and plane stress analyses are designed to extract the maximum information regarding analysis assumptions and modeling methods. Evaluation of nip parameter sensitivity to friction, elastomer compressibility, and external loading will be performed. The 3-D analyses will predominantly study axial variations in nip systems.

This research will improve our fundamental understanding of the mechanical behavior for a range of elastomeric materials and the mechanical behavior of elastomeric nip systems. These investigations will provide specific (and general) information to enable the engineering community to develop more reliable and robust technology.

Chapter 2

Theoretical Background of Hyperelastic Material Modeling

Modeling of elastomers ranging from very compressible resilient foams to nearly/fully incompressible rubbers is addressed in this research. All elastomers that will be analyzed are assumed to be isotropic, time-independent materials loaded under isothermal conditions. Because all materials are assumed isotropic, their strain-energy functions must be symmetric functions of the three principal stretch ratios. The generic Ogden-Hill form described in Chapter 1 (Equation 1.16) is used to model these materials because it is capable of predicting very nonlinear material behavior and it is based on functions of the principal stretch ratios. Presentation of these material laws is broken into two subsections: compressible formulations and nearly/fully incompressible formulations. Further detail on the following equations is found in Appendix C.

Please note that all forms of hyperelastic strain-energy densities presented have finite series representations. As such, the material parameters require indices in their definition. The index n (placed in the lower right side of the parameter) will be used to denote various finite terms for the material parameters.

2.1 Compressible Elastomers

Compressible elastomers are cellular or expanded resilient materials whose deformation under large strains is predominantly characterized as elastic. Their cellular or expanded structure allows these materials to have low effective Poisson's ratios in comparison to nearly incompressible solid rubbers. For compressible elastomers, an Ogden-Hill strain-energy function, W , of the following form is used:

$$W = \sum_{n=1}^N \frac{2\mu_n}{\alpha_n^2} \left[(\lambda_1^{\alpha_n} + \lambda_2^{\alpha_n} + \lambda_3^{\alpha_n} - 3) + \frac{1}{\beta_n} (J^{-\alpha_n \beta_n} - 1) \right] \quad (2.1)$$

where μ_n , α_n and β_n represent material parameters¹, N is the number of finite terms in the series, and the principal stretch ratios and elastic volume ratio are defined by λ_i and J , respectively.

The initial tangent shear modulus based on Hooke's law, μ_0 , as computed from a *simple-shear* deformation mode is

$$\mu_0 = \sum_{n=1}^N \mu_n. \quad (2.2)$$

The material parameters, β_n , are related to the generalized Poisson's ratio, ν_n , by

$$\beta_n = \frac{\nu_n}{1 - 2\nu_n}. \quad (2.3)$$

The initial tangent bulk modulus based on Hooke's law, K_0 , as computed from a pure dilatational (volumetric) deformation mode is

$$K_0 = \sum_{n=1}^N 2\mu_n \left(\frac{1}{3} + \beta_n \right). \quad (2.4)$$

The Ogden-Hill strain-energy function, Equation 2.1, is rather general in nature. The Blatz-Ko model for polyurethane foam, Equation 1.7, can be represented *exactly* by the Ogden-Hill form, Equation 2.1, by setting $N = 1$, $\alpha_1 = -2$, $\beta_1 = 1/2$, and $\mu_1 = \mu$. By Equation 2.3, we see that these parameters yield a Poisson's ratio of 1/4 (the same value reported by Blatz and Ko [12]). The Brockman model for moderately compressible material, Equation 1.8, can be represented *exactly* by the Ogden-Hill form, Equation 2.1, by setting $N = 1$, $\alpha_1 = 2$, $\beta_1 = \kappa/2$, and $\mu_1 = \mu$.

To obtain the appropriate constants (μ_n , α_n , β_n and N) for a given material in question, physical testing is required. Experimental stress-strain data curves for a given material under simple deformation modes are generated and used to compute the material

1. The material constants, α_n , may take on non-integer values. If material constants, β_n , are all zero, then there is no Poisson effect (see discussion in Appendix C.1).

constants. Commonly used deformation modes are uniaxial, equibiaxial, planar, volumetric, and simple-shear. Schematics of these idealized deformations are depicted in Figure 2.1. Due to reasons of practicality, a subset of these deformations is typically used in actual material testing.

Uniaxial compression and simple-shear deformation modes are chosen here to generate stress-strain data. These tests are chosen because the deformation in the nip is dominated by these modes. Furthermore, simple-shear contains both tension and compression in its deformation. Schematics of the test fixtures and test specimens are shown in Figures 2.2 - 2.4. For both test methods, the primary external load, F , was applied using an Instron tension/compression machine.

In the uniaxial compression test, rectangular specimens are compressed between two flat plates.¹ Recordings of X-direction load versus X-direction deflection are made. Also, measurements of the resultant transverse strain are made using a traveling scope.² Using the concept of work conjugacy (Appendix C), the applied nominal stress (load per original, undeformed area) is computed from W as

$$T_1^{\text{nom}} = \frac{\partial W}{\partial \lambda_1} = \frac{1}{\lambda_1} \sum_{n=1}^N \frac{2\mu_n}{\alpha_n} [\lambda_1^{\alpha_n} - J^{-\alpha_n \beta_n}]. \quad (2.5)$$

The zero transverse stress boundary condition requires

$$\sum_{n=1}^N \frac{2\mu_n}{\alpha_n} [\lambda_{\text{trans}}^{\alpha_n} - J^{-\alpha_n \beta_n}] = 0 \quad (2.6)$$

where

$$\lambda_{\text{trans}} = \lambda_2 = \lambda_3. \quad (2.7)$$

1. Cylindrical specimens were not used because it was not possible to manufacture sufficiently accurate solid cylinders.

2. For the scope used in the actual experiments, repeatability of the transverse displacement measurement was 0.12 mm.

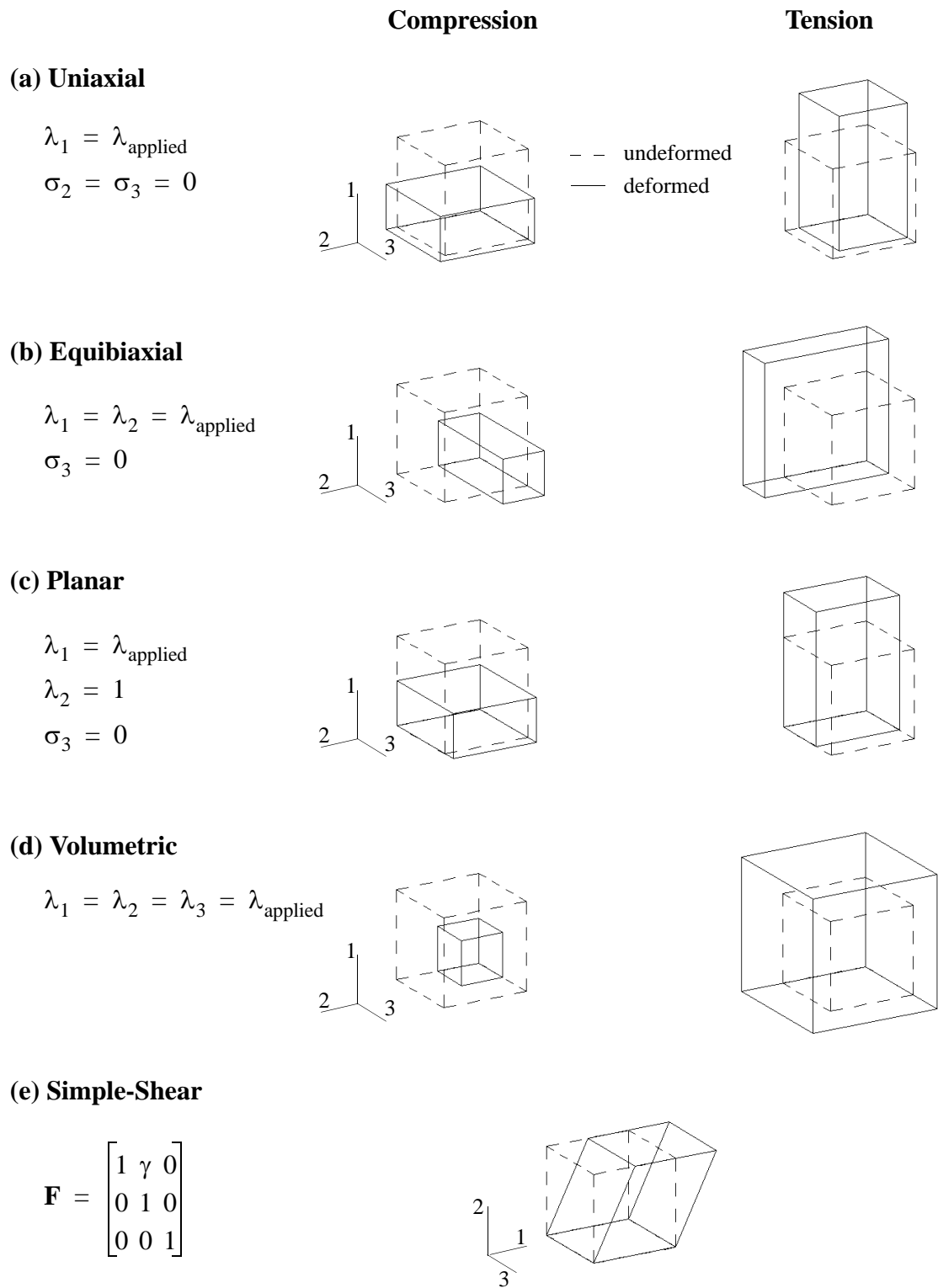
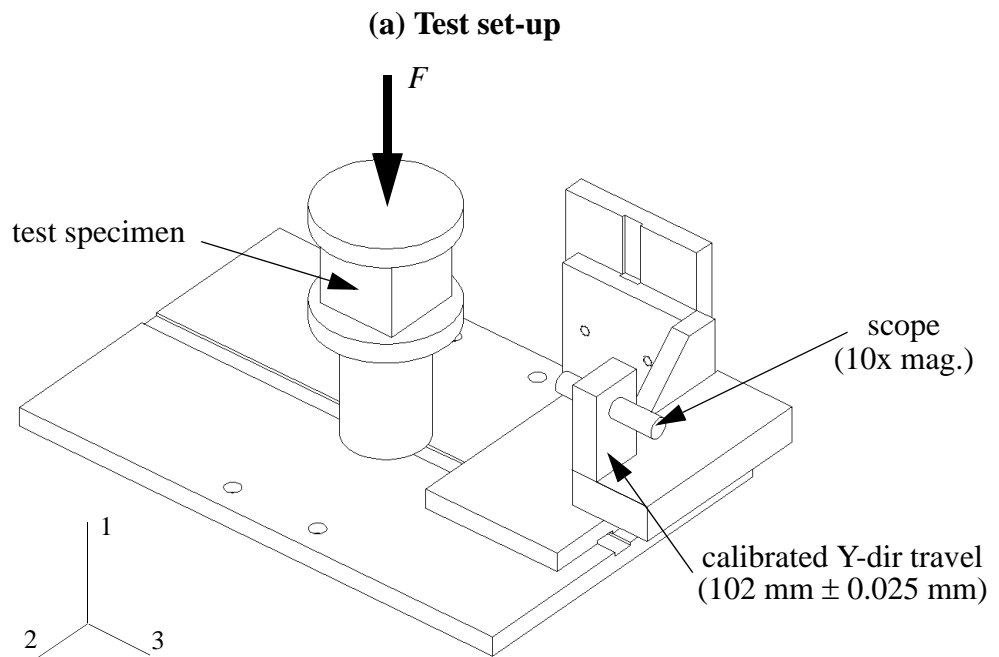
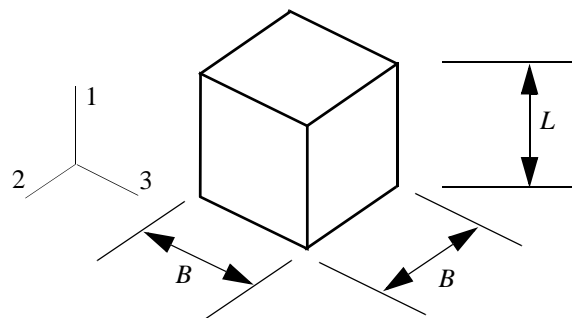


Figure 2.1: Schematics of primitive deformation modes.

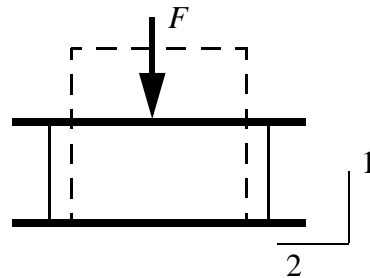


(b) Test specimen geometry (undeformed)



(c) Influence of boundary conditions

Idealized deformation (no friction)



Realistic deformation (friction)

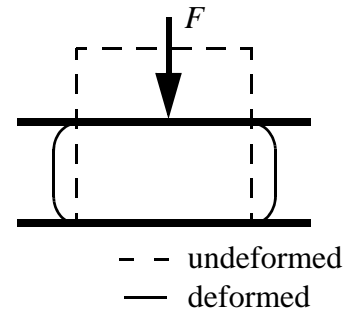


Figure 2.2: Schematic of uniaxial compression test set-up.

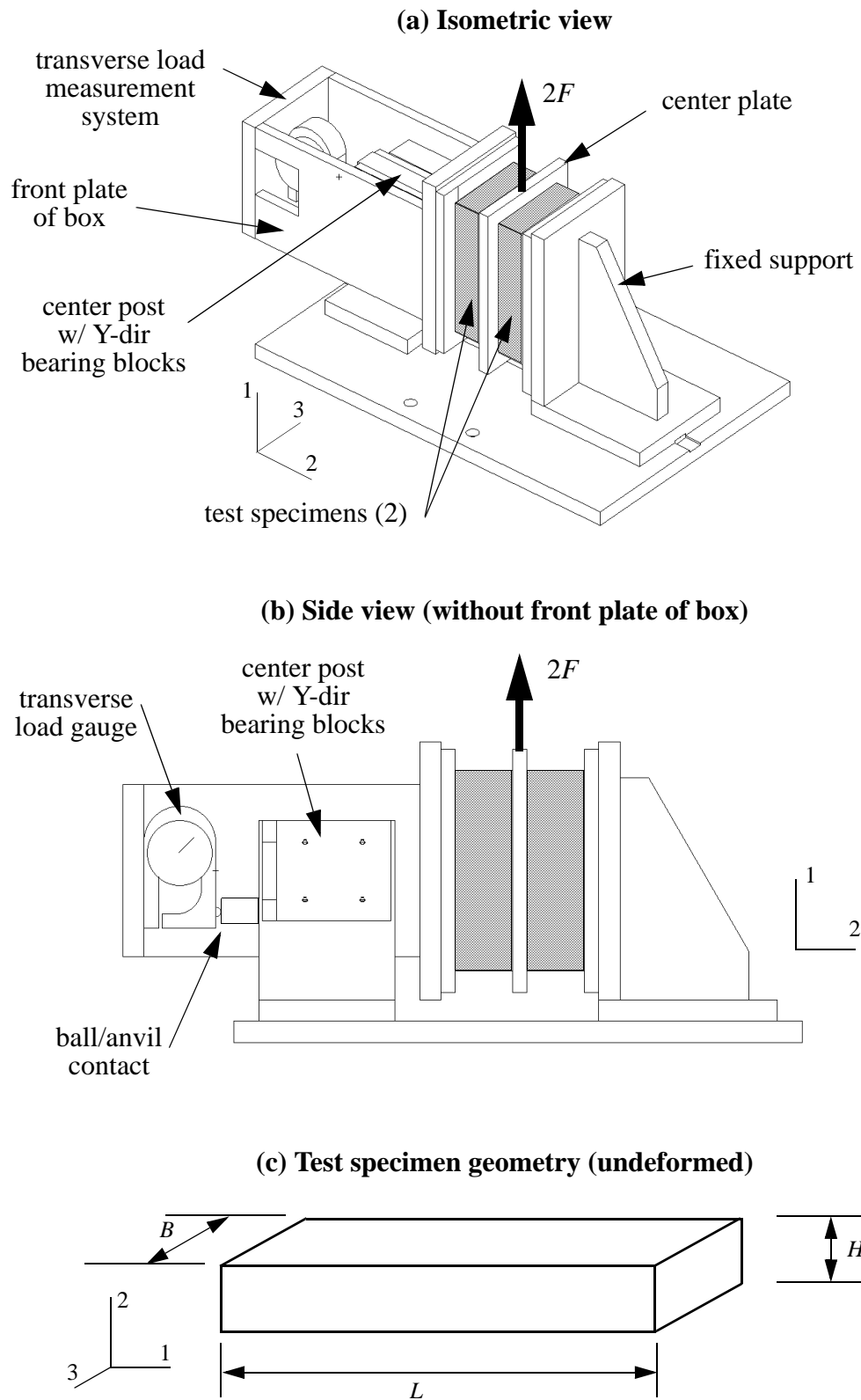


Figure 2.3: Schematic of simple-shear test set-up.

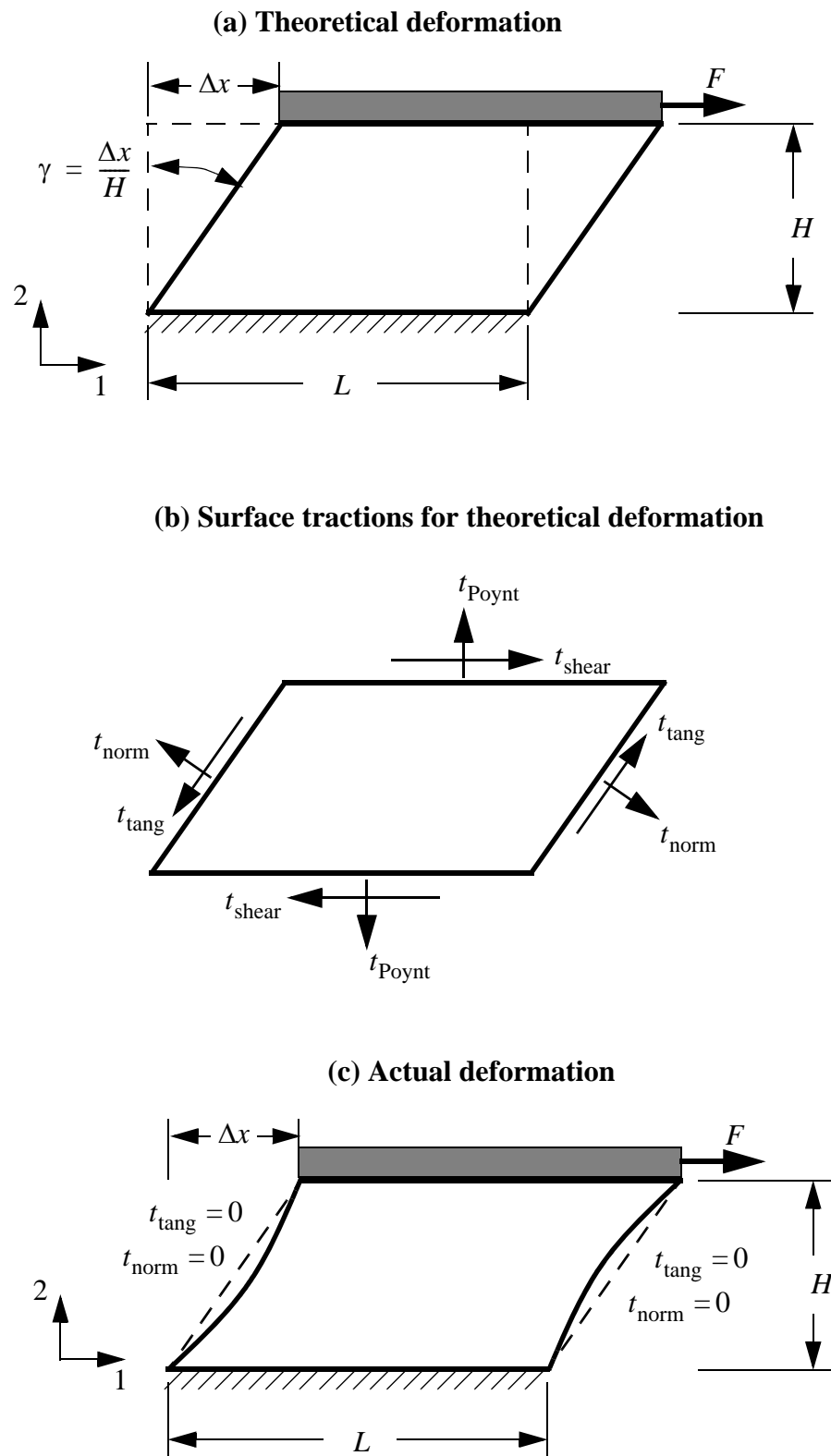


Figure 2.4: Applied stresses for simple-shear.

For the simple-shear test, two rectangular specimens are loaded as shown in Figure 2.3. Recordings of X-direction load versus X-direction deflection are made to compute the applied shear load and shear strain. The transverse load required to maintain a fixed specimen height, H , is measured using a stiff load gauge. The transverse load is divided by the specimen's area (LB) to compute the applied Poynting stress. Using the concept of work conjugacy (Appendix C), the applied nominal shear stress (shear load per original, undeformed area) and applied Poynting stress are computed from W as

$$t_{\text{shear}} = \frac{1}{\sqrt{4 + \gamma^2}} \left(\sum_{n=1}^N \frac{2\mu_n}{\alpha_n} [\lambda_1^{\alpha_n} - 1] - \sum_{n=1}^N \frac{2\mu_n}{\alpha_n} [\lambda_2^{\alpha_n} - 1] \right), \quad (2.8)$$

$$t_{\text{Poynt}} = \frac{1}{\sqrt{4 + \gamma^2}} \left(\frac{2}{\gamma + \sqrt{4 + \gamma^2}} \right) \sum_{n=1}^N \frac{2\mu_n}{\alpha_n} [\lambda_1^{\alpha_n} - 1] + \frac{1}{\sqrt{4 + \gamma^2}} \left(\frac{2}{-\gamma + \sqrt{4 + \gamma^2}} \right) \sum_{n=1}^N \frac{2\mu_n}{\alpha_n} [\lambda_2^{\alpha_n} - 1], \quad (2.9)$$

where γ is the applied shear strain and the principal stretch ratios are defined by

$$\begin{Bmatrix} \lambda_1 \\ \lambda_2 \\ \lambda_3 \end{Bmatrix} = \begin{Bmatrix} \sqrt{1 + \frac{1}{2}\gamma^2 + \frac{1}{2}\gamma\sqrt{4 + \gamma^2}} \\ \sqrt{1 + \frac{1}{2}\gamma^2 - \frac{1}{2}\gamma\sqrt{4 + \gamma^2}} \\ 1 \end{Bmatrix}. \quad (2.10)$$

To find the best values for the material coefficients, the following relative error measure is minimized

$$\text{Err} = \sum_{k=1}^{N^{\text{data}}} \left(1 - \frac{t_k^{\text{theory}}}{t_k^{\text{test}}} \right)^2 \quad (2.11)$$

where N^{data} are the number of experimental data points, t^{test} are the stress values from the experiments, and t^{theory} are the theoretical stress values based on the equations above. A nonlinear least-squares procedure is used to minimize Equation 2.11 because the stress equations are strongly nonlinear in the coefficients α_n and β_n . Procedures included in the

ABAQUS programs [50,51] are capable of performing the nonlinear fit. These procedures use the following method to obtain initial guesses of the coefficients for the nonlinear search:

1. assume all $\beta_n = 0$ and $\alpha_n = 2, -2, 4, -4, \text{ etc.}$,
2. perform linear least-squares fit to find μ_n ,
3. use the values from steps 1 and 2 as the starting point for the nonlinear search.

2.1.1 Evaluation of Non-Ideal Boundary Conditions

Both Figures 2.2c and 2.4c depict a likely problem during testing: the influence of non-ideal boundary conditions. For most problems, these end effects can be reduced by making the test specimen sufficiently large such that the area of nonuniform strain is negligibly small. In practice this is often done by evaluating a variety of sample dimensions.

Unfortunately, the uniaxial compression deformation mode does not allow tall blocks to be compressed because of buckling. Using short blocks, it is expected that some significant amount of end effect may potentially exist in the data. To remove these errors, we can test samples of various width to length ratios, B/L , and then extrapolate the results to an infinitely tall block, $B/L = 0$. To examine the validity of this approach, we first evaluate the concept numerically using infinitesimal-strain, linear finite element solutions with Hooke's law.

Figure 2.5 presents the finite element model used for the analysis. The actual model depicted in the figure was for $B/L = 1$. For taller blocks ($B/L < 1$) more elements were added to the model. Mesh density convergence checks were made to verify results. The boundary conditions in the model assume that there is sufficient friction between the rigid plates and the specimen such that no slip occurs. Two *effective* measurements are computed from the model: an effective Young's modulus (E^{eff}) and an effective Poisson's ratio (ν^{eff}). These effective measurements simulate what would be measured in an actual physical experiment.

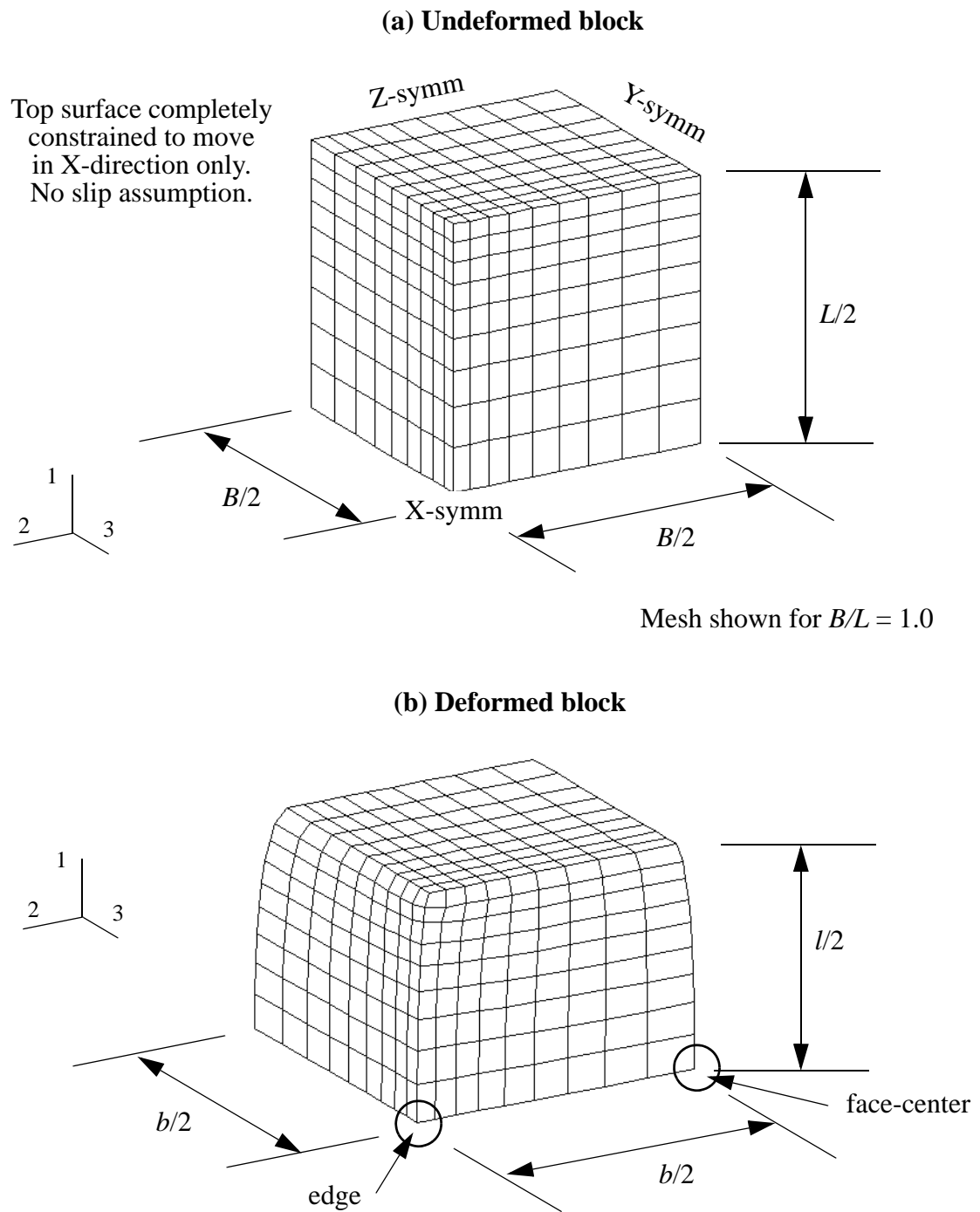


Figure 2.5: Linear finite element model used to study end effects in uniaxial compression. Model uses 1/8 symmetry.

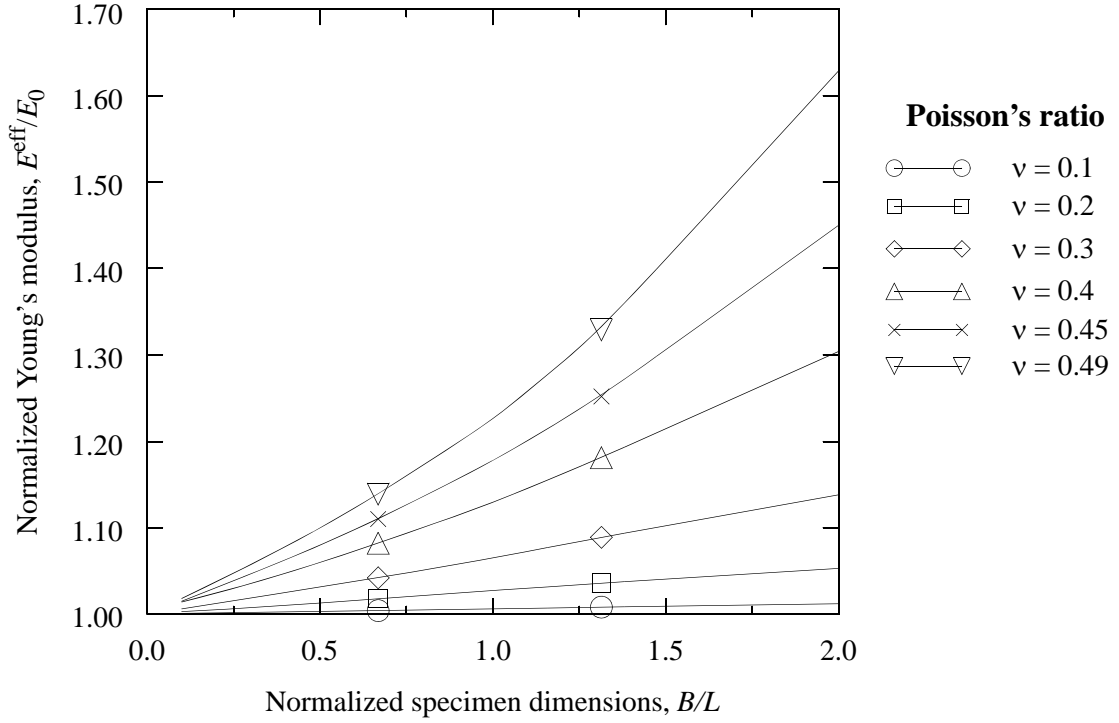


Figure 2.6: Effective values of Young's modulus for a block constrained between two rigid plates. Solution based on Hooke's law.

The effective Young's modulus is simply calculated as

$$E^{\text{eff}} = \frac{T_1}{\varepsilon_1^{\text{biot}}} = \frac{F/B^2}{(l/L) - 1}. \quad (2.12)$$

Figure 2.6 shows the results of the analysis. For shorter specimens ($B/L > 1$), the effective Young's modulus increases significantly with large values of Poisson's ratio. If $\nu < 0.35$ and $B/L < 1$, then the effective modulus is within 10% of the actual modulus.

The effective Poisson's ratio is computed as

$$\nu^{\text{eff}} = -\frac{\varepsilon_2^{\text{biot}}}{\varepsilon_1^{\text{biot}}} = -\frac{(b/B) - 1}{(l/L) - 1}. \quad (2.13)$$

Since the calculations on the block in Figure 2.5 are based on infinitesimal strains, the Biot measure of strain can be used. Calculation with logarithmic strain (or any other strain measure) would yield the same results in the limit of infinitesimal deformation. As seen in Figure 2.5b, two likely locations for measuring the effective transverse strain, ϵ_2^{biot} , exist: the edge of the block or the face-center of the block. For the actual physical experiments performed in this research, measurements were made at the edge of the block because of the optical technique utilized (see Figure 2.2).

Figure 2.7 presents the relationship of effective Poisson's ratio, ν^{eff} , as a function of the actual Poisson's ratio, ν , and the block's normalized dimensions, B/L . The graphs show three interesting regions. As B/L becomes very large, the effective measure of Poisson's ratio becomes less than actual. When B/L decreases from a large value, the measured value ν^{eff} increases beyond the actual value ν . As B/L continues to decrease and approach zero, ν^{eff} decreases and asymptotically approaches ν . The reason for this behavior is explained as follows. Consider a block made of a nearly incompressible material that is compressed with idealized boundary conditions (Figure 2.2c). The block expands uniformly in the transverse direction. If we now add the constraint that the top and bottom should not have expanded outward (no slip assumption), we must impose negative transverse motion on the top and bottom layers. This additional deformation will tend to make the block bulge further at its middle because of the material's *nearly* constant volume constraint. When the ratio B/L is large (a short, stubby block), the closeness of the transverse constraints created by the plates will inhibit this bulging. The larger the actual value of Poisson's ratio, the greater the bulge effect becomes and the closer the transverse constraints have to be to inhibit the bulging. As the block becomes taller, the bulging dominates until such a point when the end effect exists only in a small portion of the specimen. For materials with a lower Poisson's ratio, this bulging effect will be less pronounced.

Similar end-effect analyses were performed for the simple-shear deformation depicted in Figure 2.4. Results of these analyses showed that a dimension ratio of $L/H \gtrsim 7$ sufficiently minimizes the free-edge effects. This result was verified in the actual experiments by testing samples (for SE410) with $L/H = 1$, $L/H = 7$, and $L/H = 14$. Resultant stresses

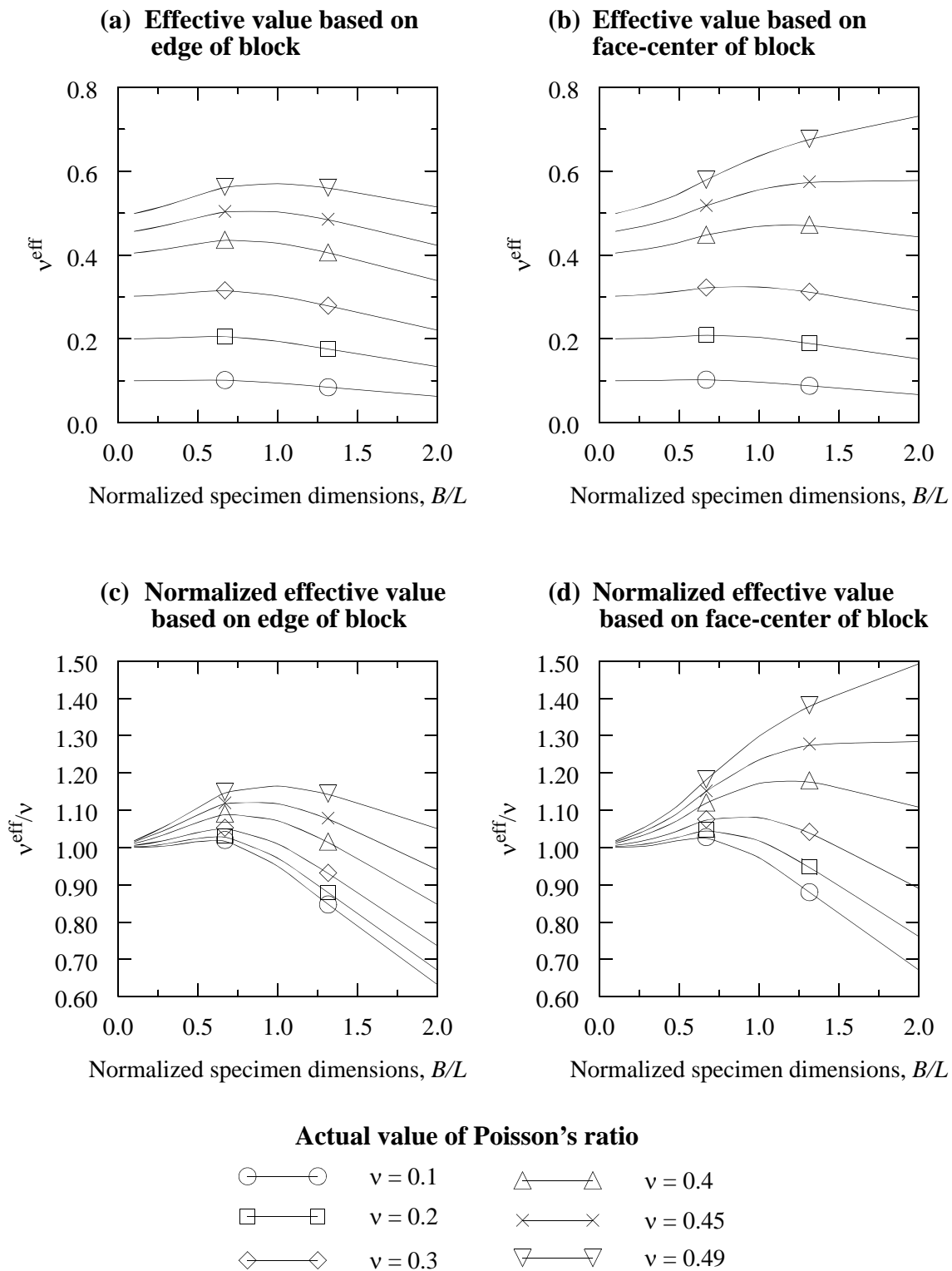


Figure 2.7: Effective values of Poisson's ratio for a block constrained between two rigid plates. Solution based on Hooke's law.

measured for $L/H = 14$ specimens were within 3% of $L/H = 7$ specimens. The values measured for $L/H = 1$ samples varied by 20% from the $L/H = 7$ samples.

2.1.2 Drucker Stability

The hyperelastic material laws being used are phenomenological models. To be sure that the material parameters describe a stable material definition, Drucker stability should be verified (see Appendix C.3 and [51] for more details). Drucker stability requires that the change in Kirchhoff stress, $d\tau_{ij}$, following an infinitesimal change in logarithmic, or *true*, strain, $d\varepsilon_{ij}^{\ln}$, must satisfy

$$d\tau_{ij} d\varepsilon_{ij}^{\ln} > 0. \quad (2.14)$$

The relationship between infinitesimal changes in Kirchhoff stress and logarithmic strain can be expressed in a hypoelastic form based on principal values as

$$d\tau_i = E_{ij} d\varepsilon_j^{\ln} \quad (2.15)$$

where \mathbf{E} is the tangent material elasticity matrix. Material stability is guaranteed when all three tensor invariants of the tangent material elasticity matrix, \mathbf{E} , are positive

$$I_1 = E_{ii} > 0, \quad (2.16)$$

$$I_2 = \frac{1}{2}(I_1^2 - E_{ij} E_{ji}) > 0, \quad (2.17)$$

$$I_3 = \det(\mathbf{E}) > 0. \quad (2.18)$$

For the strain-energy density defined in Equation 2.1, the tangent material elasticity matrix is found to be

$$[\mathbf{E}] = \sum_{n=1}^N 2\mu_n \begin{bmatrix} \lambda_1^{\alpha_n} + \beta_n J^{-\alpha_n \beta_n} & \beta_n J^{-\alpha_n \beta_n} & \beta_n J^{-\alpha_n \beta_n} \\ \beta_n J^{-\alpha_n \beta_n} & \lambda_2^{\alpha_n} + \beta_n J^{-\alpha_n \beta_n} & \beta_n J^{-\alpha_n \beta_n} \\ \beta_n J^{-\alpha_n \beta_n} & \beta_n J^{-\alpha_n \beta_n} & \lambda_3^{\alpha_n} + \beta_n J^{-\alpha_n \beta_n} \end{bmatrix}. \quad (2.19)$$

Theoretically, these stability checks need to be made for every combination of the three principal stretch ratios over the range of deformation that may be encountered. This is

generally not practical due to the computational expense required. A practical alternative is to check several basic deformation modes, such as those depicted in Figure 2.1, throughout the deformation range of interest.

When Drucker stability is not satisfied, one can evaluate the instability to see how significant it is. Sometimes the instability may be small and localized; existing only over a short range of deformation. In this case, the material law may still be usable. In the event that the instability is severe (relative large negative values from one or more of Equations 2.16 - 2.18 that continue to become more negative as the deformation is increased), the material law will likely be unusable in the region of instability. More detailed understanding of the type of instability can be obtained by evaluating the eigenvalue and associated eigenvector for the deformation values at which the failure occurred.

Material stability is, in general, a physically reasonable expectation. However, when modeling highly foamed materials, some small amounts of *real* material instability may exist. This is due to the fact that we are modeling macroscopically a structure (material) that is microscopically made of components that resemble beams, plates, and shells. It is therefore possible in highly foamed materials that the local buckling of the material cells cause macroscopic buckling of the material. As the deformation of the material continues, densification typically arrests the macroscopic buckling. Hence, this type of behavior will show up as a small localized instability in the material data and in a Drucker stability check of a fitted hyperelastic material law. When a severe instability in a Drucker stability check occurs, it often signifies that there was not sufficient data (enough deformation modes or large enough deformation range) to properly determine one or more of the material coefficients.

2.2 Nearly/Fully Incompressible Elastomers

Nearly/fully incompressible elastomers are solid rubbers whose deformation is predominantly characterized as elastic. These materials have a very large bulk modulus relative to their shear modulus. Nearly/fully incompressible elastomers are typically much stiffer than the compressible elastomers described in Section 2.1. Because the magnitude

of external loading on nip systems related to office imaging systems are limited, deformations of the nearly/fully incompressible elastomers are not expected to be large. We can, in many cases, sufficiently model these elastomers with Hooke's law.

From the discussion in Section C.3.1, we can write Hooke's law as

$$\tau_{ij} = \Lambda \varepsilon_{kk}^{\ln} \delta_{ij} + 2\mu \varepsilon_{ij}^{\ln} . \quad (2.20)$$

where all indices range from 1 to 3, τ_{ij} are the Kirchhoff stresses, ε_{ij}^{\ln} are the logarithmic strains, and Λ and μ are the Lamé constants.¹ The Lamé constants are related to Young's modulus, E , and Poisson ratio, ν , by

$$\Lambda = \frac{E\nu}{(1+\nu)(1-2\nu)} , \quad (2.21)$$

$$\mu = \frac{E}{2(1+\nu)} . \quad (2.22)$$

Since the materials described here are nearly/fully incompressible, we know that $J \approx 1$ which implies that the Kirchhoff stress tensor and the Cauchy stress tensor, σ_{ij} , are nearly equal. Thus, we define Hooke's law for this class of materials as

$$\sigma_{ij} = \Lambda \varepsilon_{kk}^{\ln} \delta_{ij} + 2\mu \varepsilon_{ij}^{\ln} . \quad (2.23)$$

From Equation 2.21 we see that if $\nu = 0.5$, then $\Lambda = \infty$. Fully incompressible materials can be analyzed if the material law is separated into its *deviatoric* and *volumetric* (dilatational) parts. Unfortunately, this is not commonly done with Hooke's law in most finite element codes. However, constitutive relationships based on separable functions of deviatoric and volumetric deformation are common for many hyperelastic formulations. Thus, we can use hyperelastic formulations as an easy method to investigate the incompressible limit of a material.²

1. The variable Λ is used to avoid confusion with the stretch ratio which is denoted as λ .

2. To evaluate completely incompressible material behavior with finite element analysis, mixed-formulation elements are used. These elements have both displacement and stress variables as degrees of freedom (see [49,51,54,62] for further details).

In a strict sense, no material is fully incompressible. If it were, its wave speed would be infinite (see Equation B.38 with $\bar{\Lambda} = \infty$ for an incompressible material). The extensive use of the *assumption* of incompressibility in numerous analyses of rubber throughout the literature and in industry is due to the fact that solid-rubber materials tend to have only minimal changes in volume under deformation. Using the incompressibility constraint eliminates one of the three material variables in the problem, i.e., $W = W(I_1, I_2)$ instead of $W = W(I_1, I_2, I_3)$.¹ For applications where the elastomer is not highly confined and where closed-form solutions are sought, the assumption of complete incompressibility provides efficient and accurate results. Typically, the importance of distinguishing between nearly incompressible and fully incompressible behavior becomes apparent when solving problems where the elastomer is in a highly confined state and volumetric deformation is important.

Moreover, an assumption of fully incompressible material behavior cannot be used with the explicit dynamic finite element method (ABAQUS/Explicit); some compressibility is required such that the wave speed is not infinite. Both nearly incompressible and fully incompressible material formulations can be used with the implicit-based, static finite element method ABAQUS/Standard.

The Ogden-Hill strain-energy function, W , for a nearly/fully incompressible elastomer is defined as [49]

$$W = \sum_{n=1}^N \left(\frac{2\mu_n}{\alpha_n^2} (\bar{\lambda}_1^{\alpha_n} + \bar{\lambda}_2^{\alpha_n} + \bar{\lambda}_3^{\alpha_n} - 3) + \frac{1}{D_n} (J - 1)^{2n} \right) \quad (2.24)$$

where μ_n , α_n and D_n represent material parameters and N is the number of finite terms in the series. The *deviatoric* principal stretch ratios, $\bar{\lambda}_i$, are defined as

$$\bar{\lambda}_i = J^{(-1/3)} \lambda_i \quad (2.25)$$

where i ranges from 1 to 3 and J is the volume ratio.

1. For complete incompressibility, an additional independent pressure variable, p , must be added to compute stresses properly. That is, the deviatoric Cauchy stress tensor, $\bar{\sigma}$, is computed from $\bar{W} = W(\bar{I}_1, \bar{I}_2)$ and the complete Cauchy stress tensor, σ , is computed as $\sigma = \bar{\sigma} - p$. See Appendix A for further details.

The initial tangent shear modulus based on Hooke's law, μ_0 , as computed from a *simple-shear* deformation mode is

$$\mu_0 = \sum_{n=1}^N \mu_n. \quad (2.26)$$

The parameter D_n are related to the bulk modulus of the material. Evaluating Equation 2.24 under a *pure dilatational* deformation mode shows that the initial tangent bulk modulus based on Hooke's law, K_0 , is related to the material parameter, D_1 , by

$$K_0 = \frac{2}{D_1} \quad (2.27)$$

where

$$K_0 = \frac{E_0}{3(1-2\nu)}. \quad (2.28)$$

If $D_n = 0$, then the material is fully incompressible.

This Ogden-Hill function can represent a neo-Hookean material by setting $N = 1$, $\alpha_1 = 2$, $\mu_1 = \mu_0$ and $D_1 = 0$. A Mooney-Rivlin material (Equation 1.4) is obtained with $N = 2$, $\alpha_1 = 2$, $\alpha_2 = -2$, $\mu_1 = 2C_1$, $\mu_2 = 2C_2$, and $D_1 = 0$. Because the parameters, α_n , are not limited to even integer powers, the Ogden-Hill form is more general than the polynomial stretch-invariant form.

In general, the calculation of material coefficients for W (Equation 2.24) follow the same basic approach described in Section 2.1.¹ Since we have limited our evaluation of nearly/fully incompressible elastomers to small deformations, we only need to consider the neo-Hookean form of the strain-energy density function. Both this form and Hooke's law are characterized by Young's modulus and Poisson's ratio.

Young's modulus can be obtained from a uniaxial tension test which is characterized by the following boundary conditions:

1. General stress calculations for materials that are governed by Equation 2.24 are described in Appendix A.4.2 and Appendix C.2.

$$\lambda_1 = \lambda_{\text{applied}}, \quad \sigma_2 = \sigma_3 = 0. \quad (2.29)$$

Applying these boundary conditions to Hooke's law, Equation 2.23, yields

$$\sigma_1 = E \ln(\lambda_1) \quad (\text{Hooke's law}). \quad (2.30)$$

For a fully incompressible neo-Hookean material, these boundary conditions require

$$\sigma_1 = \mu \left(\lambda_1^2 - \frac{1}{\lambda_1} \right) = \frac{E}{3} \left(\lambda_1^2 - \frac{1}{\lambda_1} \right) \quad (\text{neo-Hookean, } \nu = 0.5). \quad (2.31)$$

Equation 2.31 is derived by applying the uniaxial boundary conditions to Equations A.93, A.94, and C.59. The Cauchy stress equation for a nearly incompressible neo-Hookean material is derived in a similar manner with the additional use of Equation C.60.¹

To evaluate the initial tangent modulus for Equations 2.30 and 2.31, we compute the derivative of stress with respect to deformation about the undeformed state.

$$\left. \frac{d\sigma_1}{d\lambda_1} \right|_{\lambda_1=1} = E \left. \frac{1}{\lambda_1} \right|_{\lambda_1=1} = E \quad (\text{Hooke's law}) \quad (2.32)$$

$$\left. \frac{d\sigma_1}{d\lambda_1} \right|_{\lambda_1=1} = \frac{E}{3} \left(2\lambda_1 + \frac{1}{\lambda_1^2} \right) \bigg|_{\lambda_1=1} = E \quad (\text{neo-Hookean, } \nu = 0.5) \quad (2.33)$$

Hence, both material formulations yield the same initial tangent modulus.

2.2.1 Determination of Poisson's Ratio

The measurement of Poisson's ratio for nearly incompressible materials is nontrivial. The methods described in Section 2.1 are not capable of measuring Poisson's ratio accurately as ν approaches 0.5. In fact, utilizing simple techniques like those described in Section 2.1 can yield values greater than 0.5. Two techniques that can provide accurate measurement of ν while ensuring that its value is always less than 0.5 are an *ultrasound* method and a

1. The Cauchy stress equation for this case is more complicated but yields very similar results to those predicted for the incompressible case. For a nearly incompressible material with $\nu = 0.495$, the maximum difference in Cauchy stress between the two cases is 0.4% over a nominal strain range of $\pm 25\%$.

constrained piston method. Both methods are valid for computing the initial tangent value of Poisson's ratio (small strain regime).

Using an ultrasound technique, Poisson's ratio of a bulk material can be determined based on its wave speed and Young's modulus (see Martellock and Anderson [77] for complete details on the method). From Section B.2 the dilatational wave speed, c_d , of a bulk material about its undeformed state is defined by

$$c_d = \sqrt{\frac{\Lambda + 2\mu}{\rho}} \quad (2.34)$$

where Λ and μ are the Lamé constants defined previously and ρ is the density. Substituting Equations 2.21 and 2.22 into Equation 2.34 and rearranging produces

$$\frac{1 - \nu}{(1 + \nu)(1 - 2\nu)} = \frac{c_d^2 \rho}{E} = A \quad (2.35)$$

where $A > 1$ if $-1 < \nu < 0.5$. Solving for the positive value of ν in Equation 2.35 yields

$$\nu = \frac{1}{4A} (1 - A + \sqrt{9A^2 - 10A + 1}) . \quad (2.36)$$

Equation 2.36 is completely general and does not assume that the material's Poisson ratio is near 0.5. In the event that this is the case, a simpler approximation of Poisson's ratio, derived from Equation 2.35, is

$$\nu = \frac{1}{2} - \frac{E}{6\rho c_d^2} = \frac{1}{2} - \frac{1}{6A} \quad (\text{if } \nu \approx 0.5). \quad (2.37)$$

By measuring the wave speed, the density, and the Young's modulus, we can easily compute Poisson's ratio by Equation 2.36 or 2.37. From Equation 2.37 we see that $\nu < 0.5$, always. Furthermore, when ν is near 0.5, say 0.4995, we see from Equation 2.37 that variations in A of one order of magnitude only influence the last "non-nine" digit.

With the constrained piston method, Poisson's ratio is determined from Young's modulus and an apparent "constrained" modulus which is obtained by compressing, with a piston, a solid cylindrical sample inside an extremely stiff hollow cylinder. The resulting boundary conditions on the sample are (in cylindrical coordinates)

$$\varepsilon_{zz} = \varepsilon_{\text{applied}}, \quad \varepsilon_{rr} = \varepsilon_{\theta\theta} = \varepsilon_{r\theta} = \varepsilon_{rz} = \varepsilon_{\theta z} = 0. \quad (2.38)$$

Applying these constraints to Hooke's law, Equation 2.23, yields the relationship

$$\frac{1 - \nu}{(1 + \nu)(1 - 2\nu)} = \frac{\sigma_{zz}}{E \varepsilon_{zz}} \quad (2.39)$$

where σ_{zz} denotes the applied compressive stress from the piston. Comparing this result with Equation 2.35 demonstrates that

$$A = \frac{\sigma_{zz}}{E \varepsilon_{zz}}. \quad (2.40)$$

Measurements of Poisson's ratio by the constrained piston method are usually slightly lower than those determined by the ultrasound method. This is because there will always be some small amount of deformation in the piston and stiff hollow cylinder.

Chapter 3

Experimental Material Testing of Three Elastomers

To better understand the capabilities, limitations, and applications of the hyperelastic formulations utilized, three different types of elastomers are studied:

1. SE410 - a moderately compressible closed-cell EPDM¹ expanded rubber with an average density of 160 kg/m^3 in the undeformed state.
2. R600U - a highly compressible polyester-based open-cell polyurethane foam with an average density of 80 kg/m^3 in the undeformed state.
3. urethane - a nearly incompressible polyether-based polyurethane rubber with an average density of 1050 kg/m^3 in the undeformed state.

The first two materials, SE410 and R600U are compressible elastomers. These materials are made in a bulk form known as a *bun*. Specimens are cut from the bun and further machined into any required shape. Because these materials are easily deformed, dimensional accuracy is significantly less than would be expected when machining more common materials such as metals. Furthermore, the bulk manufacturing of these materials has greater variability compared to the manufacturing of most engineering materials. Because of material variability (particularly bun to bun), all material samples for a given material type are obtained from the same bun.²

The urethane rubber is made in a very different manner from the compressible elastomers. It is made by mixing polyether based polyurethane (L42 from Uniroyal) with an anti-static agent, an anti-gas agent, a chain extender (EC300), and a cross-linker (Voranol). Required

1. EPDM stands for ethylene propylene diene methylene.

2. All buns and experimental samples for SE410 and R600U were supplied by illbruck, incorporated, Rochester NY.

specimen shapes are then made by pouring the liquid mixture into molds and curing them in an oven at 80° Celsius for 17 hours.

As discussed in Chapter 2, the material testing is based on fitting the constitutive relationship to experimental stress-strain data. In obtaining the experimental data it is important to perform multiple load/unload cycles on the sample before recording the final stress-strain data. This pre-working breaks any weak bonds in the material. In the testing of the materials in this work it was found that typically 3 to 4 cycles were sufficient.

The next three sections provides experimental results, numerical analysis, and discussion regarding the evaluation of hyperelastic constitutive relationships for the three materials in question.

3.1 Material Testing of SE410

Two material tests were performed on SE410, uniaxial compression and simple-shear. Both tests were run at a nominal strain-rate of 0.4%/sec. To verify that the material was strain-rate insensitive, tests were also performed at a rate of 7.0%/sec. Negligible differences were found. Material hysteresis was evaluated in a uniaxial compression mode by loading and then immediately unloading the specimen. Figure 3.1 presents the results, a small amount of energy loss. It should be noted that, after approximately 5 to 10 seconds from the end of the test, the sample was fully recovered (no permanent deformation). Material isotropy was also checked by loading a cube in uniaxial compression through three perpendicular axes. Each of the three axes yielded very similar stress-strain curves (< 5% difference).

3.1.1 Uniaxial Compression Test Results

The compression tests were performed using three different specimen sizes: $B/L = 1.0$, 1.3, and 2.0. Tall blocks, $B/L < 1.0$, could not be tested because of buckling problems. For each specimen size, three material samples were tested. Figure 3.2 depicts the results for specimen size $B/L = 1.0$. These results are for a nominal compressive strain up to 50%. The data demonstrates that sample variability was very small for the SE410. Figure 3.2a

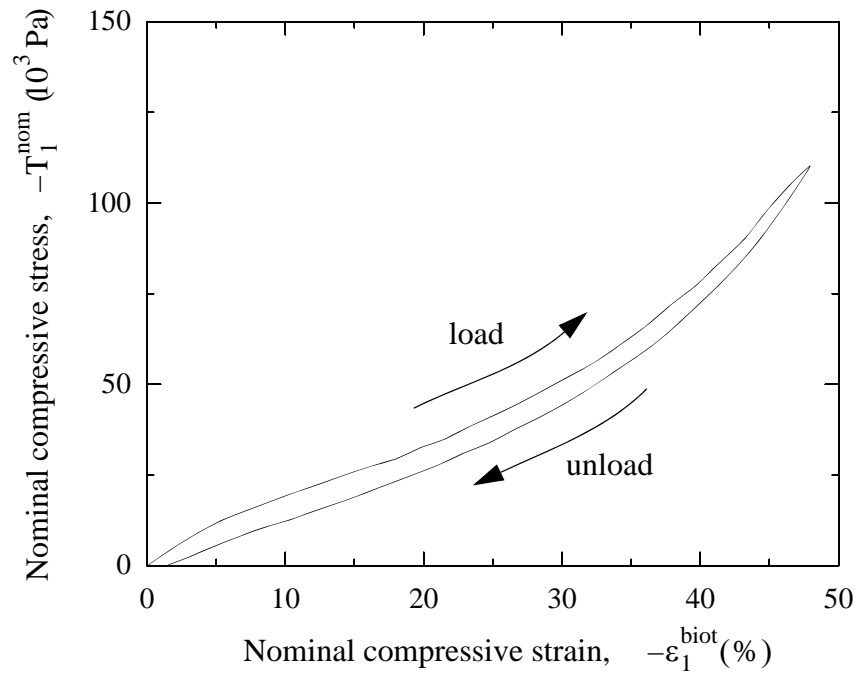


Figure 3.1: Hysteresis in SE410 as measured by uniaxial compression.

shows how the nominal stress changes as a function of nominal strain. The initial region below 5% strain is linear. The region between 5% and approximately 35% has a softer tangent modulus while the region beyond 35% strain depicts increasing stiffness caused by material densification.

Figure 3.2b demonstrates that the transverse strain varies almost linearly with the applied strain. One might think that this implies that Poisson's ratio should be a constant. However, for large deformations, Poisson's ratio relates logarithmic strains and not Biot strains. Thus, we expect to need a multiple-term material law to capture this behavior.

Figure 3.3 presents the average results for the three specimen sizes tested. Figure 3.3a shows that negligible difference was found from the nominal stress versus nominal strain data. However, Figure 3.3b shows that the nominal transverse strain behavior was affected by the specimen size. Based on the analysis of Section 2.1.1, we should be able to determine the influence of the specimen size (non-ideal boundary conditions) on this data.

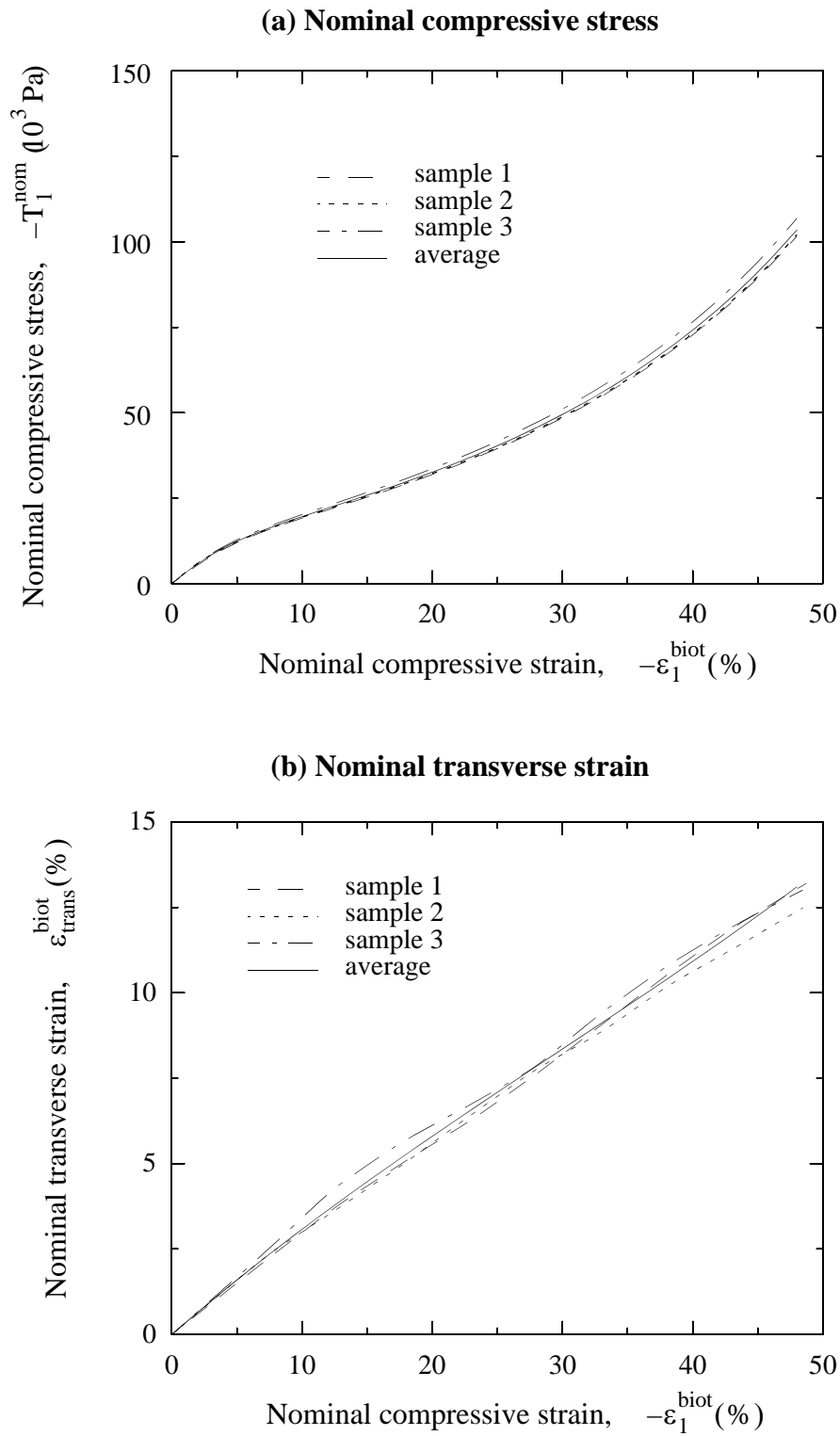
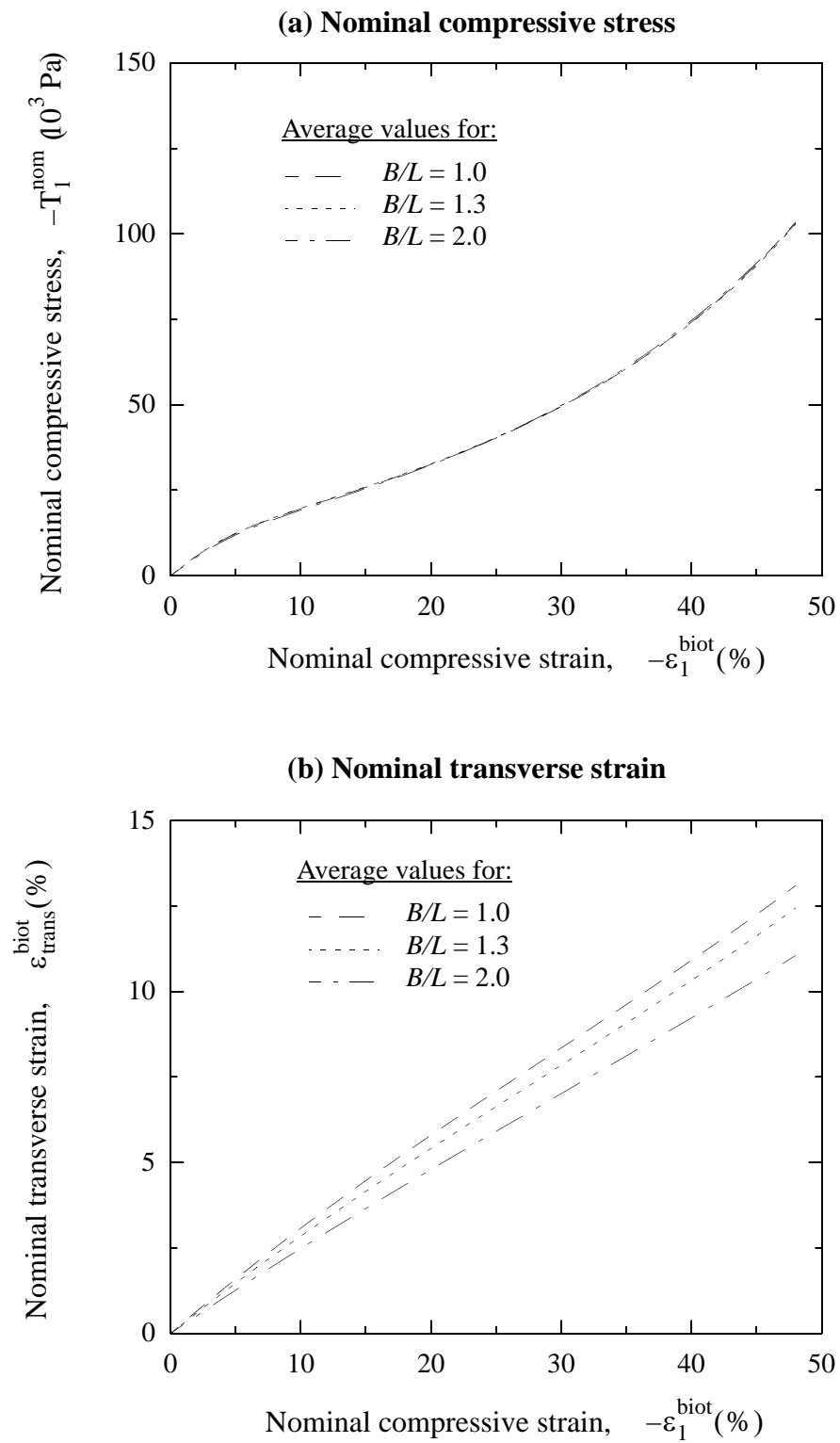


Figure 3.2: Experimental results for SE410 in compression. Specimen dimension ratio, $B/L = 1$.



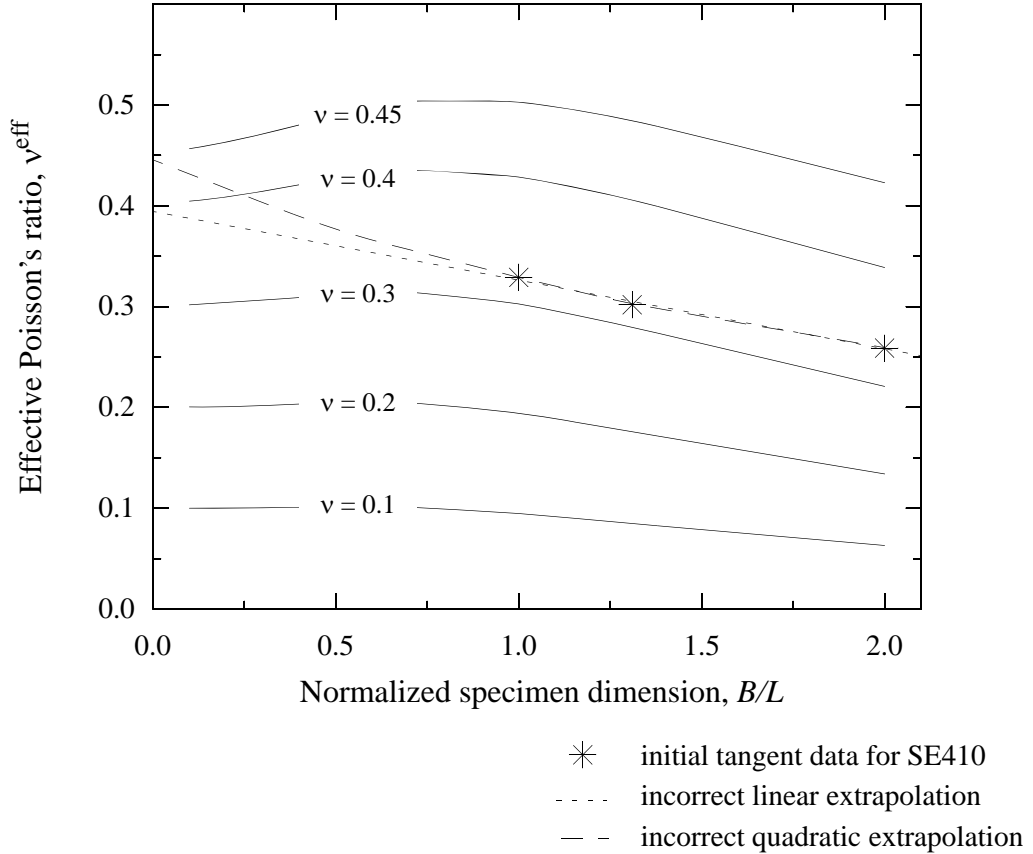


Figure 3.4: Measured value of initial tangent Poisson's ratio for SE410 correlates well with effective Poisson's ratio variation based on Hooke's law.

Figure 3.4 shows how the initial tangent Poisson's ratios for the three curves in Figure 3.3 ($\nu_0 = 0.33, 0.302, \text{ and } 0.26$ for $B/L = 1.0, 1.3, \text{ and } 2.0$, respectively) compare against the results obtain from Hooke's law (Figure 2.7a). We see that the SE410 data correlates well with the Hooke's law results. Also shown in Figure 3.4 are two extrapolated curves based solely on the SE410 test data. Without the knowledge obtained from Section 2.1.1, we would have incorrectly deduced that the initial tangent Poisson's ratio for SE410 was between 0.4 - 0.44 and would have further concluded that significant boundary influences occurred. Instead, we correctly conclude that the initial tangent Poisson's ratio for SE410

is 0.33. This initial tangent value is similar to Poisson ratio values for other expanded and foamed elastomers reported by Gent and Thomas [34] and Lederman [72].

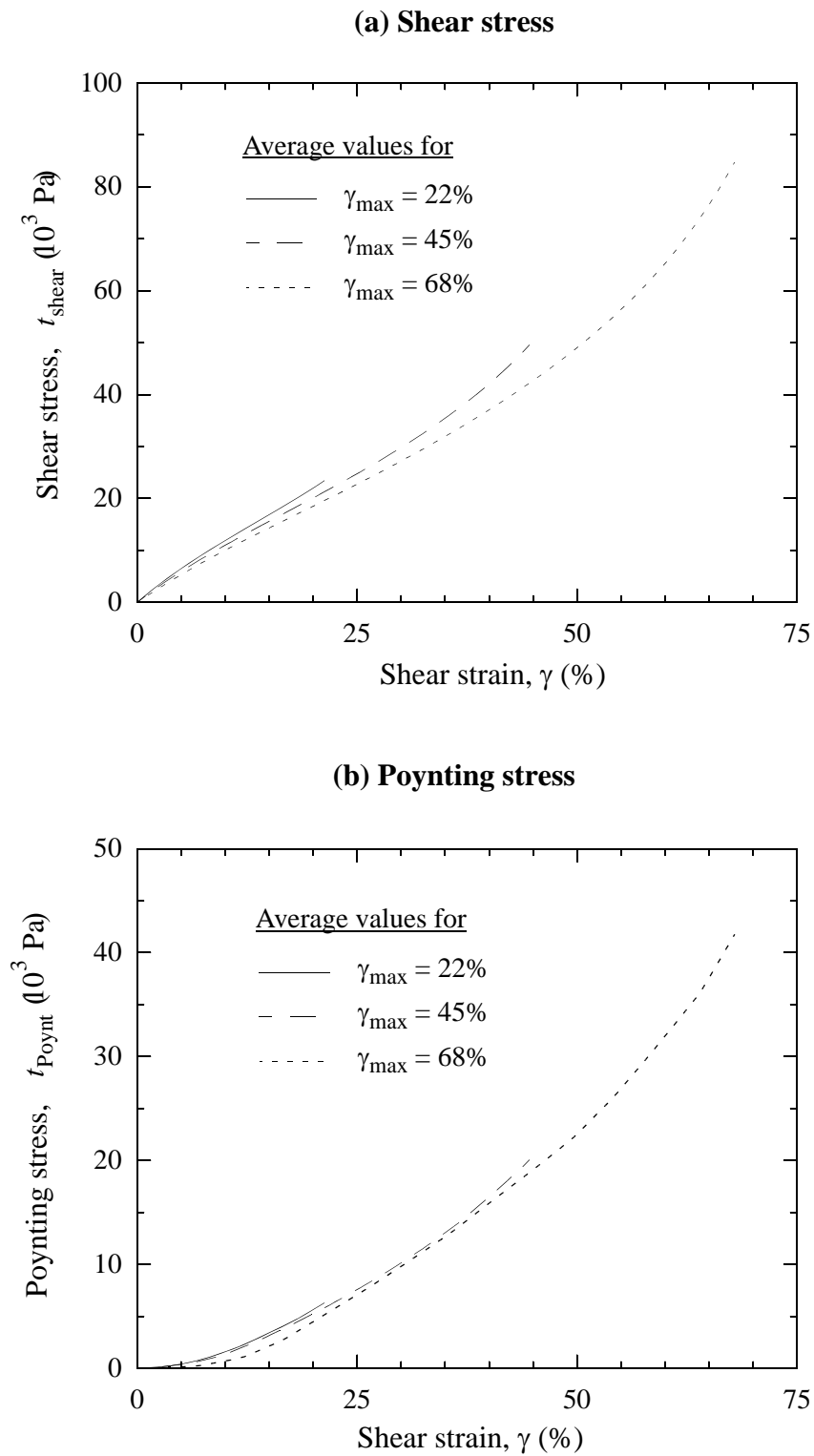
3.1.2 Simple-Shear Test Results

For the shear data, sample variation was similar to the variations seen in the uniaxial compression tests. The specimen dimensions for the simple-shear testing were $B = 50.8$ mm, $L = 178$ mm, and $H = 25.4$ mm (see Figure 2.3). To verify that non-ideal boundary conditions were negligible for $L/H \gtrsim 7$, additional specimens were tested with $L/H = 1$, and $L/H = 14$. Resultant stresses measured for $L/H = 14$ specimens were within 3% of the $L/H = 7$ specimens. The values measured for $L/H = 1$ samples varied by 20% from the $L/H = 7$ samples.

Figure 3.5 depicts the average results from three samples of SE410 under simple-shear. Figure 3.5a presents the shear stress data while Figure 3.5b presents the Poynting stress data. The plots show three different curves each. These curves represent the maximum shear strain applied in the test. As the material is deformed to greater maximum deformations, more “weak” bonds become broken and the material tends to soften.¹ This type of behavior was not seen in the compression testing of Section 3.1.1 until compressive strains were beyond 50%.² Because simple-shear contains tension as part of its deformation, the material’s weak bonds are more likely to fail.

The shear stress in Figure 3.5a depicts three regions similar to those seen in the uniaxial compression data of Figures 3.2a and 3.3a, although the shear data is not as nonlinear as the uniaxial data. The Poynting data of Figure 3.5b begins with zero slope at zero shear strain which is consistent with small deformation, linear theory. As the shear strain increases the Poynting stress increases with a tangent slope that is almost 1/2 of the shear stress tangent slope. The fact that the Poynting stress is positive implies that if the constant specimen height constraint in Figures 2.3 and 2.4 were removed, the sample height H

1. These results were measured after the samples had been pre-worked by multiple load and unload cycles.
 2. This is excluding the initial breaking of weak bonds from the virgin material.



would decrease as the shear strain increased. As we will see in the next section, this is *opposite* of the behavior predicted by the Blatz-Ko model.

3.1.3 Computing Constitutive Coefficients

The data from Sections 3.1.1 and 3.1.2 allow us to compute the needed material law parameters. From the analysis of Section 3.1.1, the uniaxial compression data used for curve fitting is based on a specimen size $B/L = 1$. The non-ideal boundary conditions are accounted for by reducing the stress values by a factor of 1.06 and transverse strains by a factor of 1.01 (see Figures 2.6 and 2.7 with $\nu = 0.33$). These factors are very close to unity which indicate that the boundary effects were very small. The simple-shear data for $\gamma_{\max} = 45\%$ is used unchanged as shown in Figure 3.5. From Equation 2.10, $\gamma_{\max} = 45\%$ equates to the maximum principal stretch ratios for this deformation of $\lambda_1 = 1.56$ and $\lambda_2 = 0.64$.

Since the material behavior is nonlinear, we know that Hooke's law is not valid. Figure 3.6 shows that the laws proposed by Blatz and Ko (Equation 1.7) and by Brockman (Equation 1.8) are also inadequate to model the behavior of SE410. These laws only predict the shear stress well. From Equations 2.8 and 2.10 it is seen that the shear stress for both the Blatz-Ko and Brockman formulations are linearly related to the shear strain γ by the shear modulus μ_0 . It is further noted that for the Poynting stress of Figure 3.6d, neither Blatz-Ko nor Brockman even quantitatively predicts the behavior.¹ Since both Blatz-Ko and Brockman assume a constant Poisson's ratio, Figure 3.6b shows that for constant Poisson's ratio the nominal transverse strain varies nonlinearly with the nominal compressive strain. This is because for large deformations, a constant Poisson's ratio represents a linear relationship between logarithmic strains only.

Two reasons are possible for why both the Blatz-Ko and Brockman models do not predict the material behavior of SE410. First, the materials that they investigated may be very different from SE410. Second, Blatz and Ko only performed tensile tests on their material and they never tested uniaxial compression or simple-shear deformations.

1. Hooke's law predicts no Poynting stress in the small strain regime and negative values for large strains.

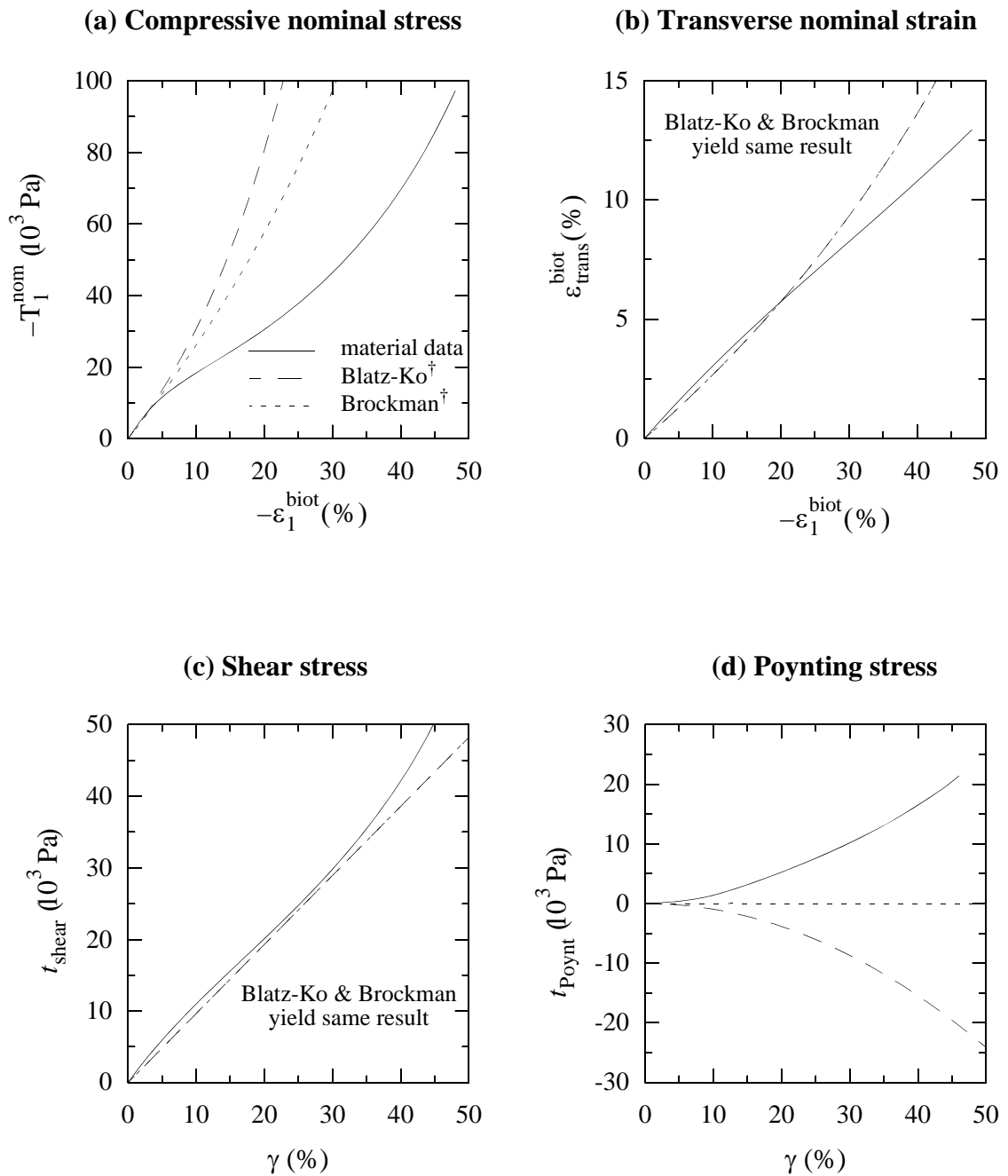


Figure 3.6: Neither Blatz-Ko nor Brockman's law adequately models SE410.

Table 3.1: Material constants for various laws to characterize SE410.

Type	N	μ_1 (10^3 Pa)	μ_2 (10^3 Pa)	$\mu_0 = \mu_1 + \mu_2$ (10^3 Pa)	α_1	α_2	ν_1	ν_2
Blatz-Ko	1	96.5	---	96.5	-2.0	---	0.25	---
Brockman	1	96.5	---	96.5	2.0	---	0.25	---
Ogden-Hill	1	82.5	---	82.5	7.11	---	0.191	---
Ogden-Hill	2	82.4	-3.87	78.5	7.22	2.34	0.176	0.508

Figure 3.7 demonstrates the capability of the Ogden-Hill formulation in fitting the data from SE410. Both the one-term and two-term models yield very satisfactory results. Table 3.1 lists the material coefficients for the various fits. The Ogden-Hill one-term and two-term coefficients were found by methods described in Section 2.1 with one slight modification related to the use of the simple-shear data. The Poynting data of Figure 3.7d and the Poynting stress equation (2.9) create a numerical problem for the relative error measure of Equation 2.11 when the shear strains are small. The magnitude of both the test data and the theoretical equation are near zero and thus the relative error measure becomes approximately 0/0. Moreover, since the Poynting stress test data points in the low strain range are very close to zero, they are not measured accurately. This result can incorrectly influence the fit. The solution to this problem was to ignore the first 10% of both shear stress and Poynting stress data.

From Figure 3.7 we see that the two-term Ogden-Hill law provides the best fit. Figure 3.8 shows how the nominal, Cauchy, and Kirchhoff stresses vary as a function of nominal compressive strain for several deformation modes using this fit. From this figure we see that all stresses increase monotonically with increasing deformation. Furthermore, we see that the uniaxial and planar deformation modes yield very similar results. This indicates that, for future modeling the difference between plane stress and plane strain will be small.

The Drucker stability checks of Figure 3.9 are computed by evaluating the three invariants of the tangent elasticity matrix (Equations 2.16 - 2.19) over the deformation range of

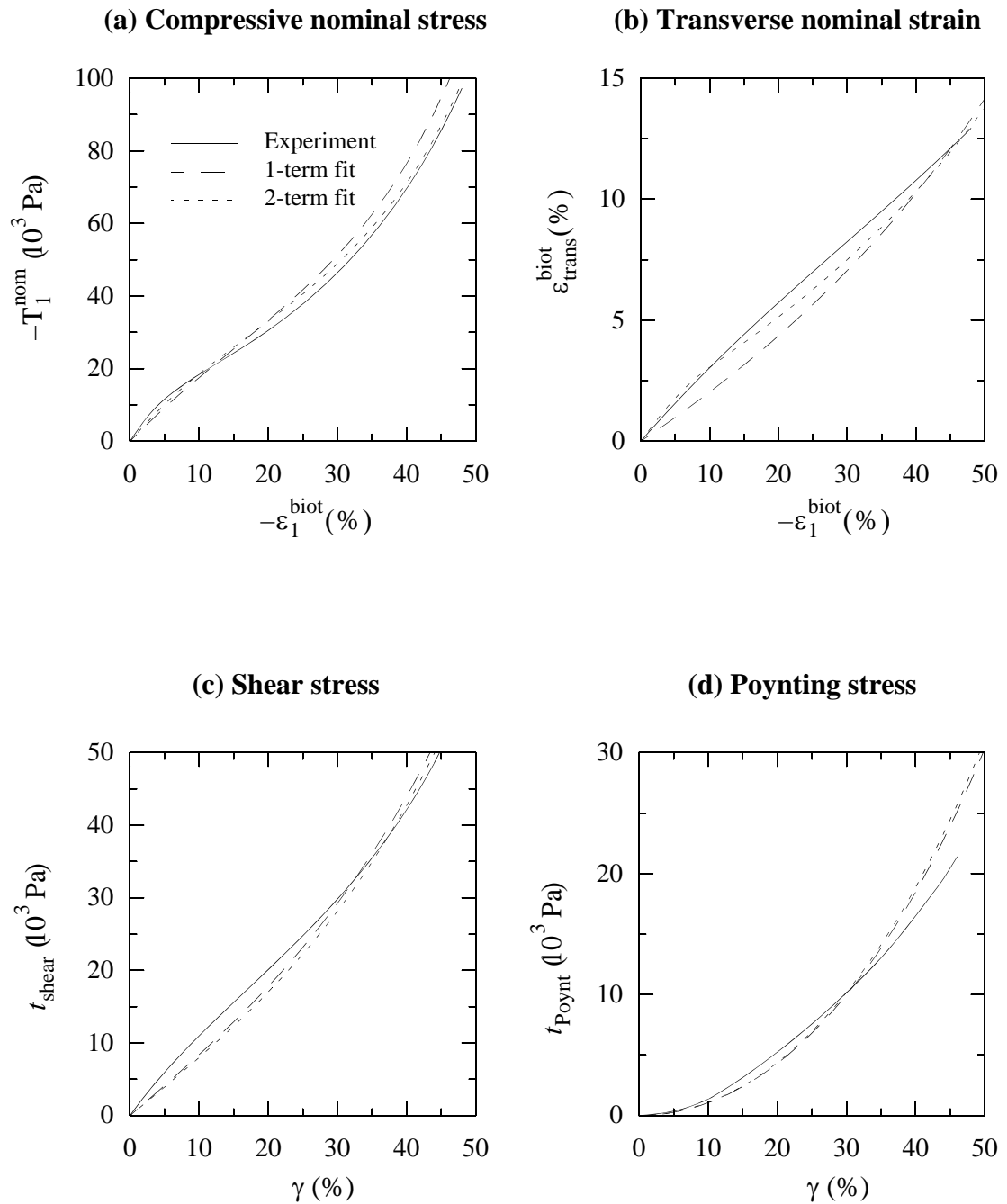


Figure 3.7: One-term and two-term Ogden-Hill fits to SE410.

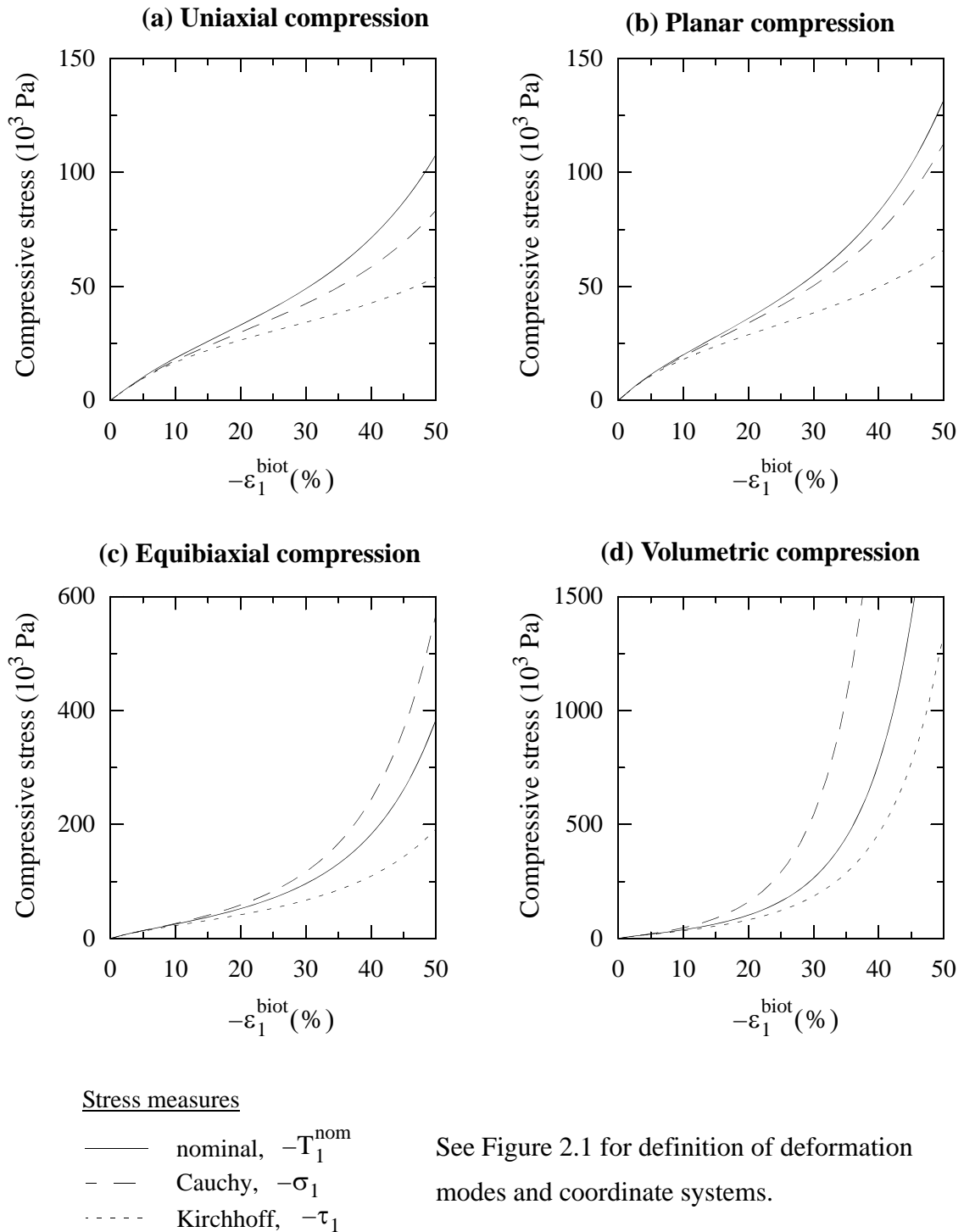
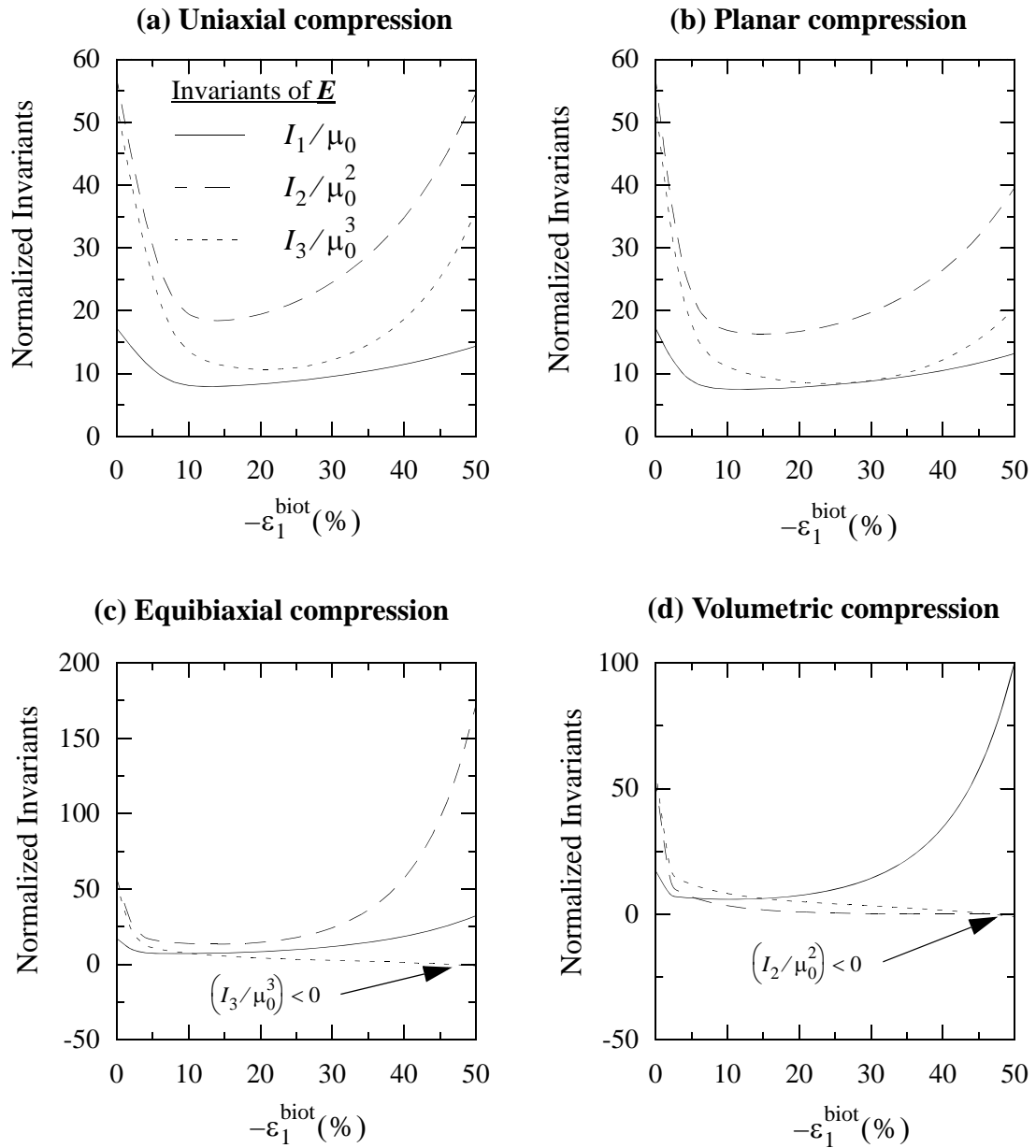


Figure 3.8: Calculated stress measures from two-term Ogden-Hill representation of SE410 for several compressive deformation modes.



See Figure 2.1 for definition of deformation modes and coordinate systems.

Figure 3.9: Calculated Drucker stability checks from two-term Ogden-Hill representation of SE410 for several compressive deformation modes.

interest for each of the modes displayed in Figure 3.8. From these curves we see that only equibiaxial and volumetric compression exhibit a very mild instability at the end of the deformation range. All the primitive deformation modes depicted in Figure 2.1 were checked in this manner over the deformation range of $0.5 < \lambda_{\text{applied}} < 1.5$. No other instabilities were found and all the various stress and strain quantities appeared reasonable with one notable exception: volumetric tension.

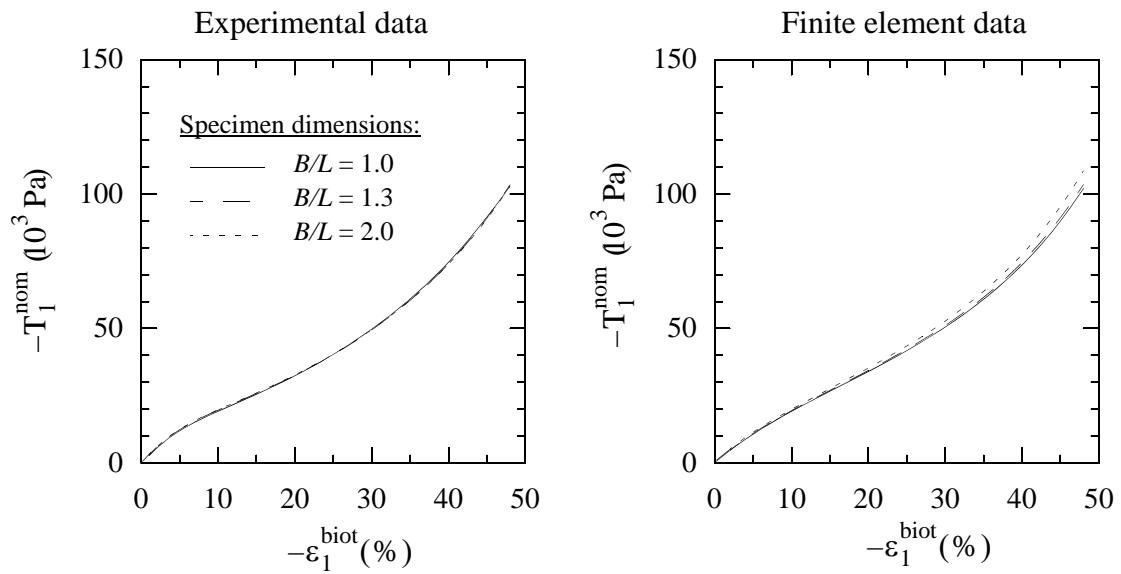
The volumetric *tension* mode for the two-term model was unrealistic and numerically “blew-up” immediately as the deformation increased. The cause of the problem is easily traced back to the power coefficients and the generalized Poisson’s ratio ν_2 . When looking at the generalized Poisson’s ratios shown in Table 3.1, it should be remembered that for the case when $N > 1$ and $\nu_n \neq \nu$, the physical meaning for the generalized Poisson’s ratio terms ν_n becomes obscure (see discussion in Appendix C.1.1). For this hydrostatic case, the value of $\nu_2 = 0.508$ ($\beta_2 = -32.1$) for the two-term Ogden-Hill law causes the hydrostatic stress, Equation C.50, to numerically blow-up when $J > 1$. This nonphysical behavior comes from the highly nonlinear nature of the Ogden-Hill strain-energy density and the complete omission of any hydrostatic tension material data during the material fit. Since volumetric tension is not expected in the nip mechanics problems we are studying, this problem is ignored.

To further check the accuracy of the material fit, nonlinear finite element models of the compression experiments were made. The models used the same general mesh as depicted in Figure 2.5 with ABAQUS/Standard C3D8 elements and a static solution algorithm. Calculations that simulated the same measurements made in the actual physical tests were performed. Figure 3.10 shows that the simulations correlate well with the actual test data, giving us further confidence in our material coefficients.

3.2 Material Testing of R600U

Considering the highly open-cell nature of R600U, we expect this material to exhibit more material variability, both locally within a sample and sample-to-sample, compared to SE410. Furthermore, it is likely to expect that this material will “stretch” our material assumptions of isotropic, time-independent behavior that are used in this study.

(a) Nominal compression stress



(b) Nominal transverse strain

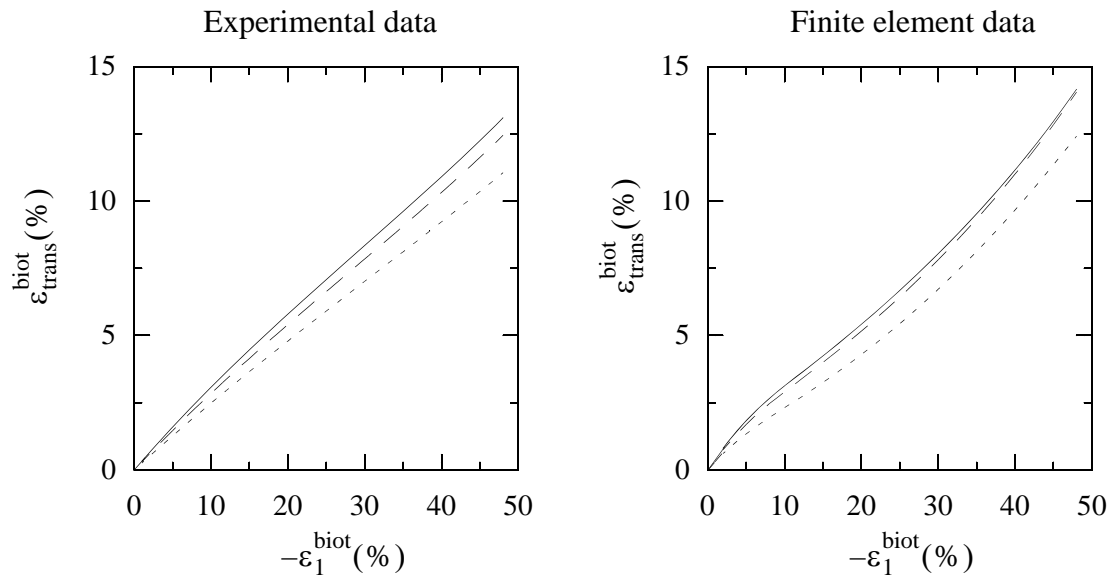


Figure 3.10: Comparison of actual experimental results from uniaxial compression of SE410 and a nonlinear finite element model of the experiment using a two-term Ogden-Hill law. FEA model includes non-ideal boundary conditions.

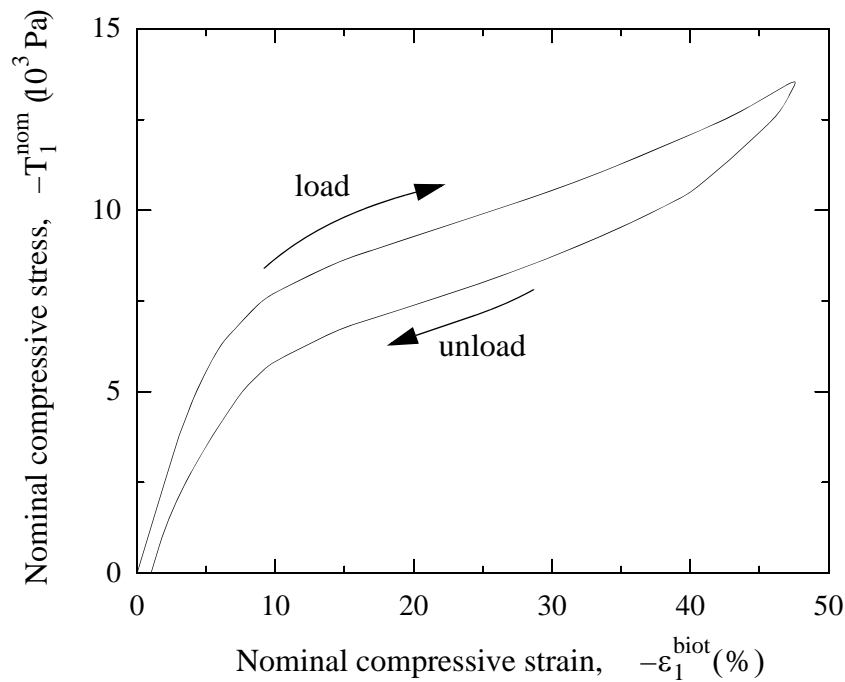


Figure 3.11: Hysteresis in R600U as measured by uniaxial compression.

Testing of R600U followed the same procedures as those used for SE410. Both compression and simple-shear tests were run at a nominal strain-rate of 0.4%/sec. To verify that the material was insensitive to strain-rate, tests were also performed at a rate of 7.0%/sec. Nominal stresses increased by less than 5% over the deformation range for a given sample. Material hysteresis was evaluated in a uniaxial compression mode by loading and then immediately unloading the specimen. Figure 3.11 demonstrates typical results, a moderate amount of energy loss. It should be noted that after approximately 5 to 10 seconds from the end of the test, the sample was fully recovered (no permanent deformation). Material isotropy was also checked by loading a cube in uniaxial compression through three perpendicular axes. Figure 3.12 shows that each of the three axes yielded moderately different stress-strain curves. The anisotropic behavior shown here can be attributed to the manufacturing method used to make this foam material. The escaping gases which create the cells, combined with the influence of gravity, orient the cellular structure.¹

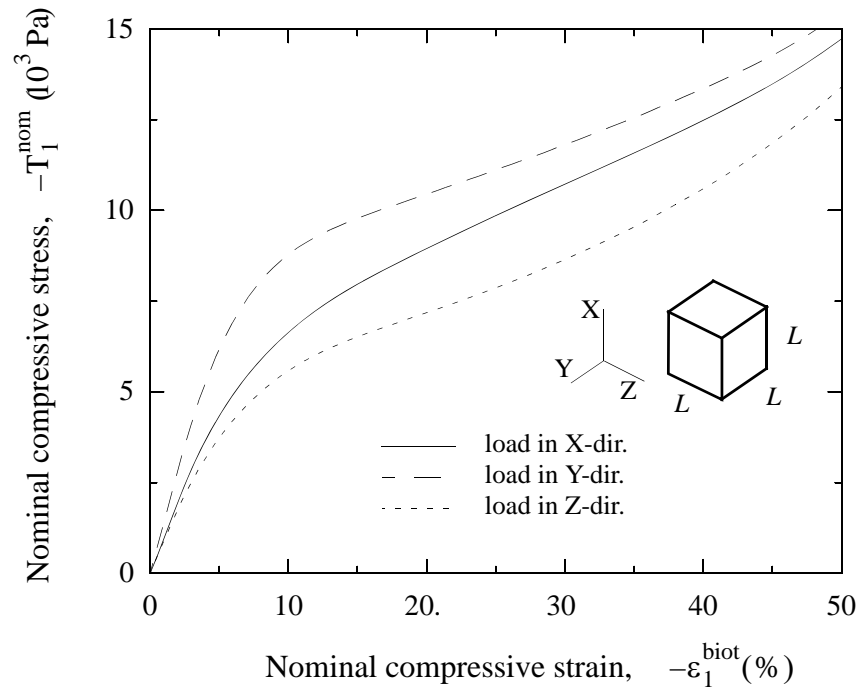


Figure 3.12: Anisotropic behavior of R600U in uniaxial compression.

The highly cellular nature of the R600U also influences the *elasticity* of the material. As we saw for SE410 (Section 3.1.2), weak bonds in the material are broken as the total maximum amount of deformation experienced by the material increases. This softens the material's stress/strain response. For SE410, this was only apparent during simple-shear testing. For R600U, this softening was also apparent in the uniaxial compression experiments. Figure 3.13 shows for a typical sample that as the maximum value of compressive strain is increased, the R600U material stiffness decreases. The curves shown in Figure 3.13 are steady state curves.¹

Although this material is not ideally elastic nor isotropic, we will show throughout the rest of this research that sufficiently accurate results can be obtained using these simplifying assumptions.

1. In general, the orientation of the cell structure for the specimens tested was unknown. Knowledge of where the samples were extracted from the bun and in what orientation relative to the bun was not available.

1. Steady state means that the material has seen multiple load/unload cycles and that the stress/strain curves no longer change with additional loading cycles.

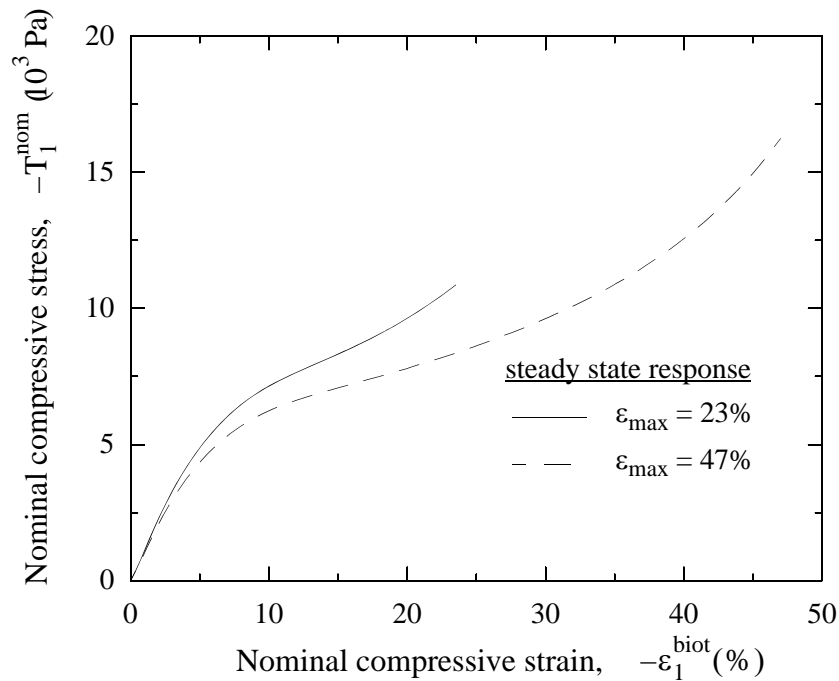


Figure 3.13: Influence of maximum applied strain on compression behavior of R600U.

3.2.1 Uniaxial Compression Test Results

The compression tests were performed using three different specimen sizes: $B/L = 1.0$, 1.35, and 2.0. Tall blocks, $B/L < 1.0$, could not be tested because of buckling problems. For each specimen size, three material samples were evaluated. Figure 3.14 depicts the results for specimen size $B/L = 1.0$. These results are for a maximum nominal compressive strain up to 50%. The data demonstrates that sample variability was greater for the R600U compared to similar measurements made on SE410 (Figure 3.2). Figure 3.14a shows that R600U exhibits the same three regions (linear, softening or buckling, and densification) as was seen for SE410. The buckling region for R600U extends farther (up to 40% nominal strain) than was found for SE410.

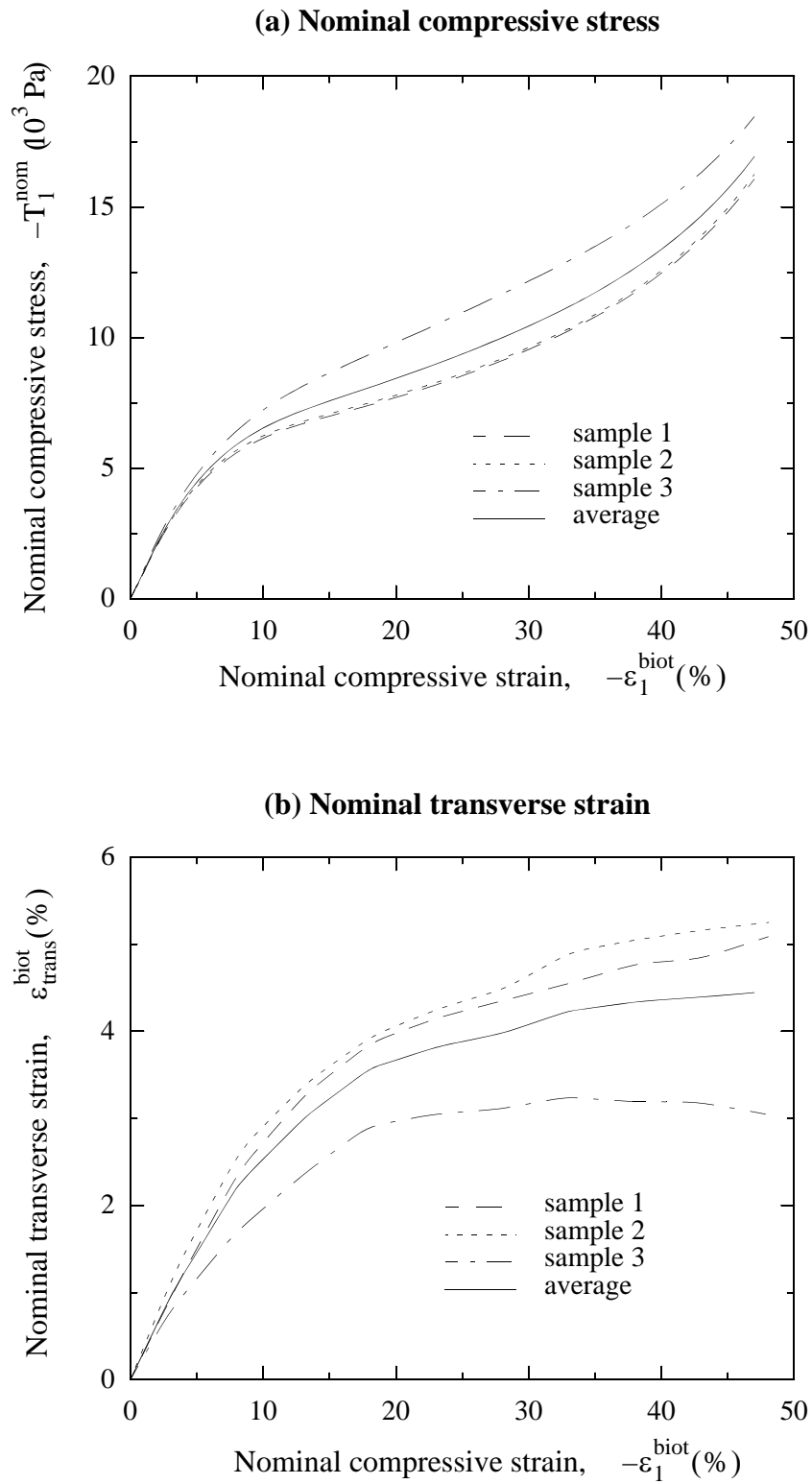


Figure 3.14: Experimental results for R600U in compression. Specimen dimension ratio, $B/L = 1$.

Figure 3.14b demonstrates that the transverse strain varies approximately linearly for only the first 10% of applied compressive strain, after which the transverse-strain rate of expansion quickly decreases to a point where its slope is nearly zero.¹ The initial tangent value of the average curve, $v_0 = 0.32$, is similar to the value of 0.33 which was found for SE410. However, unlike the behavior of SE410, the tangent value for R600U decreases quickly beyond 10% applied compressive strains.

Figure 3.15 presents the average results for the three specimen sizes tested. Both Figures 3.15a and 3.15b show differences between the average values from the three specimen sizes. Because of the non-ideal material behavior (anisotropy of Figure 3.12 and sample variation of Figure 3.14), the differences shown in Figure 3.15 do not indicate an influence from specimen size. Moreover, the lack of a definitive trend in the data of Figure 3.15 as a function of specimen size further supports the conclusion that non-ideal boundary effects were not discernible from the data. As a result, the average data from the experiments with $B/L = 1$ will be used (as shown in Figure 3.15) for the material law computations of Section 3.2.3.

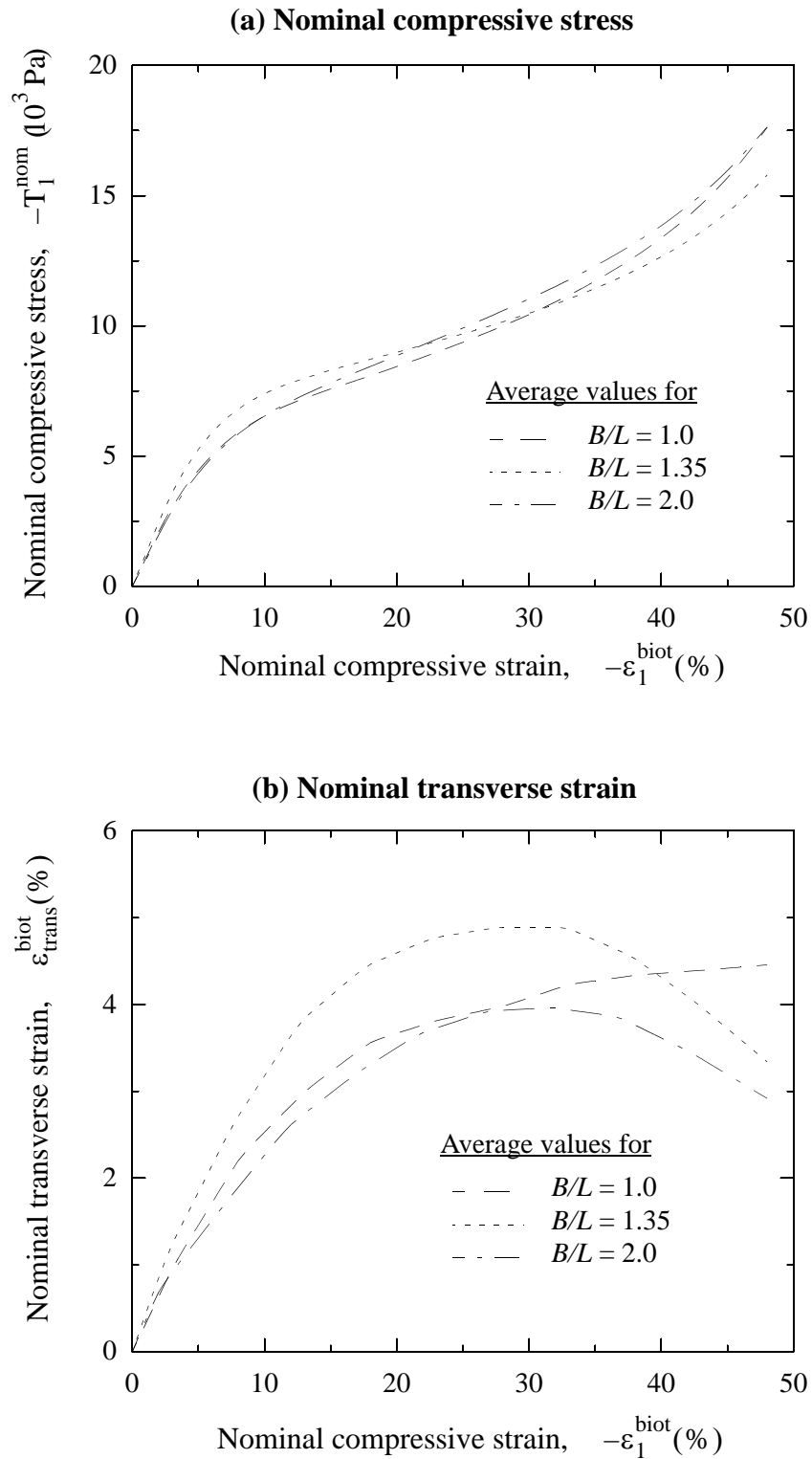
3.2.2 Simple-Shear Test Results

For the shear data, sample variation was similar to the variations seen in the uniaxial compression experiments. The specimen dimensions for the simple-shear testing were $B = 50.8$ mm, $L = 178$ mm, and $H = 25.4$ mm (see Figure 2.3).

Figure 3.16 depicts the average results from three samples of R600U measured under simple-shear. Figure 3.16a presents applied shear stress data while Figure 3.16b presents the Poynting stress data. As with the tests of SE410 in Section 3.2.2, the material tends to soften as it is deformed to greater maximum deformations.² Comparing Figures 3.16 and 3.5, we see that R600U has a greater sensitivity to this type of behavior which is primarily caused by its highly cellular nature.

1. Further deformation beyond 50% compressive strain (not presented here) showed that the transverse strain decreased back to a near-zero value at 75% compression.

2. These results were measured after the samples had been pre-worked by multiple load/unload cycles.



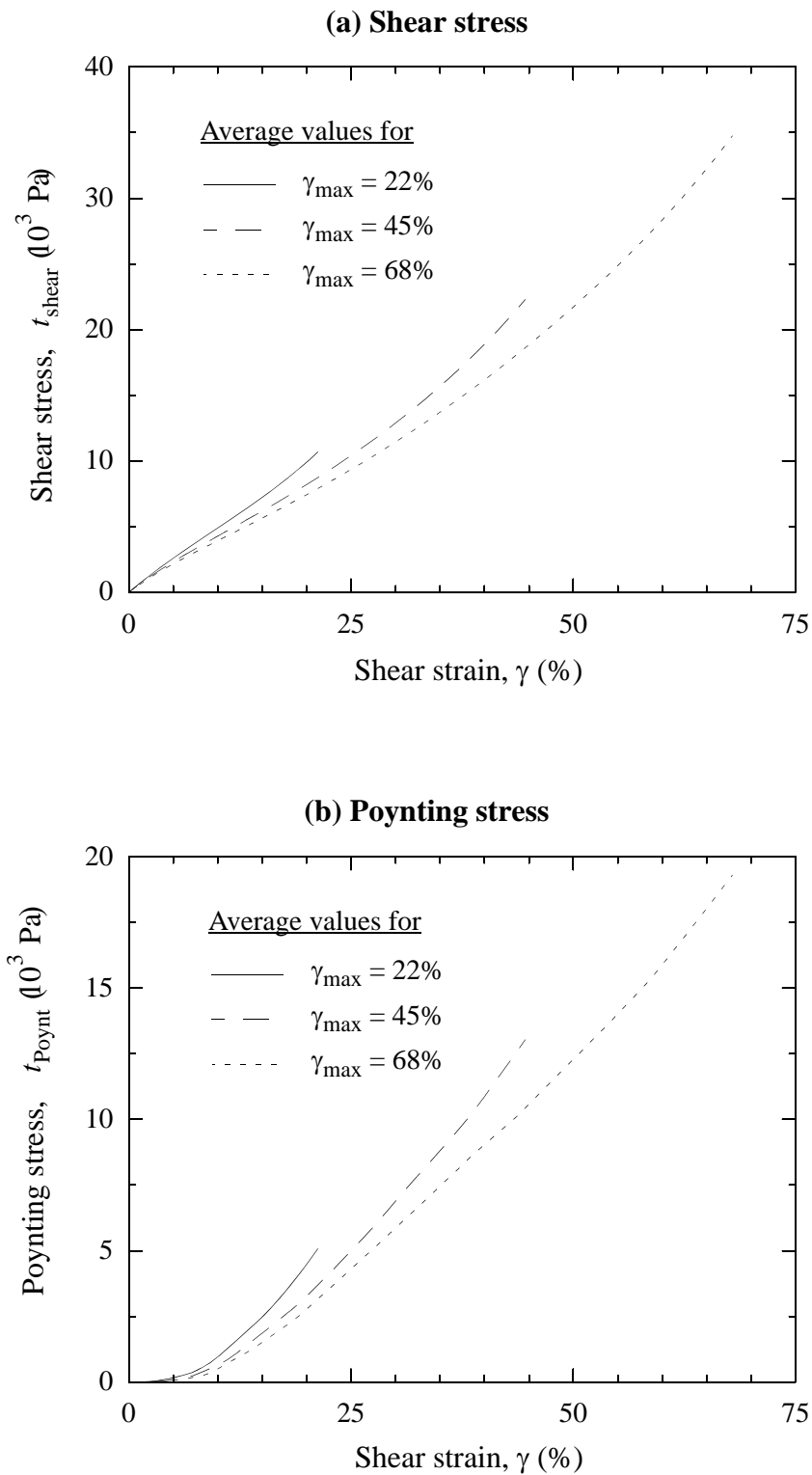


Figure 3.16: Experimental results for R600U in simple-shear. Evaluation for different maximum shear strains.

The shear stress in Figure 3.16a depicts three regions similar to those seen in the uniaxial compression data of Figures 3.14a and 3.15a (although the shear data is not as nonlinear as the uniaxial data). The Poynting data of Figure 3.16b begins with zero slope at zero shear strain. This is consistent with small-deformation, linear theory. As the shear strain increases above 10%, the Poynting stress increases with a tangent slope that is almost 1/2 of the shear stress tangent slope. Furthermore, the Poynting stress was also positive for any finite amount of strain, a behavior that is not predicted by Blatz-Ko or Brockman's formulations. Both these results are similar to that seen in SE410.

3.2.3 Computing Constitutive Coefficients

The data from Sections 3.2.1 and 3.2.2 allow us to compute the required material law parameters. From the analysis of Section 3.2.1, the average uniaxial compression data from the experiments with $B/L = 1$ shown in Figure 3.15 are used for curve fitting. The simple-shear data for $\gamma_{\max} = 45\%$ is used, unchanged, as shown in Figure 3.16.

Since the material behavior is highly nonlinear, we know that Hooke's law is not valid. Furthermore, we saw from Section 3.1.3 that neither Blatz-Ko or Brockman's formulations will be capable of modeling either the compression or simple-shear behavior (especially the Poynting behavior). Thus, only the general Ogden-Hill form is utilized to model the R600U.

Figure 3.17 shows that a two-term Ogden-Hill formulation is needed to adequately fit all the data for R600U. The one-term fit is not able to capture the highly nonlinear uniaxial compression mode.¹ Table 3.2 lists the material coefficients for the two fits depicted in Figure 3.17. The method used to obtain the material parameters listed in Table 3.2 was the same used to fit SE410 of Section 3.1.3.

1. It should also be noted that a three-term fit (not shown) to the R600U material data yielded several catastrophic instabilities and no significant improvement in the fit.

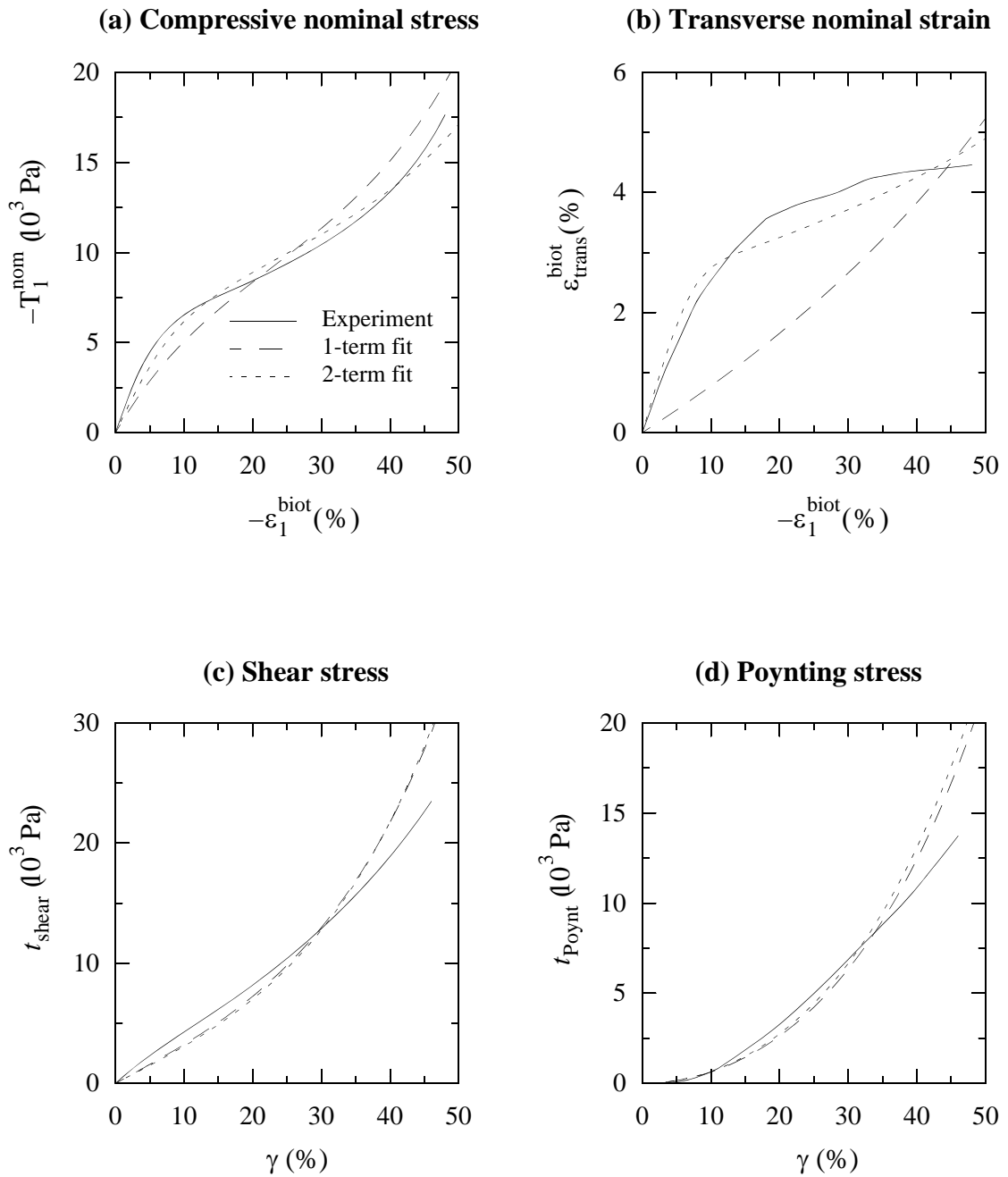


Figure 3.17: One-term and two-term Ogden-Hill fits to R600U data.

Table 3.2: Material constants for various laws to characterize R600U.

Type	N	μ_1 (10^3 Pa)	μ_2 (10^3 Pa)	$\mu_0 = \mu_1 + \mu_2$ (10^3 Pa)	α_1	α_2	ν_1	ν_2
Ogden-Hill	1	31.1	---	31.1	9.954	---	0.074	---
Ogden-Hill	2	32.6	-2.97	29.6	10.05	3.293	0.039	0.514

Figure 3.18 shows how the nominal, Cauchy, and Kirchhoff stresses computed from the 2-term fit of Table 3.2 vary as a function of nominal compressive strain for several deformation modes. Comparisons between the uniaxial and planar deformation modes demonstrate that there would be virtually no difference between a plane strain and a plane stress assumption. We also see that for deformations beyond 20% nominal compressive strain, the Kirchhoff stresses flatten out substantially. This indicates a possible problem with material stability.

Figure 3.19 shows the Drucker stability evaluations for each of the compressive deformation modes described in Figure 3.18. From these curves we see that the uniaxial and planar modes barely pass and that the equibiaxial and volumetric compression exhibit a very mild instability beyond 30% nominal compressive strain. All the primitive deformation modes depicted in Figure 2.1 were checked in this manner over the deformation range of $0.5 < \lambda_{\text{applied}} < 1.5$. No other instabilities were found and all the various stress and strain quantities appeared reasonable with one notable exception, volumetric tension. The volumetric tension mode numerically “blew-up” because of the generalized Poisson’s ratio ν_2 . This was the same problem that was found with SE410 (Section 3.1.3).

From the stability analysis we see that the two-term fit for the R600U shows two modes with very mild instabilities. Because of the highly cellular structure of this material, it is reasonable to expect that some very small macroscopic material instability may exist. Since the instabilities described in Figure 3.19 are very mild, they are not likely to cause any problems.¹

3.2.3.1 The importance of utilizing multiple deformation modes

Throughout the material law fitting of this chapter, we have used the experimental data from both the uniaxial compression and simple-shear deformation modes. What happens if only one of these deformation modes is used to fit a two-term Ogden-Hill strain energy function?

Figure 3.20 provides the results: terrible fits. This example clearly demonstrates the need for multiple modes of material data when computing the material coefficients using Ogden-Hill functions. When only uniaxial data is used, the simple-shear mode beyond 7% strain is poorly predicted. When using only simple-shear data, the uniaxial compressive nominal stress becomes completely nonphysical beyond 10% nominal compressive strain. Moreover, simple-shear yields no information regarding the Poisson behavior (transverse strain) of the material (see Section C.1.2 for further details).

The primary reason for the poor fits using only one deformation mode is the highly nonlinear nature of this class of strain-energy function. In general, the more terms used in the fit, the greater number of deformation modes that should be used to minimize the likelihood of computing material coefficients that are not sensitive to the modes tested.

Now that we see that multiple modes should be utilized in the fit, how do we know that the modes we utilized to fit both SE410 and R600U are sufficient? First, by looking at stress/strain plots and stability checks for several other modes, we see that physically reasonable material behavior is predicted (except for volumetric tension). Secondly, our final goal is to model nip mechanics problems. In these problems the elastomeric material on the rollers primarily endures compression and shear deformations. Finally, we will compare, in Chapter 4, a variety of analytical (finite element based) solutions with physical experiments to demonstrate the accuracy and limitation of the material fits computed here.

1. If problems do arise, the methods described in Section 2.1.2 can be used to further investigate the instabilities.

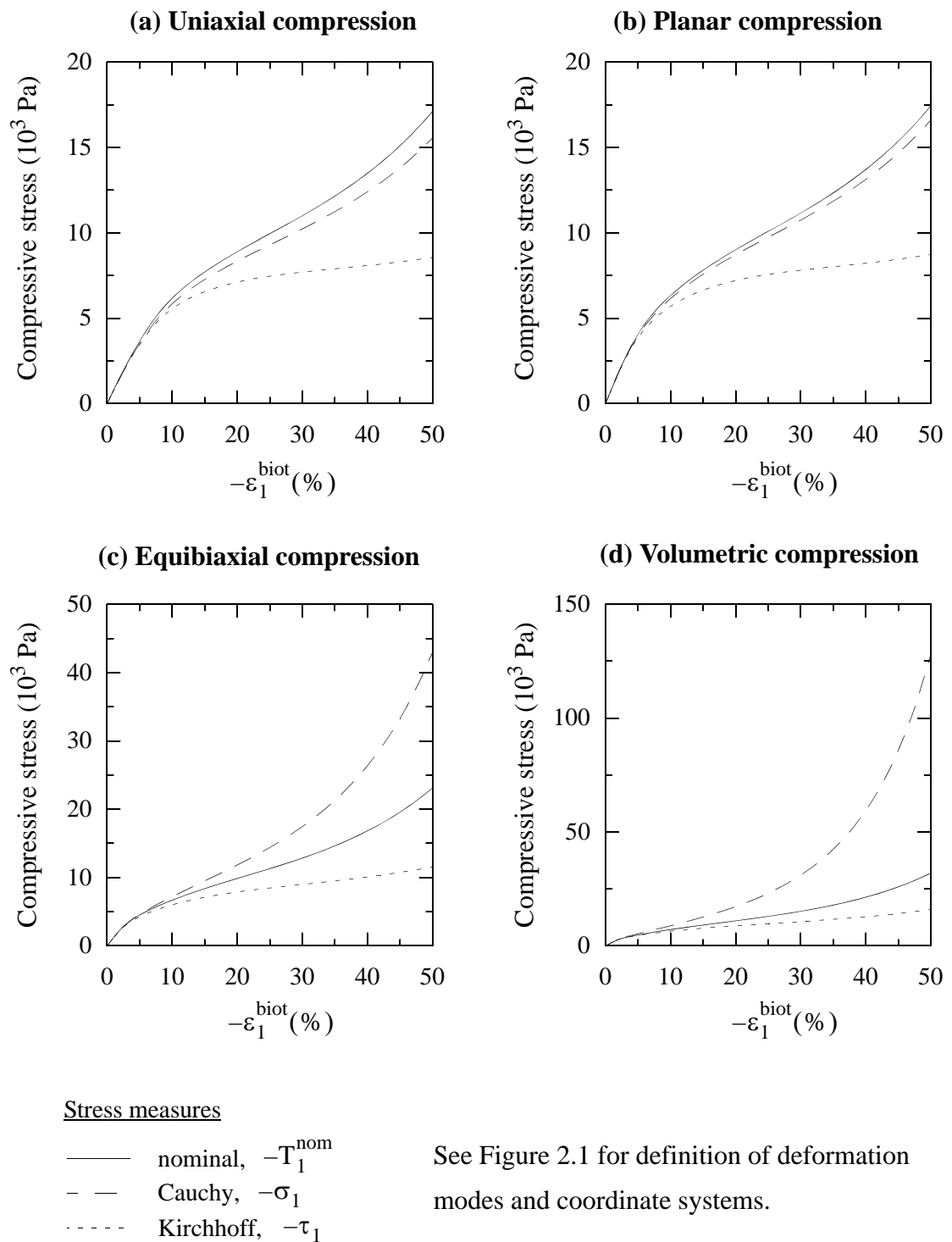
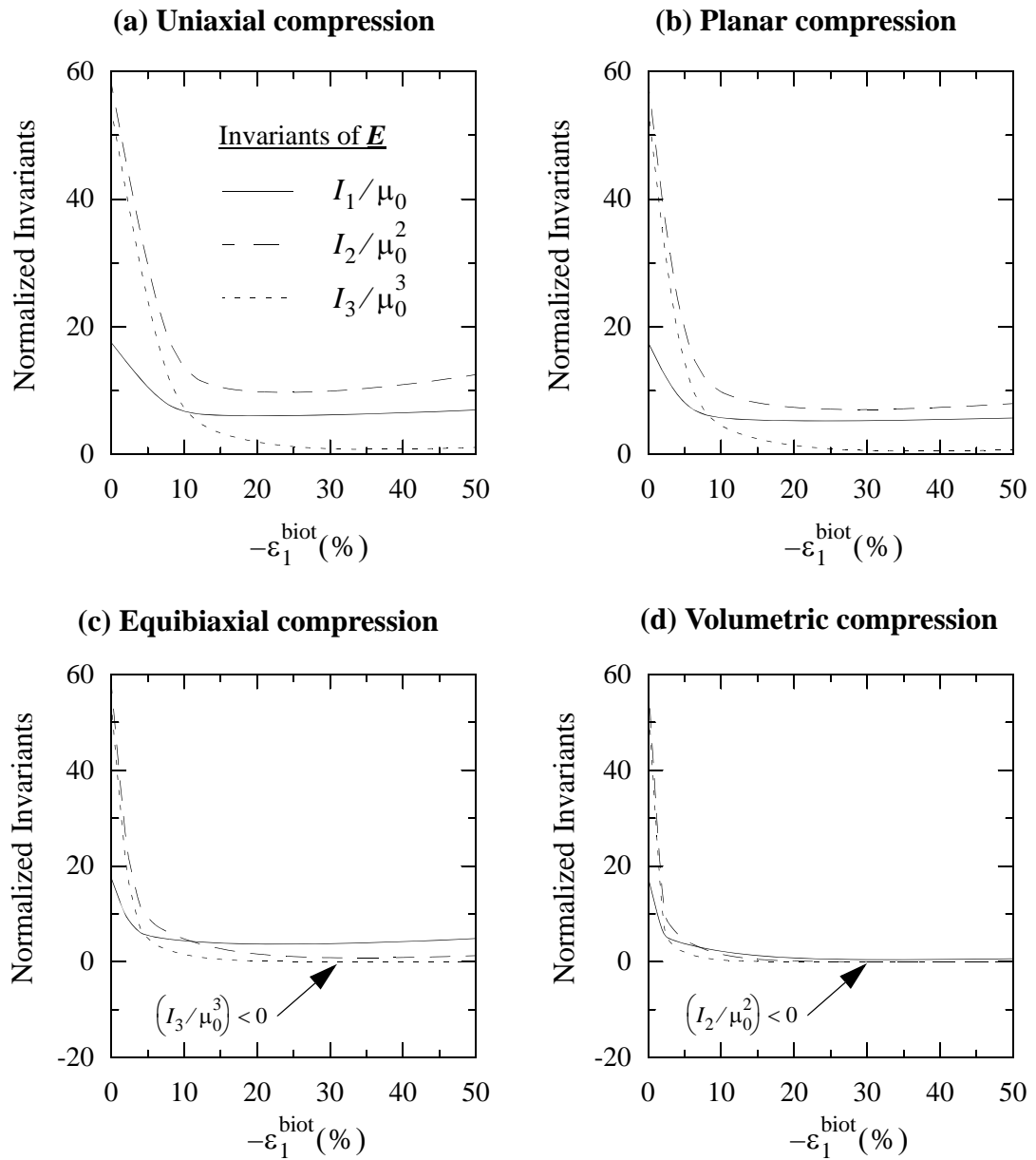
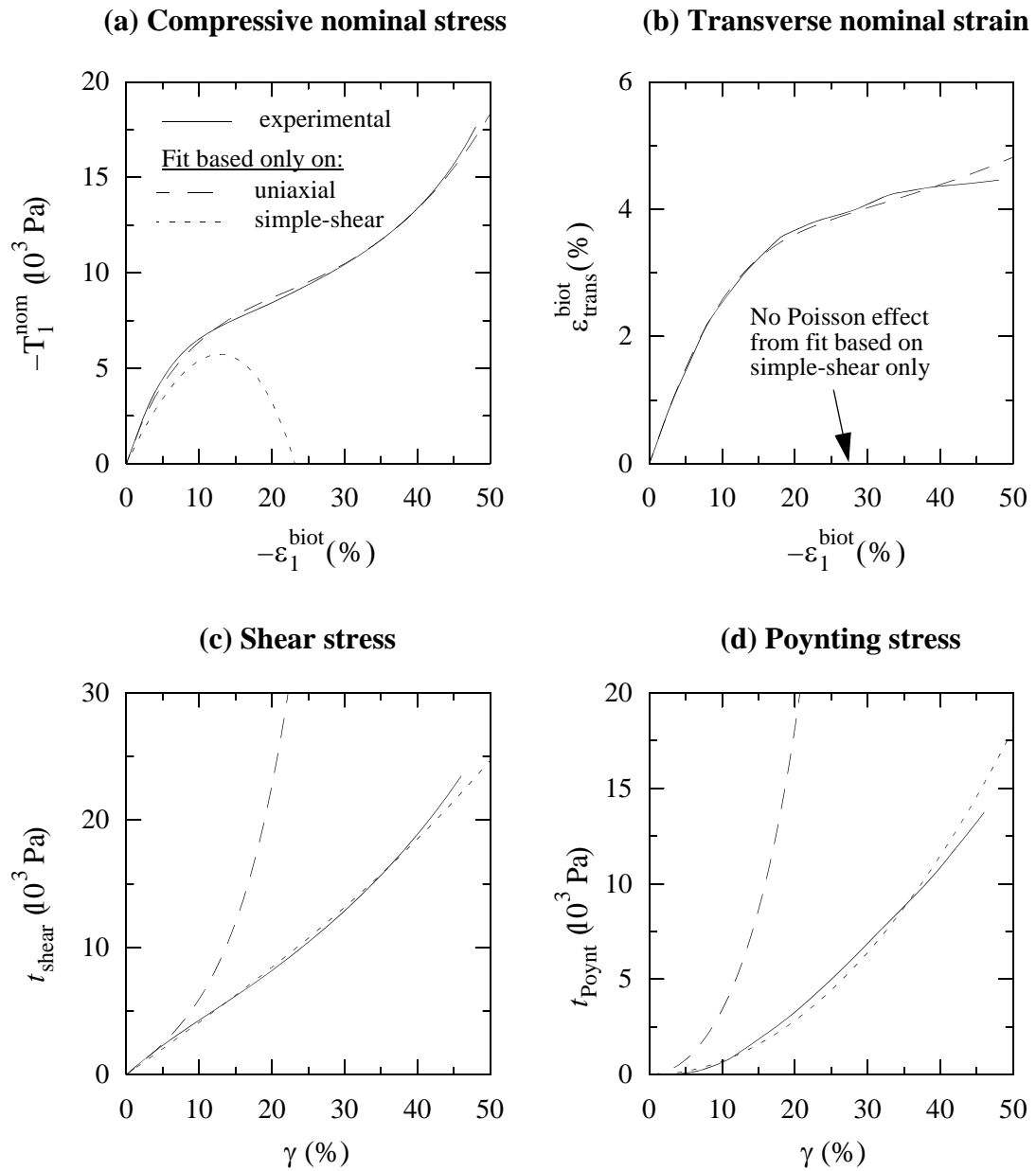


Figure 3.18: Calculated stress measures from two-term Ogden-Hill representation of R600U for several compressive deformation modes.



See Figure 2.1 for definition of deformation modes and coordinate systems.

Figure 3.19: Calculated Drucker stability checks from two-term Ogden-Hill representation of R600U for several compressive deformation modes.



Fit basis	μ_1 (10^3 Pa)	μ_2 (10^3 Pa)	$\mu_0 = \mu_1 + \mu_2$ (10^3 Pa)	α_1	α_2	ν_1	ν_2
uniaxial	62.6	-17.3	45.3	22.84	6.886	0.035	0.621
simple-shear	65.6	-24.8	40.8	4.333	-3.203	0.0	0.0

Figure 3.20: Demonstration that using data from only one deformation mode yields poor results. Fits calculated for R600U.

3.3 Material Testing of Urethane

As discussed in Section 2.2, we only need analyze the urethane in the small strain region (less than 10% nominal strain). The two required material constants, Young's modulus E and Poisson's ratio ν , are obtained from an uniaxial tension test and an ultrasound wave speed measurement, respectively.

3.3.1 Uniaxial Tension Test Results

Uniaxial tests were performed by stretching strips of urethane (one at a time) in an Instron tester while recording load and crosshead motion. Three samples were tested. Sample dimensions were 9.9 mm wide, 1.98 mm thick, and 99.0 mm long (gage length). The applied strain rate was 1.0%/sec.

The nominal stress T^{nom} and stretch ratio λ for each sample were computed from the applied load, crosshead displacement, and original specimen geometry. These values were then converted to Cauchy stress and logarithmic strain via

$$\sigma = \frac{\lambda}{J} T^{\text{nom}} \approx \lambda T^{\text{nom}}, \quad \varepsilon^{\text{ln}} = \ln(\lambda). \quad (3.1)$$

The approximation in Equation 3.1 exploits the fact that urethane is nearly incompressible. The Young's modulus was then computed utilizing linear regression of Cauchy stress and logarithmic strain material data over the deformation range $1.0 \leq \lambda \leq 1.1$. The average value of Young's modulus E was $3.85 \cdot 10^6$ Pa. Sample variation from this average value was $\pm 5\%$. The measured stress-strain data was extremely linear. At $\lambda = 1.1$, the predicted Cauchy stress based on $\sigma = E\varepsilon^{\text{ln}}$ was within 0.5% of the Cauchy stress obtained from the material data. At $\lambda = 1.5$ (well beyond the small strain region), the discrepancy was only 11% (the material data showed a slight stiffening beyond $\lambda = 1.15$).

Evaluation of material hysteresis was also performed with the uniaxial samples. Specimens were loaded up to 10% nominal strain and then immediately unloaded. Only a small amount of hysteresis was found; differences in stress values between loading and unloading were less than 5%.

3.3.2 Poisson's Ratio Measurement Test Results

Determination of Poisson's ratio utilized a Panametrics Model 5224 Ultrasonic Gage. This gage is typically used to measure the thickness of a given sample by emitting ultrasonic waves into the sample (which travel at the wave speed of the material in question) and measuring the elapsed time for the waves to be reflected back from the opposite surface. The specimen thickness is then calculated as the material wave speed times 1/2 the elapsed time. The Panametrics gage can also be used to determine the wave speed of a given material if the sample thickness is known.

Flat urethane samples with a thickness of 2.03 mm were utilized in the tests. The wave speed of the urethane was measured using a simple trial and error method. This was done by determining the required wave speed such that the gage's displacement read-out reported the known sample thickness. Ten separate measurements were made utilizing this technique. Values of measured wave speed ranged from 1455 m/sec to 1468 m/sec. From Equation 2.37 these measurements correspond to Poisson's ratio ranging from 0.499711 to 0.499715 (the last digit is not significant). From this data we take Poisson's ratio of urethane to be 0.4997.¹

Previous measurements made by the author on a similar urethane using the constrained piston test method described in Section 2.2.1 yielded a Poisson ratio value of 0.495. Based on the discussion of Section 2.2.1 we conclude that the value measured here using the ultrasound technique, $\nu = 0.4997$, is in good agreement with the previous measurement.

3.3.3 Evaluation of Neo-Hookean Material Representation

As discussed previously in Section 2.2, it will be necessary to utilize a hyperelastic material representation for urethane during studies of the limiting case of complete incompressibility. Since the material behavior is linear within the strain range of interest, we chose a neo-Hookean form (Equation 2.24 with $N = 1$ and $\alpha_1 = 2$). Based on the measured values of E and ν from the previous subsections, we find that $\mu_1 = 1.29 \cdot 10^6$ Pa.

1. We will show in Chapter 4 that the difference between $\nu = 0.4997$ and $\nu = 0.5$ is negligible for the problems studied in this research.

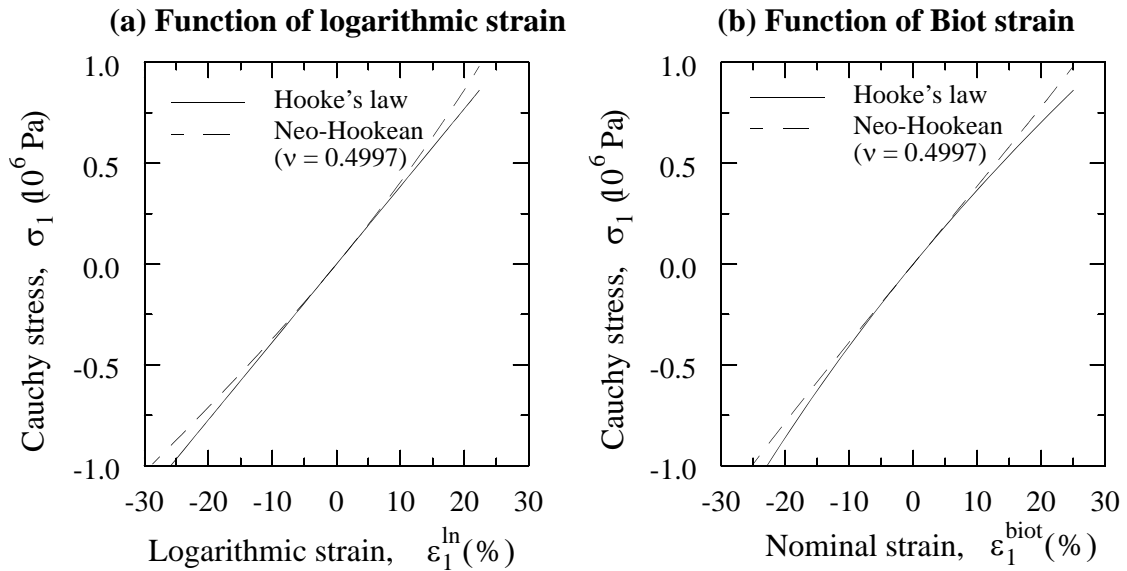
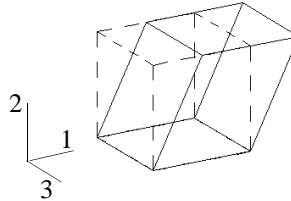


Figure 3.21: Comparison between Hooke's law and neo-Hookean material representations for an uniaxial deformation mode.

For the fully incompressible case, $\nu = 0.5$, we find from Equations, 2.27 and 2.28 that $D_1 = 0.0 \text{ Pa}^{-1}$. For the nearly incompressible case, $\nu = 0.4997$, we have $D_1 = 9.32 \cdot 10^{-10} \text{ Pa}^{-1}$. The differences in computed stresses between the fully incompressible case and nearly incompressible case will be negligibly different for all cases except a highly constrained deformation mode such as volumetric deformation.

Figure 3.21 compares Cauchy stress predictions between Hooke's law and neo-Hookean for uniaxial deformations. A value of $\nu = 0.4997$ is used for both laws. From these plots we see little difference between the two material formulations. Figure 3.22 demonstrates similar correlation for simple-shear.¹ Figure 3.23 depicts how the two material formulations compare under several compressive deformation modes. Correlation is excellent with the deformation range $0.9 < \lambda_{\text{applied}} < 1.0$.

1. It should be noted that the predicted Poynting stress values in Figure 3.22 are negative or equal to zero. We may suspect that these predictions are possibly incorrect based on the measured data of the two compressible materials described in Sections 3.1 and 3.2. Since we are only dealing in the small strain region for urethane ($\gamma < 10\%$), the Poynting stress will be very small compared to the shear stress. This fact makes this possible error in Poynting stress negligible.

(a) Schematic of simple-shear deformation**(b) Plane strain simple-shear**

$$\mathbf{F} = \begin{bmatrix} 1 & \gamma & 0 \\ 0 & 1 & 0 \\ 0 & 0 & 1 \end{bmatrix} \quad \sigma_3 = \text{unknown}$$

(c) Plane stress simple-shear

$$\mathbf{F} = \begin{bmatrix} 1 & \gamma & 0 \\ 0 & 1 & 0 \\ 0 & 0 & \lambda_3 \end{bmatrix} \quad \begin{array}{l} \sigma_3 = 0 \\ \lambda_3 = \text{unknown} \end{array}$$

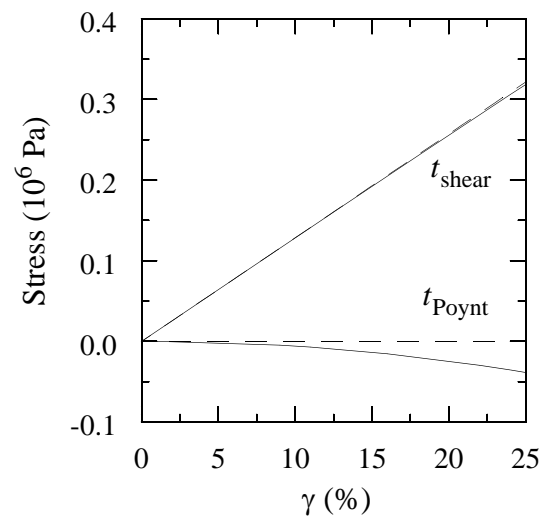
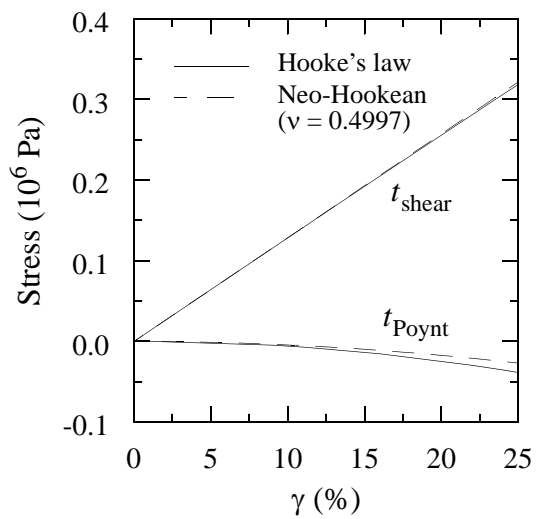
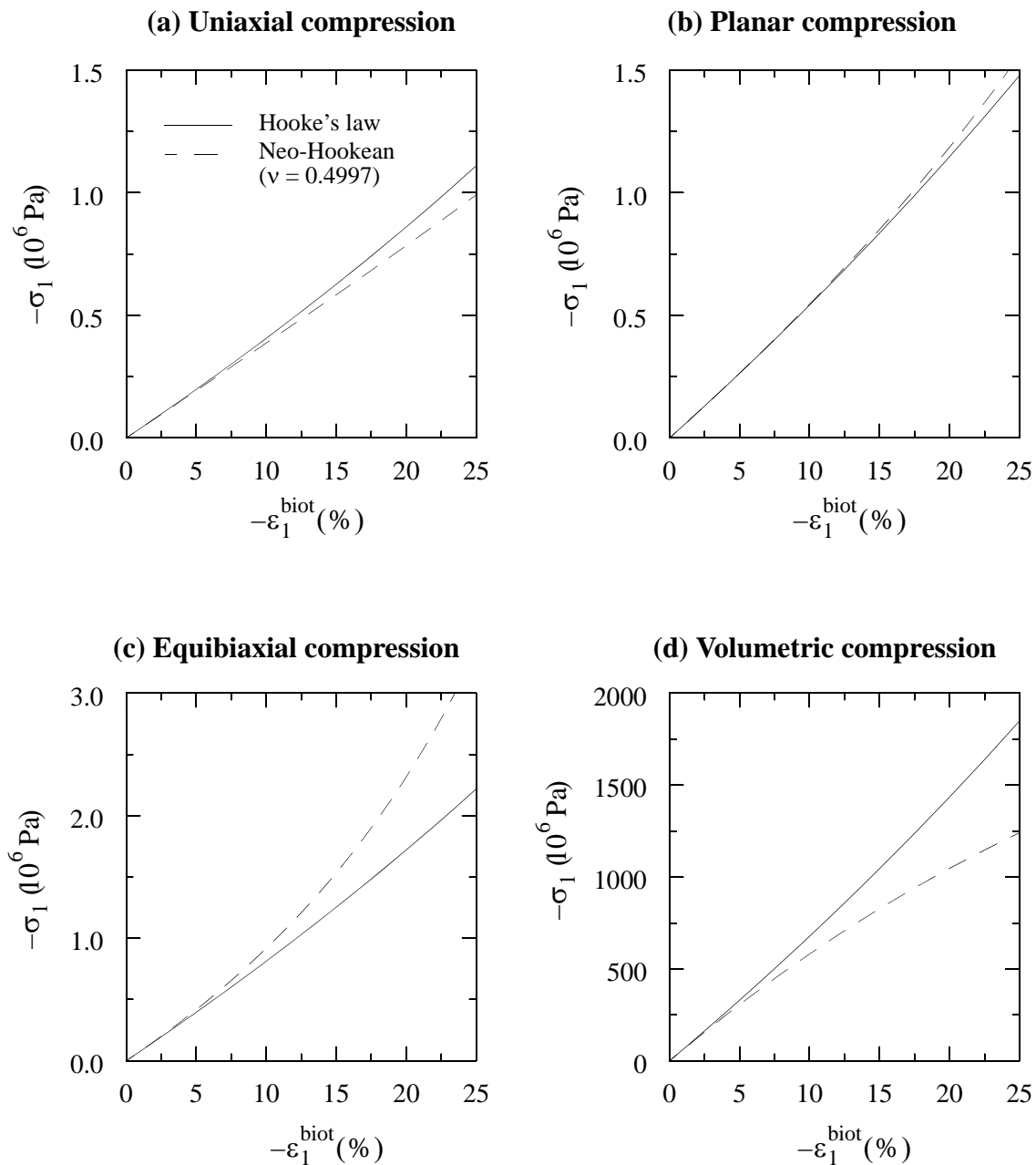


Figure 3.22: Evaluation of simple-shear stress predictions for urethane using Hooke's law and neo-Hookean material representations.



See Figure 2.1 for definition of deformation modes and coordinate systems.

Figure 3.23: Calculated Cauchy stresses from Hooke's law and neo-Hookean representations of urethane for several compressive deformation modes.

Chapter 4

Nip Mechanics: Analyses and Experiments

In this chapter we utilize the various constitutive relationships developed previously to analyze several 2-D and 3-D elastomeric nip problems. The methods of analysis are static implicit and dynamic explicit finite element models.¹ To verify the qualitative and quantitative capability of these models, many comparisons between these models and physical experiments are performed. From these studies, the influences of elastomer type, external loading, and friction on various nip parameters are assessed.

Figure 4.1 depicts two nip systems that are evaluated. Both of these designs are found in media-handling situations ranging from media manufacturing to office imaging applications such as copiers and printers. The tire-based nip system (Figure 4.1a) is very common in situations where the sheet is only transported and not processed by the nip system. The continuous elastomer-covered hollow metal drum design (Figure 4.1b) is frequently used to transport and process a sheet in subsystems such as the fuser station of a copier or printer.

Knowledge of how geometry, elastomer type, and loading influence nip pressure, nip width, and media speed ratio is important to know in order to develop robust systems. In particular, axial variations in these nip parameters can significantly degrade system performance. Figure 4.1 depicts typical axial variations. In Figure 4.1a, axial variations in the media speed ratio generate sheet skew. These axial variations can be caused by uneven external loading, nonuniform roller geometry, or other nonsymmetries in the system. The example in Figure 4.1b depicts axial variation in nip parameters such as nip contact pressure and nip width that are caused by deflections of the hollow drums. Although not

1. Although dynamic solutions are used, all problems are “slow” events in that inertial dynamic effects are negligible. The explicit dynamic method is used because we are studying rolling contact with friction. This method is more robust than the static implicit technique for problems of this type.

(a) Tire-based nip system

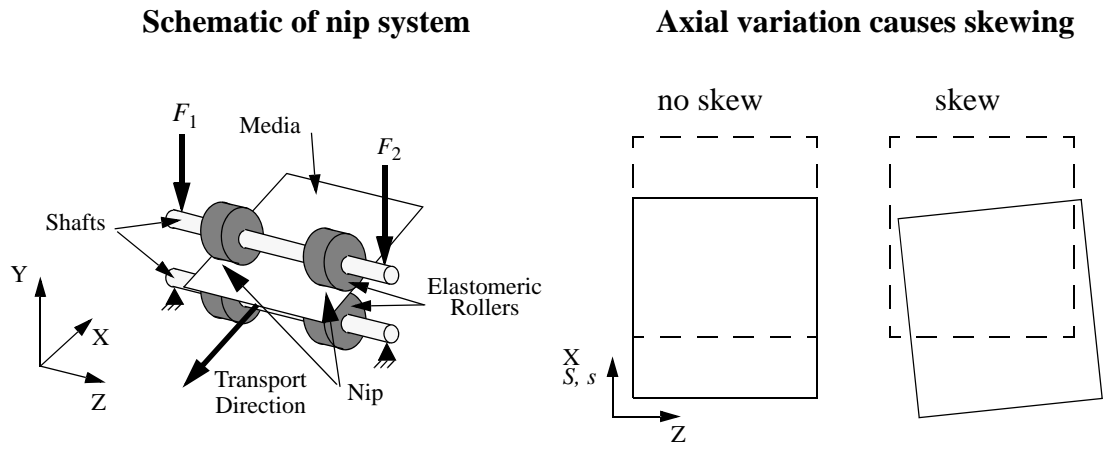
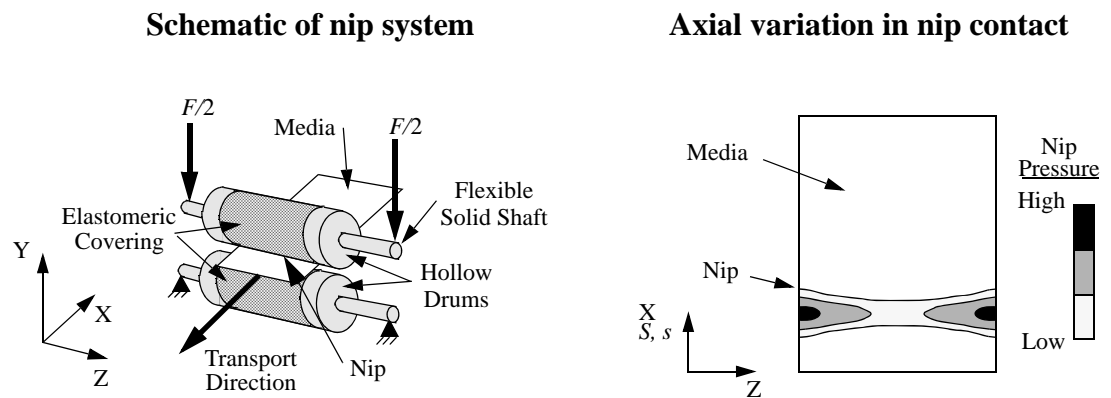
(b) Continuous nip system:
hollow drums covered with an elastomer

Figure 4.1: Schematic of nip systems evaluated.

explicitly shown in this case, the axial variation in nip pressure will also cause axial variation in the media speed ratio which may induce media wrinkling.

Of the nip parameters mentioned, media speed ratio is often the most important and most sensitive parameter in the system. To obtain a basic understanding of the mechanics that govern media speed ratio, the following simplified analysis, based on some techniques utilized by Soong and Li [104] and Cole and Piarulli [21], is undertaken.

4.1 Simplified Analysis of Media Speed Ratio

In Section 1.1.1 a general description of media speed ratio and its relationship to media overdrive and underdrive was given. Whether the media overdrives or underdrives the feed rollers is strongly dependent on the mechanical properties of the elastomeric covering on the roller and the amount of strain it is enduring. In this section, we further investigate this behavior.

For ease of description, we consider the case of a generic, plane strain, elastomer-covered roller with a rigid hub (see Figure 4.2). The sheet in the nip is extremely thin, such as paper, and is considered rigid because it has relatively high in-plane stiffness. Moreover, the Y-symmetric nature of the problem results in no bending of the sheet.¹ Therefore, only deformations of the elastomeric covering are evaluated.

Figure 4.3 shows the undeformed and deformed states of the elastomer (in the zone of the nip) for the case of *frictionless* indentation against a rigid surface (sheet). Figure 4.3b shows that significant hoop strains exist in the elastomer. If the roller is now rotated, these hoop strains will cause the outer fiber of the elastomer (in the nip) in the deformed state to travel at a speed which is different from that which would be observed if the undeformed roller (Figure 4.3a) were rotated. This effect is what governs media speed ratio.

Consider a particle, located on the outer fiber of the elastomeric covering, denoted as $B(\mathbf{X}, t)$ in its undeformed state and $B(\mathbf{x}, t)$ in its deformed state. The bold quantities \mathbf{X} and

1. More will be said about the Y-symmetric nature of the nip in Section 4.3.

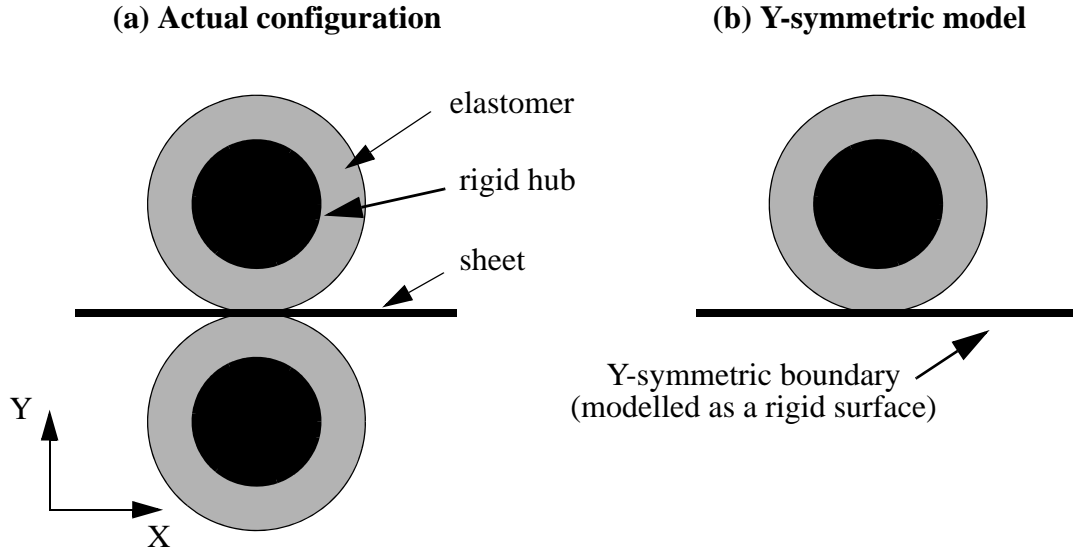


Figure 4.2: Schematic of Y-symmetric plane strain elastomer-covered roller.

x are the position vectors of B in the undeformed and deformed states, respectively.¹ During the time increment $\Delta^{21}t = {}^2t - {}^1t$, the roller is rotated and particle B travels a distance $\Delta^{21}S$ in its undeformed state and $\Delta^{21}s$ in its deformed state. The average speed of particle B in both states is defined as

$$\begin{aligned} {}^{21}V &\equiv \frac{\Delta^{21}S}{\Delta^{21}t} \\ {}^{21}v &\equiv \frac{\Delta^{21}s}{\Delta^{21}t} \end{aligned} \quad (4.1)$$

1. In Figure 4.3, the left-sided superscripts 1 and 2 applied to the position vectors X and x denote that these vectors will be different at times 1t and 2t .

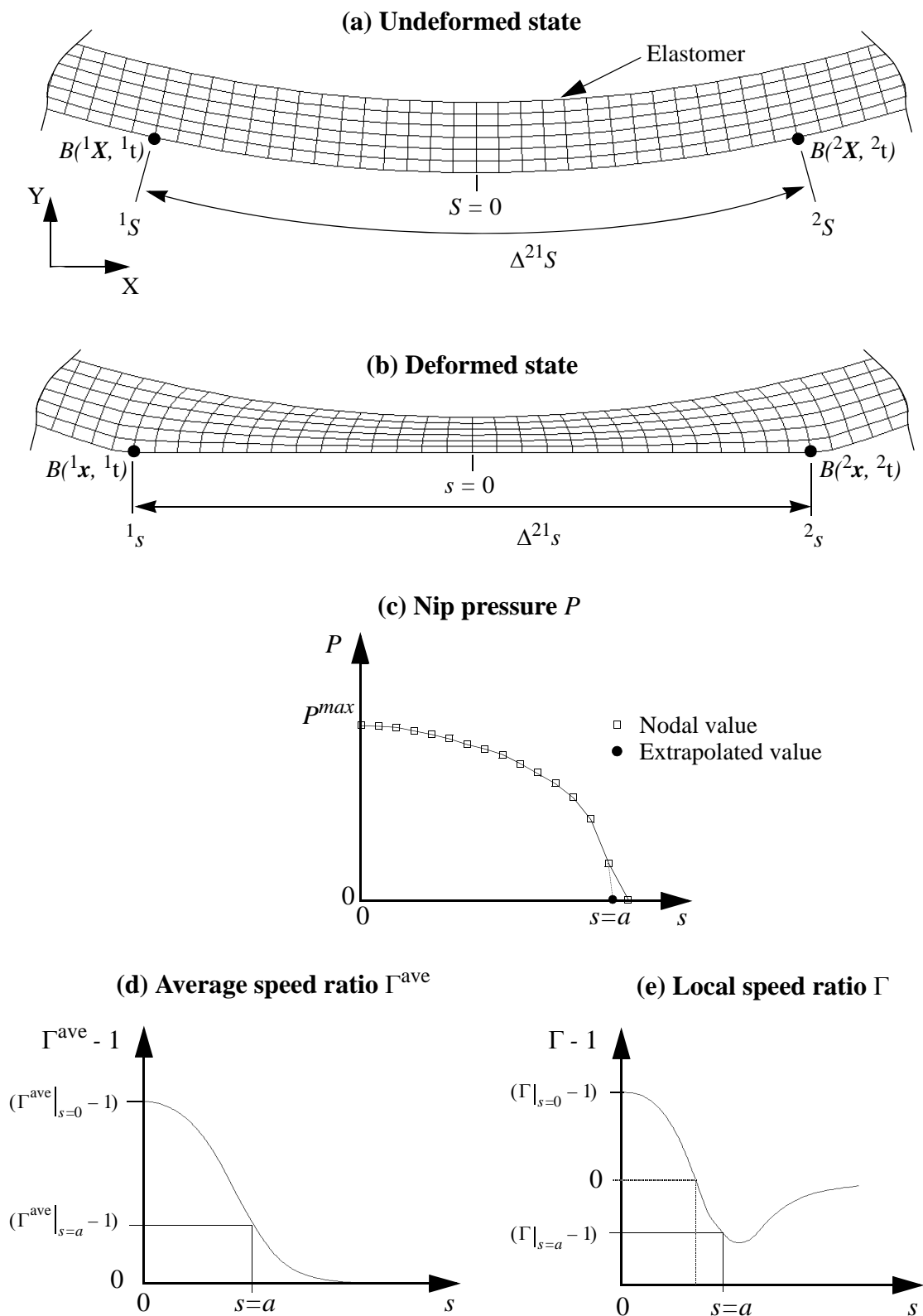


Figure 4.3: Simplified evaluation of speed ratio.

From these two average velocities, the average speed ratio of the outer fiber of the elastomer, Γ^{ave} is defined as

$$\Gamma^{\text{ave}} \equiv \frac{\Delta^{21} s}{\Delta^{21} S} \quad (4.2)$$

Taking the limit as $\Delta^{21}t$ approaches zero yields the local (or instantaneous) speed ratio of the outer fiber of the elastomer, Γ , defined as

$$\Gamma \equiv \frac{ds}{dS} \quad (4.3)$$

In a finite element model, the quantities ds and dS are approximated as individual finite element lengths in the deformed and undeformed states, respectively. The local speed ratio, Γ , is also equal to the local stretch ratio in the curvilinear coordinate system of a material particle located on the outer fiber of the elastomer. Integrating the local speed ratio over the time increment $\Delta^{21}t$ yields the average speed ratio Γ^{ave} .

The bounds of the nip are defined by the locations where the normal contact pressure, P , becomes zero and are denoted as $S = \pm A$ and $s = \pm a$ in the undeformed and deformed states, respectively. Figure 4.3c shows a typical X-symmetric nip pressure profile as computed from a finite element model. The figure shows that the half nip width a (and A) is computed from an extrapolation of the nodal contact pressures. This extrapolation is a consequence of the discrete nature of the finite element method.

The times 1t and 2t depicted in Figure 4.3a and Figure 4.3b are arbitrarily chosen at the beginning and end of the nip. If these times are symmetrically chosen closer to or farther from the center of the nip, different values of the average speed ratio Γ^{ave} are computed. This is shown in Figure 4.3d. Note that $\Gamma^{\text{ave}} - 1$ has been plotted since Γ^{ave} typically has values close to unity. For overdrive $\Gamma^{\text{ave}} - 1 > 0$. For underdrive $\Gamma^{\text{ave}} - 1 < 0$. Note that far from the nip, $\Gamma^{\text{ave}} - 1 \rightarrow 0$ as the elastomer deformation approaches zero. Figure 4.3e depicts a similar plot for the local speed ratio, Γ . Again, $\Gamma - 1$ is plotted. For a X-symmetric nip, we have

$$\Gamma^{\text{ave}}(s=0) = \Gamma(s=0) \quad (4.4)$$

An impressive result of this analysis is that we can obtain relative velocity information from a static, non-rolling, indentation solution. One obvious short coming of this approach is that we have only considered the elastomeric covering. We must relate these quantities to the subsequent behavior of the media. In this simplified analysis we have *assumed* that decoupling the media deformation from that of the nip is valid. This assumption has produced several ambiguous results. To predict the actual media speed ratio \bar{v} , do we use the average or local estimate of the elastomer's outer fiber speed ratio, Γ^{ave} or Γ , respectively? Moreover, both of these estimates vary through the nip. Since the sheet is very stiff in-plane and considered rigid, the media must only have a single value of speed ratio; it cannot vary through the nip.¹ In actuality, the media/elastomer system is coupled because there is friction between the elastomeric roller and the sheet. Therefore, the influence of friction must be evaluated to obtain the actual sheet speed ratio, \bar{v} .

The inclusion of friction (or any other energy dissipating process such as material hysteresis) is particularly difficult because it is nonconservative. This makes the problem history dependent. Valid solutions with friction must account for the loading path. For rolling contact problems with soft elastomer-covered rollers, numerical solutions can require a rotation of greater than 10 degrees and possibly as much as 360 degrees to obtain steady state results. This makes rolling solutions significantly more expensive (computationally) than non-rolling predictions. Due to this cost, we must fully investigate the capabilities and limitations of non-rolling estimates of media speed ratio.

By looking at the results obtained for the frictionless case depicted in Figure 4.3 we see that significant hoop straining occurred. If the indentation analysis had included friction, the resulting frictional shear stresses would have restricted the amount of hoop strain and lowered the predicted speed ratio. A complete rolling analysis with friction will likely yield a solution that is between the frictionless and frictional indentation estimates.² This

1. The analysis later in this chapter will demonstrate that Γ^{ave} evaluated at the nip edge provides the best estimate.

2. During these studies we will need to determine a method of obtaining a single estimate of the media speed ratio from the non-constant values presented in this section.

hypothesis will be thoroughly evaluated in Section 4.3 on nip systems made from SE410, R600U, and urethane.

4.2 Non-Rolling Nip Problems

Before analyzing the complex problem of a rolling nip, we first analyze some non-rolling nip problems. The purpose of this section is to further validate the material laws from Chapter 3 for problems governed by nontrivial stress and strain states. The first set of nip analyses and experiments evaluate an elastomeric roller (with a solid steel hub) as it is compressed between two flat rigid plates. Experimental measurements of applied load and nip width as a function of roller deformation are compared against several finite element models. These comparisons also aid in the determination of certain modelling techniques, such as the artificial increase in event speed used in the explicit dynamic method.

The roller compression experiments were performed using the same apparatus described in Figure 2.2. Rollers tested were made from SE410, R600U, and urethane. Each specimen tested was sufficiently pre-worked by compressing the roller multiple times up to the maximum effective radial strain for the given test. The sample was then rotated 30 degrees and again compressed multiple times. A total of 5 rotations were performed to assure that all material on the roller had been pre-worked (see the beginning of Chapter 3 for a discussion of pre-working). Measurements of applied load and crosshead displacement were recorded at the same strain rates used in the original material testing. For the SE410 and R600U specimens, nip width measurements were made using the microscope shown in Figure 2.2. Nip width measurements for urethane specimens were made using Fuji Prescale Film For Ultra Low Pressure. The following three subsections describe the results of the finite element analyses and the accompanying physical experiments.

4.2.1 SE410

The roller specimens used for SE410 had the following nominal dimensions: 10.54 mm hub diameter, 31.4 mm thick elastomeric covering, and 35.6 mm depth (length). Figure 4.4a depicts the mesh used for the finite element models. The mesh is made from

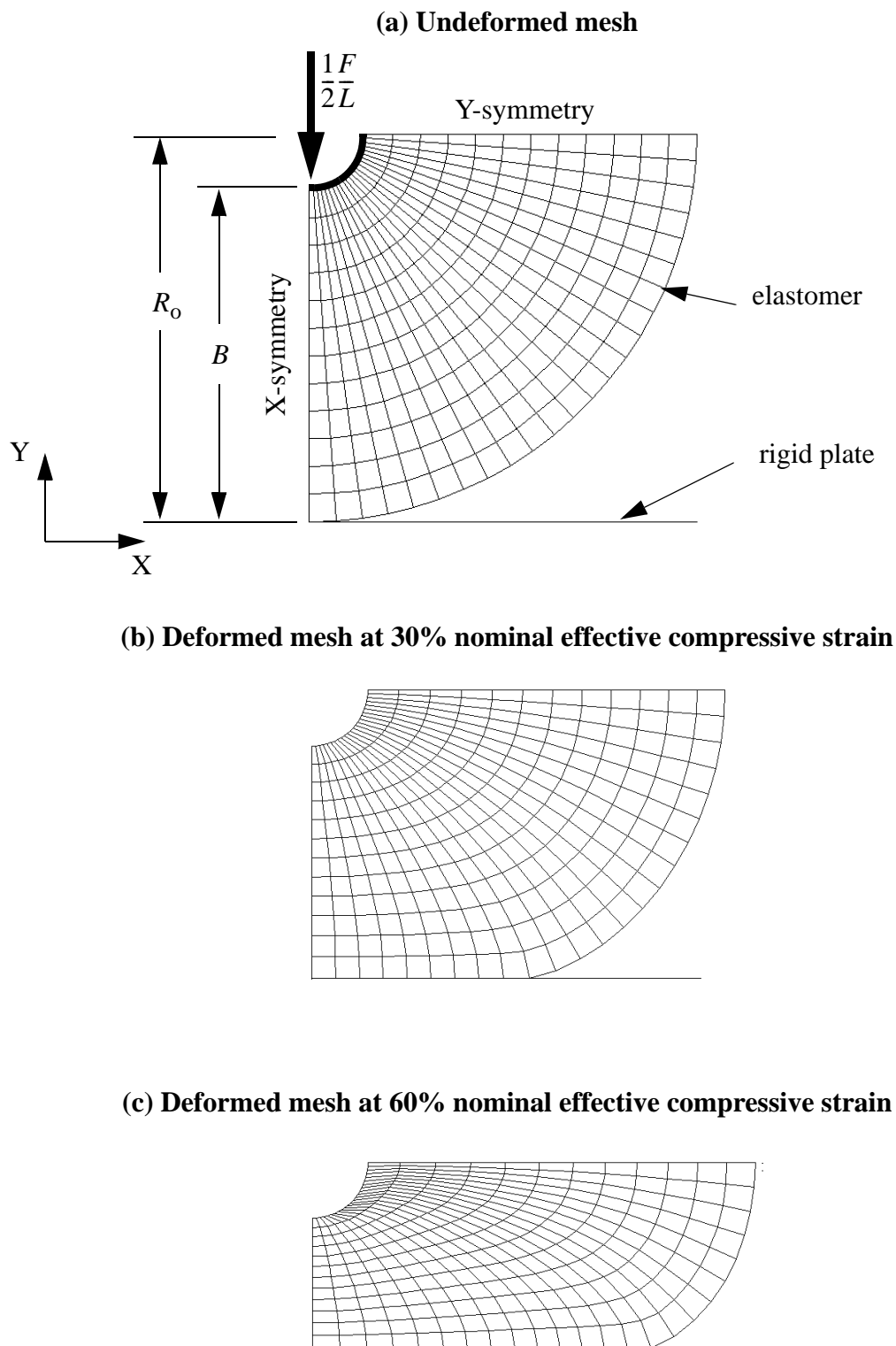


Figure 4.4: Standard finite element model for compression test of a SE410 roller.

first-order plane strain elements: type CPE4 for Standard solutions and CPE4R for Explicit solutions.¹ Also shown in Figure 4.4 are deformed shapes predicted by the finite element models for 30% and 60% nominal compressive effective radial strain, $-\varepsilon^{\text{eff}}$.² The solutions shown in this figure were produced by the Standard algorithm. Several solutions using the Explicit (dynamic) method are displayed in Figure 4.5. As described in Section 1.3.2 and Appendix B.2, we artificially decrease the event time (speed up the loading) for the solution because the computational solution time is directly related to the event time. In the actual physical experiments, the total event time to compress a roller 60% was 150 seconds. From Figure 4.5a we see that a solution whose event time is artificially decreased by a factor of 150,000 has significant inertial dynamic effects. Event time reductions by factors of 15,000 and 1500 *appear* to show no significant inertial dynamic effects when compared against the static solutions of Figure 4.4.

Figure 4.6 further assesses the explicit dynamic solutions by evaluating several nip parameters. Figures 4.6a and 4.6b further quantify the inertial dynamic effect of the “fast” Explicit solution. These plots also show the medium and slow Explicit solutions are nearly indistinguishable from the Standard solution. Figure 4.6c shows that a small amount of inertial dynamic effect exists in the predictions of nip pressure for these solutions. Because the nip pressure is a nodal quantity, it is more sensitive to dynamic solution effects, especially *ringing*. The applied load, which is an integrated quantity, tends to average out these effects.

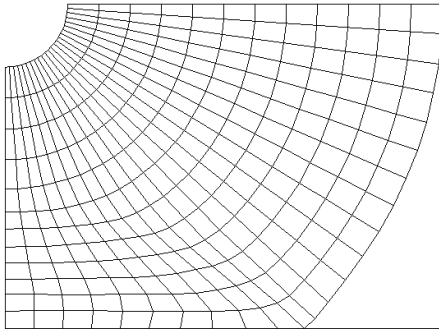
Figure 4.7 evaluates approximate measures of speed ratio quantities for the outer fiber of the roller. Although we are only analyzing the non-rolling problem in this subsection, we can still use the approximate method outline in Section 4.1 to see how these variables would be affected by computing them with the Explicit method (this will be important for the study of rolling problems). As seen in the figure, these quantities are more sensitive to

1. All solutions presented in this subsection are based on large deformations and hyperelastic material laws.

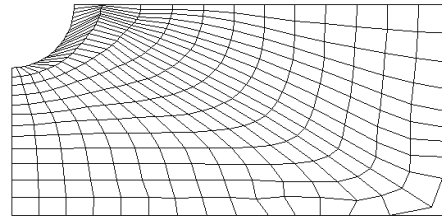
2. Nominal refers to a Biot measure of strain (See Appendix A for further details). Effective radial strain means that the radial strain is measured based on the net change in thickness of the elastomer due to deformation. The actual radial strain will vary through the thickness of the elastomer and will, in some locations, be greater than the effective radial strain.

(a) Fast solution: total event time = 10^{-3} seconds

$$\varepsilon^{\text{eff}} = -30\%$$

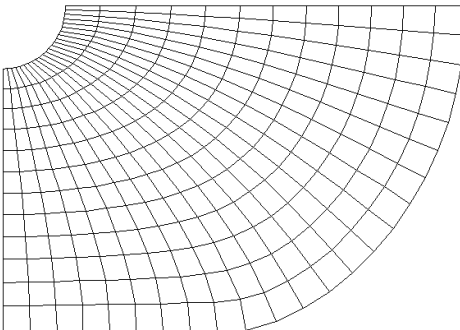


$$\varepsilon^{\text{eff}} = -60\%$$

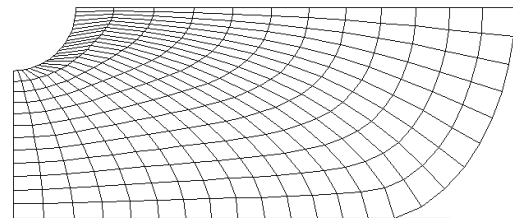


(b) Medium solution: total event time = 10^{-2} seconds

$$\varepsilon^{\text{eff}} = -30\%$$

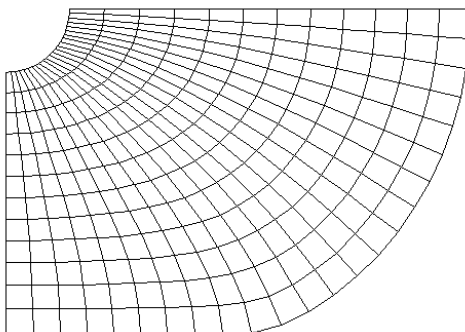


$$\varepsilon^{\text{eff}} = -60\%$$



(c) Slow solution: total event time = 10^{-1} seconds

$$\varepsilon^{\text{eff}} = -30\%$$



$$\varepsilon^{\text{eff}} = -60\%$$

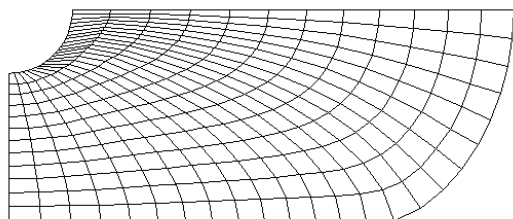
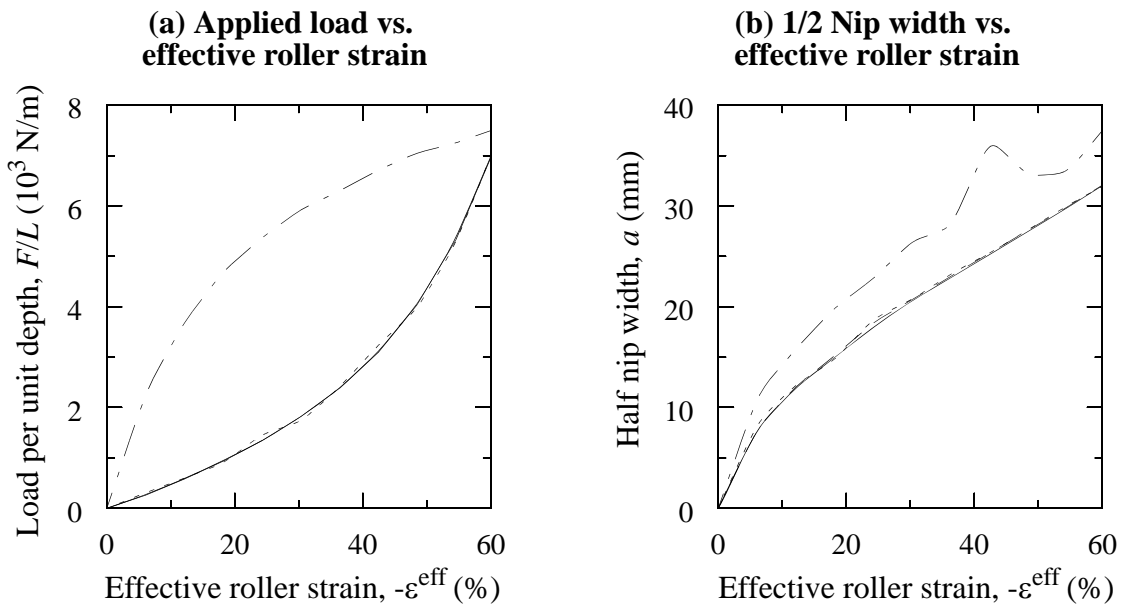
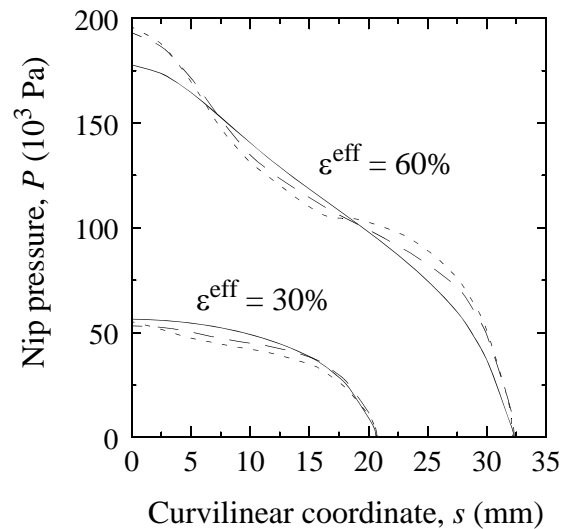


Figure 4.5: Several Explicit finite element solutions for compression test of a SE410 roller.



(c) Nip pressures at 30% and 60% effective roller strain



Result for fast
Explicit sol'n
not plotted.

- Standard sol'n
- - Slow Explicit sol'n
- Medium Explicit sol'n
- · - Fast Explicit sol'n

Figure 4.6: Comparing different nip measures to evaluate Explicit solutions of SE410 roller compression.

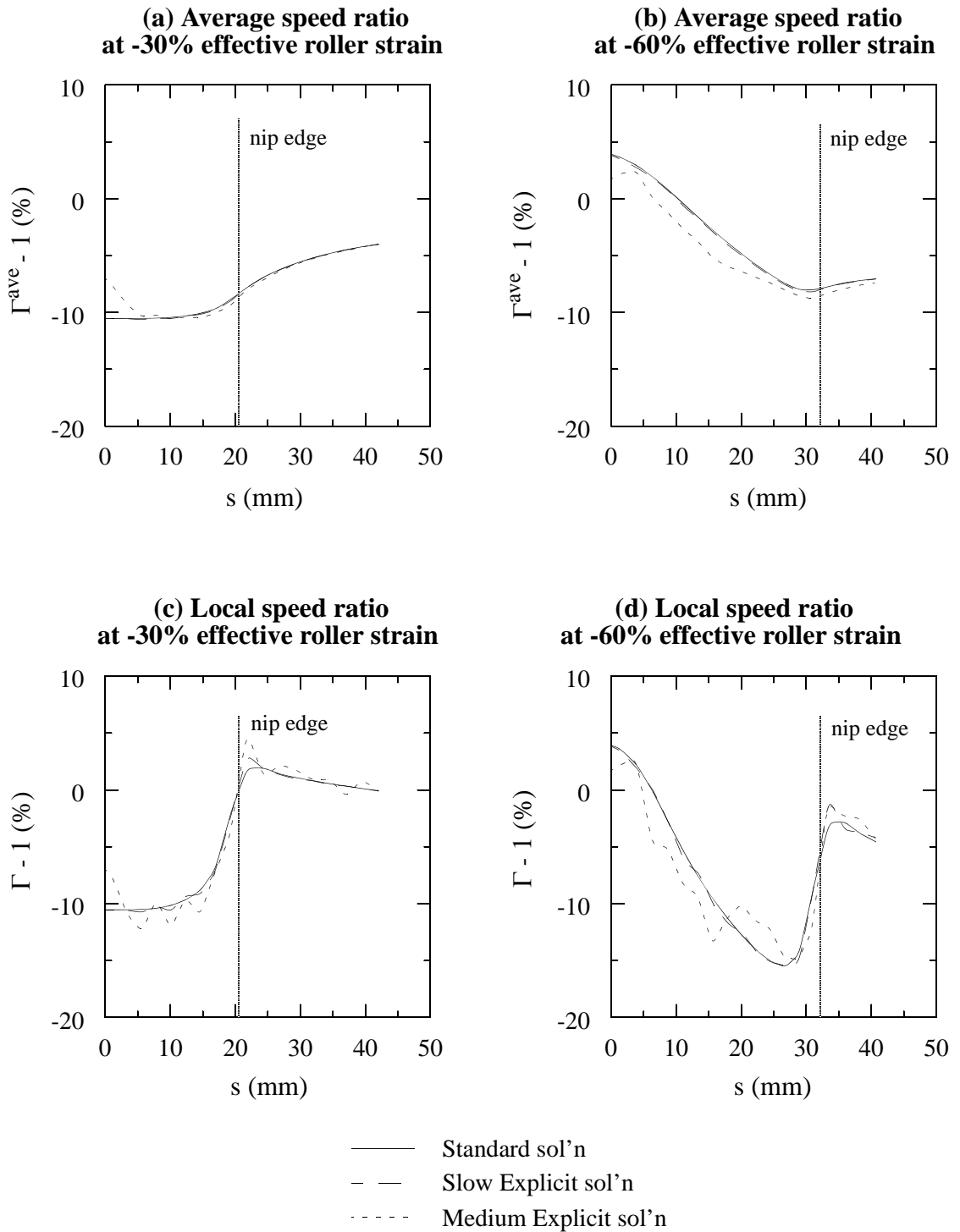


Figure 4.7: Comparing approximate measures of speed ratio to evaluate Explicit solutions for SE410 roller compression.

solution speed than those shown in Figure 4.6. From the variables plotted in Figure 4.7 we see that the “slow” solution is the preferred speed.

Figure 4.8 compares results from the finite element models and actual physical experiments. The finite element results plotted are from the Standard model.¹ The function denoted in Figure 4.8b as a “simple geometric estimate” is based on equations describing the segment of a circle (see Figure 4.9). The correlation presented in Figure 4.8 further verifies the capability of the Ogden-Hill hyperelastic strain-energy density to characterize the SE410 material.

The analytical results presented in Figure 4.8 assumed that the loading was frictionless. The physical experiment did have friction between the roller and the plates. The static coefficient of friction, f_{μ} , in these interfaces was experimentally measured to be 0.9. Finite element models, both Standard and Explicit, were also evaluated with friction included. Negligible differences were found for the quantities plotted in Figure 4.8. Significant differences caused by friction were found for the speed ratio estimates plotted in Figure 4.7 (as expected). Figure 4.10 shows that friction inhibits the hoop strain of the elastomeric roller in the nip. More will be said regarding the frictional influence on these variables in Section 4.3.

4.2.2 R600U

The roller specimens used for R600U had the following nominal dimensions: 8.38 mm hub diameter, 33.9 mm thick elastomeric covering, and 76.2 mm depth (length). The finite element models of these rollers used the same mesh depicted in Figure 4.4a, except with the dimensions defined above. Evaluations of Standard and Explicit models similar to those used for the SE410 rollers were undertaken. These evaluations showed that an event time of 10^{-1} seconds provided good correlation between Explicit and Standard solutions for the R600U rollers.

1. The previous discussion demonstrated that the Explicit method (with a slow solution time) yields equally good correlations.

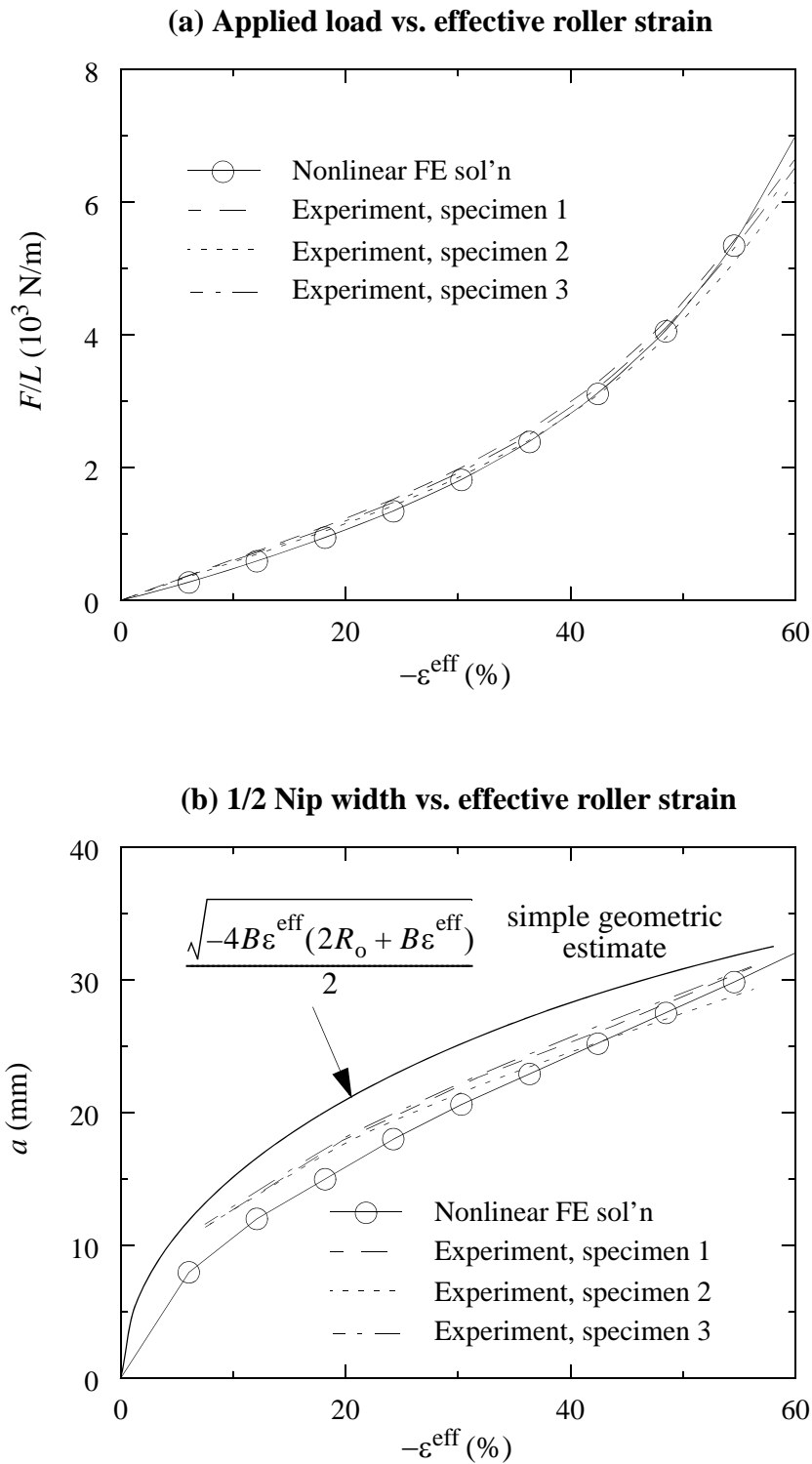


Figure 4.8: Finite element prediction correlates well with experimental data from the non-rolling SE410 roller compression test.

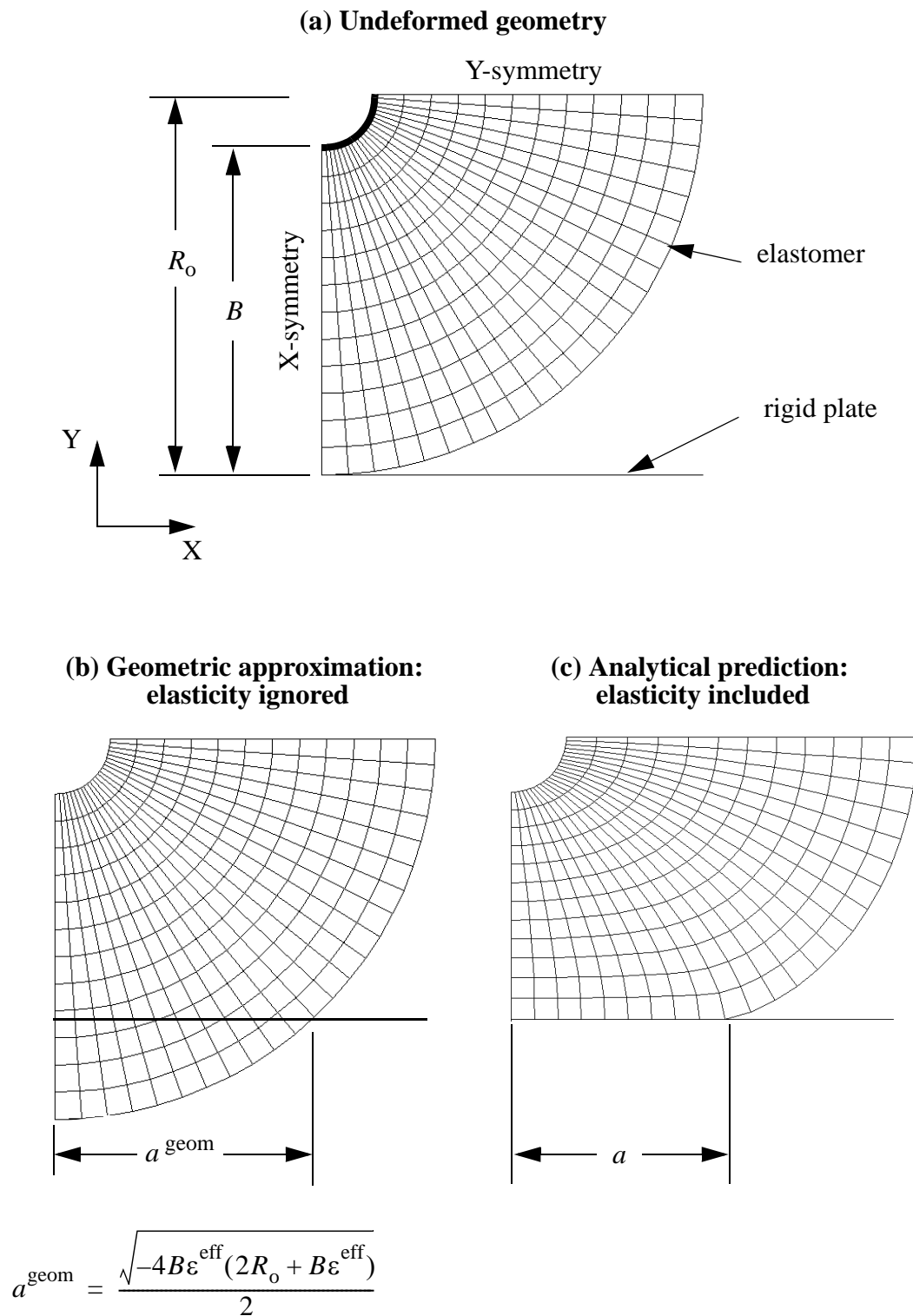


Figure 4.9: Geometric approximation of nip width.

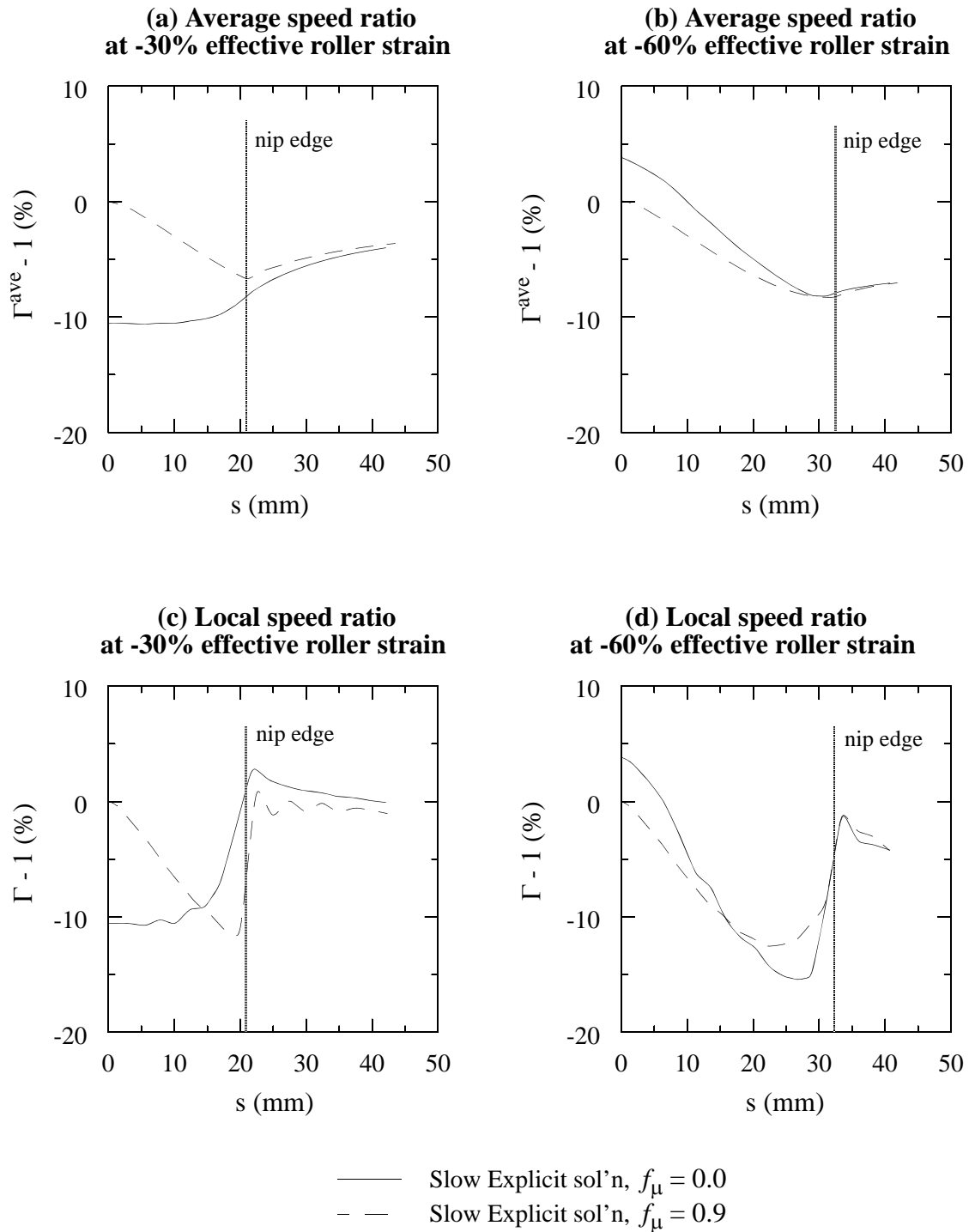


Figure 4.10: Influence of friction on approximate measures of speed ratio. Solutions from Explicit models of SE410 roller compression.

Figure 4.11 compares a linear solution (small deformations, Hooke's law, etc.), a nonlinear solution (large deformations, hyperelastic material law, etc.), and experimental data from the compression of R600U rollers between two flat plates. Both the linear and nonlinear solutions were computed using the Standard method. For the linear solution, an initial tangent shear modulus, $\mu_0 = 29.6 \cdot 10^3$ Pa, and initial tangent Poisson's ratio, $\nu_0 = 0.3$, were used (see Section 3.2). The experimental data was measured from three specimens. Each specimen was first tested to a maximum compressive effective strain of approximately 25%. The samples were then re-tested to a maximum compressive effective strain of approximately 55%. Softening in the load-deflection curves of the re-tested samples (Figure 4.11a with $\epsilon_{\max}^{\text{eff}} \approx -55\%$) is caused by the additional breaking of weak bonds within the R600U foam.

Figure 4.11a further demonstrates the limitation of Hooke's law and small deformation assumptions for an analysis of compressible elastomeric rollers under large strains. Significant improvement in accuracy is seen by the use of the nonlinear model. The nonlinear model still behaves slightly over stiff in the large strain regions. The discrepancy in this region is likely due to the fact that the actual strains in the roller are, in certain locations, much greater than the maximum compressive effective strain of 55%. Figure 4.12 demonstrates this fact using the nonlinear finite element model described previously. Hence, more cellular damage of the R600U has likely occurred than has been taken into account in the hyperelastic model used to represent the material.

Figure 4.11b demonstrates that the prediction of half nip width versus effective roller strain is not sensitive to nonlinear stiffness or geometric effects; both the linear and nonlinear models predict essentially the same results. Both of these models slightly underpredict the measured nip widths. This is likely caused by the fact that the models, based on continuum elasticity theories, can not simulate the very local, cellular, deformations (localized buckling) that were observed in the physical experiments. When localized buckling occurs, little additional load is transmitted to the adjacent material cells which, in turn, lessens further deformation of these cells. The simple geometric estimate depicted in Figure 4.9 can be considered a limiting case of a material that exhibits

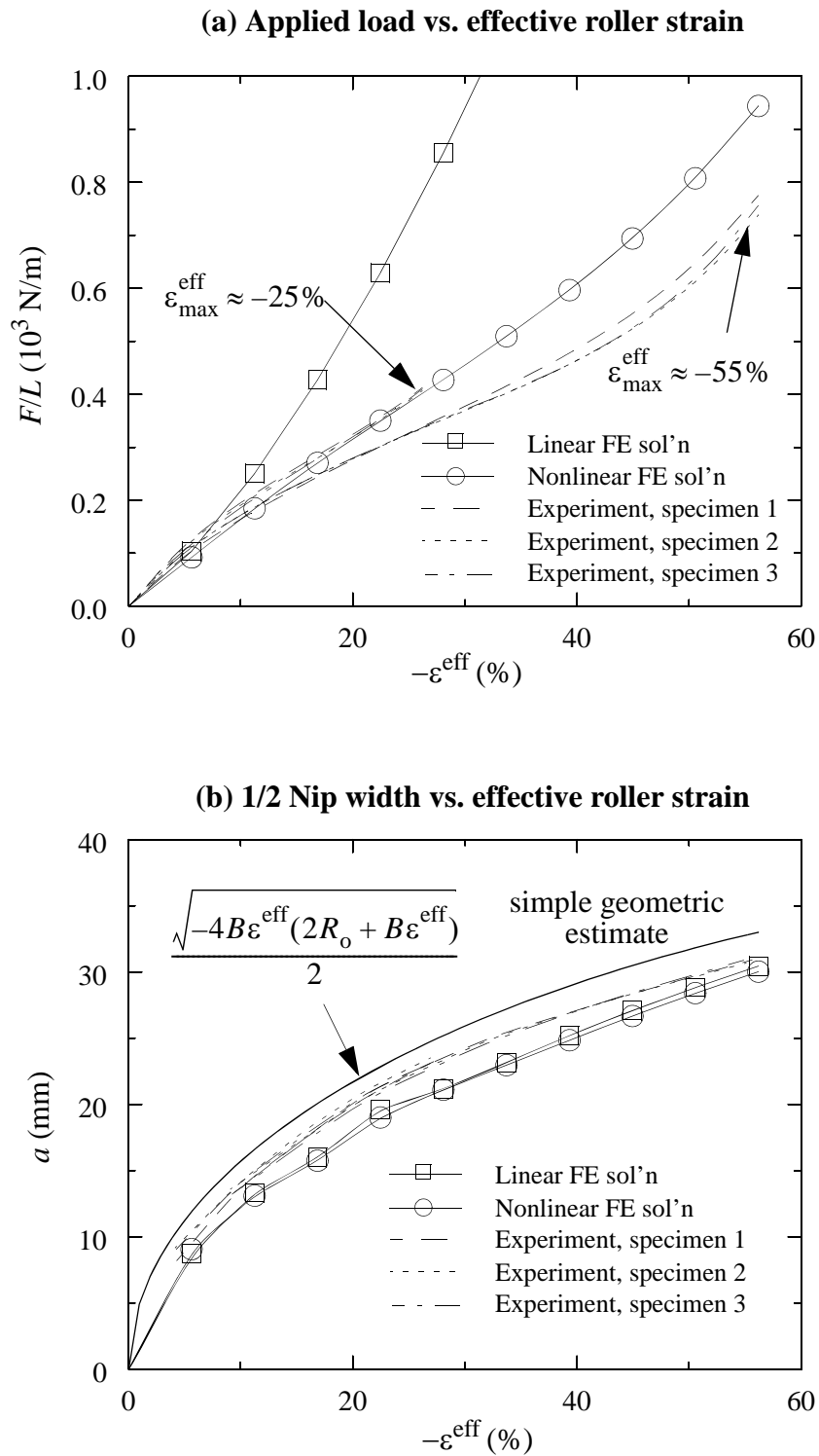


Figure 4.11: Finite element prediction compared to experimental data: non-rolling R600U roller compression test.

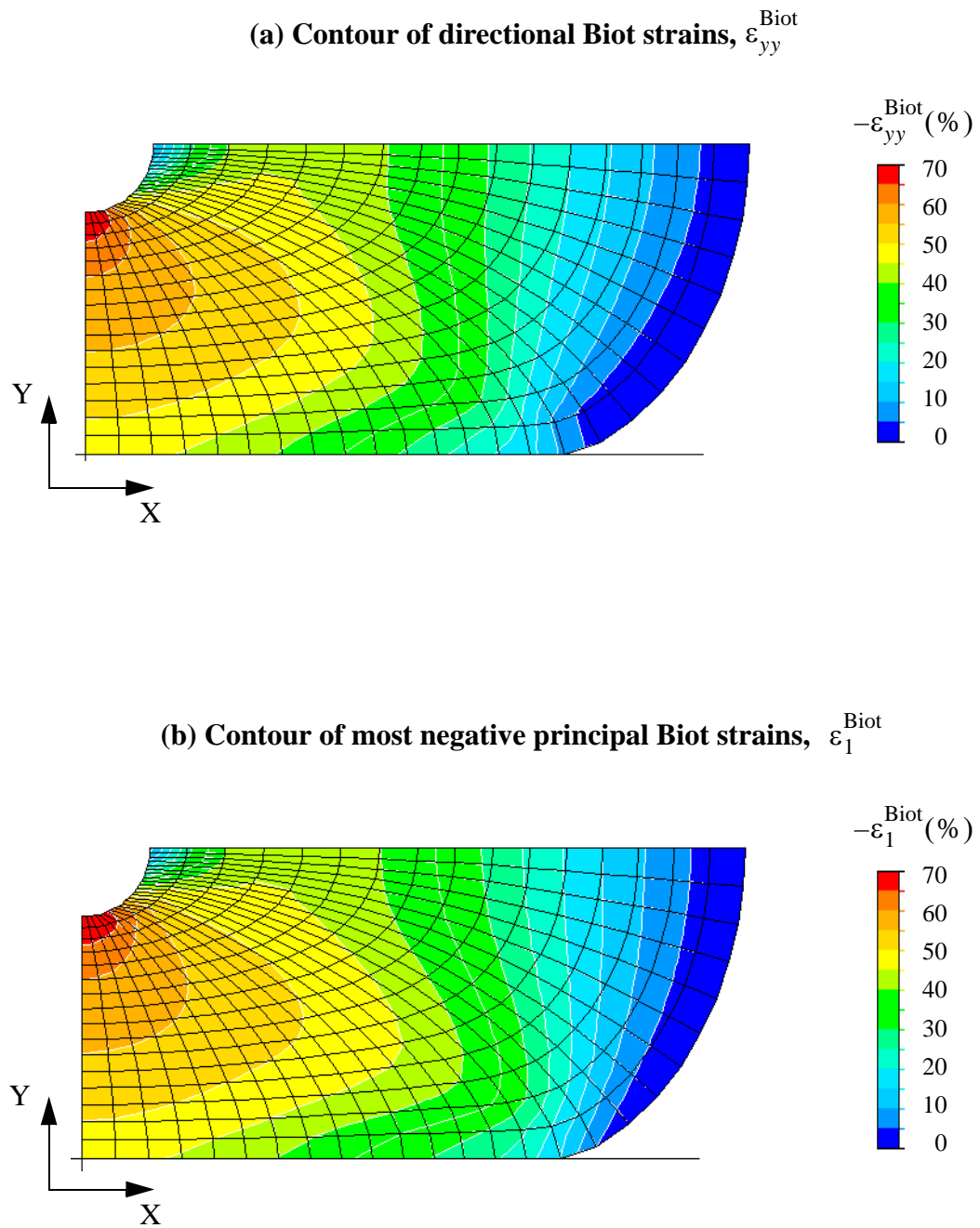


Figure 4.12: Strain contours in a R600U roller under 56% nominal compressive effective radial strain. Predictions from nonlinear finite element model.

extensive localized buckling. Hence, the finite element model and the geometric estimate bound the physical experiment.

A result of practical importance is that if the half nip width is plotted as a function of applied load (F/L), significant sensitivity to nonlinearities would be observed. Typical nip measurements that are made experimentally are done by compressing a roller with an applied load, not an applied displacement (strain). As we can see from Figure 4.11, measuring the nip width with an applied displacement will significantly decrease the sensitivity of the measurement to nonlinear effects.

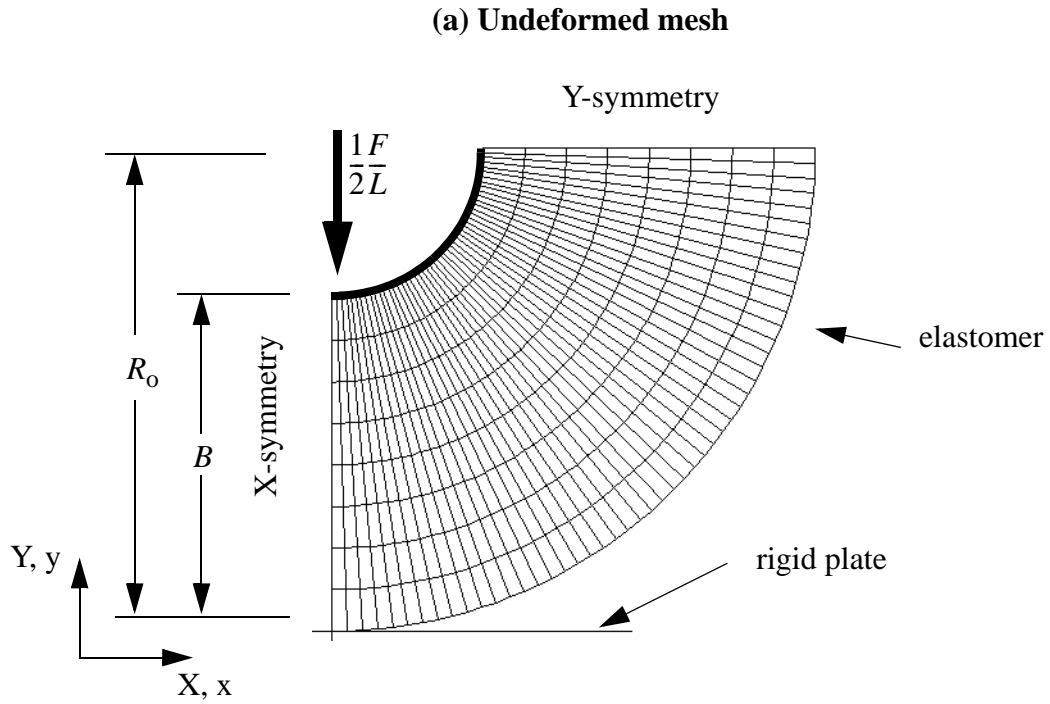
4.2.3 Urethane

The roller specimens used for the urethane evaluation had the following nominal dimensions: 15.88 mm hub diameter and 17.46 mm thick elastomeric covering. Four specimens of length L equal to 76.2 mm, 50.8 mm, 25.4 mm, and 12.7 mm were tested. The 2-D finite element mesh used in the analysis of these rollers is depicted in Figure 4.13. The maximum effective compressive radial strain studied was 15%.

Figure 4.14 compares finite element predictions (via Standard) and experimental data. The solutions presented in Figure 4.14 utilized Hooke's law with $E = 3.85 \cdot 10^6$ Pa and $\nu = 0.4997$ (material constants obtained in Section 3.3). The solution algorithm used nonlinear, large strain formulations to be consistent with the neo-Hookean solutions that will be discussed shortly.¹ In Figure 4.14a the influence of roller length is compared against a plane strain and a plane stress solution. As expected, the two analyses bound the physically measurements. Figure 4.14b demonstrates that accurate predictions of nip width are computed by the model.

As with the other materials, evaluations of urethane rollers via the Explicit method is of interest. In an explicit dynamic method, the size of the time increment in the solution (and thus the computational effort) is governed by material properties and mesh density. For a

1. Utilizing small strain (linear) formulation produces 10% less load at $-\epsilon^{\text{eff}} = 15\%$. Differences between linear and nonlinear solution algorithms for nip width predictions were less than a few percent.



(b) Deformed mesh at 15% nominal compressive effective radial strain

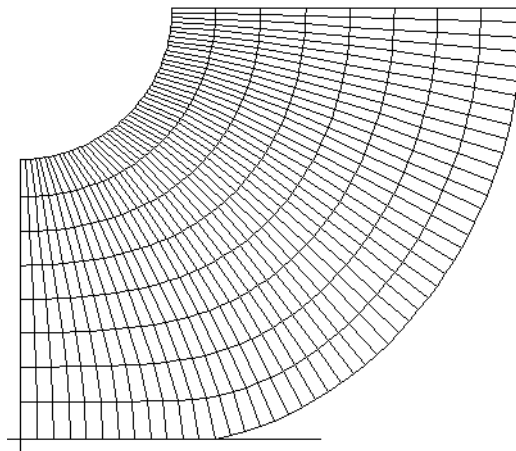


Figure 4.13: Standard 2-D finite element model for compression of a urethane roller.

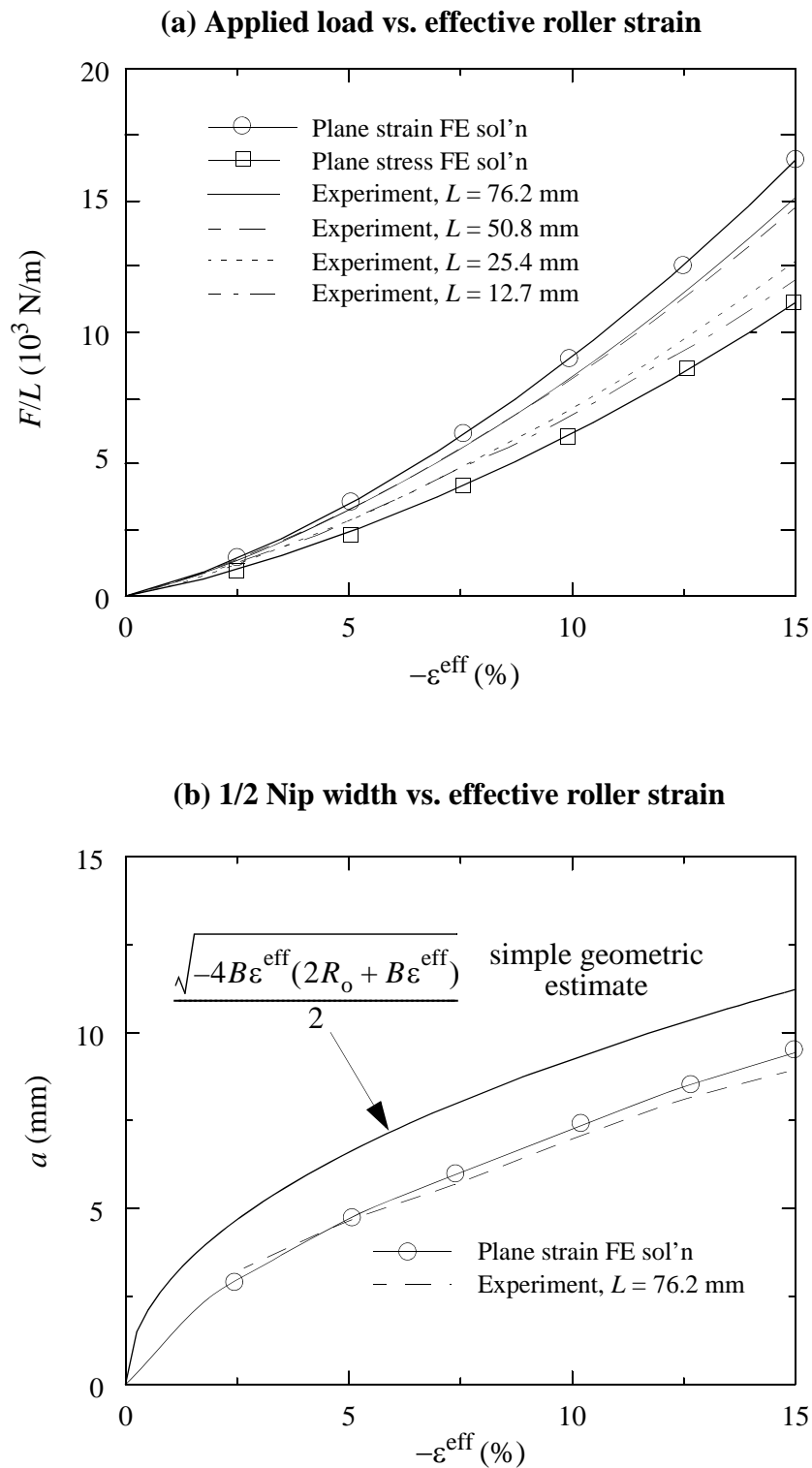


Figure 4.14: Finite element predictions compared to experimental data: non-rolling urethane roller compression test.

material that obeys Hooke's law and is under small strains, the stability limit of the mesh can be written as

$$\Delta t = \min \left[l^{\text{eff}} (\sqrt{1 + \xi^2} - \xi) \sqrt{\rho/E} \sqrt{\frac{(1 + \nu)(1 - 2\nu)}{(1 - \nu)}} \right]_{\text{elem}} \quad (4.5)$$

where l^{eff} is the characteristic element length in the deformed state, ξ is the fraction of critical damping in the highest mode, and ρ is the current density.¹ Rearranging this equation yields (for a given element)

$$\tilde{\Delta t} = \frac{\Delta t}{l^{\text{eff}} (\sqrt{1 + \xi^2} - \xi) \sqrt{\rho/E}} = \sqrt{\frac{(1 + \nu)(1 - 2\nu)}{(1 - \nu)}} \quad (4.6)$$

where $\tilde{\Delta t}$ is a nondimensional measure of the stability limit. Equation 4.6 clearly indicates the problem of analyzing a fully incompressible material with explicit dynamics; the stability limit will be zero! From Section 3.3.2, we measured Poisson's ratio for urethane to be 0.4997. This equates to $\tilde{\Delta t} = 0.042$. If we instead use $\nu = 0.495$ (a value previously measured by the author for other urethanes), the nondimensional time changes to $\tilde{\Delta t} = 0.172$, an increase by a factor of 4.1. A value of $\nu = 0.30$ makes the stability limit increase by a factor of 20 to $\tilde{\Delta t} = 0.862$. The obvious question is how small can we make Poisson's ratio to save computational effort without generating significant errors in our predictions.

Figure 4.15 assesses the influence of Poisson's ratio on several nip parameters. All solutions in this figure were produced with the Standard method. For cases with $\nu \neq 0.5$, Hooke's law and a CPE4 element type were used. For the case of $\nu = 0.5$, calculations utilized a neo-Hookean law ($\mu_1 = 1.29 \cdot 10^6$ Pa and $D_1 = 0.0$ Pa⁻¹) and a CPE4H element type.² From Figures 4.15a and 4.15b we see that negligible differences over the range $0.5 > \nu > 0.49$ are computed for load and nip width. Figure 4.15c demonstrates that the average speed ratio is more sensitive to the value of Poisson's ratio. Negligible differences

1. See Appendix B.2 for further details.

2. Solutions of the cases with $\nu \neq 0.5$ using CPE4 elements yield the same results as solutions using CPE4H elements. Only the CPE4H elements can be used for the case of $\nu = 0.5$ because of the need for a pressure degree of freedom to deal with incompressibility.

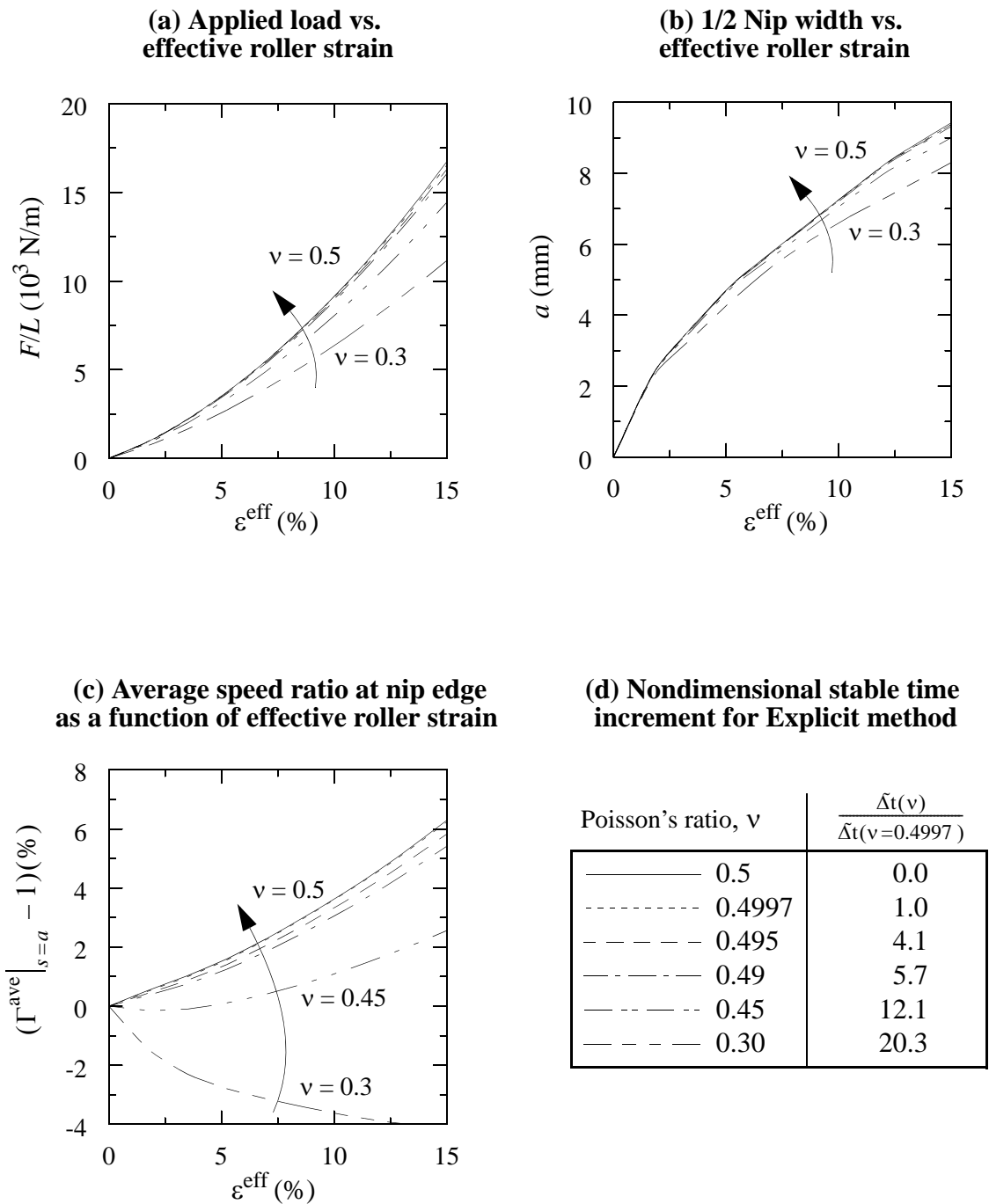


Figure 4.15: Evaluating the influence of Poisson's ratio on nip behavior and stable time increment.

are seen over the range of $0.5 > \nu > 0.4997$ and small differences are found over the range $0.5 > \nu > 0.49$. Moreover, Figure 4.15c demonstrates that when $\nu = 0.3$, the average speed ratio predicts dramatically different behavior (underdrive). Considering the influence of Poisson's ratio on the stable time increment and various nip parameters, we conclude that using a value of $\nu = 0.495$ for the explicit dynamic method will allow for more efficient solutions without generating significant errors in our predictions.

Solutions using Explicit with Hooke's law and $\nu = 0.495$ were nearly identical to the Standard calculations depicted in Figure 4.15 ($\nu = 0.495$). The analysis showed that an event time of 10^{-1} seconds provided efficient Explicit solutions with negligible inertial dynamic effects.

4.3 Rolling Nip Problems

This section studies symmetrically loaded rollers feeding paper to assess media speed ratio as a function of roller deformation and roller material. Complete numerical solutions including friction are utilized as well as less expensive approximate speed ratio estimates computed from non-rolling indentation solutions with and without friction. All analytical models are compared with experimental measurements obtained from the test apparatus depicted in Figure 4.16a. Comparing the various analytical models with physical experiments for three different roller materials provides a quantifiable measure of the accuracy and appropriateness of the different analytical approaches. These comparisons will also indicate some limitations of the purely elastic material representation used in the analyses.

The physical measurements of media speed ratio as a function of roller deformation were made for SE410, R600U, and urethane tires. Each specimen tested was sufficiently pre-worked by compressing it up to a given maximum effective radial strain while rotating it against its mating tire for at least 20 revolutions. Theoretically, media speed ratios can be computed by measuring the sheet motion in the X-direction per roller revolution for a given roller deformation, ϵ^{eff} , and dividing that by the *reference distance* defined as the circumferential distance of the undeformed tire. In practice, sufficiently accurate

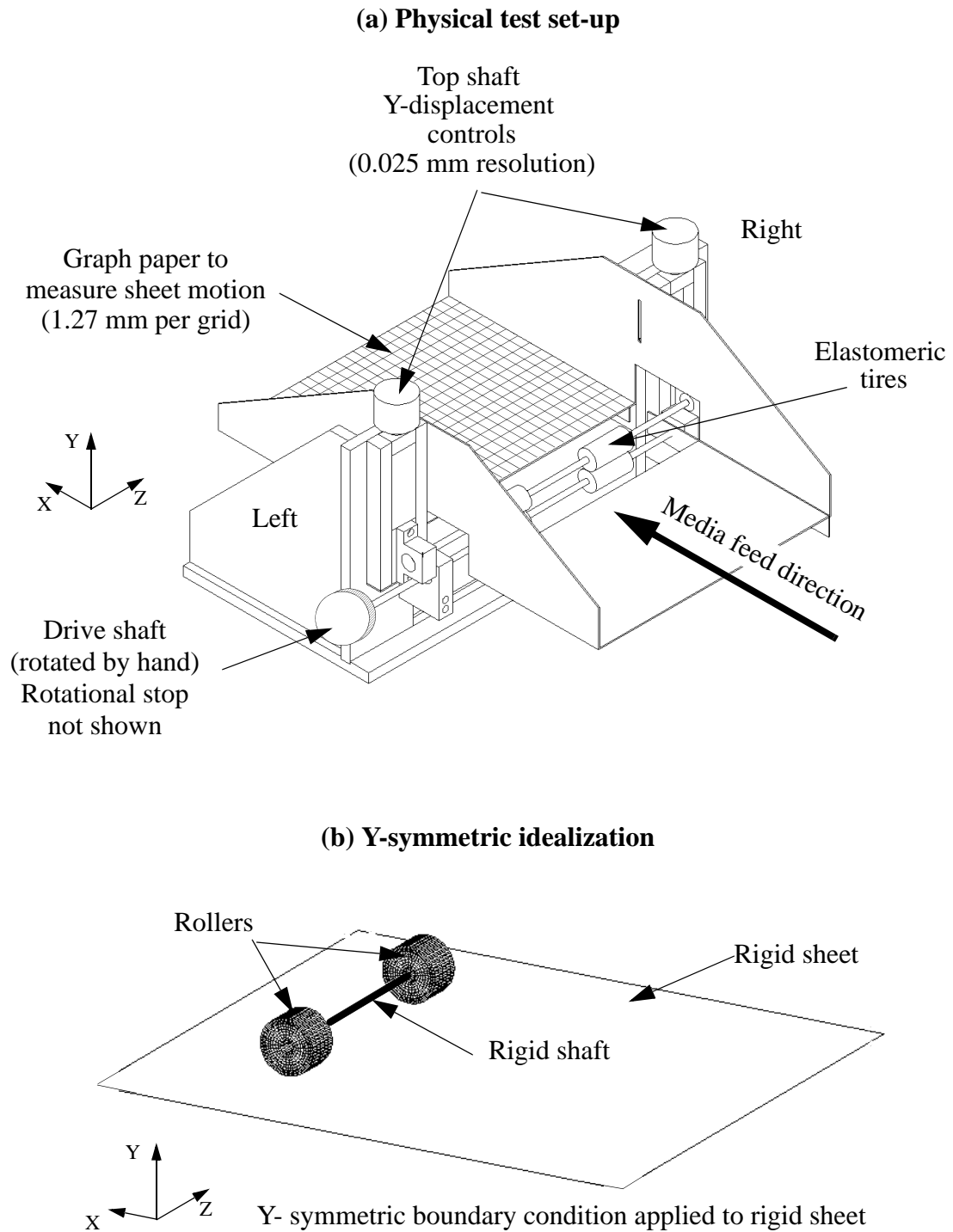


Figure 4.16: Schematic of physical testing apparatus to measure media speed ratio and media skew.

measurement of the undeformed tire circumference (to at least 1%) is extremely difficult, especially for foam and foam rubber materials. An alternative method to obtain the *reference distance* is to measure the sheet motion in the X-direction per roller revolution when the nip is just closed ($\epsilon^{\text{eff}} \approx 0$). The media speed ratios computed from the experiments utilized this alternative method for measuring the *reference distance*.¹

To completely model all four tires of Figure 4.16a would be prohibitively expensive (computationally). Figure 4.16b shows the Y-symmetric idealization made for the nip system. This assumption is valid as long as bearing drag on the non-driven rollers is negligibly small and material hysteresis in the elastomeric tires is negligibly small. As we have seen in Chapter 3, the material hysteresis of SE410 and R600U is not negligible. The inclusion of material hysteresis into the hyperelastic material representations defined previously is extremely difficult, especially if the hysteresis is itself a nonlinear deformation-dependent behavior.² In this current study we are focusing on the influence of nonlinear elastic material behavior on nip systems. By comparing our analyses with the physical experiments, we can assess the limitations of a purely elastic material assumption and determine under what conditions these limitations are severe enough to justify the significant effort and complexity required to include material hysteresis.

The following four subsections describe the finite element models and accompanying experimental results for each of the three materials.

4.3.1 SE410

The tire specimens used for SE410 had the following nominal dimensions: 12.7 mm hub diameter, 19.05 mm thick elastomeric covering, and 33.0 mm length. Each shaft had two tires that were placed 173 mm apart, centered between the bearings. Since the shafts are

1. It is important to remember that the relative change in the media's motion as a function of ϵ^{eff} is the key quantity. It is further noted that using the measured circumference (or diameter) of the undeformed tire as the reference distance in the experiments creates results that frequently yield a $\bar{v} \neq 1$ when $\epsilon^{\text{eff}} = 0$.

2. The difficulty here is two-fold. The development of a consistent theoretical model for nonlinear large-strain elastic and inelastic deformations is very complex. Moreover, finding the additional material constants needed to model the inelastic (hysteresis) component of the material is very difficult, especially if it is nonlinear.

equally displaced in the Y-direction (see Figure 4.16a), no sheet skew is expected and only one pair of tires needs to be considered. Utilizing the Y-symmetric idealization, we model the problem with only one tire and a rigid sheet.

Figure 4.17 shows the Explicit plane strain model of the nip system. The initial conditions used for the dynamic solution are that the entire roller is rotating about its center with a rotational velocity ω and the sheet is traveling in the +X-direction with a velocity ωR_0 . The static coefficient of friction, f_μ , between the tire and the sheet is 1.1. The roller is then deformed against the sheet by constraining the roller's center translation and moving the sheet in the +Y-direction with a velocity of the form

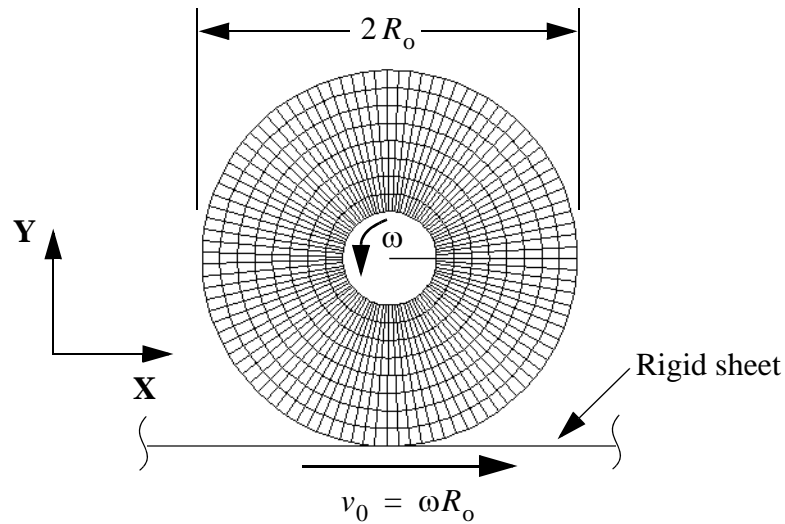
$$v_y(t) = \frac{\delta_y}{t_{\text{ramp}}} \cos\left(2\pi \frac{t}{t_{\text{ramp}}} + \pi\right) \quad (4.7)$$

where δ_y is the amount of Y-displacement, t^{ramp} is the period for which the velocity is applied and t is time. This velocity profile is chosen because it ensures that the vertical motion of the sheet into the roller begins and ends with zero acceleration. This minimizes any impact vibrations which add unwanted noise into the solution. The maximum effective radial strain applied to the SE410 roller was -33.3% ($\delta_y = 6.35$ mm). This deformation was applied over a ramp time of 1/2 a roller revolution ($t^{\text{ramp}} = 0.05$ sec and $\omega = 10$ rev/sec = 62.8 rad/sec). The roller was rotated two complete revolutions to verify that a steady state solution was obtained. The entire Explicit solution in Figure 4.17 took 54,353 increments and 75 cpu minutes on a Sun Sparc 20.

Figure 4.18 presents the nip pressure and shear stress that exist between the sheet and the elastomeric roller. All three graphs in Figure 4.18 show two types of plots. The symbols denote nodal stress values (in the nip) evaluated at an instant in time ($t = 2 \text{ rev}/\omega$). The line-trace denotes nodal stress values of a single node as it passes through the nip over time ($t \approx 1 \text{ rev}/\omega$). Since the dynamic solution takes many small time increments, the line-traces in each graph contain more than 1000 data points.

All plots in Figure 4.18 show relatively steady state behavior. The spike in Figure 4.18a (made from 1 data point) is the initial impact of the node when it first enters the nip. This

- (a) Undeformed roller initially rotating with rotational velocity ω .
(Sheet is initially traveling with velocity v_0).



- (b) Rotating roller deformed to $\varepsilon^{\text{eff}} = -33.3\%$
(Sheet travels at new velocity v).

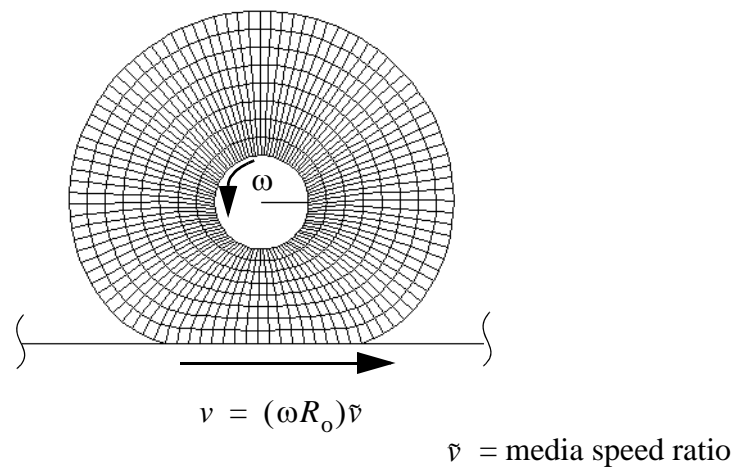


Figure 4.17: Explicit finite element model of feeding a rigid sheet with a SE410 tire.

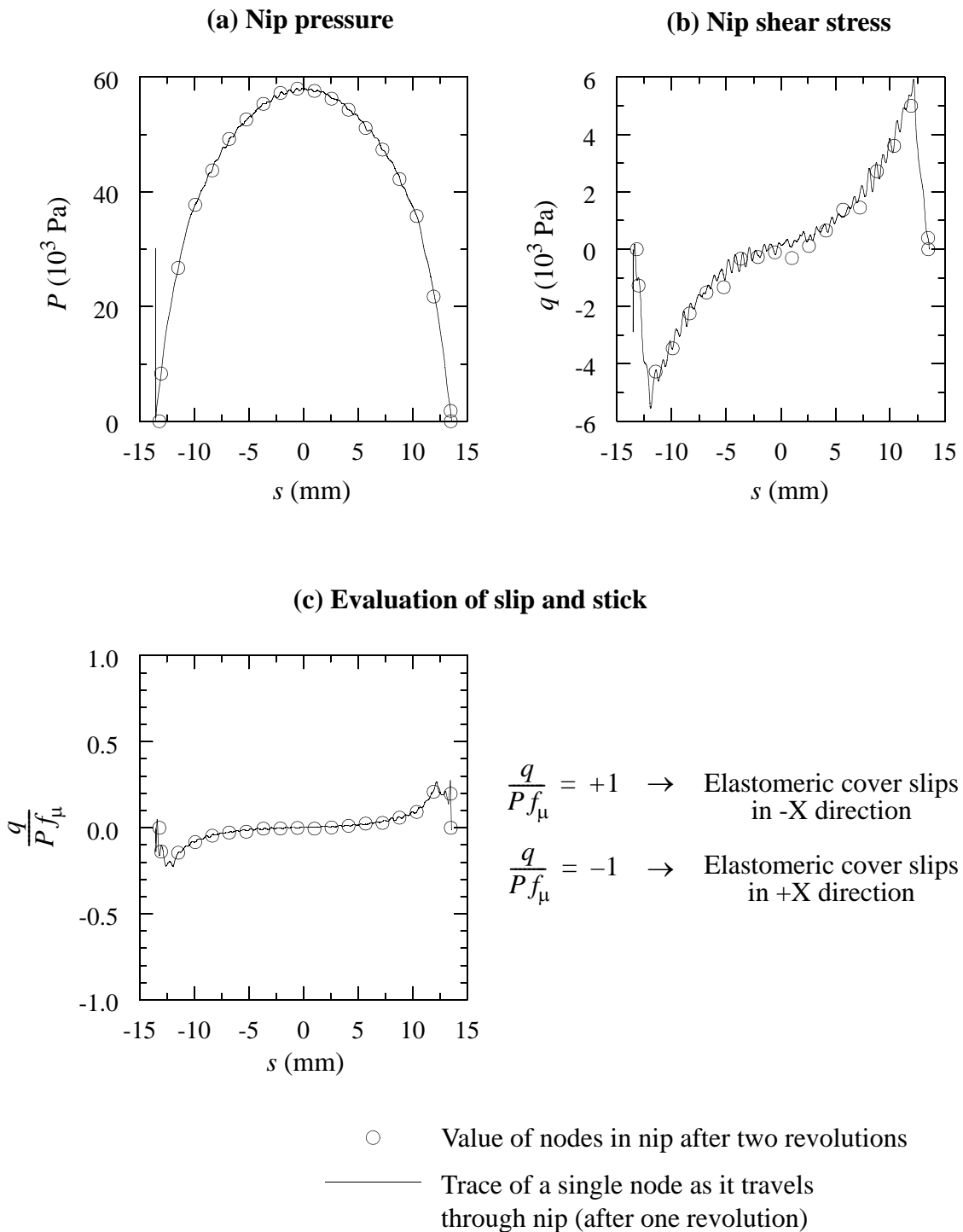


Figure 4.18: Evaluation of nip pressure and interfacial shear stress from Explicit rolling solution of SE410 roller. $\epsilon^{eff} = -33.3\%$.

is caused by the discrete nature of the model and is not taken as physically accurate nor important. The shear stress q plotted in Figure 4.18b is defined as the tangential stress that is applied on the roller from the interface. This figure shows that the outer fiber of the elastomeric roller wants to move inward toward the center of the nip (negative hoop strain). Figure 4.18c demonstrates that the entire nip is in stick because of the high frictional coefficient. From this figure we can also see that for slip to occur, the coefficient of friction must be decreased from 1.1 to approximately 0.3.

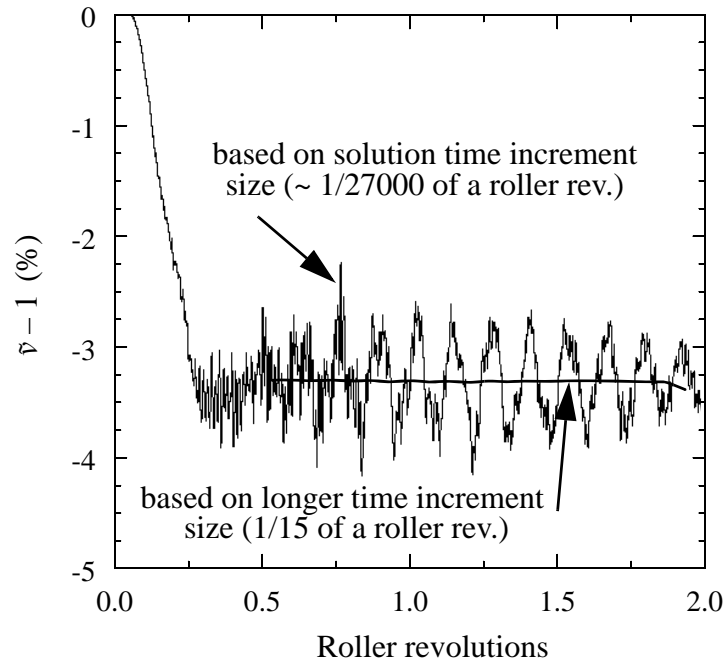
Figure 4.19 indicates that the SE410 roller produces a nip system which underdrives, a result that is opposite from the commonly observed overdrive of rubber rollers. The definition of speed ratio, \bar{v} , is the ratio of the actual transport speed of the sheet, v , to the nominal (undeformed-roller) calculated speed, v_0 . Figure 4.19a depicts two calculations of the sheet's speed ratio: one based on velocities computed at each solution time increment (noisy) and one based on velocities computed over much longer time periods. The later method eliminates the noise and yields a steady state value is $\bar{v} = 0.967$. Figure 4.19b shows the tangential (hoop) stretch-ratio on the contact surface of the elastomeric covering. The mean value through the nip is equal to \bar{v} found in Figure 4.19a.¹ The oscillation of the elemental values about the mean value is again caused by the discrete nature of the model and the dynamic solution.

Figure 4.20 evaluates the media speed ratio as a function of effective radial roller strain. The figure compares several estimates of speed ratio based on less expensive nonrolling calculations to the prediction of the media speed ratio computed from the more expensive rolling model. The prediction based on the rolling model, denoted as \bar{v} , utilized five different solutions computed at the strains noted at the bottom of Figure 4.20. For each of these solutions, the steady state response was obtained using the "long time" technique presented in Figure 4.19a.

The estimates of the media speed ratio (in Figure 4.20) that were computed from nonrolling models were obtained by the methods outlined in Section 4.1. These models

1. This is expected since the entire nip is in stick.

(a) Speed ratio of sheet computed from sheet velocities calculations



(b) Tangential stretch ratio on the contact surface of the elastomeric covering

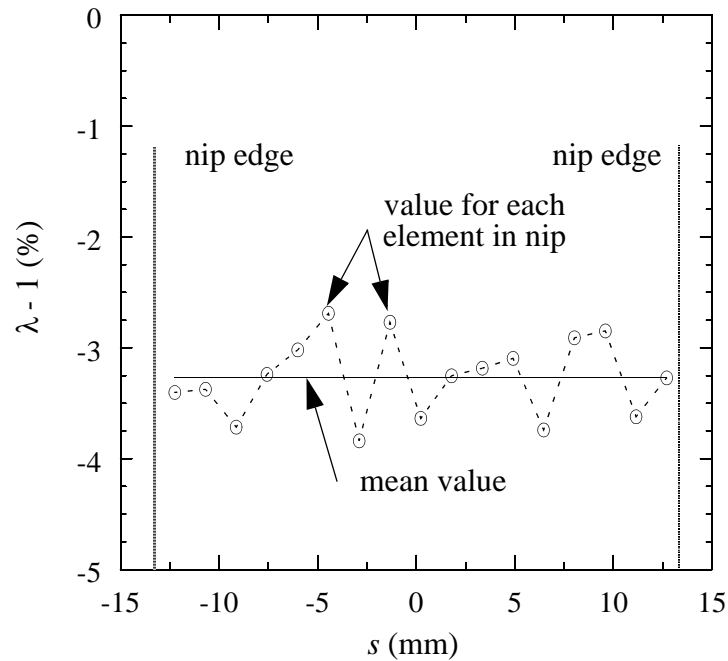
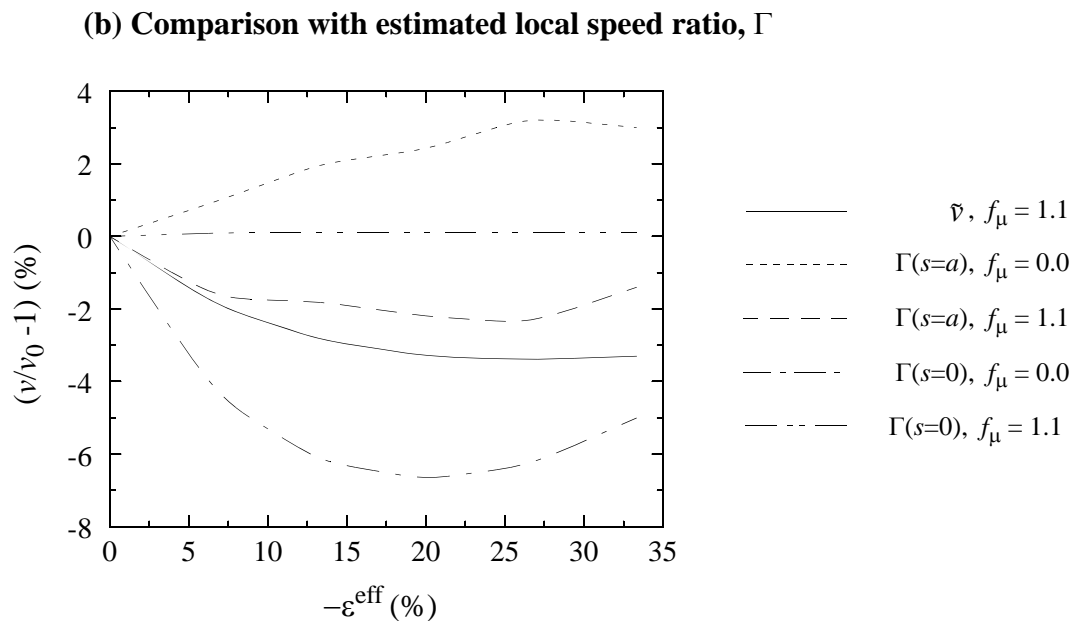
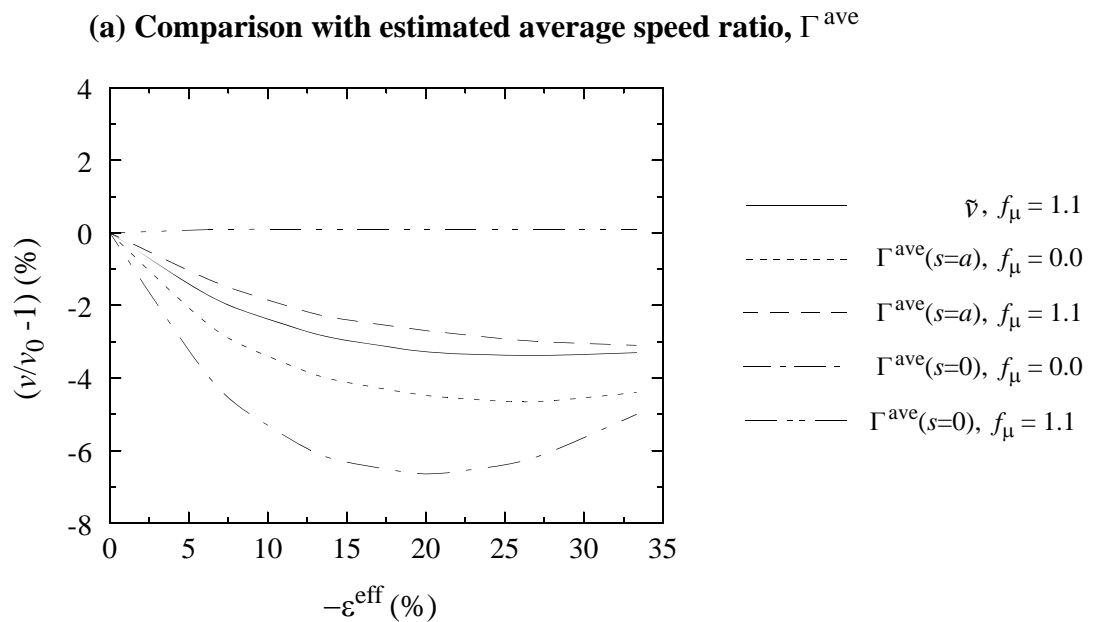


Figure 4.19: Predictions of media speed ratio of sheet from Explicit rolling solution of SE410 roller. $\epsilon^{\text{eff}} = -33.3\%$



Notes: 1.) Each curve is produced from 5 solutions computed at:

$$-\varepsilon^{\text{eff}} = 6.7\%, 13.3\%, 20.0\%, 26.7\%, 33.3\%.$$

2.) The prediction based on a rolling model is denoted by \bar{v} .

All other estimates are from nonrolling solutions.

Figure 4.20: Comparing estimates of media speed ratio for a SE410 roller based on nonrolling models to predictions based on a rolling model.

utilized half of the mesh depicted in Figure 4.17a (positive X side) with an additional X-symmetric boundary condition. The curves plotted for these estimates were based on evaluating the average and local estimates, $\Gamma^{\text{ave}}(s)$ and $\Gamma(s)$, at the center ($s = 0$) and edge ($s = a$) of the nip for each value of ε^{eff} stated.¹ From Equation 4.4 we know that $\Gamma^{\text{ave}}(s=0) = \Gamma(s=0)$. Figure 4.20 demonstrates that with no friction, these estimates computed at the nip center significantly overestimate the underdrive relative to the rolling solution. When friction is included, these estimates computed at the nip center predict neither overdrive nor underdrive because no hoop straining occurs at the center of the nip due to the large coefficient of friction. Figure 4.20a shows that using $\Gamma^{\text{ave}}(s=a)$ with and without friction bound the prediction created by the rolling solution. Looking at the two plots of $\Gamma(s=a)$ in Figure 4.20b shows that only the case with friction gives a reasonable estimate of the rolling solution. Revisiting the plots of Figure 4.10 indicate that the estimate of speed ratio based on $\Gamma(s=a)$ has an extreme gradient in the neighborhood of $s = a$. Hence, small errors in the prediction of nip width a can create large errors in the value reported for Γ at the nip edge. This is not the case for $\Gamma^{\text{ave}}(s=a)$ because it has a much smaller gradient in the neighborhood of the nip edge.

From this analysis we find that $\Gamma^{\text{ave}}(s=a)$ modelled with and without friction bounds the prediction of \tilde{v} computed from a rolling solution. The question to ask is “why use a nonrolling estimate when a rolling solution is available?” The answer is “computational effort.” The curve defining how \tilde{v} changes as a function of ε^{eff} was computed from 5 different Explicit solutions, each taking approximately 75 cpu minutes for a total of 375 cpu minutes.² All the approximate nonrolling curves were computed with only 2 Explicit solutions, one with friction and one without. Each of these solutions required only 6 cpu minutes. Hence, these total solution time of the nonrolling models was 31 times faster. Solution of the nonrolling model without friction using the Standard method was

1. See Figure 4.10 for the general shape of the $\Gamma^{\text{ave}}(s)$ and $\Gamma(s)$ curves. Note, the roller dimensions and effective radial roller strains for the curves plotted in Figure 4.10 are slightly different than those evaluated in this subsection.

2. Rolling analyses were attempted in a single solution where the roller was compressed to a given ε^{eff} , rotated until steady state, then compressed further, rotated again until steady state and so on. Unfortunately, every additional compression portion of the solution added more dynamic disturbances which required an excessive amount of time to dampen out (even using a loading profile of the form of Equation 4.7). Computing individual solutions with only one compression portion each yielded the final results faster.

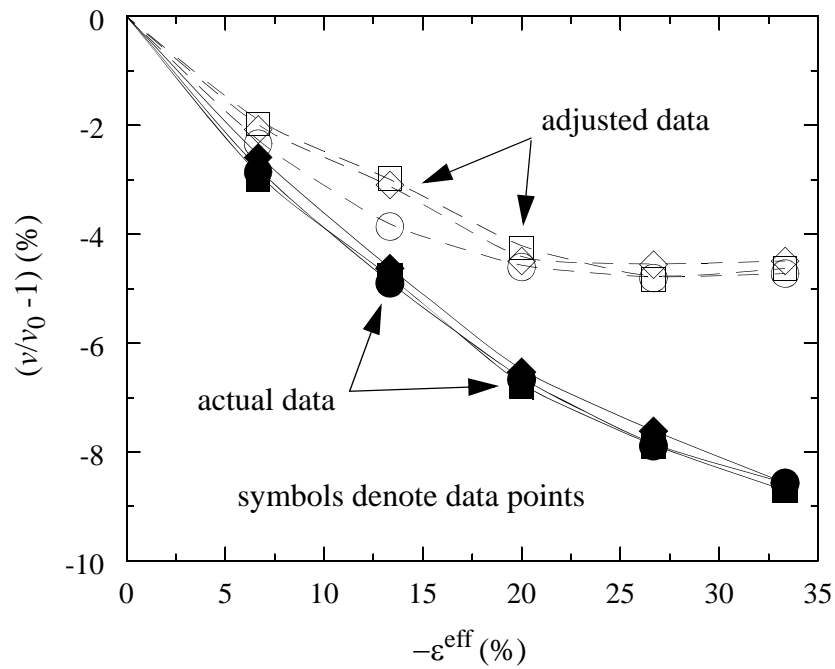
extremely fast, only 2.1 cpu minutes. When the Standard method was used with friction, the solution suffered from frictional chatter and slowed to approximately 25 cpu minutes.¹ Thus, we see that the nonrolling estimates may prove to be an acceptable alternative when solution effort is considered. This will become even more apparent later.

Figure 4.21a presents results of physical experiments using three sets of SE410 rollers in the test set-up of Figure 4.16a. The *actual* measured speed ratio for a given value of ϵ^{eff} was obtained by rotating the bottom set of rollers in Figure 4.16a one revolution and measuring the distance traveled by a stiff sheet (280 mm x 430 mm, 110 lb card stock) loaded into the nip. This distance was then divided by the reference distance (as described at the beginning of Section 4.3) to obtain the *actual* measured speed ratio. Before this data was measured, an assessment of the Y-symmetric idealization (Figure 4.16b) was performed. Figure 4.21b depicts how the validity of this assumption was analyzed. After one rotation, the painted lines should again align if the system were truly Y-symmetric. This check showed that the undriven roller always lagged the driven roller, signifying a nonsymmetry in the system. As we identified previously, bearing friction and material hysteresis are the two major contributors to this loss. Since high quality ball bearings were used, we assume that most of the lag is caused by material hysteresis in the SE410 which causes some nonsymmetric behavior across the nip. To account for this influence, we adjust the measured sheet motion by adding to it the value of the lag measured between the rollers for a given value of ϵ^{eff} . In this simplified adjustment, we are adding back to the physical measurement a loss that our model does not have the capability to simulate (material hysteresis). This adjusted data is also depicted in Figure 4.21a. The difference in the adjusted data and the actual data is significant and suggests that highly accurate quantitative predictions from a purely elastic model are not probable.

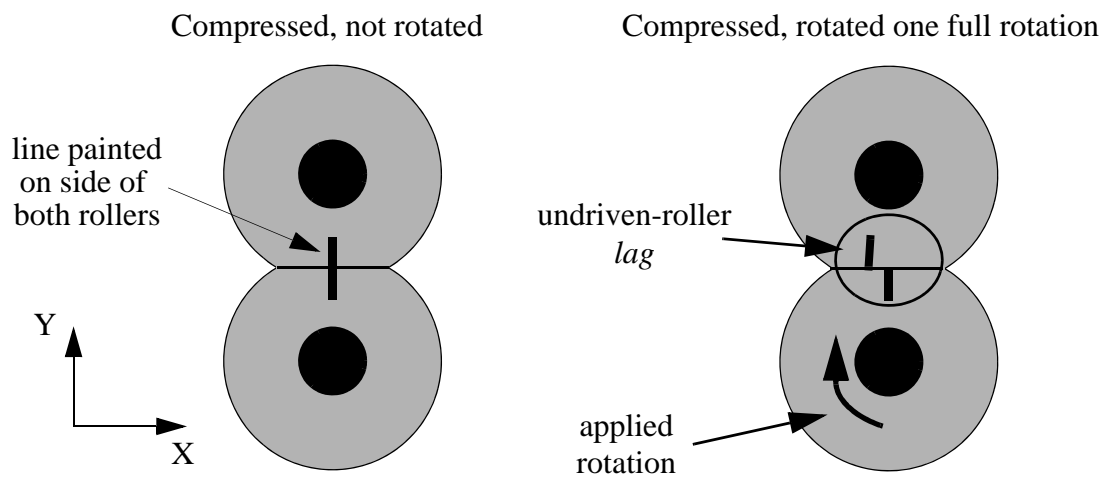
Figure 4.22 compares the adjusted physical data with the results computed from the Explicit rolling model. The results indicate reasonable correlation. The analytical prediction estimates approximately 75% of the *adjusted* underdrive observed. One cause for the discrepancy is the simplistic method by which we adjusted the actual physical data

1. Standard solutions of the rolling model had fatal convergence problems caused by frictional chatter.

(a) Actual and adjusted sheet speed ratio measurements
(3 samples tested)



(b) Schematic of measurement used to adjust measured speed ratio data



Note: No sheet is in the nip during this evaluation.

Figure 4.21: Experimental measurements of speed ratio for a stiff sheet fed by SE410 rollers.

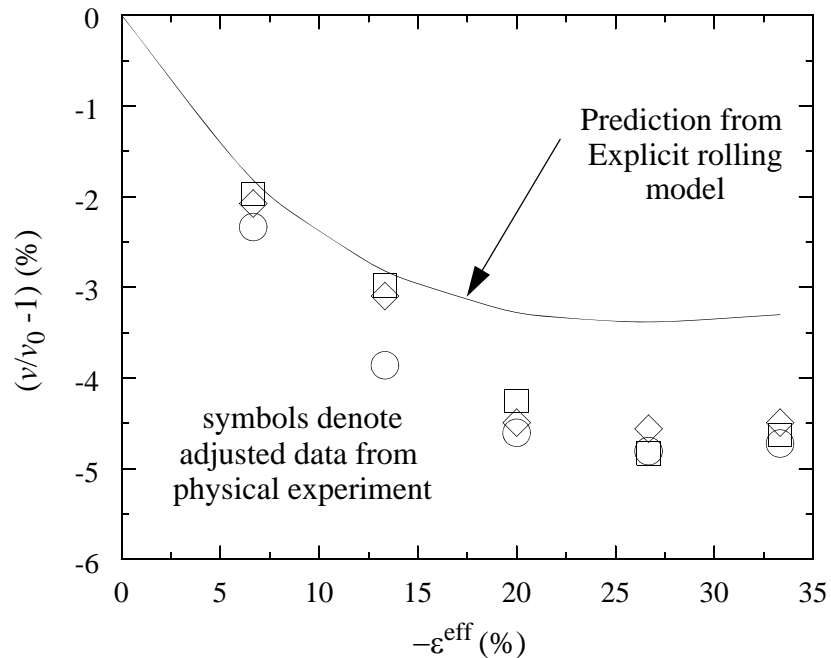


Figure 4.22: Comparison of adjusted experimental data and analytical prediction of speed ratio for a SE410 roller feeding a sheet.

to remove the non-ideal roller lag. Unfortunately, no other method, short of modelling the material hysteresis, is available to make such an adjustment. Another potential cause for the discrepancy is the hyperelastic model used to model the SE410 roller. The deformation modes that each individual material “particle” of the roller endures as it travels through the nip are more complex than the two primitive deformation modes used to compute the material laws. However, this is likely to be a small effect since other predictions of noncyclic problems (Figures 3.7, 3.10, and 4.8) correlated well with the experimental data. The correlation here is considered reasonable because we correctly predict that the nip underdrives (not overdrives) and the analytical model shows the same plateau region as the adjusted experimental data.

4.3.2 R600U

Evaluation of this material followed the same approach as that used for the SE410 of the previous subsection. The tire specimens used for R600U had the same dimensions as the

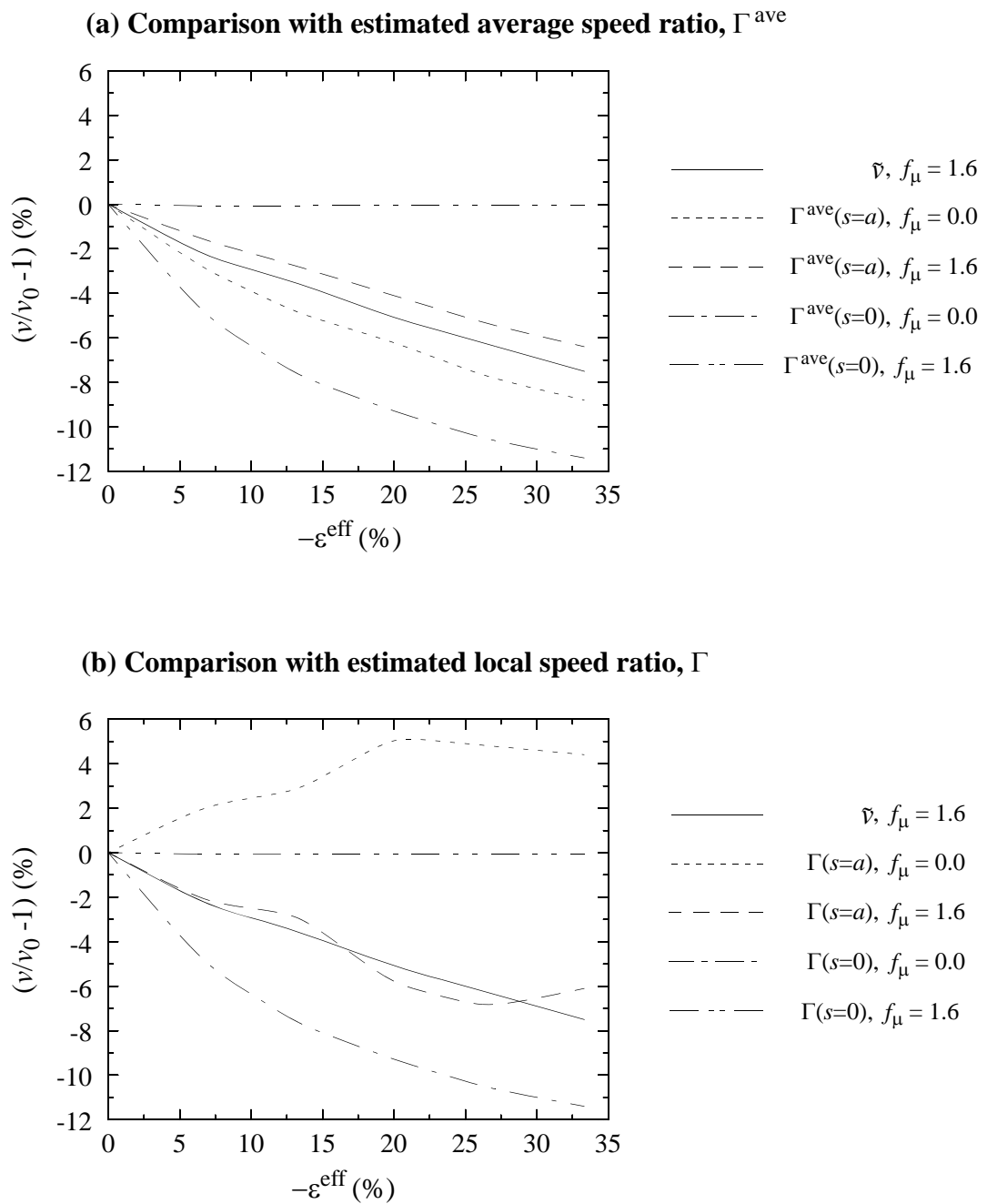
SE410 rollers and used the same plane strain mesh (Figure 4.17a). The static coefficient of friction between the roller and sheet was measured to be 1.6. Calculations of nip pressure, shear stress, and slip similar to those of Figure 4.18 (SE410) were performed. This analysis showed that the nip was in complete stick and that the coefficient of friction would need to be decreased from 1.6 to approximately 0.6 for slip to begin.

Figure 4.23 evaluates several predictions of media speed ratio as a function of effective radial roller strain. Comparisons between the various estimates made from nonrolling models and the prediction computed from a rolling model are similar to those discussed for the SE410 roller. We again find that $\Gamma^{\text{ave}}(s=a)$, modelled with and without friction, are the best estimates to the prediction of \bar{v} computed from the rolling model.¹

Figure 4.24 presents both the experimentally measured speed ratio data and its comparison to the analytical prediction using an Explicit rolling model. The adjusted data was calculated using the same method used for the SE410 roller data. The absolute amount of roller lag removed from the R600U data was greater than for the SE410. This is consistent with the hysteresis evaluations of Figures 3.1 and 3.11. The correlation between the model and the adjusted data for the R600U (Figure 4.24b) is very good up to 15% roller compression, after which the model begins to increasingly under predict the underdrive.

The error in the media speed ratio prediction for the R600U material is greater than was the case for the SE410 material. This is to be expected because the hyperelastic representation of the R600U was not as good as for the SE410 (compare Figures 3.17 and 4.11 relative to Figure 3.7, and 4.8). The correlation here is considered acceptable because: 1) we correctly predict that the nip underdrives (not overdrives), 2) the analytical model and the adjusted experimental data display the same behavior (no plateau region),

1. The estimate $\Gamma(s=a)$ with friction appears to be a better estimate than $\Gamma^{\text{ave}}(s=a)$. However, $\Gamma(s)$ changes rapidly in the neighborhood of $s=a$. Experience of the author has shown that this estimate should not be used because small errors in the prediction of the nip half width, a , will cause large errors in the speed ratio estimate from this measure.



Notes: 1.) Each curve is produced from 5 solutions computed at:
 $-\varepsilon^{\text{eff}} = 6.7\%, 13.3\%, 20.0\%, 26.7\%, 33.3\%$.

2.) The prediction based on a rolling model is denoted by \bar{v} .
 All other estimates are from nonrolling solutions.

Figure 4.23: Comparing estimates of media speed ratio for a R600U roller based on nonrolling models to predictions based on a rolling model.

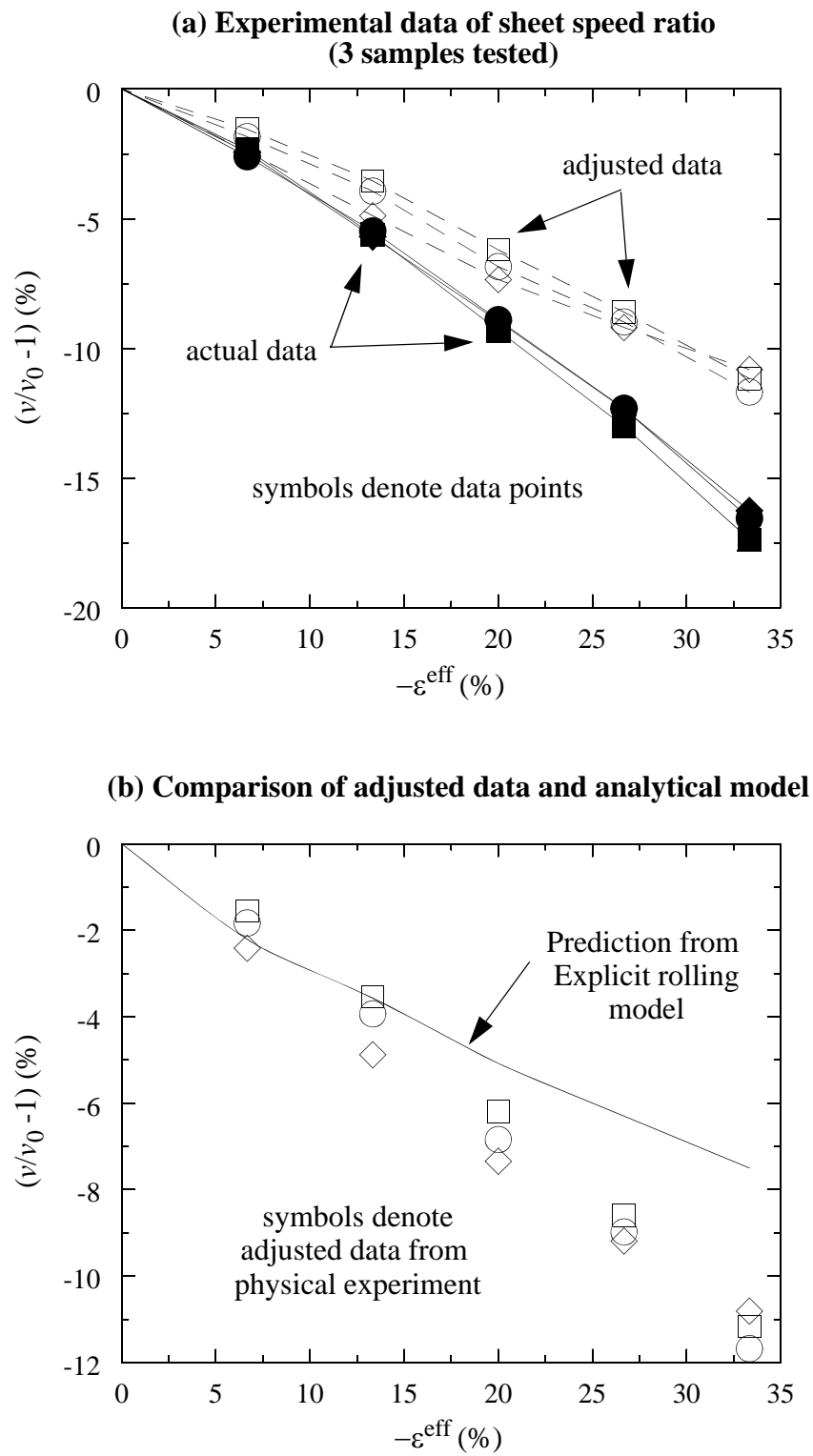


Figure 4.24: Comparison of experimental data and analytical prediction of speed ratio for a R600U roller feeding a sheet.

and 3) both the model and adjusted experimental data demonstrate that the R600U nip underdrives more than the SE410 nip.

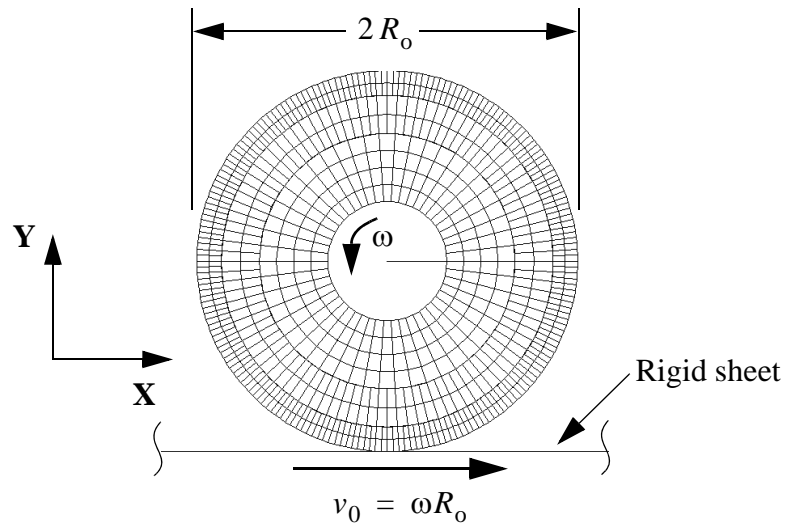
4.3.3 Urethane

The tire specimens used for urethane had the following nominal dimensions: 15.88 mm hub diameter, 17.46 mm thick elastomeric covering, and 38.1 mm length. Each shaft had two tires that were placed 166 mm apart, centered between the bearings. Evaluation of this material followed the same approach as that used for the previous materials. Figure 4.25a depicts the plane strain model initially used in the analysis. The mesh is subsectioned into three regions where each interfacing boundary is connected via a contact algorithm that enforces no relative motion between the bounding nodes of each adjacent region. Mesh convergence studies with *regular* meshes (of the form depicted in Figure 4.17a) were performed to verify the validity of this mesh. The advantage of this mesh is that the smallest elements are utilized on the outside of the roller to minimize the discretization-induced noise in the solution while keeping the solution time to a minimum.¹ For all rolling solutions analyzed, steady state response was obtained within one roller revolution.

Based on the analysis of Section 4.2.3, the urethane was modelled using Hooke's law with $\nu = 0.495$. The entire plane strain Explicit solution depicted in Figure 4.25b (only one revolution) took 61,104 increments and 70 cpu minutes on a Sun Sparc 20. Comparing these to the solution effort required for the SE410 roller of Section 4.3.1 (which was rotated two revolutions), we see that the urethane solution took approximately twice as long per revolution. The increase in computational effort is caused by the nearly incompressible nature of the urethane which requires very small time increments relative to the SE410.

1. Using a *regular* mesh would require even smaller elements around the hub of the roller. This would enforce a smaller than needed time increment on the solution because the time increment in an explicit dynamic technique is a function of the smallest element size (see Equations 4.5 and B.41).

- (a) Undeformed roller initially rotating with rotational velocity ω .
(Sheet is initially traveling with velocity v_0).



- (b) Rotating roller deformed to $\varepsilon^{\text{eff}} = -17.5\%$
(Sheet travels at new velocity v).

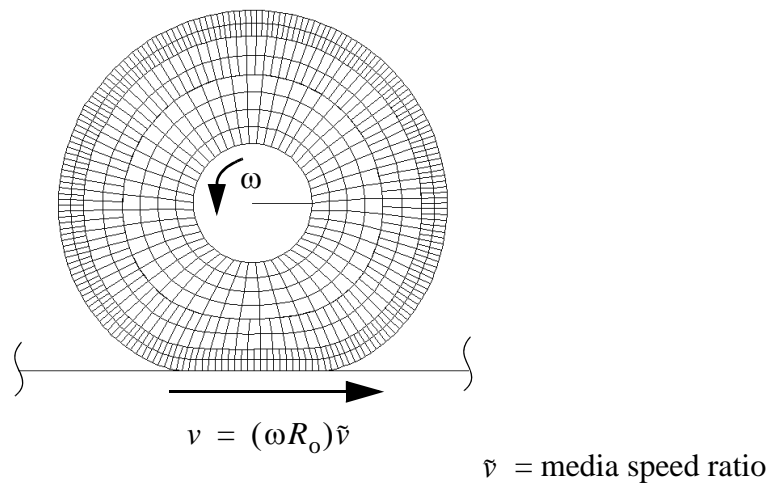


Figure 4.25: Plane strain Explicit finite element model of feeding a rigid sheet with a urethane tire.

Figure 4.26 compares the estimates of media speed ratio from nonrolling models against the prediction of \bar{v} from a rolling model. The static coefficient of friction between the urethane roller and sheet used in the analysis was equal to the experimentally measured value of 1.2. Analysis of the rolling model showed that the nip was in complete stick and that the coefficient of friction would need to be decreased from 1.2 to approximately 0.6 for slip to begin. Again, we find that $\Gamma^{\text{ave}}(s=a)$, modelled with and without friction, are the best estimates to the prediction of \bar{v} computed from the rolling model. Figure 4.26b demonstrates that $\Gamma(s=a)$ with friction significantly overestimates the value of \bar{v} .

Figure 4.27a compares experimental measurements of speed ratio for the urethane nip with predictions from the Explicit rolling model. The values of the effective radial strain, ϵ^{eff} , for the experimental data were computed based on shaft displacements at the rollers instead of the bearing housings to avoid errors caused by shaft bending. From the experimental data, we see that only a small amount of roller lag was observed, little discrepancy exists between the actual and adjusted physical data. This is consistent with the observations of Section 3.3.1 which reported that material hysteresis of urethane was small.

Figure 4.27a depicts three analytical results based on plane strain, plane stress, and 3-D models. The plane strain prediction (which is the same rolling prediction shown in Figure 4.26) significantly over predicts the overdrive of the urethane roller. The cause of the error is the enforcement of a plane strain condition. Since urethane is nearly incompressible, requiring $\lambda_3 = 1$ forces the hoop strain to be greater than in reality. In the actual physical problem, the roller is allowed to bulge in the axial direction. Looking back at Figure 4.14 further verifies that a roller length of 38.1 mm is between a plane strain and plane stress condition and, therefore, requires a 3-D model to properly predict its behavior. Using the 3-D Explicit rolling model shown in Figure 4.27b we obtain a very accurate prediction of the sheet overdrive (Figure 4.27a with the solid line). This analysis demonstrates that when modeling nearly incompressible rollers, a plane strain assumption (which is typically used) can introduce large errors in the prediction of media motion.¹

4.3.4 Comparisons between SE410, R600U, and Urethane

In this subsection we compare the media speed ratio predictions from the Explicit rolling models of all three materials to the experimental data. This allows us to obtain a good assessment of overall capabilities for the analytical models developed.

Figure 4.28 presents graphs summarizing the media speed ratio behavior for SE410, R600U, and urethane nips. These graphs demonstrate that the analytical models show good correlation to the physical experiments. In particular, the models are able to capture the range of behavior from overdrive of urethane to underdrive of R600U. Figure 4.28 also shows that the best correlation is for the urethane nips and the worst correlation is for the R600U nips. This is consistent with the complexity of the given material behavior and the amount of material hysteresis exhibited. *These comparisons establish that purely elastic material formulations do capture the dominate behavior and provide sufficient accuracy for use in nip-system design.* For improved accuracy in the prediction of materials such as SE410 and R600U, the material's hysteretic behavior must be included into the constitutive relationship.

4.4 Axial Variations

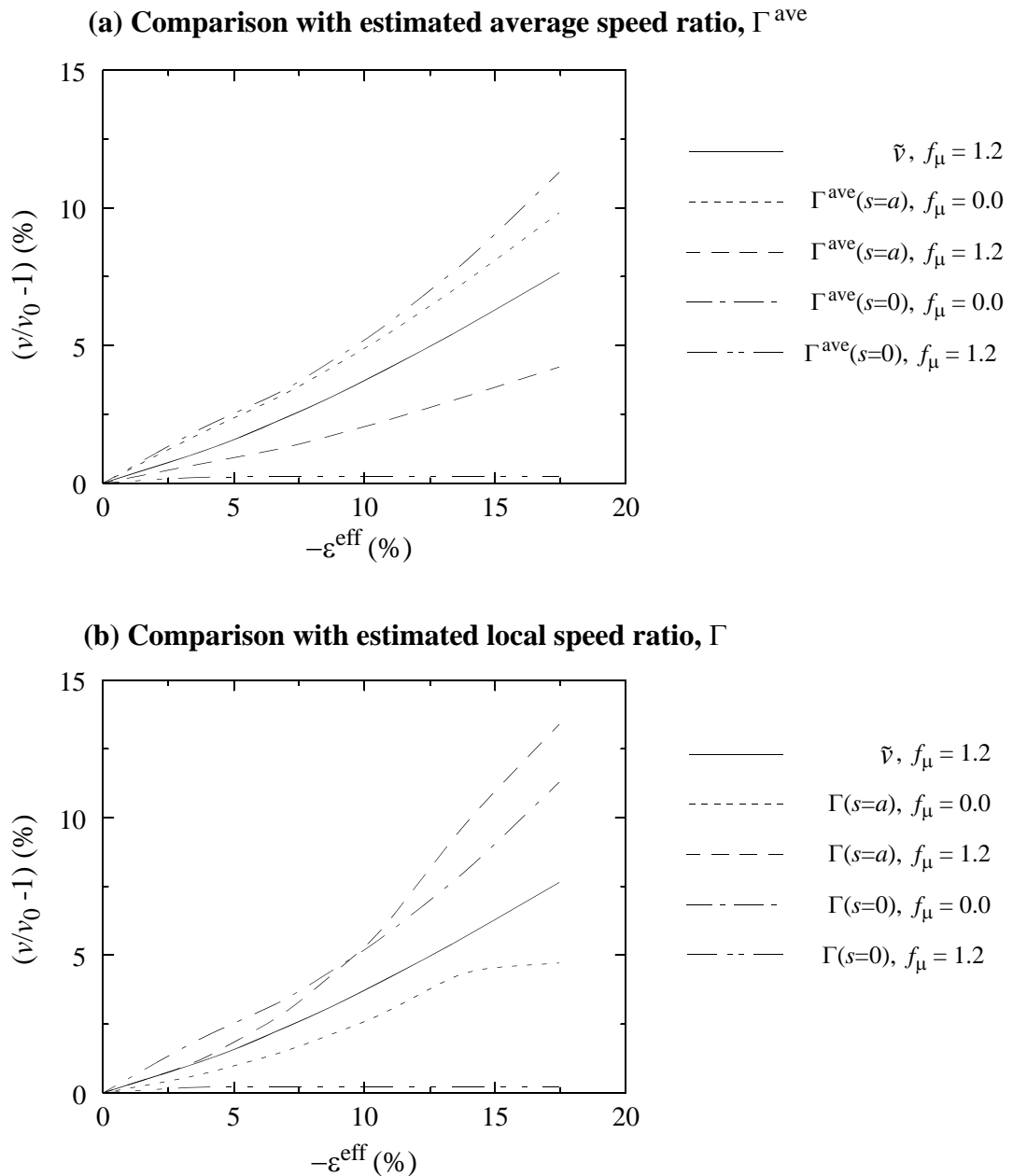
This section describes analyses of axial variations in the two nip systems depicted in Figure 4.1. The first analysis models skew in a tire-based nip system made of R600U. The second analysis evaluates axial variations in two continuous nip systems: one made of a relatively soft rubber and one made of a relatively hard rubber.

4.4.1 Skew in a R600U Tire-Based Nip System

Sheet skew was studied experimentally with the set-up depicted in Figure 4.16 and analytically using the 3-D model displayed in Figure 4.29.¹ The tire specimens and shafts

1. When evaluating substantially more compressible materials such as SE410 and R600U, this effect is very small and plane strain models are usually sufficient.

1. Mesh convergence analysis was performed to validate the model discretization.



- Notes: 1.) The prediction based on a rolling model is denoted by \tilde{v} and was created from 4 solutions computed at: $-\varepsilon^{\text{eff}} = 4.4\%, 8.7\%, 13.1\%, 17.5\%$
- 2.) All other estimates are from nonrolling solutions. Each of these curves was created from 5 solutions computed at: $-\varepsilon^{\text{eff}} = 3.5\%, 7.0\%, 10.5\%, 14.0\%, 17.5\%$

Figure 4.26: Comparing estimates of media speed ratio for a urethane roller based on nonrolling models to predictions based on a rolling model. All solutions are plane strain.

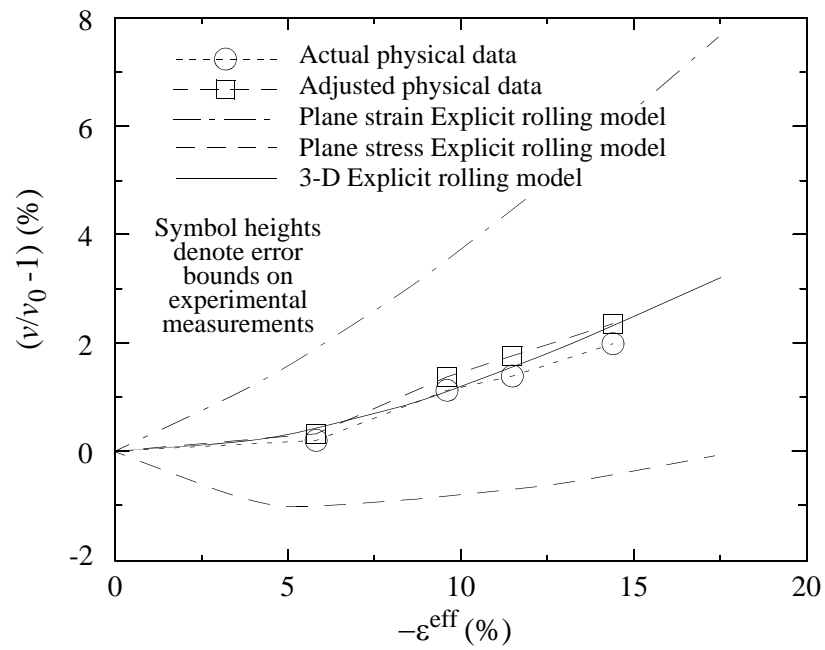
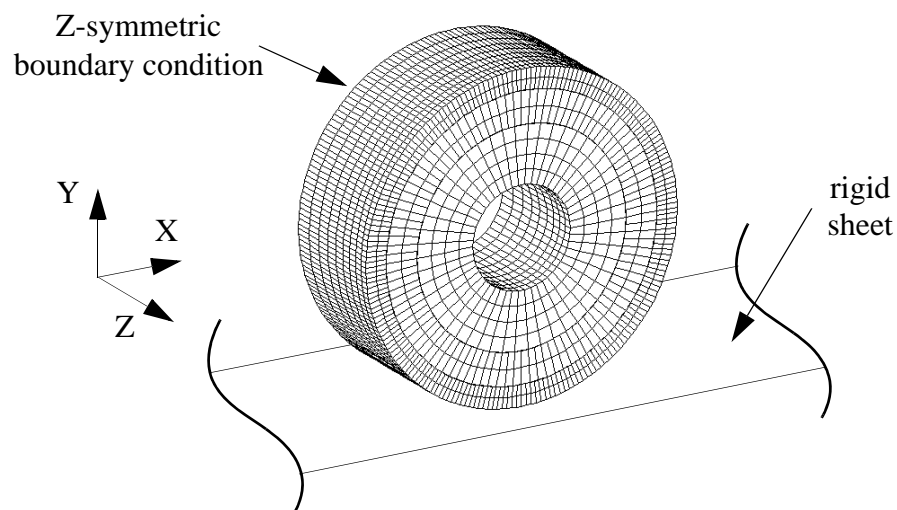
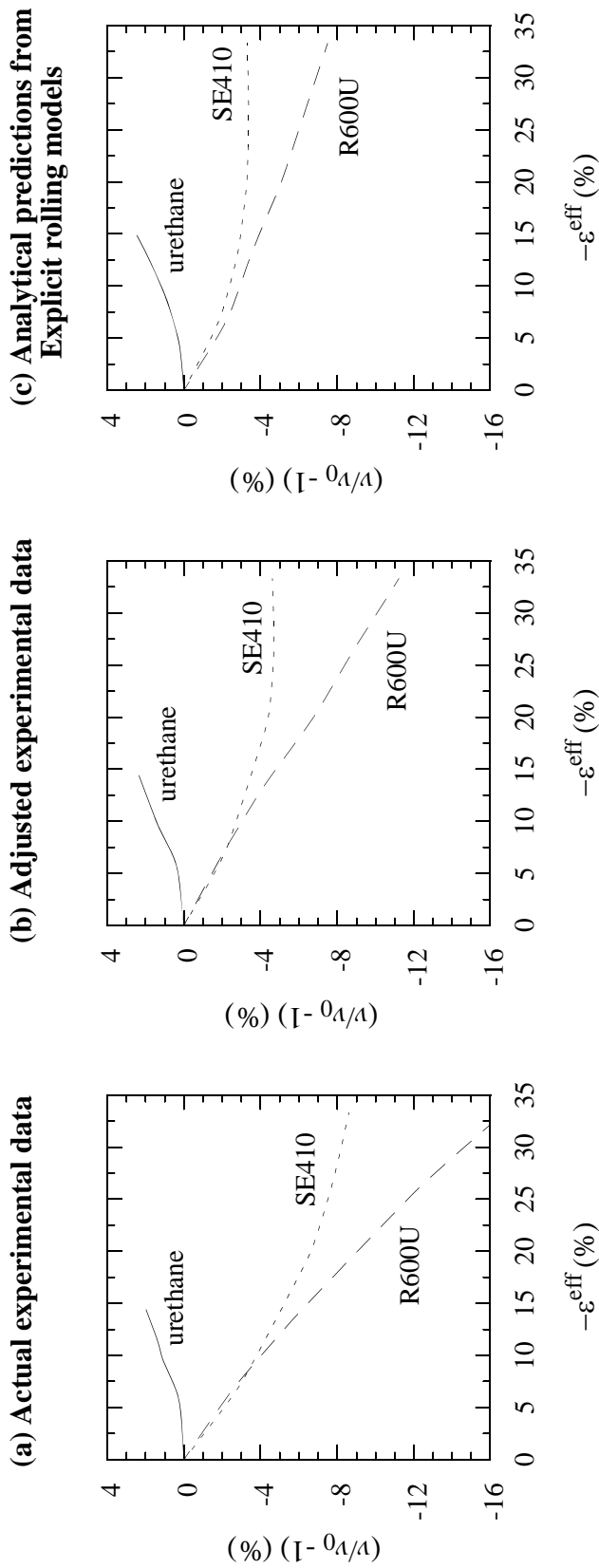
(a) Comparison of experimental and analytical results**(b) 3-D Explicit rolling model**

Figure 4.27: Comparison of experimental data and analytical predictions of speed ratio for a urethane roller feeding a sheet.

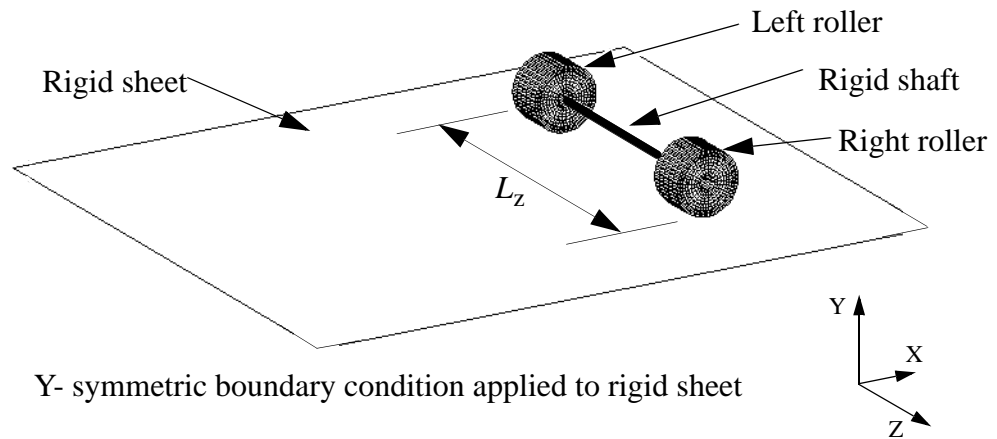


Notes:

- 1) Curves for both the actual and adjusted experimental data are produced by averaging the data samples presented previously.
- 2) Analytical predictions are based on plane strain models for SE410 and R600U and 3-D models for urethane.

Figure 4.28: Final assessment of the analytical modeling capability to predict media speed ratio for three elastomers: SE410, R600U, and urethane.

(a) Complete 3-D model of tire system



(b) Close-up of 3-D model for the tire

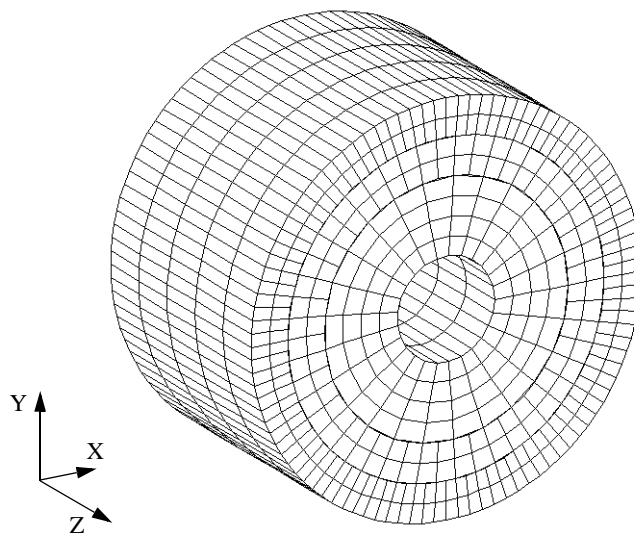


Figure 4.29: 3-D Explicit rolling model used to analyze sheet skew in a R600U nip system.

were the same as those described in Section 4.3.2. Sheet skew was created in the experimental set-up by setting the right Y-displacement control at a fixed location and then placing the left Y-displacement control at several locations above and below the fixed location. Figure 4.30a defines the definition of sheet skew and Figure 4.30b lists the effective roller strains that were applied to the left and right rollers to induce sheet skew.¹

Figure 4.30c presents results from both test measurements and analytical models. The symbols in this figure are the experimentally measured values of skew from three different roller sets. The solid line represents the analytical prediction from the model in Figure 4.29. From the figure we see that the finite element prediction under estimates the sheet skew. This error in the model is consistent with the previous evaluation of R600U speed ratio predictions (Section 4.3.2).

The dashed line in Figure 4.30c is an estimate of what the skew would be based on the measured speed ratio behavior from Figure 4.24a (actual data) and the following equation:

$$\theta = \frac{\arcsin\left(\frac{2\pi R_o(\tilde{v}_{\text{right}}^{\text{sheet}} - \tilde{v}_{\text{left}}^{\text{sheet}})}{L_z}\right)}{2\pi} \approx \frac{R_o(\tilde{v}_{\text{right}}^{\text{sheet}} - \tilde{v}_{\text{left}}^{\text{sheet}})}{L_z} . \quad (4.8)$$

Equation 4.8 states that the sheet skew per revolution, θ , is a function of the differences in speed ratio between two points (denoted as left and right) on the leading edge of the sheet separated by a distance L_z . The dashed line in Figure 4.30c is an estimate because we have assumed that the values $\tilde{v}_{\text{right}}^{\text{sheet}}$ and $\tilde{v}_{\text{left}}^{\text{sheet}}$ can be replaced by speed ratio measurements of a non-skewed sheet at the given values of ε^{eff} . Thus, the estimate ignores any coupling that may occur between the left and right rollers. Figure 4.30c demonstrates that some coupling does occur since the estimate and measured data are slightly different. A similar approximation for the analytical prediction was computed based on the speed ratio function plotted in Figure 4.24b (Explicit rolling prediction) and Equation 4.8. This estimate was within 5% of the fully 3-D prediction. This result, based on a purely elastic

1. The change of ε^{eff} in the right roller is caused by the fact that the rollers are located inward from the Y-displacement controls (see Figure 4.16).

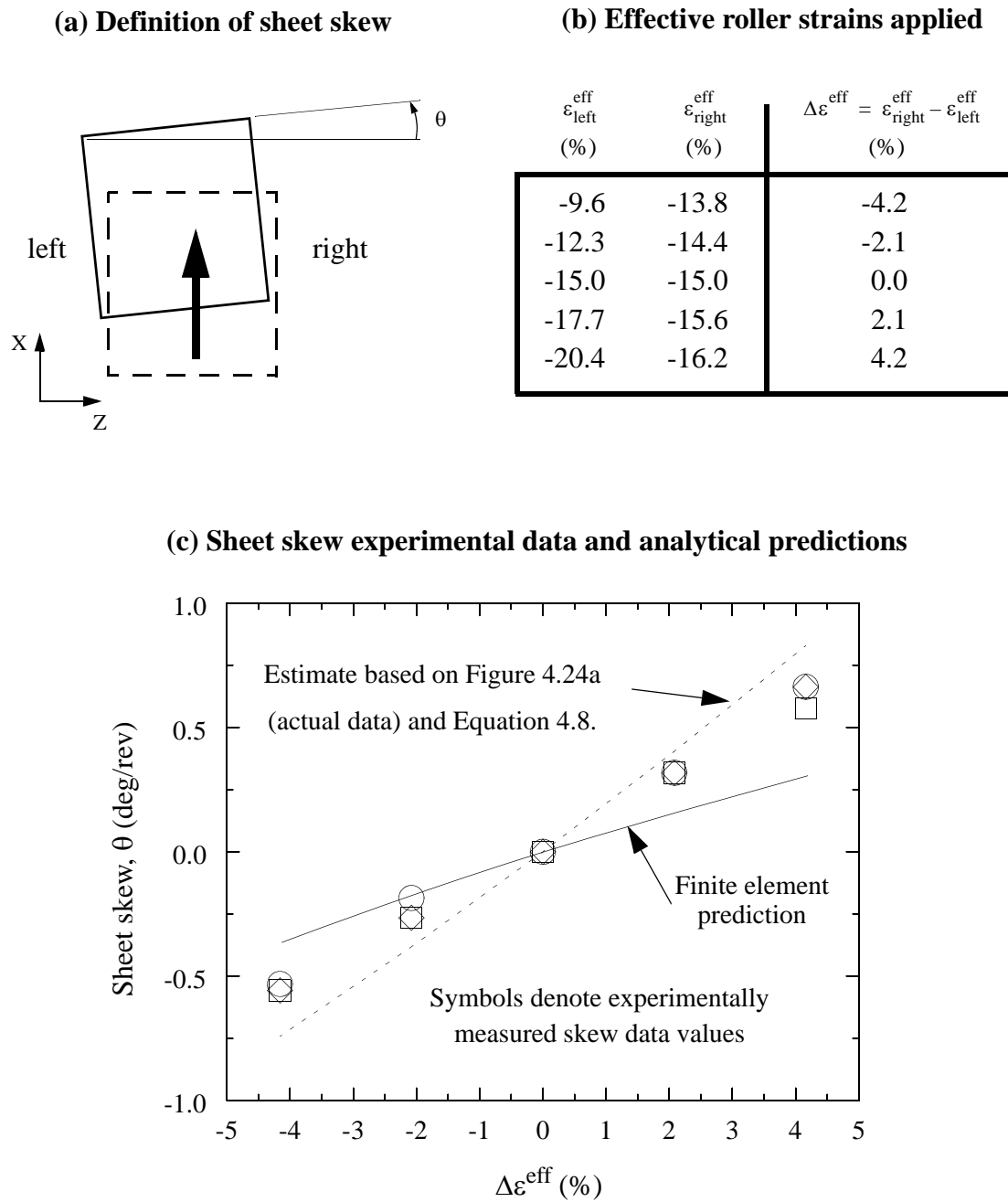


Figure 4.30: Results from R600U nip system sheet skew evaluation.

model, implies that the coupling seen from the experimental data evaluation is probably caused by a material hysteresis effect.

Figure 4.30c also demonstrates that underdriving nips cause sheets to skew in the direction of the roller with the most radial deformation. This behavior is opposite of the commonly observed behavior for overdriving nips (such as urethane and other nearly incompressible rubbers).

4.4.2 Axial Variations in Continuous Nip Systems

This final analysis evaluates axial variations in continuous nip systems of the kind depicted in Figure 4.1b. In this example we compare the influence of soft and hard elastomeric coverings (0.2 cm thick) on several nip parameters. The soft rubber is taken as the urethane previously analyzed ($E = 3.85 \cdot 10^6$ Pa and $\nu = 0.495$). The hard rubber is assumed to be 50 times stiffer ($E = 1.93 \cdot 10^8$ Pa and $\nu = 0.495$). The hollow drums are made of aluminum with an internal radius of 7.6 cm and an external radius of 8.4 cm. Their axial length (not including the shafts) is 28 cm. The end-cap of the drum has a thickness of 0.8 cm. The drum has a solid aluminum shaft attached to the end-cap that is 8.0 cm long, 3.5 cm in radius, and is simply supported. For all analyses of this design, the total applied loading, F , was 2.45 kN (see Figure 4.1b).

Figure 4.31 shows both the shell and beam models used in the analysis. The models depicted here are significantly more complex than the models previously presented in this research. This added complexity is required to obtain the axial variations of nip parameters caused by the drum deformation. Because of the computational requirements of these models, it is desirable to model the actual rolling nip problem as a frictionless, static indentation problem. From these indentation analyses we can obtain axial variations in nip pressure and nip width. Using the methods outlined in Section 4.1, we can also compute axial variations in the estimated average media speed ratio, $\Gamma^{\text{ave}}(s=a, Z)$.

The models depicted in Figure 4.31 take full advantage of all possible symmetries. The elastomeric covering is only modelled in the neighborhood of the nip because it is thin and its deformation is highly localized. The shell model uses elements that include transverse

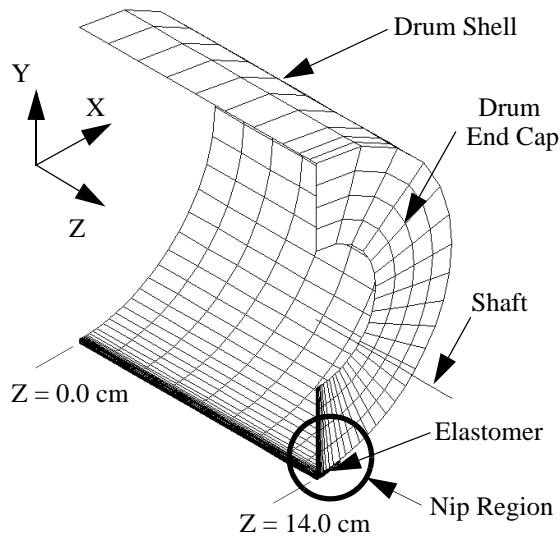
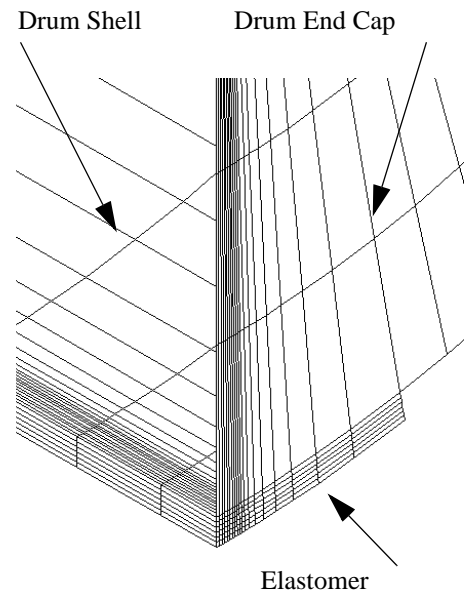
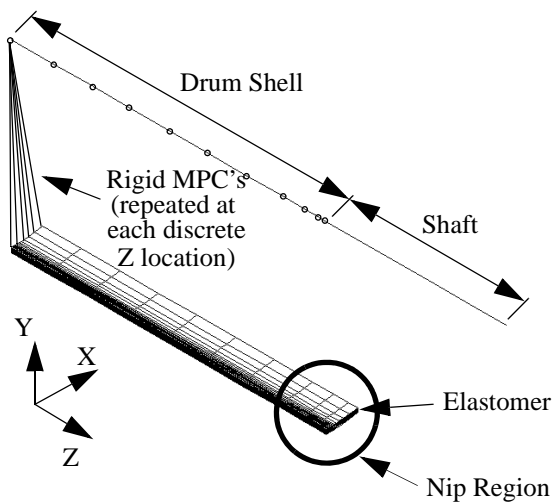
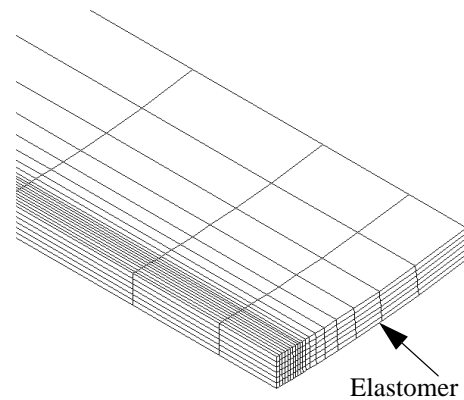
(a) Shell model*Blow-Up of Nip Region***(b) Beam model***Blow-Up of Nip Region*

Figure 4.31: Finite element models used to evaluate the continuous hollow-drum design. Meshes shown for hard-rubber case.

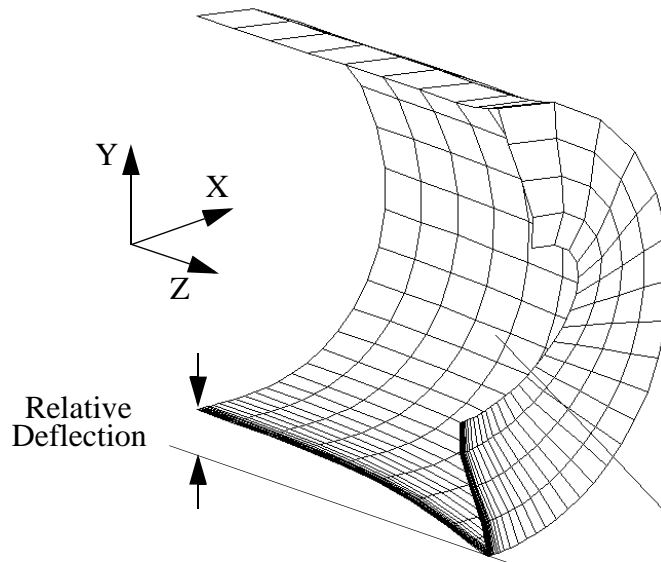
shear flexibility. The equivalent beam model assumes Timoshenko beam theory with shear flexibility. Inclusion of shear flexibility in the beam model reduces the nominal bending stiffness predicted by only Euler-Bernoulli bending by approximately 40%. In the beam model, the drum is connected to the elastomer by rigid MPC's (multipoint constraints).

Figure 4.32a shows the deformed shape of the drum (magnified 1000 times) predicted by the shell model for a simulation with the hard rubber. As seen in the figure, the drum “indents” more at the middle of the drum ($Z = 0$ cm) than near the end-cap. This is due to the increased hoop stiffness that the end-cap provides for the drum. A similar deformed shape results with the soft elastomer. Figure 4.32b shows the drum deflections relative to the end-cap deflection. For the beam models, the deflection is taken about the centroid of the beam since it is rigidly attached to the elastomer with MPCs. As seen in the plot, the shell models predict greater relative deflection than the beam models. This is because the shell models account for the drum hoop stiffness and allow for radial compliancy in the drum. The beam model ignores the drum radial compliancy.

It is interesting to note that for the shell models, the design with hard rubber produced less relative drum deflection than the design with the soft rubber. This result appears counterintuitive but is explained as follows. With a hard elastomer, the contact pressure is concentrated more near the end-caps than for the soft elastomer, which distributes the load more evenly over the entire length of the drum (see Figure 4.33). By careful inspection of Figure 4.32b, it is seen that near the end-cap ($Z = 14$ cm), the relative shell deflection is larger for the hard-elastomer model than for the soft-elastomer model.

These axial variations in drum deflections are the primary cause of axial variations in nip parameters for this design. Figure 4.33 shows how the contact pressure and nip width vary axially along the nip. The highest pressure is always nearest the end-caps. Note that this peak pressure is not exactly at the end of the drum, but slightly inside the drum edge ($Z < 14$ cm). This is due to the free-edge effect of the elastomer. At the end of the drum, the elastomer is not constrained (axially) and tends to behave softer. The strong axial variation predicted by the shell models is caused by the decrease in hoop stiffness from the edge of the drum, where the endcaps are located, to the middle of the drum. The beam model, having no hoop stiffness capability, cannot capture the substantial axial variation in

(a) Deformed drum shape for shell model with hard rubber
(magnification factor = 1000)



(b) Y-Coordinate deflection of drum relative to edge of drum
(various solutions)

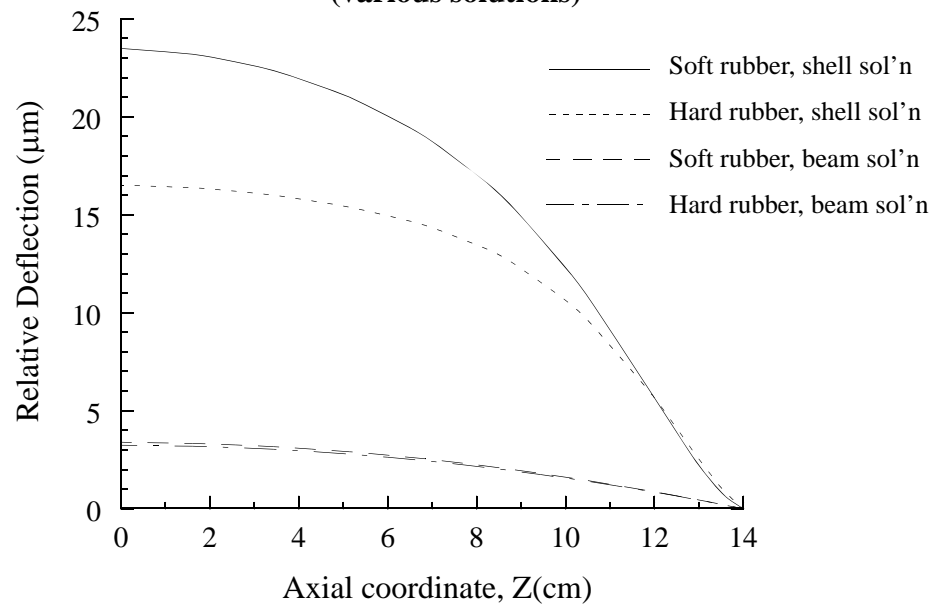
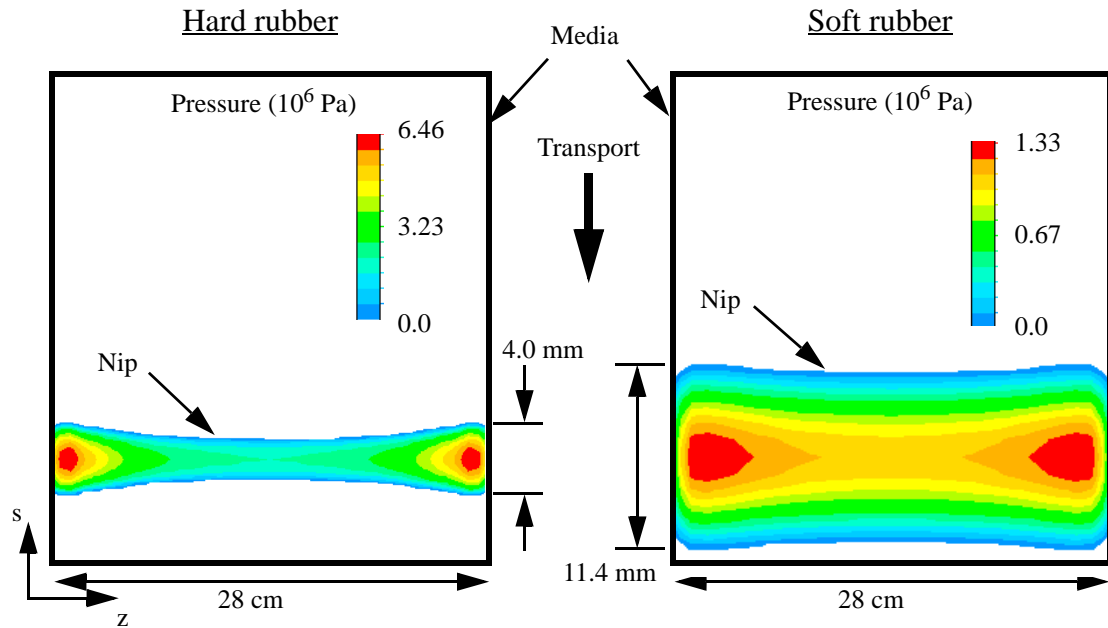


Figure 4.32: Primary cause of axial variation in nip parameters: drum deflections.

(a) Nip pressure predicted by shell models



(b) Nip pressure predicted by beam models

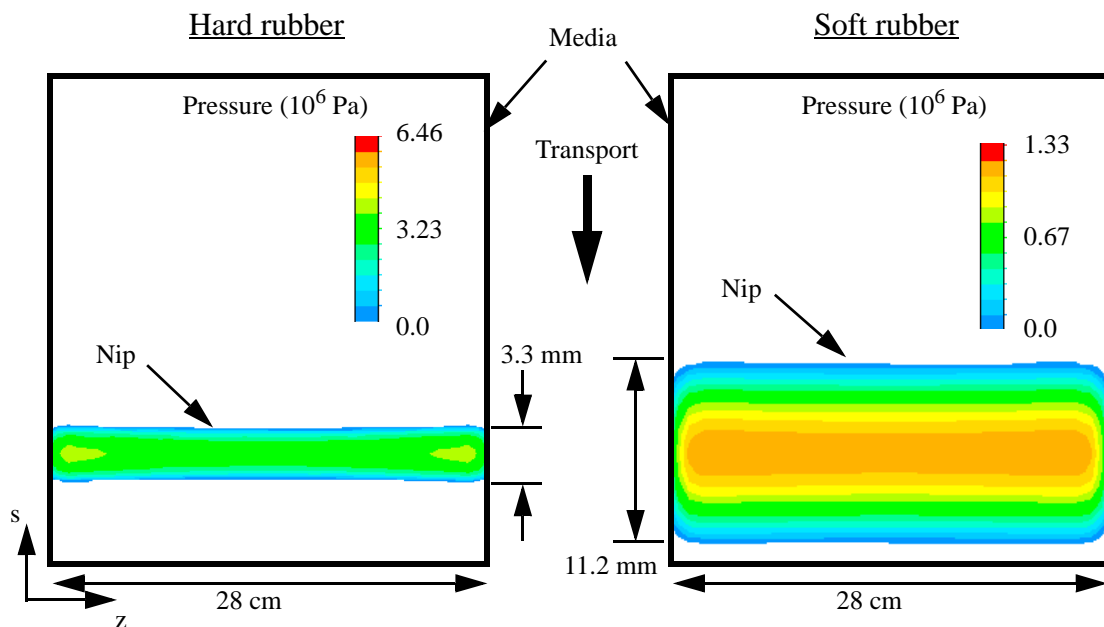


Figure 4.33: Comparison of shell and beam model predictions of axial variation in nip pressure for hollow-drum designs.

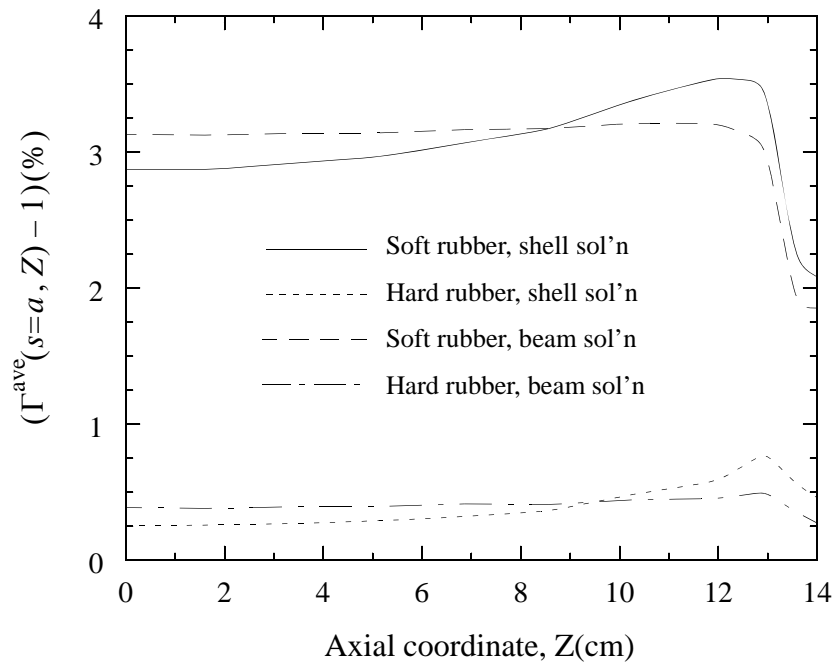


Figure 4.34: Comparing predictions of the axial variation in average speed ratio evaluated at nip edge for beam and shell models.

nip pressure and nip width, especially for the hard-elastomer case. If the cylinder in this problem was long, slender, and thick, then beam approximations would be valid to model the axial behavior.

Figure 4.34 shows that the average speed ratio estimates follows similar trends as the nip pressure plots. In all the plots, the speed ratio is greatest nearest the peak pressure point because that is where the elastomer is deformed the greatest. Since these solutions are frictionless, we expect that the magnitude of the overdrives predicted in Figure 4.34 to decrease if friction is included.

One common cause of media wrinkling is axial variations in transport conditions. The results displayed in Figure 4.34 can be used to assess the type of wrinkling pattern that may occur in the media. As stated previously, we have decoupled the media from the nip, ignored the actual stick/slip behavior that occurs in the nip, and ignored the deformation of

the media. Because of these approximations, the axial variations in speed ratio depicted in Figure 4.34 can only define the general form of the boundary conditions that should be used in a media wrinkling analysis. Benson et. al. [9] has utilized this approach to simulate several basic wrinkling patterns.

Chapter 5

Conclusions

The technology of nip mechanics is vital to devices that process and transport thin sheets of media such as web manufacturing equipment, photocopiers, printers, and facsimile machines. The primary thrust of this research was to improve our understanding of elastomeric nip systems by enhancing our analytical capabilities of simulating such systems. Results demonstrated that the analytical models show good correlation to the physical experiments.

The specific objectives of this study were to

1. thoroughly evaluate the capability of representing elastomeric materials with the general family of Ogden-Hill strain-energy density functions,
2. measure Ogden-Hill material constants for three particular elastomers classified as highly compressible (R600U), moderately compressible (SE410), and nearly incompressible (urethane),
3. verify the qualitative and quantitative capability of modeling non-inertial 2-D and 3-D elastomeric rolling nip problems by comparing models with experiments,
4. assess the sensitivity of various nip-system parameters to elastomer type and loading conditions.

5.1 Material Modeling

Understanding the constitutive relationship that governs a given elastomer is extremely important for developing analytical models of nip systems. For this study, we have concentrated on the main deformation mechanism of elastomers — elasticity. The first two materials, R600U and SE410, are grouped into the general category of compressible elastomers. The last material, urethane, is denoted as a nearly incompressible material because its Poisson's ratio is very near to 0.5. Large strain deformations were studied for

both compressible materials. Evaluation of the nearly incompressible urethane was limited to small strains because its stiffness is sufficiently high to prevent, in many practical nip systems, large strains from occurring.

Analytical representations of these materials assumed they were isotropic and homogeneous and that they exhibit completely elastic, time-independent behavior. Physical testing demonstrated that (for the three materials tested) the greater the material's compressibility, the greater the complexity in the material's structural response. Experimental evaluation of urethane established that these assumptions were quite appropriate for this material within the ranges of strain and strain-rate studied. The SE410 showed some hysteretic behavior which caused errors in any analytical predictions that included cyclic loading such as rolling. R600U, a highly cellular elastomer, "stretched" the use of our material assumptions. The R600U experimentally exhibited sample-to-sample variation as well as some anisotropic and hysteretic behavior.

5.1.1 Theoretical Background

Chapter 2 provided the theoretical background for the material modelling of both compressible materials (R600U and SE410) and nearly incompressible materials (urethane) using the general family of Ogden-Hill strain-energy density functions and Hooke's law, respectively. The analysis demonstrated that previous strain-energy functions proposed by Blatz and Ko [12], Brockman [14], Mooney [79], and Rivlin [94-99] are all special cases of the general Ogden-Hill form. This chapter also described analytical methods of obtaining the required constitutive constants by employing equations derived from the concept of work conjugacy. This enabled the use of experimentally measured *nominal* stress and *nominal* strain data (in the large strain region) from various primitive deformation modes to determine material constants.

5.1.1.1 Compressible materials

For the compressible materials, the use of uniaxial compression and simple-shear deformation modes was described in detail. Because these materials are easily deformed, a non-contact, optical method of measuring the transverse strains from the uniaxial

compression tests was discussed. For the simple-shear mode, a specially designed test fixture capable of measuring Poynting stress was presented. The Poynting stress, which is not commonly measured, provides additional information during the determination of material constants. The analytical equations for each primitive deformation mode assume a uniform deformation state throughout the sample. During the physical testing of uniaxial compression, the frictional (stick) boundary conditions between the compression plates and the sample created non-ideal boundary conditions.¹ Analysis using linear finite element models and Hooke's law demonstrated that the extraction of the *true* Poisson's ratio from the *effective* Poisson's ratio (computed from measured transverse strain data) must be performed with care; simple extrapolation based on tests of different sample heights is not valid. The variation of *effective* Poisson's ratio as a function of normalized specimen dimensions (B/L) was shown to have a maximum near $B/L = 1$. For the simple-shear tests, non-ideal boundary conditions were caused by free edges at the two ends of the sample. This potential problem was minimized to a negligible influence by using samples with a height-to-length ratio greater than seven.

5.1.1.2 Nearly/fully incompressible materials

Hooke's law was sufficient to characterize nearly incompressible urethane because its deformation was limited to small strains.² For the limiting case of $\nu = 0.5$, Hooke's law could only be used if it was written as separable functions of deviatoric and volumetric deformations; something that is not commonly done in the finite element method. A more common method to deal with this special case is to use a neo-Hookean material representation based on a hyperelastic strain-energy density function. Both material representations require Young's modulus and Poisson's ratio. Measurement of Poisson's ratio via the optical technique used for the compressible elastomers was not sufficiently accurate. Two techniques, an ultrasound method and a constrained piston method, were described to measure Poisson's ratio accurately in the neighborhood of the incompressible limit.

1. The theoretical equations assume there is no friction between the compression plates and the sample.
2. Hooke's law is a special case of the general family of Ogden-Hill strain-energy density functions.

5.1.2 Experimental Results

Chapter 3 detailed the experimental material test results from the three elastomers in question. The compressible materials were tested in uniaxial compression and simple-shear up to 50% applied nominal strains. The nearly incompressible urethane was tested only in the small strain region.

5.1.2.1 Compressible materials: SE410 and R600U

The first compressible material described in Chapter 3 was SE410. Experimentally acquired compressive uniaxial stress/strain data showed that this material exhibited a region of softened stiffness between 5% and 35% applied nominal strains. Beyond 35% strain, stress stiffening was observed. Evaluation of the SE410's initial tangent Poisson's ratio showed good agreement with the analytical analysis of *true* and *effective* Poisson's ratio from Chapter 2. The nominal transverse strain varied fairly linearly with the nominal applied strain over the deformation range tested. Simple-shear data from this material showed that the shear stress varied in a similar manner to the uniaxial data, although not as nonlinear. Measurements of Poynting stress yielded tensile values, a result that is opposite of what the Blatz and Ko [12] model predicts (Brockman [14] predicts zero Poynting stress).

Experimental evaluation of R600U demonstrated that its highly cellular construction caused a relatively greater amount (compared to the SE410) of stiffness-softening in the region between 5% and 35% applied nominal strains. The magnitude of the transverse strain response for the R600U was significantly lower than that of the SE410 and the response was strongly nonlinear. The R600U simple-shear behavior, both shear stress and Poynting stress, was similar to the SE410's response, although about half the magnitude.

The nonlinear behavior of both SE410 and R600U prohibited the use of Hooke's law. Moreover, neither of the laws utilized by Blatz and Ko [12] for foamed polyurethane nor Brockman [14]¹ for compressible rubber could characterize either of these materials;

1. Brockman's [14] formulation is a subset of the generalized Blatz-Ko form. Brockman states that the generalized Blatz-Ko theory is limited in its ability to quantitatively model a general class of elastomers.

significant errors in nominal stress were computed from uniaxial compression beyond 5% deformation. For simple-shear Poynting stress, the so-called “Blatz-Ko” model for polyurethane foams predicted compressive behavior, but experimental test data from both SE410 and R600U indicated tensile stresses. This result is important because several researchers (Beatty [8], Carroll and Horgan [17], and Chung and Horgan [18]) have emphasized the use of “Blatz-Ko”. The relatively simplistic nature of this constitutive model lends itself to closed-form theoretical analysis. Unfortunately, these three papers present no experimental evidence to further verify the general applicability of this law for either the original polyurethane foam tested by Blatz and Ko (originally tested under tensile modes only) or any other types of compressible elastomers. The evaluation of compressible materials in this research (SE410 and R600U, a polyurethane foam) demonstrated that the “Blatz-Ko” model is not a generic law for polyurethane foams or for foamed rubbers in general.

The highly nonlinear and generic nature of the Ogden-Hill formulation provides more flexibility to simulate a variety of hyperelastic materials. The results from both SE410 and R600U demonstrate that one-term Ogden-Hill provided reasonable fits and two-term Ogden-Hill provided improved fits. These curve-fits were based on the uniaxial compression and simple-shear deformation modes summarized previously. To further assess the applicability of these curve-fits, other primitive deformation modes and Drucker stability were evaluated analytically. Also addressed in this analysis was the importance of using data from as many deformation modes as possible when computing material constants. It is recognized by this author that the Ogden-Hill constants computed here are not generically applicable to all deformation ranges. For example, predictions of volumetric tension were completely unrealistic for the two-term models of both SE410 and R600U. However, this range of deformation was not of interest in the nip mechanics analyses studied.

5.1.2.2 Nearly incompressible urethane

Experimental evaluation of urethane utilized uniaxial tension to obtain Young’s modulus. The Cauchy stress versus logarithmic strain was extremely linear up to a stretch ratio of 1.1. At a stretch ratio of 1.5, the measured Cauchy stress was only 11% greater than that

predicted by Hooke's law. Poisson's ratio was obtained using the ultrasound technique described previously because of its simplicity and accuracy.¹ These experiments yielded a Poisson's ratio value of 0.4997.

5.2 Nip Mechanics

Chapter 4 concentrated on the application of these material laws to nip mechanics. The chapter began with a simplified analysis of media speed ratio. This theoretical evaluation demonstrated that the elastomeric covering's outer-fiber hoop strain inside the nip governs the media speed ratio. This analysis led to methods of computing estimates of the speed ratio from non-rolling indentation analyses.

Chapter 4 also detailed several experiments and analyses of non-rolling and rolling nip problems. All of the analytical nip models were developed using Lagrangian-based nonlinear finite element algorithms available in ABAQUS/Standard and ABAQUS/Explicit. The Standard code utilizes a traditional implicit static solution algorithm while the Explicit code is based on an explicit dynamics formulation. The explicit method, which typically requires more computational effort, was used on the frictional rolling problems because it did not suffer from the convergence problems of the implicit method (caused by algorithmic frictional chatter). Besides investigating several nip related parameters, these studies provided further validation of the elastomeric material laws. Evaluations of cyclic problems such as rolling indicated some limitations of the purely elastic constitutive formulations used.

5.2.1 Non-Rolling Nip Results

The first set of nip experiments were non-rolling tests where an elastomeric roller (with a solid steel hub) was compressed between two flat plates. Measurements of applied load and nip width as a function of roller compression were compared against finite element models using the material constants obtained from Chapter 3. Excellent correlation was

1. The compliance of the support equipment in the constrained piston method creates more difficulty in reducing the data.

achieved between experimental measurements and analytical predictions of applied load and nip width versus effective roller strain (up to 60% strain) for SE410. Good correlation was obtained for R600U over the same range. The urethane nip models were only tested up to 15% compressive effective roller strains and they yielded excellent correlation to the physical testing. For all non-rolling cases, the influence of friction on the nip quantities of load and nip width was found to be negligible.

These non-rolling analyses were also used to initially assess the explicit dynamic algorithm's accuracy and to determine the maximum amount of *artificial decrease* in event-time (solution speed-up) that could be applied to produce efficient solutions without introducing significant inertial dynamic effects. The analyses showed that the local hoop strains in the nip were the most sensitive parameters to this artificial solution speed-up. The overall results established that the actual event time could be decreased by approximately 1500 times. For the nearly incompressible urethane it was also demonstrated that the Explicit solution-time is strongly influenced by the value of Poisson's ratio. Analyses established that solution efficiency could be increased by a factor of 4.1 if Poisson's ratio was relaxed from the measured value of 0.4997 to a value of 0.495. Artificially lowering Poisson's ratio below a value of 0.495 would begin to cause significant errors in media speed ratio predictions.

5.2.2 Rolling Nip Results

Rolling investigations, both experimental and analytical, established that both SE410 and R600U produced nip systems that underdrove while urethane produced a nip system that overdrove. Material hysteresis effects were present in the measured values of speed ratio, especially for the SE410 and R600U materials. A simple adjustment based on the amount of lag measured from the undriven roller (with no media in the nip) was used to remove, as best as possible, the hysteretic behavior from the experimental results. Overall analytical predictions produced from Explicit-based 2-D and 3-D rolling models correlated well against the adjusted experimental measurements. In particular, the models were able to capture the range of behavior from overdrive of urethane to underdrive of R600U. The best correlation was achieved with the urethane nips and the worst correlation was found for the R600U nips. This was consistent with the complexity of the given material

behavior and the amount of material hysteresis exhibited. These comparisons established that purely elastic material formulations do capture the dominate behavior and provide sufficient accuracy for use in nip-system design. For improved accuracy in the prediction of materials such as SE410 and R600U, the material's hysteretic behavior must be included into the constitutive relationship.

The analysis with nearly incompressible urethane demonstrated that imposing the plane strain assumption can cause significant errors in overdrive estimates for tire-based nip systems made of such materials. Because of the material volume constraint, the enforcement of zero axial strain caused the plane strain models to overpredict the hoop strain and resulting media speed ratio. Analysis showed that 3-D models which allow the roller to bulge were significantly more accurate. This result is important considering the fact that most of the previous work cited in the literature review (Section 1.2.1) utilized the plane strain assumption.

Comparisons of the rolling Explicit models with non-rolling (indentation) Standard and Explicit models demonstrated that estimates based on the average speed ratio evaluated at the nip edge ($\Gamma^{\text{ave}}(s=a)$) modelled with and without friction) bounded the predictions from the rolling models. Due to the significant decrease in computational effort of the non-rolling estimates, these approximations are good alternatives to the more expensive rolling solutions.

All materials had sufficiently high coefficients of friction such that no slip occurred in the rolling investigations. The coefficient of friction would need to be decreased by at least 50% for slip to begin. Hence, variations of less than 50% in the coefficient of friction would cause no change in nip system response.

5.2.3 Axial Variations

The analytical models' ability to simulate axial variations was also investigated. Sheet skew in a tire-based system made of R600U was evaluated experimentally and analytically. This problem showed that underdriving nips cause sheets to skew in the direction of the roller which has the most radial deformation. This behavior is opposite of

the commonly observed behavior for overdriving nips. The analytical models correctly predicted the direction of skew but underpredicted its value, by approximately a factor of $1/2$, when compared with the experimental data. The primary reason for this discrepancy was the omission of material hysteresis in the models. A simplified estimate of skew based on speed ratio knowledge of a non-skewed system was shown to be as good as the complete 3-D model and significantly less expensive.

The final problem looked at axial variations in continuous nip system made from rubber-covered, short, aluminum, hollow drums. This example demonstrated the power of utilizing the finite element method to study a more complicated 3-D nip system. The results showed that shell representations of the hollow drum were required to predict the strong localized axial gradients in nip parameters, especially when the rubber cover was relatively stiff. The example also described how axial variations of speed ratio estimates could be used to approximate boundary conditions for an analysis of media wrinkling.

5.3 Summary

In summary, this research has improved our fundamental understanding of the mechanical behavior of several elastomeric materials and has shown how these materials influence the behavior of nip systems. It has been shown that the Ogden-Hill family of hyperelastic strain-energy functions are capable of modelling a wide variety of elastomers. Constitutive constants for three particular materials that range from a highly compressible foam to a nearly incompressible rubber have been determined. Comparisons with numerous experimental results from nip system investigations have demonstrated that the analytical models yield good qualitative and reasonable quantitative predictions. These comparisons established that purely elastic material formulations do capture the dominate behavior and that it is the omission of material hysteresis which causes errors in quantitative accuracy. Assessment of the sensitivity of nip parameters to elastomer type and loading conditions has shown that the media speed ratio is the most sensitive variable and nip width is the least. These investigations have provided general and specific information that will enable the engineering community to develop more reliable and robust technology for the future.

5.4 Suggestions For Future Work

The two main areas that could benefit from further research are material modelling of elastomers and numerical analysis of nip systems.

Additional study on the general applicability of the Ogden-Hill material laws utilized for SE410 and R600U would be beneficial. In particular, comparisons between experimental data and analytical predictions for deformation modes, other than those already presented, would further assess capabilities and limitations. The general nature of the finite element method allows for *relatively* easy application of this material knowledge to other geometries and boundary conditions such as the study of elastomeric materials in seats, gaskets, linings, shock absorbers, and tires in general.

In addition, the highly nonlinear nature of the Ogden-Hill form allows for the possibility of multiple local minima to exist in the nonlinear least-squares curve fitting used to obtain the material parameters. A search for other minima using different starting points would yield further insights and potentially an improved set of material constants.

The inclusion of material hysteresis into the constitutive relationships would allow improved predictions of problems involving cyclic loading. Because of the nonlinear nature of the compressible materials described, the equations that would govern material hysteresis will probably be nonlinear functions of deformation and stress. Inclusion of hysteresis with hyperelastic material formulations must be done with care so that the problem formulation remains consistent with respect to measures used for deformation (and strain) and rate of deformation.

The explicit dynamic method, which is computationally expensive, was utilized because the implicit static techniques of ABAQUS/Standard had significant convergence problems with rolling friction. Current research by Stack [107] has focused on the development of an implicit, static, nonlinear finite element algorithm specifically designed for frictional rolling problems. Stack's formulation has shown promise and does not display these convergence difficulties.

References

- [1] Alexander, H., "A Constitutive Relation For Rubber-Like Materials," *International Journal of Engineering Science*, Vol. 6, 1968, pp. 549-563.
- [2] Ashby, M. F., "The Mechanical Properties of Cellular Solids," *Metallurgical Transactions A*, Vol. 14A, Sept., 1983, pp. 1755-1769.
- [3] Atkin, R. J., Fox, N., *An Introduction to the Theory of Elasticity*, Longman, New York, 1980.
- [4] Augenblick, K. B., Unpublished Results, Eastman Kodak Company, January 8, 1975.
- [5] Bass, Jon M., "Three-Dimensional Finite Deformation, Rolling Contact of a Hyperelastic cylinder: Formulation of the Problem and Computation Results," *Computers & Structures*, Vol. 26, No. 6, 1987, pp. 991-1004.
- [6] Bathe, K. J., *Finite Element Procedures in Engineering Analysis*, Prentice-Hall, 1982.
- [7] Batra, R. C., "Rubber Covered Rolls-The Nonlinear Elastic Problem," *Journal of Applied Mechanics*, Vol. 47, March 1980, pp 82-86.
- [8] Beatty, M. F., "Topics in finite elasticity: Hyperelasticity of rubber, elastomers, and biological tissues — with examples," *Applied Mechanics Review*, Vol. 40, No. 12, December, 1987, pp. 1699-1734.
- [9] Benson, R. C., Chiu, H. C., LaFleche, J. E., Stack, K. D., "Simulation of Wrinkling Patterns Due to Non-Uniform Transport Conditions," *Proceedings of the Second International Conference on Web Handling*, Oklahoma State University, Stillwater, OK, June 6-9, 1993.
- [10] Bentall, R. H., Johnson, K. L., "Slip in the Rolling Contact of Two Dissimilar Elastic Rollers," *International Journal of Mechanical Science*, Vol. 9, 1967, pp. 389-404.
- [11] Bentall, R. H., Johnson, K. L., "An Elastic Strip in Plane Rolling Contact," *International Journal of Mechanical Science*, Vol. 10, 1968, pp. 637-663.
- [12] Blatz, P. J., Ko, W. L., "Application of Finite Elastic Theory to the Deformation of Rubbery Materials," *Transactions of the Society of Rheology*, VI, 1962, pp. 223-251.
- [13] Borchardt, H. A., "Rolling Radius of Rubber-Covered Cylinders," *Machine Design*, April 30, 1959, pp. 120-122.
- [14] Brockman, R. A., "On the Use of the Blatz-Ko Constitutive Model in Nonlinear Finite Element Analysis," *Computers & Structures*, Vol. 24, No. 4, 1986, pp. 607-611.

- [15] Burden, R. L., Faires, J. D., *Numerical Analysis: Third Edition*, Prindle, Weber & Schmidt, 1985.
- [16] Campos, L. T., Oden, J. T., and N. Kikuchi, "A Numerical Analysis of a Class of Contact Problems With Friction in Elastostatics," *Computer Methods in Applied Mechanics and Engineering*, 34, 1982, pp. 821-845.
- [17] Carroll, M. M., Horgan, C. O., "Finite Strain Solutions for a Compressible Elastic Solid," *Quarterly of Applied Mathematics*, Vol. XLVIII, No. 4, December, 1990, pp. 767-780.
- [18] Chung, D. -T., Horgan, C. O., "The Finite Deformation of Internally Pressurized Hollow Cylinders and Spheres for a Class of Compressible Elastic Materials," *International Journal of Solids and Structures*, Vol. 22, No. 12, 1986, pp. 1557-1570.
- [19] Cole, K., Unpublished Results, Eastman Kodak Company, April 21, 1983.
- [20] Cole, K., Piarulli, V., Unpublished Results, Eastman Kodak Company, February 14, 1985.
- [21] Cole, K., Piarulli, V., Unpublished Results, Eastman Kodak Company, February 14, 1985.
- [22] Cole, K., Personal notes on a 2-D nip model, original date 1986, received by T. Diehl in 1992.
- [23] Cole, K., Personal Communication, 1993.
- [24] Cook, R. D., Malkus, D. S., Plesha, M. E., *Concept and Applications of Finite Element Analysis: Third Edition*, John Wiley & Sons, 1989.
- [25] Crisfield, M. A., *Non-linear Finite Element Analysis of Solids and Structures, Volume 1: Essentials*, John Wiley and Sons, New York, 1991.
- [26] Diehl, T., Unpublished Results, Eastman Kodak Company, May 12, 1992.
- [27] Diehl, T., Unpublished Results, Eastman Kodak Company, June 23, 1992.
- [28] Diehl, T., Unpublished Results, Eastman Kodak Company, July 31, 1992.
- [29] Diehl, T., Stack, K. D., Benson, R. C., "A Study of Three-Dimensional Nonlinear Nip Mechanics," *Proceedings of the Second International Conference on Web Handling*, Oklahoma State University, Stillwater, OK, June 6-9, 1993.
- [30] Diehl, T., "Formulation of a User MPC to Simulate Beam-Type Transport Problems," *MFSP Internal Report*, Department of Mechanical Engineering, University of Rochester, NY, June 16, 1993.
- [31] Diehl, T., "Simulating the Transport of Very Flexible Sheets: Beam-Type Solutions," *ABAQUS Users' Conference Proceedings*, Aachen, Germany, June 23-25, 1993, pp. 165-179.

- [32] Flanagan, D. P., Belytschko, T., "A Uniform Strain Hexahedron and Quadrilateral with Orthogonal Hourglass Control," *International Journal for Numerical Methods in Engineering*, Vol. 17, 1981, pp. 679-706.
- [33] Flanagan, D. P., Belytschko, T., "Eigenvalues and Stable Time Steps for the Uniform Strain Hexahedron and Quadrilateral," *Journal of Applied Mechanics*, Vol. 51, March 1984, pp. 35-39.
- [34] Gent, A. N., Thomas, A. G., "The Deformation of Foamed Elastic Materials," *Journal of Applied Polymer Science*, Vol. I, No 1, 1959, pp. 107-113.
- [35] Gibson, L. J., Ashby, M. F., Schajer, G. S., Robertson, C. I., "The Mechanics of Two-Dimensional Cellular Materials," *Proceedings of the Royal Society of London*, A 382, 1982, pp. 25-42.
- [36] Gibson, L. J., Ashby, M. F., "The Mechanics of Three-Dimensional Cellular Materials," *Proceedings of the Royal Society of London*, A 382, 1982, pp. 43-59.
- [37] Green, A. E., Zerna, W., *Theoretical Elasticity: Second Edition*, Dover, New York, 1992.
- [38] Greenwood, J. A., Minshall, H., Tabor, D., "Hysteresis Losses in Rolling and Sliding Friction," *Proceedings of the Royal Society of London*, A 259, 1961, pp. 480-507.
- [39] Gurtin, M. E., *An Introduction to Continuum Mechanics*, Academic Press, New York, 1981.
- [40] Hahn, H. T., Levinson, M., "Indentation of an Elastic Layer(s) Bonded to a Rigid Cylinder—I. Quasistatic Case Without Friction," *International Journal of Mechanical Science*, Vol. 16, 1974, pp. 489-502.
- [41] Hahn, H. T., Levinson, M., "Indentation of an Elastic Layer Bonded to a Rigid Cylinder—II. Unidirectional Slipping With Coulomb Friction," *International Journal of Mechanical Science*, Vol. 16, 1974, pp. 503-514.
- [42] Haines, D. W., Wilson, W. D., "Strain-energy Density Function for Rubber-Like Materials," *Journal of the Mechanics and Physics of Solids*, Vol. 27, 1979, pp. 345-360.
- [43] Hannah, M., "Contact Stress and Deformation in a Thin Elastic Layer," *Quarterly Journal of Mechanics and Applied Mathematics*, Vol. IV, Pt. 1, 1951, pp. 94-105.
- [44] Hertz, H., "Über die Berührung Fester Elastischer Körper (On the Contact of Elastic Solids)," *J. Reine und Angewandte Mathematik*, Vol. 92, 1882, pp. 156-171. (For English translation see *Miscellaneous Papers by H. Hertz*, Editors. Jones and Schott, London, Macmillan, 1896.)
- [45] Hibbitt, H. D., *Basic Relations for Geometric Nonlinearities: Formulations for Geometrically Nonlinear Numerical Analysis of Solids and Structures*, Transcript of Notes, 1980 (Available from Hibbitt, Karlsson, and Sorensen Inc.).

- [46] Hibbitt, Karlsson, Sorensen, *ABAQUS/Explicit Example Problems Manual*, V 5.2, HKS, 1992.
- [47] Hibbitt, Karlsson, Sorensen, *ABAQUS/Explicit User's Manual*, V 5.2, HKS, 1992.
- [48] Hibbitt, Karlsson, Sorensen, *ABAQUS/Standard Example Problems Manual*, V 5.2, HKS, 1992.
- [49] Hibbitt, Karlsson, Sorensen, *ABAQUS/Standard User's Manual*, Volume I, V 5.2, HKS, 1992.
- [50] Hibbitt, Karlsson, Sorensen, *ABAQUS/Standard User's Manual*, Volume II, V 5.2, HKS, 1992.
- [51] Hibbitt, Karlsson, Sorensen, *ABAQUS Theory Manual*, V 5.2, HKS, 1992.
- [52] Hibbitt, Karlsson, Sorensen, *ABAQUS Verification Manual*, V 5.2, HKS, 1992.
- [53] Hibbitt, Karlsson, Sorensen, *An Introduction to ABAQUS/Explicit*, Course notes, HKS, 1992.
- [54] Hibbitt, Karlsson, Sorensen, *Analysis of Rubber Components with ABAQUS*, Course notes, HKS, 1991.
- [55] Hibbitt, Karlsson, Sorensen, *Using ABAQUS: An Introductory Course*, Course notes, HKS, 1990.
- [56] Hibbitt, H. D., Marcal, P. V., Rice, J. R., "A Finite Element Formulation For Problems of Large Strain and Large Displacement," *International Journal of Solids and Structures*, Vol. 6, 1970, pp. 1069-1086.
- [57] Hill, R., "On Constitutive Inequalities For Simple Materials–I," *Journal of the Mechanics and Physics of Solids*, Vol. 16, 1968, pp. 229-242.
- [58] Hill, R., "On Constitutive Inequalities For Simple Materials–II," *Journal of the Mechanics and Physics of Solids*, Vol. 16, 1968, pp. 315-322.
- [59] Hill, R., "Aspects of Invariance in Solid Mechanics," *Advances in Applied Mechanics*, Vol. 18, 1978, pp. 1-75.
- [60] Hinton, E, *NAFEMS Introduction to Nonlinear Finite Element Analysis*, NAFEMS, Glasgow, Great Britain, 1992.
- [61] Hopkins, H. G., Discussion on the paper by L. R. G. Treloar, "The Mechanics of Rubber Elasticity," *Proceedings of the Royal Society of London*, A 351, 1976, pp. 322-328.
- [62] Hughes, T. J. R., *The Finite Element Method: Linear Static and Dynamic Finite Element Analysis*, Prentice-Hall Inc., New Jersey, 1987.
- [63] James, A. G., Green, A., Simpson, G. M., "Strain Energy functions of Rubber. I. Characterization of gum Vulcanizates," *Journal of Applied Polymer Science*, Vol. 19, 1975, pp. 2033-2058.
- [64] Johnson, K. L., *Contact Mechanics*, Cambridge University Press, Cambridge, 1989.

- [65] Jones, R. M., *Mechanics of Composite Materials*, McGraw-Hill, 1975.
- [66] Kalker, J. J., "Transient Phenomena in Two Elastic Cylinders Rolling Over Each Other With Dry Friction," *Journal of Applied Mechanics*, September, 1970, pp. 677-688.
- [67] Kalker, J. J., "A Minimum Principle for the Law of Dry Friction, With Application to Elastic Cylinders in Rolling Contact. Part 1: Fundamentals—Application to Steady Rolling," *Journal of Applied Mechanics*, December, 1971, pp. 875-880.
- [68] Kalker, J. J., "A Minimum Principle for the Law of Dry Friction. Part 2: Application to Nonsteady Rolling Elastic Cylinders," *Journal of Applied Mechanics*, December, 1971, pp. 881-887.
- [69] Kalker, J. J., "The Computation of Three-Dimensional Rolling Contact With Dry Friction," *International Journal For Numerical Methods in Engineering*, Vol. 14, October, 1978, pp. 1293-1307.
- [70] Keene, F., Personal Communication, work done in 1988, communicated to T. Diehl in 1991.
- [71] Kikuchi, N., Oden, J. T., *Contact Problems in Elasticity: A Study of Variational Inequalities and Finite Element Methods*, Siam, Philadelphia, 1988.
- [72] Lederman, J. M., "The Prediction of Tensile Properties of Flexible Foams," *Journal of Applied Polymer Science*, Vol. 15, 1971, pp. 693-703.
- [73] Li, G., "Large Strain Analysis of Rubbers by a Mixed Finite Element Method," *Ph. D. Thesis, University of Akron*, January, 1991.
- [74] Ling, Y., Engel, P. A., Brodsky, W. L., Yifan, G., "Finding the Constitutive Relation for a Specific Elastomer," *The American Society of Mechanical Engineers - Winter Annual Meeting*, November, 1992, 92-WA/EEP-22.
- [75] Mal, A. K., Singh, S. J., *Deformation of Elastic Solids*, Prentice Hall, New Jersey, 1991.
- [76] Malvern, L. E., *Introduction to the Mechanics of a Continuous Medium*, Prentice-Hall, New Jersey, 1969.
- [77] Martellock, A., Anderson, C., Unpublished Results, Eastman Kodak Company, May 24, 1988.
- [78] Martins, J. A. C., Oden, J. T., Simoes, F. M. F., "A Study of Static and Kinetic Friction," *International Journal of Engineering Science*, Vol. 28, No. 1, 1990, pp. 29-92.
- [79] Mooney, M., "A Theory of Large Elastic Deformation," *Journal of Applied Physics*, Vol. 11, September, 1940, pp. 582-592.
- [80] Morman, K. N., "An Adaptation of Finite Linear Viscoelasticity Theory for Rubber-Like Viscoelasticity by use of a Generalized Strain Measure," *Rheologica Acta*, Vol. 27, 1988, pp. 3-14.

- [81] *MSC/NASTRAN Quick Reference Guide: Version 67*, The MacNeal-Schwendler Corporation, 1992.
- [82] Nagtegaal, J. C., Taylor, L. M., “Comparison of Implicit and Explicit Finite Element Methods for Analysis of Sheet Forming Problems,” *VDI Berichte*, NR. 894, 1991, pp. 705-725.
- [83] Nobel, B., Daniel, J. W., *Applied Linear Algebra: Second Edition*, Prentice-Hall, 1977.
- [84] Oden, J. T., Bass, J. M., Lin, T. L., “A Finite Element Analysis of the General Rolling Contact Problem For Viscoelastic Rubber Cylinder,” *Tire Society, Fifth Annual Meeting and Conference on Tire Science and Technology*, 1986.
- [85] Oden, J. T., Lin, T. L., “On the General Rolling Contact Problem For Finite Deformations of a Viscoelastic Cylinder,” *Computer Methods in Applied Mechanics and Engineering*, 57, 1986, pp. 297-367.
- [86] Ogden, R. W., “Compressible Isotropic Elastic Solids Under Finite Strain-Constitutive Inequalities,” *The Quarterly Journal of Mechanical and Applied Mathematics*, Vol. 23, Pt. 4, 1970, pp. 11-22.
- [87] Ogden, R. W., “Large Deformation Isotropic Elasticity – On the Correlation of Theory and Experiment for Incompressible Rubberlike Solids,” *Proceedings of the Royal Society of London*, A 326, 1972, pp. 565-584.
- [88] Ogden, R. W., “Large Deformation Isotropic Elasticity – On the Correlation of Theory and Experiment for Compressible Rubberlike Solids,” *Proceedings of the Royal Society of London*, A 328, 1972, pp. 567-583.
- [89] Ogden, R. W., *Non-Linear Elastic Deformations*, John Wiley and Sons, New York, 1984.
- [90] Parish, G. J., “Measurements of Pressure Distribution Between Metal and Rubber Covered Rollers,” *British Journal of Applied Physics*, Vol. 9, April 1958, pp 158-161.
- [91] Parish, G. J., “Calculation of the Behaviour of Rubber-Covered Pressure Rollers,” *British Journal of Applied Physics*, Vol. 12, July 1961, pp 333-336.
- [92] Reynolds, O., “On Rolling Friction,” *Philosophical Transactions of the Royal Society of London*, Vol. 166 – Part 1, 1876, pp. 155-174.
- [93] Raous, M., “Numerical Methods in Mechanics of Contact Involving Friction,” *Journal of Theoretical and Applied Mechanics: Special Issue*, Supplement n°1 to Vol. 7, 1988.
- [94] Rivlin, R. S., “Large Elastic Deformations of Isotropic Materials: I. Fundamental Concepts,” *Philosophical Transactions of the Royal Society of London*, A240, 1948, pp. 459-490.

- [95] Rivlin, R. S., "Large Elastic Deformations of Isotropic Materials: II. Some Uniqueness Theorems For Pure, Homogeneous Deformation," *Philosophical Transactions of the Royal Society of London*, A240, 1948, pp. 491-508.
- [96] Rivlin, R. S., "Large Elastic Deformations of Isotropic Materials: III. Some Simple Problems in Cylindrical Polar Co-ordinates," *Philosophical Transactions of the Royal Society of London*, A240, 1948, pp. 509-525.
- [97] Rivlin, R. S., "Large Elastic Deformations of Isotropic Materials: IV. Further Developments of the General Theory," *Philosophical Transactions of the Royal Society of London*, A241, 1948, pp. 379-397.
- [98] Rivlin, R. S., Saunders, D. W., "Large Elastic Deformations of Isotropic Materials: VII. Experiments on the Deformation of Rubber," *Philosophical Transactions of the Royal Society of London*, A243, 1950, pp. 251-288.
- [99] Rivlin, R. S., Thomas, A. G., "Large Elastic Deformations of Isotropic Materials: VIII. Strain Distribution Around a Hole in a Sheet," *Philosophical Transactions of the Royal Society of London*, A243, 1950, pp. 289-298.
- [100] Saleeb, A. F., Chang, T. Y. P., Arnold, S. M., "On the Development of Explicit Robust Schemes for Implementation of a Class of Hyperelastic Models in Large-Strain Analysis of Rubbers," *International Journal for Numerical Methods in Engineering*, Vol. 33, 1992, pp. 1237-1249
- [101] Shames, I. H., Dym, C. L., *Energy and Finite Element Methods in Structural Mechanics*, Hemisphere Publishing corp., New York, 1985.
- [102] Soong, T. C., Li, C., "On the Unbonded Contact Between Plates and Layered Cylinders," *Journal of Applied Mechanics*, Vol. 47, December, 1980, pp. 841-846.
- [103] Soong, T. C., Li, C., "The Steady Rolling Contact of Two Elastic Layer Bonded Cylinders With a Sheet in the Nip," *International Journal of Mechanical Science*, Vol. 23, 1981, pp. 263-273.
- [104] Soong, T. C., Li, C., "The Rolling Contact of Two Elastic-Layered-Covered Cylinders Driving a Loaded Sheet in the Nip," *Journal of Applied Mechanics*, Vol. 48, December, 1981, pp. 889-894.
- [105] Spengos, A. C., "Experimental Investigation of Rolling Contact," *Journal of Applied Mechanics*, December 1965, pp 859-865.
- [106] Srinivasan, R., Perucchio, R., "Finite Element Analysis of Anisotropic Nonlinear Incompressible Elastic Solids By a Mixed Model," submitted for journal publication, 1993.
- [107] Stack, K. D., "A Nonlinear Finite Element Model of Axial Variation in Nip Mechanics With Applications to Conical Rollers," *Ph. D. Thesis, University of Rochester*, To be published.
- [108] Stack, K. D., Benson, R. C., "The Effects of Axial Variation in Nip Mechanics," *Proceedings of the Second International Conference on Advanced Mechatronics*, Meiji University, Tokyo, Japan, 1993.

- [109] Storakers, B., "On Material Representation and Constitutive Branching in Finite Compressible Elasticity," *Journal of the Mechanics and Physics of Solids*, Vol. 34, No. 2, 1986, pp. 125-145.
- [110] Tabor, D., "The Mechanism of Rolling Friction: I. The Elastic Range," *Proceedings of the Royal Society of London, A*, Vol. 229, 1955, pp. 198-220.
- [111] Timoshenko, S. P., Goodier, J. N., *Theory of Elasticity: Third Edition*, McGraw-Hill, 1987.
- [112] Treloar, L. R. G., *The Physics of Rubber Elasticity: Third Edition*, Clarendon Press, Oxford, 1975.
- [113] Treloar, L. R. G., "The Mechanics of Rubber Elasticity," *Proceedings of the Royal Society of London, A* 351, 1976, pp. 301-330.
- [114] Twizell, E. H., Ogden, R. W., "Non-Linear Optimization of the Material Constants in Ogden's Stress-Deformation Function for Incompressible Isotropic Elastic Materials," *Journal of the Australian Mathematical Society, B*, Vol 24, 1983, pp. 424-434.
- [115] Valanis, K. C., Landel, R. F., "The Strain-Energy Function of a Hyperelastic Material in Terms of Extension Ratios," *Journal of Applied Physics*, Vol. 38, No. 7, June, 1967, pp 2997-3002.
- [116] Ward, I. M., *Mechanical Properties of Solid Polymers: Second Edition*, John Wiley and Sons, New York, 1983.
- [117] Warren, W. E., Kraynik, A. M., "The Linear Elastic Properties of Open-Cell Foams," *Journal of Applied Mechanics*, June 1988, Vol. 55, pp. 341-346.
- [118] Wylie, C. R., Barrett, L. C., *Advanced Engineering Mathematics: Fifth Edition*, McGraw-Hill, 1982.
- [119] Zeman, R., Personal communication, Eastman Kodak Company, July, 1993.
- [120] Zeid, I., Padovan, J., "Finite Element Modeling of Rolling Contact," *Computers & Structures*, Vol. 14, No. 1-2, 1981, pp. 163-170.
- [121] Zeid, I., Padovan, J., "Cubic Isoparametric Rolling/Traveling Finite Elements," *Computers & Structures*, Vol. 15, No. 1, 1982, pp. 11-22.
- [122] Zienkiewicz, O. C., *The Finite Element Method, Third Edition*, McGraw-Hill, New York, 1977.

Appendix A

Large Deformation Mechanics

This appendix provides a concise overview of many equations used in large deformation mechanics. The equations listed are based on a Lagrangian (or material) description where all material behavior is described in terms of the initial particle coordinates.¹ Additional details on some of the following equations are found in [3,8,25,39,45,57,60,75,89].

In this Appendix Cartesian tensors are assumed. Vectors and first-order tensors are denoted as bold characters with a tilde underline ($\underline{\mathbf{n}}$). Matrices and second-order tensors are denoted as bold characters (\mathbf{F}). Components of these quantities are denoted with subscripts i and j which have ranges from 1 to 3.

A.1 Kinematics of Deformation in 1-D

In this section we introduce common measures of deformation used in nonlinear mechanics. Consider the 1-D bar in Figure A.1 . The deformation of the bar is quantified by the stretch ratio, λ , as

$$\lambda = \frac{l}{L} \quad (\text{A.1})$$

where l is the current (deformed) length and L is the original (undeformed) length. In an undeformed state ($l = L$), the stretch ratio equals unity. Since the current length must always be positive, the stretch ratio is always greater than zero;

$$\lambda > 0. \quad (\text{A.2})$$

A variety of strain measures, ε , can be defined as functions of the stretch ratio, λ ;

$$\varepsilon = f(\lambda). \quad (\text{A.3})$$

The function f can be very general provided that the following restrictions are satisfied:

1. In a Lagrangian viewpoint, a change of time implies the *same particle* is potentially at a different position. The particle is permanently labelled with its original coordinates.

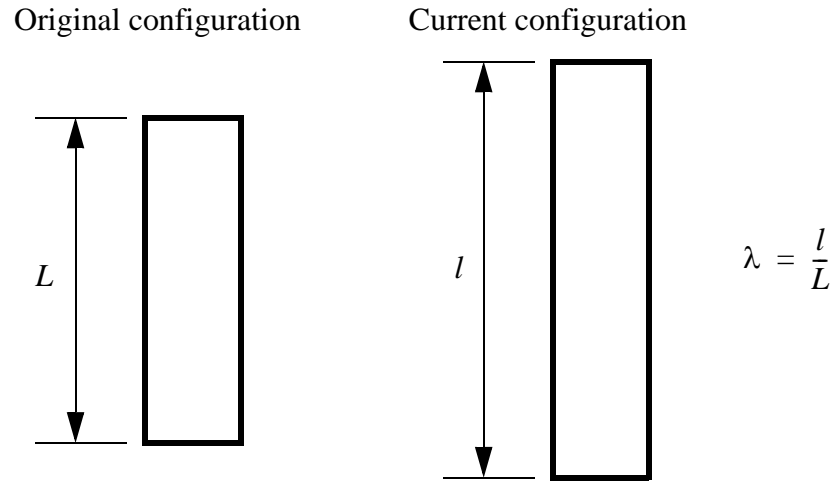


Figure A.1: One-dimensional stretching of a bar.

$$f(\lambda=1) = 0, \quad (\text{A.4})$$

$$\frac{df}{d\lambda} > 0, \text{ for all } \lambda > 0, \quad (\text{A.5})$$

$$\frac{df}{d\lambda}(\lambda=1) = 1. \quad (\text{A.6})$$

These restrictions are pictorially represented in Figure A.2. Equation A.4 ensures that in the undeformed state, the value of strain is zero. Equation A.5 states that there is a unique mapping between strain and stretch ratio. Equation A.6 requires that for very small length changes, the measure of strain reduces to the linear, small deformation form

$$\varepsilon^{\text{lin}} = \frac{\Delta L}{L} \quad (\text{A.7})$$

where $\Delta L = l - L$. Equation A.6 comes from a Taylor series expansion of Equation A.3. There are many measures of strain that meet these requirements. Some commonly used measures are:

$$\text{Biot's strain} \quad \varepsilon^{\text{b}} = \lambda - 1 \quad (\text{A.8})$$

$$\text{Logarithmic (true) strain} \quad \varepsilon^{\text{ln}} = \int_L^l \frac{d\hat{l}}{\hat{l}} = \ln \lambda \quad (\text{A.9})$$

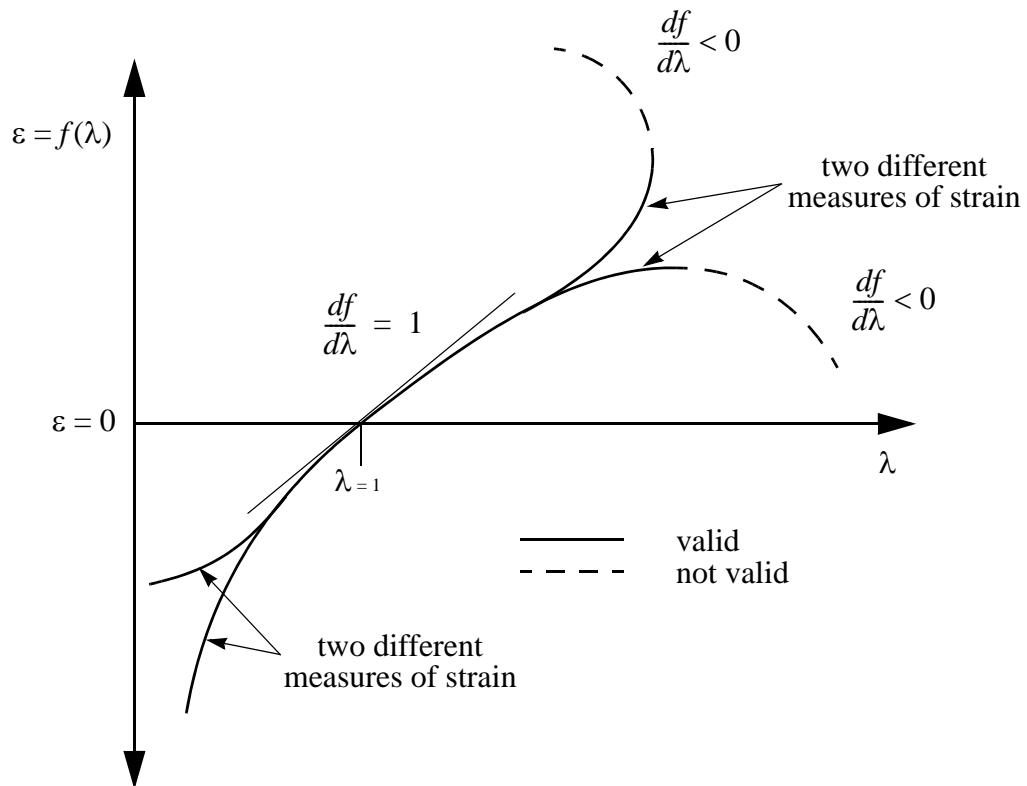


Figure A.2: Schematic of relationship between strain and stretch ratio.

$$\text{Green's strain} \quad \varepsilon^g = \frac{1}{2}(\lambda^2 - 1) \quad (\text{A.10})$$

$$\text{Almansi's strain} \quad \varepsilon^a = \frac{1}{2}(1 - \lambda^{-2}) \quad (\text{A.11})$$

Biot's strain is the traditional linear measure of strain. Logarithmic strain is the so-called "true" measure of strain. Green's strain is a computationally convenient measure that is often used in general 2-D and 3-D Lagrangian formulations (see next section). Almansi's strain is a similar measure to Green's strain, but used with Eulerian formulations. Figure A.3 compares the various strain measures for a 1-D domain.

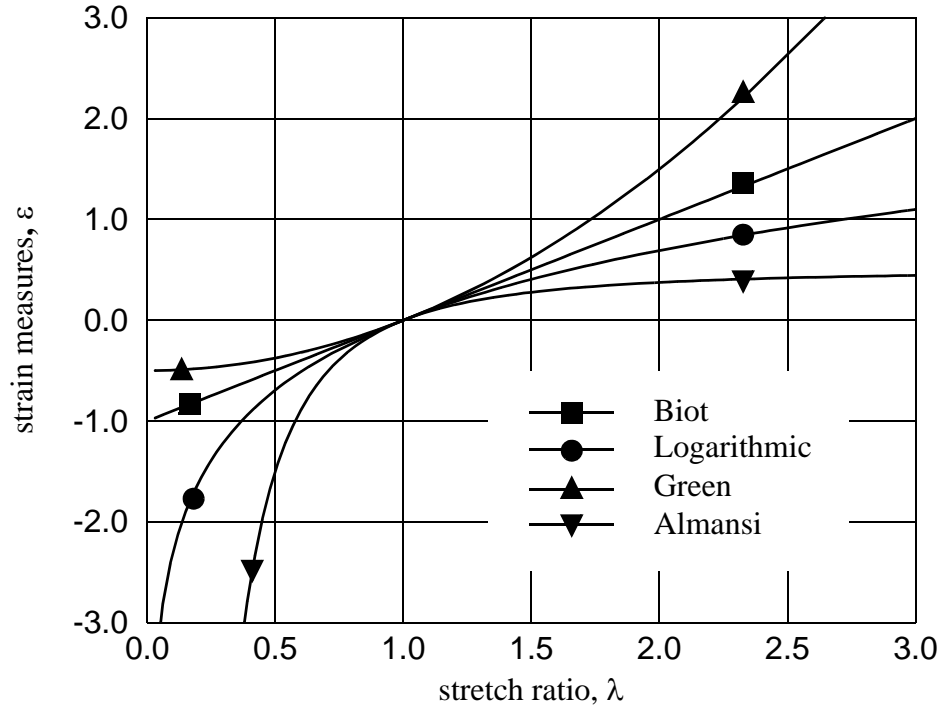


Figure A.3: Comparison of several strain measures

A.2 Kinematics of Deformation for General Motions

This section generalizes the concept of stretch ratio and strain for a three-dimensional continuum. Consider the body in Figure A.4. The body is depicted in two states: undeformed (original state) and deformed (current state). The spatial position vector of material particle P in the undeformed state is $\underline{\underline{X}}$. The spatial position vector of the same material particle P in the current state is $\underline{\underline{x}}$. The infinitesimal gauge length between particle P and a neighboring particle, Q, is $d\underline{\underline{X}}$ in the original state and $d\underline{\underline{x}}$ in the current state. In a Lagrangian description, all behavior is described in terms of the initial particle coordinates, $\underline{\underline{X}}$, at time $t = 0$;

$$\underline{\underline{x}} = \underline{\underline{x}}(\underline{\underline{X}}, t). \quad (\text{A.12})$$

Hence, the current spatial position vector of particle P is expressed as

$$\underline{\underline{x}} = \underline{\underline{X}} + \underline{\underline{u}}(\underline{\underline{X}}, t) \quad (\text{A.13})$$

where $\underline{\underline{u}}(\underline{\underline{X}}, t)$ is the displacement vector of particle P. From Equation A.12, we have

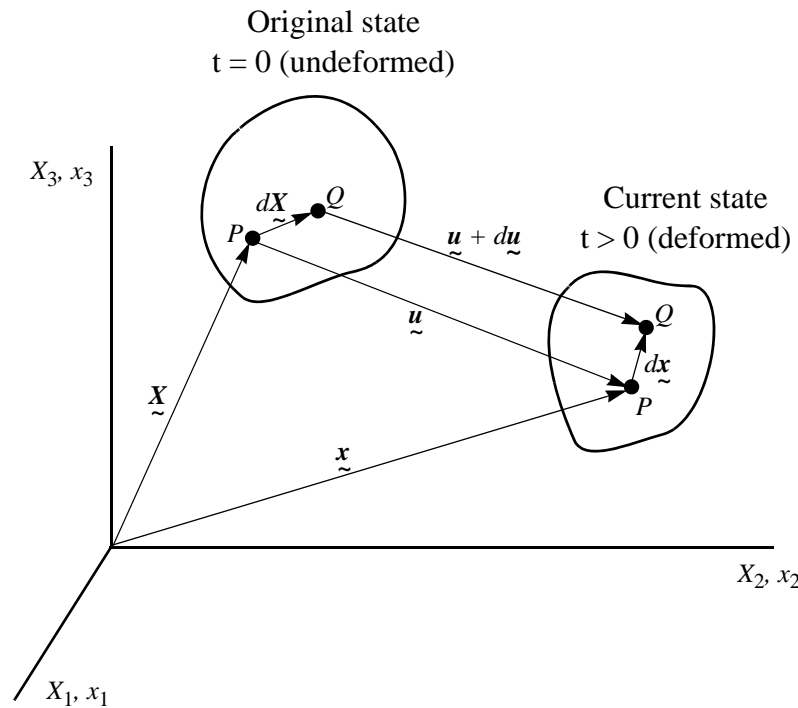


Figure A.4: Kinematics of deformation for general motions

$$d\tilde{\mathbf{x}} = \left[\frac{\partial \tilde{\mathbf{x}}}{\partial \tilde{\mathbf{X}}} \right] d\tilde{\mathbf{X}} = \mathbf{F} d\tilde{\mathbf{X}} \quad (\text{A.14})$$

where the deformation gradient tensor, \mathbf{F} , is defined as

$$\mathbf{F} = \left[\frac{\partial \tilde{\mathbf{x}}}{\partial \tilde{\mathbf{X}}} \right] = \begin{bmatrix} \frac{\partial x_1}{\partial X_1} & \frac{\partial x_1}{\partial X_2} & \frac{\partial x_1}{\partial X_3} \\ \frac{\partial x_2}{\partial X_1} & \frac{\partial x_2}{\partial X_2} & \frac{\partial x_2}{\partial X_3} \\ \frac{\partial x_3}{\partial X_1} & \frac{\partial x_3}{\partial X_2} & \frac{\partial x_3}{\partial X_3} \end{bmatrix}. \quad (\text{A.15})$$

The deformation gradient tensor, \mathbf{F} , contains both distortion (stretching) and rigid body rotation. Because \mathbf{F} contains rigid body rotation, it is generally not symmetric and cannot be diagonalized in general.

From the polar decomposition theorem, the total deformation can be defined as: 1) stretching followed by rigid body rotation or equivalently as 2) rigid body rotation followed by stretching.

$$\mathbf{F} = \mathbf{R} \mathbf{U} \quad \begin{array}{l} \text{stretch 1st,} \\ \text{then rotate} \end{array} \quad (\text{A.16})$$

$$\mathbf{F} = \mathbf{V} \mathbf{R} \quad \begin{array}{l} \text{rotate 1st,} \\ \text{then stretch} \end{array} \quad (\text{A.17})$$

\mathbf{U} is the right stretch tensor and it represents the stretch of a given material point in an *unrotated* configuration. \mathbf{V} is the left stretch tensor and it represents the stretch of a given material point in a *rotated* configuration. Both \mathbf{U} and \mathbf{V} are symmetric tensors that are related by the rigid body rotation matrix, \mathbf{R} ;

$$\mathbf{V} = \mathbf{R} \mathbf{U} \mathbf{R}^T. \quad (\text{A.18})$$

The rigid body rotation matrix is orthonormal.

$$\mathbf{R}^T = \mathbf{R}^{-1} \quad (\text{A.19})$$

Using the rigid body rotation matrix, \mathbf{R} , we have a general transformation between the unrotated configuration and the rotated configuration:

$${}^r\mathbf{A} = \mathbf{R} {}^u\mathbf{A} \mathbf{R}^T \quad \text{unrotated} \rightarrow \text{rotated} \quad (\text{A.20})$$

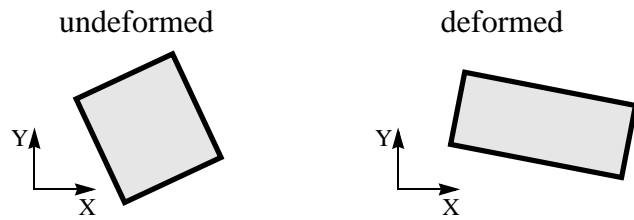
where ${}^u\mathbf{A}$ is any second order tensor (such as stretch, strain, stress, etc.) in the unrotated configuration and ${}^r\mathbf{A}$ is the same second order tensor *rotated* into the rotated configuration. Likewise we have

$${}^u\mathbf{A} = \mathbf{R}^T {}^r\mathbf{A} \mathbf{R} \quad \text{rotated} \rightarrow \text{unrotated} \quad (\text{A.21})$$

Figure A.5 demonstrates this difference between measures based on the unrotated and rotated configurations.

The three principal stretch ratios, $\lambda_1, \lambda_2, \lambda_3$, characterize the stretching of the body at a given material point and are equal to the principal values of \mathbf{U} and \mathbf{V} (both yield the same principal values). The three principal stretch ratios can also be calculated from the deformation gradient tensor by solving either of the following eigenvalue problems:

(a) Original and current configuration



(b) Deformation without rigid body rotation



$$\mathbf{U} = \begin{bmatrix} U_{11} & U_{12} & U_{13} \\ U_{12} & U_{22} & U_{23} \\ U_{13} & U_{23} & U_{33} \end{bmatrix} \quad \mathbf{A}^u = \begin{bmatrix} A_{11}^u & A_{12}^u & A_{13}^u \\ A_{12}^u & A_{22}^u & A_{23}^u \\ A_{13}^u & A_{23}^u & A_{33}^u \end{bmatrix} \quad \mathbf{V} = \begin{bmatrix} V_{11} & V_{12} & V_{13} \\ V_{12} & V_{22} & V_{23} \\ V_{13} & V_{23} & V_{33} \end{bmatrix} \quad \mathbf{A}^r = \begin{bmatrix} A_{11}^r & A_{12}^r & A_{13}^r \\ A_{12}^r & A_{22}^r & A_{23}^r \\ A_{13}^r & A_{23}^r & A_{33}^r \end{bmatrix}$$

Results

$$\begin{aligned}
 U_{ij} &= V_{ij} \\
 A_{ij}^u &= A_{ij}^r
 \end{aligned}$$

(c) Deformation with rigid body rotation



$$\mathbf{U} = \begin{bmatrix} U_{11} & U_{12} & U_{13} \\ U_{12} & U_{22} & U_{23} \\ U_{13} & U_{23} & U_{33} \end{bmatrix} \quad \mathbf{A}^u = \begin{bmatrix} A_{11}^u & A_{12}^u & A_{13}^u \\ A_{12}^u & A_{22}^u & A_{23}^u \\ A_{13}^u & A_{23}^u & A_{33}^u \end{bmatrix} \quad \mathbf{V} = \begin{bmatrix} V_{11} & V_{12} & V_{13} \\ V_{12} & V_{22} & V_{23} \\ V_{13} & V_{23} & V_{33} \end{bmatrix} \quad \mathbf{A}^r = \begin{bmatrix} A_{11}^r & A_{12}^r & A_{13}^r \\ A_{12}^r & A_{22}^r & A_{23}^r \\ A_{13}^r & A_{23}^r & A_{33}^r \end{bmatrix}$$

Results

$$\begin{aligned}
 U_{ij} &\neq V_{ij} \\
 A_{ij}^u &\neq A_{ij}^r
 \end{aligned}$$

Figure A.5: Influence of rigid body rotation on unrotated and rotated configuration measures.

$$(\mathbf{C} - \lambda^2 \mathbf{I})\underline{\mathbf{N}} = \mathbf{0} \quad (\text{A.22})$$

$$(\mathbf{B} - \lambda^2 \mathbf{I})\underline{\mathbf{n}} = \mathbf{0} \quad (\text{A.23})$$

where \mathbf{I} is the identity tensor. \mathbf{C} is the *right Cauchy-Green tensor* and \mathbf{B} is the *left Cauchy-Green tensor*, defined by

$$\mathbf{C} = \mathbf{F}^T \mathbf{F}, \quad (\text{A.24})$$

$$\mathbf{B} = \mathbf{F} \mathbf{F}^T. \quad (\text{A.25})$$

Tensors \mathbf{C} and \mathbf{B} are symmetric. Both Equation A.22 and A.23 yield the same three principal stretch ratios, $\lambda_1, \lambda_2, \lambda_3$. Equation A.22 also yields three orthogonal unit eigenvectors, $\underline{\mathbf{N}}_{\text{I}}, \underline{\mathbf{N}}_{\text{II}}, \underline{\mathbf{N}}_{\text{III}}$ which correspond to the three principal directions of stretch in the unrotated configuration.¹ The three orthogonal unit eigenvectors, $\underline{\mathbf{n}}_{\text{I}}, \underline{\mathbf{n}}_{\text{II}}, \underline{\mathbf{n}}_{\text{III}}$ from Equation A.23 represent the three principal directions of stretch in the rotated configuration. The eigenvectors of both configurations are related by the rigid body rotation matrix, \mathbf{R} , as

$$\begin{aligned} \underline{\mathbf{n}}_{\text{I}} &= \mathbf{R} \underline{\mathbf{N}}_{\text{I}} \\ \underline{\mathbf{n}}_{\text{II}} &= \mathbf{R} \underline{\mathbf{N}}_{\text{II}} \\ \underline{\mathbf{n}}_{\text{III}} &= \mathbf{R} \underline{\mathbf{N}}_{\text{III}} \end{aligned} \quad (\text{A.26})$$

The two sets of eigenvectors are also related by

$$\begin{aligned} \underline{\mathbf{n}}_{\text{I}} &= \frac{1}{\lambda_1} \mathbf{F} \underline{\mathbf{N}}_{\text{I}} \\ \underline{\mathbf{n}}_{\text{II}} &= \frac{1}{\lambda_2} \mathbf{F} \underline{\mathbf{N}}_{\text{II}} \\ \underline{\mathbf{n}}_{\text{III}} &= \frac{1}{\lambda_3} \mathbf{F} \underline{\mathbf{N}}_{\text{III}} \end{aligned} \quad (\text{A.27})$$

From the unit eigenvectors defined in Equations A.22 and A.23, two principal rotation matrices, \mathbf{l}^{N} and \mathbf{l}^{n} , can be defined which will rotate the unrotated and rotated configurations to the same principal coordinate system:

1. The subscripts I, II, III, on **bold** vectors indicate that there are three different vectors. *They do not refer to the vector components themselves.*

$$\boldsymbol{I}^N = \begin{bmatrix} \tilde{N}_{I_1} & \tilde{N}_{I_2} & \tilde{N}_{I_3} \\ \tilde{N}_{II_1} & \tilde{N}_{II_2} & \tilde{N}_{II_3} \\ \tilde{N}_{III_1} & \tilde{N}_{III_2} & \tilde{N}_{III_3} \end{bmatrix} \quad \begin{array}{l} \text{Rotate unrotated} \\ \text{configuration to} \\ \text{principal coordinate} \\ \text{system} \end{array} \quad (\text{A.28})$$

$$\boldsymbol{I}^n = \begin{bmatrix} \tilde{n}_{I_1} & \tilde{n}_{I_2} & \tilde{n}_{I_3} \\ \tilde{n}_{II_1} & \tilde{n}_{II_2} & \tilde{n}_{II_3} \\ \tilde{n}_{III_1} & \tilde{n}_{III_2} & \tilde{n}_{III_3} \end{bmatrix} \quad \begin{array}{l} \text{Rotate rotated} \\ \text{configuration to} \\ \text{principal coordinate} \\ \text{system} \end{array} \quad (\text{A.29})$$

where $\boldsymbol{I}^{N^T} = \boldsymbol{I}^{N^{-1}}$ and $\boldsymbol{I}^{n^T} = \boldsymbol{I}^{n^{-1}}$ (both \boldsymbol{I}^N and \boldsymbol{I}^n are orthonormal). From Equations A.22, A.23, A.28, and A.29, we find by tensor rotations that

$$\boldsymbol{I}^N \mathbf{C} \boldsymbol{I}^{N^T} = \boldsymbol{I}^n \mathbf{B} \boldsymbol{I}^{n^T} = \begin{bmatrix} \lambda_1^2 & 0 & 0 \\ 0 & \lambda_2^2 & 0 \\ 0 & 0 & \lambda_3^2 \end{bmatrix}. \quad (\text{A.30})$$

Both \mathbf{U} and \mathbf{V} can also be computed from the principal stretch ratios and eigenvectors of Equations A.22 and A.23 as

$$\mathbf{U} = \lambda_1 \tilde{N}_{I_1} \tilde{N}_{I_1}^T + \lambda_2 \tilde{N}_{II_1} \tilde{N}_{II_1}^T + \lambda_3 \tilde{N}_{III_1} \tilde{N}_{III_1}^T \quad (\text{A.31})$$

$$\mathbf{V} = \lambda_1 \tilde{n}_{I_1} \tilde{n}_{I_1}^T + \lambda_2 \tilde{n}_{II_1} \tilde{n}_{II_1}^T + \lambda_3 \tilde{n}_{III_1} \tilde{n}_{III_1}^T. \quad (\text{A.32})$$

Hence, knowing \mathbf{F} , we can compute \mathbf{U} and \mathbf{V} from Equations A.22, A.23, A.31, and A.32. Then we can use Equations A.16 or A.17 to find \mathbf{R} by either of the following equations:

$$\mathbf{R} = \mathbf{F} \mathbf{U}^{-1}, \quad (\text{A.33})$$

$$\mathbf{R} = \mathbf{V}^{-1} \mathbf{F}. \quad (\text{A.34})$$

The volume ratio, J , is computed from the deformation gradient tensor, \mathbf{F} , by

$$J = |\mathbf{F}| = \lambda_1 \lambda_2 \lambda_3. \quad (\text{A.35})$$

The volume ratio is the current volume, v , divided by the original volume, V . These volumes are for an infinitesimal volume of material located at a given material particle.

A.2.1 Common Measures of Strain for General Motions

The previous descriptions of 1-D strain (Equations A.8 - A.11) can be expanded into 3-D measures using generic forms of Equations A.31 and A.32. Generic strain tensors can be written as

$${}^u\boldsymbol{\varepsilon} = f(\lambda_1) \underline{\underline{N}}_I \underline{\underline{N}}_I^T + f(\lambda_2) \underline{\underline{N}}_{II} \underline{\underline{N}}_{II}^T + f(\lambda_3) \underline{\underline{N}}_{III} \underline{\underline{N}}_{III}^T , \quad (\text{A.36})$$

$${}^r\boldsymbol{\varepsilon} = f(\lambda_1) \underline{\underline{n}}_I \underline{\underline{n}}_I^T + f(\lambda_2) \underline{\underline{n}}_{II} \underline{\underline{n}}_{II}^T + f(\lambda_3) \underline{\underline{n}}_{III} \underline{\underline{n}}_{III}^T . \quad (\text{A.37})$$

where ${}^u\boldsymbol{\varepsilon}$ is the strain tensor in the unrotated configuration, ${}^r\boldsymbol{\varepsilon}$ is the strain tensor in the rotated configuration, and $\lambda_1, \lambda_2, \lambda_3$ are the three principal stretch ratios previously defined. The function f can be any measure of strain that satisfies Equations A.4 – A.6.

Defining strain in this manner is very general but also computationally expensive because principal values must be computed. Certain forms of strain can be computed directly from the deformation gradient tensor, \mathbf{F} . In particular, the tensorial version of Green's strain¹ (Equation A.10) can be shown to be

$${}^u\boldsymbol{\varepsilon}^g = \frac{1}{2}(\mathbf{F}^T \mathbf{F} - \mathbf{I}) = \frac{1}{2}(\mathbf{C} - \mathbf{I}) , \quad (\text{A.38})$$

$${}^r\boldsymbol{\varepsilon}^g = \frac{1}{2}(\mathbf{F} \mathbf{F}^T - \mathbf{I}) = \frac{1}{2}(\mathbf{B} - \mathbf{I}) . \quad (\text{A.39})$$

where the left-sided superscripts (u and r) have the same meaning as above.

The logarithmic measure of strain, which is easily computed using Equation A.9, A.36, and A.37, is sometimes written as

$${}^u\boldsymbol{\varepsilon}^{\ln} = \ln(\mathbf{U}) , \quad (\text{A.40})$$

$${}^r\boldsymbol{\varepsilon}^{\ln} = \ln(\mathbf{V}) . \quad (\text{A.41})$$

The Biot measure of strain, Equation A.8, can be expanded into 3-D using Equations A.36 and A.37. It can also be computed directly from the right and left stretch tensors as

1. Equation A.38 is typically referred to as Green's strain tensor in the literature. This definition is more commonly used than Equation A.39.

$${}^u \boldsymbol{\varepsilon}^b = \mathbf{U} - \mathbf{I}, \quad (\text{A.42})$$

$${}^r \boldsymbol{\varepsilon}^b = \mathbf{V} - \mathbf{I}. \quad (\text{A.43})$$

The Almansi measure of strain in 3-D is computed using Equations A.11, A.36 and A.37. It can also be calculated by

$${}^u \boldsymbol{\varepsilon}^a = \frac{1}{2}(\mathbf{I} - \mathbf{C}^{-1}), \quad (\text{A.44})$$

$${}^r \boldsymbol{\varepsilon}^a = \frac{1}{2}(\mathbf{I} - \mathbf{B}^{-1}). \quad (\text{A.45})$$

For problems with small strains but large rigid body rotations, Equations A.38 and A.39 provide efficient methods of computing strains. If the strains are small (all principal stretches are near unity) and rotations are small, then all strain measures are indistinguishable (see Equations A.6, A.26, A.36, and A.37). If strains are small but rotations are large, then all strain measures computed in the unrotated configuration, ${}^u \boldsymbol{\varepsilon}$, are indistinguishable and all strains computed in the rotated configuration, ${}^r \boldsymbol{\varepsilon}$, are indistinguishable (but components ${}^u \varepsilon_{ij}$ and ${}^r \varepsilon_{ij}$ are not the same).

If strains are large, then the use of Green, Biot, or Almansi strain, becomes less generally applicable.¹ In particular, when evaluating Poisson's ratio at finite strains, only the logarithmic measure of strain, Equation A.9 with Equations A.36 and A.37 (or Equations A.40 and A.41), provides physical results.²

All of the measures of strain defined depend solely on the deformation gradient tensor, \mathbf{F} , and any rigid body rotation, \mathbf{R} . These strain measures are path independent because they rely only on the original and current states.

1. It is recognized that Green and Almansi strain have been successfully used in many analyses of small strain and large rotation as well as analyses of large deformation hyperelastic material behavior throughout the literature.

2. This is easy to show using an uniaxial deformation ($\varepsilon_2 = \varepsilon_3 = -\nu \varepsilon_1$) with Poisson's ratio, ν , equal to 0.5. The volume ratio, J , should be computed as unity. This is only true if ε is the logarithmic measure.

A.2.2 Principal Measures of Strain

All of the measures of deformation and strain previously described are symmetric tensors with one notable exception: the deformation gradient tensor, \mathbf{F} . Principal values for any of the symmetric tensors can be computed by tensor rotation from either the unrotated or rotated configuration using the principal rotation matrices, \mathbf{I}^N and \mathbf{I}^n , defined in Equations A.28 and A.29. Computation of principal values by this method is rather expensive. Fortunately, easier methods are available.

The three principal values of any strain measure can be computed by evaluating its 1-D strain function (Equations A.8 - A.11) for each of the three principal stretch ratio's. For example, the three principal logarithmic strain values are computed as

$$\varepsilon_i^{\ln} = \ln(\lambda_i) . \quad (\text{A.46})$$

Similarly, the principal strain measures for Biot, Green, and Almansi strain are computed as

$$\varepsilon_i^{\text{b}} = \lambda_i - 1 , \quad (\text{A.47})$$

$$\varepsilon_i^{\text{g}} = \frac{1}{2}(\lambda_i^2 - 1) , \quad (\text{A.48})$$

$$\varepsilon_i^{\text{a}} = \frac{1}{2}(1 - \lambda_i^{-2}) . \quad (\text{A.49})$$

A.2.3 Stretch Invariants

In the analysis of nonlinear mechanics, the three invariants of a tensor are commonly required. The general equations for the invariants for any second-order tensor, \mathbf{A} , are

$$I_1(\mathbf{A}) = \mathbf{A}_{ii} , \quad (\text{A.50})$$

$$I_2(\mathbf{A}) = \frac{1}{2}(I_1(\mathbf{A})^2 - \mathbf{A}_{ij} \mathbf{A}_{ji}) , \quad (\text{A.51})$$

$$I_3(\mathbf{A}) = |\mathbf{A}| . \quad (\text{A.52})$$

Equations A.50 - A.52 are valid for both symmetric and nonsymmetric tensors. Furthermore, the results from Equations A.50 - A.52 are the same regardless of the configuration that tensor \mathbf{A} is computed from.

In the analysis of hyperelastic material laws, three invariants of the left Cauchy-Green tensor, \mathbf{B} , are commonly used. These invariants, called the *stretch invariants*, are functions of the three principal stretch ratios; namely

$$I_1 = \mathbf{B}_{ii} = \lambda_1^2 + \lambda_2^2 + \lambda_3^2, \quad (\text{A.53})$$

$$I_2 = \frac{1}{2}(I_1^2 - \mathbf{B}_{ij} \mathbf{B}_{ji}) = \lambda_1^2 \lambda_2^2 + \lambda_2^2 \lambda_3^2 + \lambda_1^2 \lambda_3^2, \quad (\text{A.54})$$

$$I_3 = |\mathbf{B}| = \lambda_1^2 \lambda_2^2 \lambda_3^2. \quad (\text{A.55})$$

The same invariants are found using the right Cauchy-Green tensor, \mathbf{C} , since both tensors (\mathbf{B} and \mathbf{C}) have the same principal values.¹ The third invariant, I_3 (Equation A.55), is related to the volume ratio, J , by

$$J = \sqrt{I_3}. \quad (\text{A.56})$$

For materials that are assumed to be incompressible, the volume does not change;

$$J = I_3 = 1 \quad (\text{incompressible assumption}) \quad (\text{A.57})$$

For this special case, the second stretch invariant (Equations A.54) reduces to

$$I_2 = \lambda_1^{-2} + \lambda_2^{-2} + \lambda_3^{-2} \quad (\text{incompressible assumption}) \quad (\text{A.58})$$

A.3 Measures of Stress

Similar to the many measures of strain that have been presented, there are many measures of stress. The Cauchy (true) stress tensor in the rotated configuration, ${}^r\boldsymbol{\sigma}$, is related to the surface traction vector, ${}^r\tilde{\mathbf{t}}$, in the rotated configuration by

$${}^r\tilde{\mathbf{t}} = {}^r\boldsymbol{\sigma}^T {}^r\tilde{\mathbf{n}} \quad (\text{A.59})$$

1. The principal values of \mathbf{B} and \mathbf{C} are $\lambda_1^2, \lambda_2^2, \lambda_3^2$.

where $\tilde{\mathbf{n}}^s$ is the unit outward surface normal in the rotated configuration on an infinitesimal volume at a given material particle. The surface traction, $\tilde{\mathbf{t}}^r$, represents the loads per unit current (deformed) surface area and acts in the direction of the rotated configuration. From moment equilibrium, we know that the Cauchy stress is symmetric

$$\tilde{\boldsymbol{\sigma}}^r = {}^r\boldsymbol{\sigma}^T \quad (\text{A.60})$$

and thus

$$\tilde{\mathbf{t}}^r = {}^r\boldsymbol{\sigma} \tilde{\mathbf{n}}^s. \quad (\text{A.61})$$

Typically in the literature, the Cauchy stress is simply denoted as $\boldsymbol{\sigma}$ where the rotated configuration is implied.

$$\boldsymbol{\sigma} = {}^r\boldsymbol{\sigma} \quad (\text{A.62})$$

Like the previous measures of deformation and strain, measures of stress can be presented in both unrotated and rotated configurations by use of Equations A.20 and A.21. The Cauchy stress in the unrotated configuration is

$${}^u\boldsymbol{\sigma} = \mathbf{R}^T {}^r\boldsymbol{\sigma} \mathbf{R}. \quad (\text{A.63})$$

Another common stress tensor is the Kirchhoff stress tensor, $\boldsymbol{\tau}$. This is commonly defined in the rotated configuration as

$$\boldsymbol{\tau} = {}^r\boldsymbol{\tau} = J {}^r\boldsymbol{\sigma}. \quad (\text{A.64})$$

The Kirchhoff stress tensor in the unrotated configuration is

$${}^u\boldsymbol{\tau} = \mathbf{R}^T {}^r\boldsymbol{\tau} \mathbf{R} = J {}^u\boldsymbol{\sigma}. \quad (\text{A.65})$$

The Piola-Kirchhoff stress tensor, \mathbf{T} , is related to the Cauchy and Kirchhoff stresses as

$$\mathbf{T} = J {}^r\boldsymbol{\sigma} \mathbf{F}^{-T} = J \mathbf{R} {}^u\boldsymbol{\sigma} \mathbf{U}^{-1} = {}^r\boldsymbol{\tau} \mathbf{F}^{-T} = \mathbf{R} {}^u\boldsymbol{\tau} \mathbf{U}^{-1} \quad (\text{A.66})$$

where \mathbf{F}^{-T} is the inverse of the transpose of \mathbf{F} . The first Piola-Kirchhoff stress tensor, \mathbf{T}^P , is the transpose of the Piola-Kirchhoff stress tensor, \mathbf{T} , and is related to the previous stresses by

$$\mathbf{T}^p = \mathbf{T}^T = J \mathbf{F}^{-1} {}^r \boldsymbol{\sigma} = J \mathbf{U}^{-1} {}^u \boldsymbol{\sigma} \mathbf{R}^T = \mathbf{F}^{-1} {}^r \boldsymbol{\tau} = J \mathbf{U}^{-1} {}^u \boldsymbol{\tau} \mathbf{R}^T. \quad (\text{A.67})$$

Both Piola-Kirchhoff stress tensors are, in general, nonsymmetric because \mathbf{F} contains rotation and may be nonsymmetric. Furthermore, they are *neither* in the unrotated or rotated configuration because they cannot be diagonalized due to their nonsymmetry.

The Piola-Kirchhoff and first Piola-Kirchhoff stress tensors are related to the *nominal* surface tractions as seen by the following equation:

$${}^r \underline{\boldsymbol{\tau}}^o = \mathbf{T} \underline{\mathbf{N}}^s = \mathbf{T}^p \underline{\mathbf{N}}^s \quad (\text{A.68})$$

where $\underline{\mathbf{N}}^s$ is the unit outward surface normal in the *unrotated* configuration and ${}^r \underline{\boldsymbol{\tau}}^o$ is the nominal surface traction (force per unit *original, undeformed*, surface area) directed in the *rotated* configuration (see [45, pp. 6.6] for a detailed derivation of this relationship). Thus, the Piola-Kirchhoff and first Piola-Kirchhoff stress tensors provide information about the nominal stresses (force per unit original area).

The second Piola-Kirchhoff stress tensor, \mathbf{S} , is a symmetric tensor and is related to the previous stress measures by

$${}^u \mathbf{S} = J \mathbf{F}^{-1} {}^r \boldsymbol{\sigma} \mathbf{F}^{-T} = J \mathbf{C}^{-1} {}^u \boldsymbol{\sigma} = \mathbf{F}^{-1} \mathbf{T}, \quad (\text{A.69})$$

$${}^r \mathbf{S} = J \mathbf{F}^{-T} \mathbf{F}^{-1} {}^r \boldsymbol{\sigma} = J \mathbf{B}^{-1} {}^r \boldsymbol{\sigma} = \mathbf{T} \mathbf{F}^{-1}. \quad (\text{A.70})$$

These two measures of stress are typically used with the Green strain tensors, Equation A.38 and A.39, respectively. The definition of second Piola-Kirchhoff stress given by the first part of Equation A.69 is generally used in the literature. The second Piola-Kirchhoff stress tensors are not physical and are therefore difficult to interpret in a general sense.¹

It is further noted that like all the previous strain measures, all the various stress measures presented are indistinguishable for small deformations and small rotations. For the case of

1. It is recognized that the second Piola-Kirchhoff stress tensor has been successfully used in many analyses of small strain and large rotation as well as analyses of large deformation hyperelastic material behavior throughout the literature.

small deformations and large rotations, all tensor components of the various stress measures computed in a given configuration are indistinguishable.

A.4 Using Conjugate Pairs to Compute Stresses from a Strain-Energy Density Function

For large-deformation elastic problems the relationship between stress and strain is typically based on a material strain-energy density function.¹ The strain-energy density is a scalar function that embodies information which characterizes how a material interrelates stresses and strains. When computing stresses from a strain-energy density function, W , the following equation is used:

$$\tau_{ij}^{\text{con}} = \frac{\partial W}{\partial \varepsilon_{ij}^{\text{con}}} \quad (\text{A.71})$$

where τ_{ij}^{con} and $\varepsilon_{ij}^{\text{con}}$ are any work-conjugate pair of stress and strain in a common configuration. We now develop some frequently used work conjugate pairs.

The concept of work conjugacy states that the work-rate per unit original volume (strain-energy density rate) should be the same for any conjugate pair of stress and strain. The work-rate per unit original volume, dW , is

$$dW = \tau_{ij}^{\text{con}} d\varepsilon_{ij}^{\text{con}}. \quad (\text{A.72})$$

The total strain energy density (strain energy per unit original volume) is

$$W = \int_{\varepsilon_{ij}^{\text{con}}{}^o}^{\varepsilon_{ij}^{\text{con}}{}^c} \tau_{ij}^{\text{con}} d\varepsilon_{ij}^{\text{con}} \quad (\text{A.73})$$

where $\varepsilon_{ij}^{\text{con}}{}^o$ and $\varepsilon_{ij}^{\text{con}}{}^c$ represent strain in the original and current state. The typical goal is to compute stresses given a particular strain-energy density, W . There are two general material categories for which strain-energy density functions are commonly defined: 1) compressible materials where the effective Poisson ratio is *not* near 0.5 (resilient foams

1. Often the term strain-energy density is shortened to strain-energy where density is implied. This is also sometimes called a strain-energy potential.

and foamed elastomers) and 2) nearly or fully incompressible materials where the effective Poisson ratio is very near or equal¹ to 0.5 (rubbers).

A.4.1 Compressible Materials

For the Ogden-Hill family of compressible-material strain-energy functions, W is written in terms of the principal stretch ratios $W(\lambda_1, \lambda_2, \lambda_3)$.² Following the basic form of Equation A.71, we compute the three principal *nominal* stresses, T_i^{nom} , as

$$T_i^{\text{nom}} = \frac{\partial W}{\partial \lambda_i}. \quad (\text{A.74})$$

It is important to note that the principal nominal stresses, T_i^{nom} , *are not* generally the principal values of the Piola-Kirchhoff stress tensor, \mathbf{T} . This is because \mathbf{T} is, in general, nonsymmetric and therefore cannot be diagonalized (has no principal values). Similarly, the principal stretch ratios, λ_i , *are not* generally the principal values of the deformation gradient tensor, \mathbf{F} . Only if there is no rigid body rotation will \mathbf{T} and \mathbf{F} be symmetric. In this special case, principal values of \mathbf{T} and \mathbf{F} can be obtained and will be equal to the principal values T_i^{nom} and λ_i , respectively.

The principal Cauchy stresses, σ_i , are computed as

$$\sigma_i = \frac{\lambda_i}{J} T_i^{\text{nom}} = \frac{\lambda_i}{J} \frac{\partial W}{\partial \lambda_i} \quad (\text{no sum on } i). \quad (\text{A.75})$$

The principal Kirchhoff stresses, τ_i , are related to the principal Cauchy stresses by the volume ratio, J , as

$$\tau_i = J \sigma_i = \lambda_i T_i^{\text{nom}} = \lambda_i \frac{\partial W}{\partial \lambda_i} \quad (\text{no sum on } i). \quad (\text{A.76})$$

Looking back at the principal logarithmic strain formula, Equation A.46, we note the following:

-
1. No real material is truly incompressible because that would imply an infinite wave speed.
 2. The equations that follow are valid for any strain-energy function, W . They are not limited to the Ogden-Hill family.

$$d\varepsilon_i^{\text{ln}} = d(\ln(\lambda_i)) = \frac{1}{\lambda_i} d\lambda_i \quad (\text{no sum on } i). \quad (\text{A.77})$$

Thus, the principal Kirchhoff stresses can also be computed as

$$\tau_i = \frac{\partial W}{\partial \varepsilon_i^{\text{ln}}}. \quad (\text{A.78})$$

The principal second Piola-Kirchhoff stresses, S_i , are found to be

$$S_i = J \frac{\sigma_i}{\lambda_i^2} = \frac{\tau_i}{\lambda_i^2} = \frac{T_i^{\text{nom}}}{\lambda_i} = \frac{1}{\lambda_i} \frac{\partial W}{\partial \lambda_i} \quad (\text{no sum on } i). \quad (\text{A.79})$$

Looking back at the principal Green strain formula, Equation A.48, we note the following:

$$d\varepsilon_i^{\text{g}} = d\left(\frac{1}{2}(\lambda_i^2 - 1)\right) = \lambda_i d\lambda_i \quad (\text{no sum on } i). \quad (\text{A.80})$$

Thus, the principal second Piola-Kirchhoff stresses can also be computed as

$$S_i = \frac{\partial W}{\partial \varepsilon_i^{\text{g}}}. \quad (\text{A.81})$$

Therefore, we have the following conjugate pairs in a principal coordinate system: $(T_i^{\text{nom}}, \lambda_i)$, $(\tau_i, \varepsilon_i^{\text{ln}})$, and $(S_i, \varepsilon_i^{\text{g}})$. By using the two principal rotation matrices, \mathbf{I}^{N} and \mathbf{I}^{n} (Equations A.28 and A.29), each of these principal measures can be rotated into the unrotated and rotated configurations. This yields the following conjugate pairs in the unrotated configuration: $({}^{\text{u}}\mathbf{T}^{\text{nom}}, \mathbf{U})$, $({}^{\text{u}}\boldsymbol{\tau}, {}^{\text{u}}\boldsymbol{\varepsilon}^{\text{ln}})$, and $({}^{\text{u}}\mathbf{S}, {}^{\text{u}}\boldsymbol{\varepsilon}^{\text{g}})$. In the rotated configuration we have: $({}^{\text{r}}\mathbf{T}^{\text{nom}}, \mathbf{V})$, $({}^{\text{r}}\boldsymbol{\tau}, {}^{\text{r}}\boldsymbol{\varepsilon}^{\text{ln}})$, and $({}^{\text{r}}\mathbf{S}, {}^{\text{r}}\boldsymbol{\varepsilon}^{\text{g}})$. One additional conjugate pair is (\mathbf{T}, \mathbf{F}) . As stated previously, \mathbf{T} and \mathbf{F} are generally nonsymmetric and are neither in the unrotated or rotated configuration. The symmetric nominal-stress tensor \mathbf{T}^{nom} is not commonly defined and is rarely used; the nonsymmetric Piola-Kirchhoff tensor, \mathbf{T} , is more commonly utilized.

A.4.1.1 Other formulae to calculate Cauchy stresses for compressible materials

The previous method described to compute stresses is easily performed if the principal stretch ratios and principal directions are known. A more general equation to compute the Cauchy stress tensor, ${}^r\boldsymbol{\sigma}$, is¹

$${}^r\boldsymbol{\sigma} = \frac{2}{J} \left[\left(\frac{\partial W}{\partial I_1} + I_1 \frac{\partial W}{\partial I_2} \right) \mathbf{B} - \frac{\partial W}{\partial I_2} (\mathbf{B}\mathbf{B}) \right] + \frac{\partial W}{\partial J} \mathbf{I} \quad (\text{A.82})$$

where \mathbf{I} is the identity tensor and the stretch invariants, I_1 , and I_2 , are defined in Equations A.53 and A.54. Equation A.82 can also be written in direct index notation as

$${}^r\sigma_{ij} = \frac{2}{J} \left[\left(\frac{\partial W}{\partial I_1} + I_1 \frac{\partial W}{\partial I_2} \right) B_{ij} - \frac{\partial W}{\partial I_2} (B_{ik} B_{kj}) \right] + \frac{\partial W}{\partial J} \delta_{ij} \quad (\text{A.83})$$

where the indices i, j , and k range from 1 to 3 and δ_{ij} is the Kronecker delta. Using the Cayley-Hamilton theorem², Equation A.82 can also be written as

$${}^r\boldsymbol{\sigma} = \frac{2}{J} \left(\frac{\partial W}{\partial I_1} \mathbf{B} - (J^2) \frac{\partial W}{\partial I_2} \mathbf{B}^{-1} \right) + \left(\frac{2I_2}{J} \frac{\partial W}{\partial I_2} \mathbf{I} + \frac{\partial W}{\partial J} \mathbf{I} \right). \quad (\text{A.84})$$

Equations A.82 - A.84 require the derivatives of the strain-energy function, W , with respect to the stretch invariants, I_1 and I_2 . For the Ogden-Hill family of strain-energy functions, these calculations become rather involved (see [51,73,100] for details).

A.4.2 Nearly and Fully Incompressible Materials

For nearly and fully incompressible materials, strain-energy functions are often written as separable functions of the deviatoric and volumetric deformations:³

$$W(\boldsymbol{\lambda}) = W^{\text{dev}}(\bar{\boldsymbol{\lambda}}) + W^{\text{vol}}(J) \quad (\text{A.85})$$

1. See [3,75] for a derivation of this basic form.

2. The Cayley-Hamilton theorem says that a matrix satisfies its own characteristic equation.

3. $W(\boldsymbol{\lambda})$ implies $W(\lambda_1, \lambda_2, \lambda_3)$ and $W(\bar{\boldsymbol{\lambda}})$ implies $W(\bar{\lambda}_1, \bar{\lambda}_2, \bar{\lambda}_3)$.

where the deviatoric principal stretch ratios, $\bar{\lambda}_i$, are defined as

$$\bar{\lambda}_i = J^{(-1/3)} \lambda_i. \quad (\text{A.86})$$

It is also common to separate second-order tensors into deviatoric and volumetric components. Consider a generic second-order tensor \mathbf{A} . This tensor can be written as the sum of a deviatoric tensor and a volumetric scalar:

$$\mathbf{A} = \text{DEV}(\mathbf{A}) + \frac{1}{3} A_{ii} \mathbf{I} = \bar{\mathbf{A}} + a^{\text{vol}} \mathbf{I} \quad (\text{A.87})$$

Following the same methodology used in Section A.4.1, we can compute the principal values of nominal stress as

$$\mathbf{T}_i^{\text{nom}} = \frac{\partial W(\lambda)}{\partial \lambda_i} = \frac{\partial W^{\text{dev}}(\bar{\lambda})}{\partial \lambda_i} + \frac{\partial W^{\text{vol}}(J)}{\partial \lambda_i}. \quad (\text{A.88})$$

Noting that the partial derivative of J with respect to λ_i is

$$\frac{\partial J}{\partial \lambda_i} = \frac{J}{\lambda_i}, \quad (\text{A.89})$$

we find from the chain rule that

$$\mathbf{T}_i^{\text{nom}} = \frac{\partial W^{\text{dev}}(\bar{\lambda})}{\partial \lambda_i} + \frac{J}{\lambda_i} \frac{\partial W^{\text{vol}}(J)}{\partial J}. \quad (\text{A.90})$$

From Equation A.75 we can compute the principal Cauchy stresses as

$$\sigma_i = \frac{\lambda_i}{J} \mathbf{T}_i^{\text{nom}} = \underbrace{\frac{\lambda_i}{J} \frac{\partial W^{\text{dev}}(\bar{\lambda})}{\partial \lambda_i}}_{\text{Deviatoric}} + \underbrace{\frac{\partial W^{\text{vol}}(J)}{\partial J}}_{\text{Volumetric}} \quad (\text{no sum on } i). \quad (\text{A.91})$$

For a material which has any compressibility (*nearly* incompressible), the hydrostatic pressure, p , is computed from the local deformation as¹

1. The hydrostatic pressure is equal to the *negative* of the volumetric part of the stress tensor defined in Equation A.87.

$$p = \frac{-\partial W^{\text{vol}}(J)}{\partial J}. \quad (\text{A.92})$$

For a *fully* incompressible material, the hydrostatic pressure, p , is undetermined by the local deformation.¹

From Equation A.91 we see that the deviatoric principal Cauchy stresses are

$$\bar{\sigma}_i = \frac{\lambda_i}{J} \frac{\partial W^{\text{dev}}(\bar{\lambda})}{\partial \lambda_i} \quad (\text{no sum on } i). \quad (\text{A.93})$$

Thus, the complete (deviatoric plus hydrostatic) principal Cauchy stresses, σ_i , are

$$\sigma_i = \bar{\sigma}_i - p. \quad (\text{A.94})$$

The principal Kirchhoff stresses and principal second Piola-Kirchhoff stresses are computed from the principal Cauchy stresses (Equation A.94) as described previously:

$$\tau_i = J \sigma_i, \quad (\text{A.95})$$

$$S_i = J \frac{\sigma_i}{\lambda_i^2} = \frac{\tau_i}{\lambda_i^2} \quad (\text{no sum on } i). \quad (\text{A.96})$$

In the previous equations, the partial derivatives of $\bar{\lambda}$ with respect to λ are required. From Equation A.86 we find

$$\frac{\partial \bar{\lambda}_i}{\partial \lambda_j} = \frac{J^{(-1/3)}}{3} \begin{bmatrix} 2 & \frac{-\lambda_1^2 \lambda_3}{J} & \frac{-\lambda_1^2 \lambda_2}{J} \\ \frac{-\lambda_2^2 \lambda_3}{J} & 2 & \frac{-\lambda_1 \lambda_2^2}{J} \\ \frac{-\lambda_2 \lambda_3^2}{J} & \frac{-\lambda_1 \lambda_3^2}{J} & 2 \end{bmatrix}. \quad (\text{A.97})$$

1. For fully incompressible materials, ABAQUS/Standard uses a modified form of the volumetric portion of the strain-energy function. This portion of W is augmented with a volumetric constraint imposed by a Lagrange multiplier representing the pressure. See [51] for more details.

By using the two principal rotation matrices, I^N and I^n (Equations A.28 and A.29), each of principal stress measures previously described can be rotated into the unrotated and rotated configurations.

A.4.2.1 Other formulae to calculate Cauchy stresses for nearly and fully incompressible materials

The previous method described to compute stresses is easily performed if the principal stretch ratios and principal directions are known. A more general equation to compute the deviatoric Cauchy stress tensor in the rotated configuration, ${}^r\bar{\boldsymbol{\sigma}}$, is¹

$${}^r\bar{\boldsymbol{\sigma}} = \frac{2}{J} \text{DEV} \left[\left(\frac{\partial W}{\partial I_1} + \bar{I}_1 \frac{\partial W}{\partial I_2} \right) \bar{\mathbf{B}} - \frac{\partial W}{\partial I_2} (\bar{\mathbf{B}} \bar{\mathbf{B}}) \right] \quad (\text{A.98})$$

where \bar{I}_1 and \bar{I}_2 are the first and second *deviatoric* stretch invariants defined as

$$\bar{I}_1 = \bar{\lambda}_1^2 + \bar{\lambda}_2^2 + \bar{\lambda}_3^2, \quad (\text{A.99})$$

$$\bar{I}_2 = \bar{\lambda}_1^2 \bar{\lambda}_2^2 + \bar{\lambda}_2^2 \bar{\lambda}_3^2 + \bar{\lambda}_1^2 \bar{\lambda}_3^2. \quad (\text{A.100})$$

$\bar{\mathbf{B}}$ is the *deviatoric* left Cauchy-Green tensor defined by

$$\bar{\mathbf{B}} = \bar{\mathbf{F}} \bar{\mathbf{F}}^T. \quad (\text{A.101})$$

The modified deformation gradient, $\bar{\mathbf{F}}$, is the total deformation gradient, \mathbf{F} , with the volume change removed; namely

$$\bar{\mathbf{F}} = J^{(-1/3)} \mathbf{F}. \quad (\text{A.102})$$

The complete Cauchy stress tensor in the rotated configuration, ${}^r\boldsymbol{\sigma}$, is found as

$${}^r\boldsymbol{\sigma} = {}^r\bar{\boldsymbol{\sigma}} - p. \quad (\text{A.103})$$

where p is the hydrostatic pressure previously defined in this section. It should be noted that the hydrostatic pressure, p , is an invariant and is the same regardless of configuration (compare Equations A.50 and A.87).

1. DEV means “take the deviatoric part of” the tensor. See Equation A.87.

Appendix B

Comparison of Implicit and Explicit Finite Element Methods

This appendix provides relevant discussion of the two finite element methods used in this thesis: the implicit static method (Standard) and the explicit dynamic method (Explicit).

B.1 Standard Algorithm: Implicit, Static

The purpose of this section is to supply a relatively detailed derivation of the general equations used in nonlinear Lagrangian-based implicit finite element methods. The equations in this section are based on a combination of the following sources [6,24,25,45,56,51,55,60,62,101,122]. In particular [25,45,51,55,60] provide the best overview of the equations for the implicit finite element method. In order to provide detailed equations, index notation and Cartesian tensors are used.

The following derivation is developed using the concept of virtual displacements. The derivation can also be developed in a rate form, based on virtual velocities. The rate-form derivation is found in [45,51].

All quantities in this section, such as stress, surface traction vectors, and surface normals, are based on the rotated configuration in the deformed state. For ease of reading, the left-side superscript that is used to denote this fact is omitted here. In the later portion of this appendix, a left-side superscript is used instead to denote the iteration.

The translational static equilibrium equations are

$$\frac{\partial \sigma_{ji}}{\partial x_j} + b_i = 0 \quad \begin{array}{l} i = 1..3 \\ j = 1..3 \end{array} \quad (\text{B.1})$$

where σ_{ij} is the Cauchy stress tensor, x_i is the current (deformed) coordinate location, and b_i denotes body forces. The subscripts i and j denote the three Cartesian directions

(x, y, z). The Cauchy stress is related to the surface traction vector t_i in the deformed state by

$$t_i = \sigma_{ji}n_j \quad (\text{B.2})$$

where n_i is the unit outward surface normal on the deformed body. Evaluation of moment equilibrium shows that the Cauchy stress matrix is symmetric.

$$\sigma_{ij} = \sigma_{ji} \quad (\text{B.3})$$

Using this fact, Equation B.1 and Equation B.2 are rewritten as

$$\frac{\partial \sigma_{ij}}{\partial x_j} + b_i = 0, \quad (\text{B.4})$$

$$t_i = \sigma_{ij}n_j. \quad (\text{B.5})$$

Equation B.4 is the *strong* form of equilibrium and must be satisfied at every point in the body. In finite element analysis we relax the equilibrium equations by using a scalar equation governing the entire body. Using virtual displacements, we obtain the *weak* form of equilibrium

$$\int_v \left(\frac{\partial \sigma_{ij}}{\partial x_j} + b_i \right) \delta u_i dv = 0 \quad (\text{B.6})$$

where δu_i is an arbitrary virtual displacement that satisfies all kinematic constraints (such as boundary conditions) and v denotes the current (deformed) volume. Equation B.6 represents the virtual work for the system. Equilibrium in this equation is only satisfied in an average sense. Using the chain rule, Gauss' divergence theorem, and Equation B.5, we arrive at the principle of virtual work:

$$\int_v \sigma_{ij} \frac{\partial \delta u_i}{\partial x_j} dv = \int_s t_i \delta u_i ds + \int_v b_i \delta u_i dv \quad (\text{B.7})$$

virtual work done by internal forces	virtual work done by surface tractions	virtual work done by body forces
--	--	--

where s is the deformed surface.

Equation B.7 is a scalar equation governing the entire body. For finite elements, general field variables such as displacements are interpolated by shape functions from nodal variables over discrete elements. For the next portion of equation development, we assume that the body in question is *one* finite element. Hence, all equations developed are elemental in nature.

The mapping of a given element's nodal displacements to the general displacement field is written as

$$u_i = \sum_{n=1}^{N^{\text{el}}} {}_n\Psi {}_n\tilde{u}_i = {}_n\Psi {}_n\tilde{u}_i \quad (\text{B.8})$$

where N^{el} is the number of nodes in the element, ${}_n\Psi$ are the shape functions, and ${}_n\tilde{u}_i$ are the discrete nodal displacements (the \sim denoting a nodal quantity). The left-sided subscripts of a variable denote nodal counters and the usual Einstein summation convention is applied to these subscripts.¹ The same form of Equation B.8 applies to the mapping of original coordinate vectors, X_i , and to the deformed coordinate vectors, x_i . The first variation of u_i , namely δu_i , is mapped as

$$\delta u_i = {}_n\Psi \delta {}_n\tilde{u}_i \quad (\text{B.9})$$

and its partial derivative with respect to current location as

$$\frac{\partial \delta u_i}{\partial x_j} = \delta {}_n\tilde{u}_i \frac{\partial {}_n\Psi}{\partial x_j} = \delta {}_n\tilde{u}_i {}_nB_j \quad (\text{B.10})$$

where the gradient operator, ${}_nB_j$, is defined as

$${}_nB_j = \frac{\partial {}_n\Psi}{\partial x_j}. \quad (\text{B.11})$$

1. The right-sided subscripts still denote Cartesian directions. Note: unlike Cartesian coordinates that have a range from 1 to 3, the nodal indices, n , have a range from 1 to N^{el} where N^{el} may be greater than 3.

Substituting Equations B.9 and B.10 into Equation B.7 and rearranging yields the scalar equation

$$\delta_n \tilde{u}_i \left[\int_v {}_n B_j \sigma_{ij} dv - \left(\int_s {}_n \Psi t_i ds + \int_v {}_n \Psi b_i dv \right) \right] = 0 . \quad (\text{B.12})$$

Equation B.12 actually represents N^{el} scalar equations. Since $\delta_n \tilde{u}_i$ are independent virtual displacements of arbitrary value (provided that they satisfy kinematic constraints), we can, for any equation n , select one to be nonzero and all others to be exactly zero. Repeating this for all nodes yields a system of N^{el} vector equilibrium equations

$$\underbrace{\int_v {}_n B_j \sigma_{ij} dv}_{\tilde{f}_i^{\text{int}}} - \underbrace{\left(\int_s {}_n \Psi t_i ds + \int_v {}_n \Psi b_i dv \right)}_{\tilde{f}_i^{\text{ext}}} = 0 \quad (\text{B.13})$$

that can be represented as

$$\tilde{f}_i^{\text{int}} - \tilde{f}_i^{\text{ext}} = 0 . \quad (\text{B.14})$$

This discrete form of equilibrium represents a balance of internal (f^{int}) and external (f^{ext}) forces for a given element. Equation B.14 represents $3N^{\text{el}}$ equations (i ranges 1 to 3 and n ranges 1 to N^{el}). The complete solution of the entire body entails the assembly of all the elemental quantities (by summing all the integral equations for each element) into a global system in the usual way (see [6,24,62,122]).

The form of Equation B.13 is very general; no specific limitations have been imposed on the relationship between stress and strain or between strain and deformation. This equation might look somewhat unfamiliar compared with typical linear finite element equations. In linear finite elements, the equations of static equilibrium for an element, written in matrix notation, are represented as

$$[K^{\text{elem}}] \{ \tilde{u} \} = \{ \tilde{f}^{\text{ext}} \} \quad (\text{B.15})$$

where $\{ \tilde{u} \}$ are the nodal displacements, $\{ \tilde{f}^{\text{ext}} \}$ are the external forces, and the stiffness matrix for an element, $[K^{\text{elem}}]$, is defined as

$$[K^{\text{elem}}] = \int_V [B_0]^T [E] [B_0] dV \quad . \quad (\text{B.16})$$

The matrix $[B_0]$ is the linear version of the gradient operator defined in Equation B.11 and $[E]$ is the material elasticity matrix. For linear theory it has been assumed that Hooke's law relating stress to strain is valid

$$\sigma = E\varepsilon \quad \rightarrow \quad [\sigma] = [E][\varepsilon] = [E][B_0]\{\tilde{u}\} \quad . \quad (\text{B.17})$$

It is also assumed that the deformation is small enough such that equilibrium can be taken about the original undeformed configuration (V denotes original volume) and that all measures of stress, σ , and strain, ε , are equivalent, respectively. Comparing Equations B.15 - B.17 to Equation B.13, we see that the element stiffness times the nodal displacements yields the internal forces. Hence, Equations B.15 - B.17 are restricted forms of the equilibrium equation B.13.

Equations B.13 and B.14 allow for the consideration of geometrical and material nonlinearities which are required for the solutions to nonlinear nlp mechanics problems. Because the equilibrium equations are nonlinear, the Newton-Raphson method is used for solution. This method requires the development of a Jacobian matrix (tangent stiffness matrix plus a load stiffness matrix).

To develop the Newton-Raphson method we generalize the static equilibrium equation for a given element, Equation B.14, as

$${}_n\tilde{F}_i({}_m\tilde{u}_h) = \tilde{f}_i^{\text{int}} - \tilde{f}_i^{\text{ext}} = 0 \quad \begin{array}{ll} m = 1..N^{\text{el}} & n = 1..N^{\text{el}} \\ h = 1..3 & i = 1..3 \end{array} \quad (\text{B.18})$$

where \tilde{F} denotes a general nonlinear function of nodal displacements. This function can be generalized to other degrees of freedom besides displacements; such a resultant rotations (used in beams, shells, and certain forms of rotational constraints). Since the equations are nonlinear, iteration is expected. After some iteration, ι , we have an approximation, ${}^{\iota}\tilde{u}_h$, to the actual solution. The error in our approximation is ${}^{\iota+1}\tilde{c}_h$ (also termed the *displacement correction*). In terms of the approximate solution and its correction, equilibrium is written as

$${}_n\tilde{F}_i({}_m^l\tilde{u}_h + {}_m^{l+1}\tilde{c}_h) = 0 . \quad (\text{B.19})$$

Expanding by a Taylor series yields

$${}_n\tilde{F}_i({}_m^l\tilde{u}_h) + \frac{\partial_n\tilde{F}_i({}_m^l\tilde{u}_h)}{\partial_p\tilde{u}_j} {}_p^{l+1}\tilde{c}_j + \frac{1}{2!} \frac{\partial_n\tilde{F}_i({}_m^l\tilde{u}_h)}{\partial_p\tilde{u}_j \partial_q\tilde{u}_k} {}_p^{l+1}\tilde{c}_j {}_q^{l+1}\tilde{c}_k + \text{H.O.T.} = 0 \quad (\text{B.20})$$

where the indices have the following ranges

$$\begin{aligned} m &= 1..N^{\text{el}} & n &= 1..N^{\text{el}} & p &= 1..N^{\text{el}} & q &= 1..N^{\text{el}} \\ h &= 1..3 & i &= 1..3 & j &= 1..3 & k &= 1..3 \end{aligned} \quad (\text{B.21})$$

Assuming ${}_m^l\tilde{u}_h$ to be a good approximation to the solution, the correction ${}_m^{l+1}\tilde{c}_h$ will be small relative to ${}_m^r\tilde{u}_h$ and all terms that are quadratic and above can be neglected. Hence

$${}_{np}^l K_{ij} {}_p^{l+1}\tilde{c}_j \approx -{}_n\tilde{F}_i({}_m^l\tilde{u}_h) \quad (\text{B.22})$$

where the element Jacobian matrix is defined as

$${}_{np}^l K_{ij} = \frac{\partial_n\tilde{F}_i({}_m^l\tilde{u}_h)}{\partial_p\tilde{u}_j} \quad (\text{B.23})$$

and the next approximation to the correct solution is

$${}_m^{l+1}\tilde{u}_h = {}_m^l\tilde{u}_h + {}_m^{l+1}\tilde{c}_h . \quad (\text{B.24})$$

Equation B.22 represents the elemental version of the Newton-Raphson equations. These elemental equations are assembled into a global system in the same manor as would be used for Equation B.14. For solution to the nonlinear finite element problem, the global version of Equation B.22 is solved by inverting the global Jacobian matrix to find the solution corrections, ${}_m^{l+1}\tilde{c}_h$. This is repeatedly solved until the displacement corrections are driven sufficiently close to zero. When the corrections are driven to zero, the general function \tilde{F} , which measures the *residual* forces (non-equilibrium), is also driven to zero.

In the ABAQUS/Standard solution algorithms, the default convergence determination is based on residual forces, displacement corrections, and any constraints relationships

imposed. When the absolute values of all residual forces are less than 1/2% of the average nodal force value for the entire system, the largest displacement correction is less than 2% of the largest displacement increment, and all the constraints are satisfied, then equilibrium is considered satisfied and the solution is converged. Further detail on these convergence criteria can be found in [49].

From Equations B.18 and B.23 we see that the Jacobian matrix is

$${}_{np}K_{ij} = \frac{\partial_n \tilde{F}_i({}_m\tilde{u}_h)}{\partial_p \tilde{u}_j} = \frac{\partial_n \tilde{f}_i^{\text{int}}}{\partial_p \tilde{u}_j} - \frac{\partial_n \tilde{f}_i^{\text{ext}}}{\partial_p \tilde{u}_j}. \quad (\text{B.25})$$

The displacement gradient of the internal forces is called the *tangent stiffness* and the displacement gradient of the external forces is termed the *load stiffness*. Substituting Equation B.13 into Equation B.25, the tangent stiffness is written as

$$\frac{\partial_n \tilde{f}_i^{\text{int}}}{\partial_p \tilde{u}_k} = \frac{\partial}{\partial_p \tilde{u}_k} \left[\int_V {}_nB_j \sigma_{ij} dv \right] = \frac{\partial}{\partial_p \tilde{u}_k} \left[\int_V {}_nB_j \sigma_{ij} J dV \right] \quad (\text{B.26})$$

where J , typically called the Jacobian, is the ratio of the deformed volume to the undeformed volume. To avoid problems with index notation, the dummy index j in Equation B.25 has been replaced by the dummy index k in Equation B.26 (both indices have the same range). Applying the chain rule yields

$$\frac{\partial_n \tilde{f}_i^{\text{int}}}{\partial_p \tilde{u}_k} = \underbrace{\left[\int_V \frac{\partial_n B_j}{\partial_p \tilde{u}_k} \tau_{ij} dV \right]}_{\text{geometric stiffness}} + \underbrace{\left[\int_V {}_nB_j \frac{\partial \tau_{ij}}{\partial_p \tilde{u}_k} dV \right]}_{\text{small displacement stiffness}} \quad (\text{B.27})$$

where the Kirchhoff stress tensor, τ_{ij} , is defined as

$$\tau_{ij} = \sigma_{ij} J. \quad (\text{B.28})$$

Similar evaluation of the load stiffness quantity yields

$$\frac{\partial_n \tilde{f}_i^{\text{ext}}}{\partial_p \tilde{u}_k} = \frac{\partial}{\partial_p \tilde{u}_k} \left[\int_n \Psi t_i ds + \int_v \Psi b_i dv \right]. \quad (\text{B.29})$$

B.2 Explicit Algorithm: Central-Difference, Dynamic

The purpose of this section is to supply a relatively detailed discussion of the general equations used in nonlinear Lagrangian-based explicit finite element methods. The equations in this section are based on a combination of the following sources [24,32,33,47,53,62,82,122]. In particular [24,47,53] provide the best overview of the equations.

The explicit dynamics algorithm is rather simple to describe because it uses explicit (direct) time integration and does not require a Jacobian stiffness matrix (tangent stiffness plus load stiffness matrices). The equilibrium equations for the explicit approach will be discussed at a global system level; as apposed to the more complicated implicit equations of Section B.1 which were primarily developed for one element. Furthermore, quantities such as displacement, velocity, acceleration, internal forces, and external forces will all be nodal variables. To limit notational book-keeping, the tilde symbol (\sim) located above all nodal values is deleted. A left-side superscript denotes the time increment. Lastly, matrix notation is used for ease of reading.¹

The explicit method uses a dynamic equilibrium statement of the form

$$\mathbf{M} \tilde{\ddot{\mathbf{u}}} = \tilde{\mathbf{f}}^{\text{ext}} - \tilde{\mathbf{f}}^{\text{int}} \quad (\text{B.30})$$

where \mathbf{M} is a diagonal (lumped) mass matrix, $\tilde{\ddot{\mathbf{u}}}$ is the nodal acceleration vector, $\tilde{\mathbf{f}}^{\text{ext}}$ is the vector of externally applied nodal loads, $\tilde{\mathbf{f}}^{\text{int}}$ is the vector of internal nodal forces, and τ denotes the time. The length of each of the vectors in Equation B.30 equals the total degrees of freedom in the model. The internal forces, $\tilde{\mathbf{f}}^{\text{int}}$, are the nodal contributions of

1. A **bolded** variable with a (\sim) below it means that the variable represents a vector. A **bolded** variable *without* a (\sim) below it means that the variable represents a matrix. Also, the use of index notation in this thesis is only used when value is added. The extensive use of index notation in Section B.1 was required for a thorough discussion of the Jacobian stiffness matrix.

the internal forces from Equation B.13. The nodal accelerations at the beginning of a given time increment, ι , are

$${}^{\iota}\tilde{\mathbf{u}} = \mathbf{M}^{-1} ({}^{\iota}\tilde{\mathbf{f}}^{\text{ext}} - {}^{\iota}\tilde{\mathbf{f}}^{\text{int}}). \quad (\text{B.31})$$

Since \mathbf{M} was restricted to being diagonal, the inversion of \mathbf{M} is trivial. All terms in the inverted matrix are zero except the diagonal terms;

$$M_{ii}^{-1} = \frac{1}{M_{ii}}, \quad (\text{no sum on } i). \quad (\text{B.32})$$

For first order elements, the lumped mass matrix (for any reasonably refined model) provides a sufficiently good approximation.¹ If a consistent mass matrix (mass is mapped to the nodes though the shape functions) is used, the inversion calculation would be too expensive because the mass matrix would be nondiagonalized. The use of higher order elements is not practical because lumped mass matrices provide poor dynamic response. Furthermore, the contact algorithms of an explicit code requires efficient contact tracking logic; the most efficient of which is based on faceted surfaces (made of first order elements).

The current accelerations computed by Equation B.31 can be integrated using the central difference operator to obtain the velocities and displacements as

$${}^{\iota+1/2}\tilde{\mathbf{u}} = {}^{\iota-1/2}\tilde{\mathbf{u}} + \left(\frac{{}^{\iota+1}\Delta t + {}^{\iota}\Delta t}{2} \right) {}^{\iota}\tilde{\mathbf{u}} \quad (\text{B.33})$$

$${}^{\iota+1}\tilde{\mathbf{u}} = {}^{\iota}\tilde{\mathbf{u}} + {}^{\iota+1}\Delta t {}^{\iota+1/2}\tilde{\mathbf{u}}. \quad (\text{B.34})$$

This central difference scheme is second order accurate and is equivalent to a Newmark- β method with $\gamma = 1/2$ and $\beta = 0$.² Equations B.33 and B.34 are written in a slightly non-standard form to allow for the ability to have a variable time increment which is required for large deformation analysis where the effective stiffness of the material points may substantially change during the solution. Typical computational time for these nodal calculations (Equations B.33, and B.34) requires only a small percentage of the total

1. For further discussion on mass matrix approximations, see [24].

2. See Hughes [62] for a full description of the general Newmark- β method.

computation time; typically only 5%. Most of the computational expense is required for computing the internal forces related to Equations B.13 and for the tracking of contact.

The central difference integration formulae of Equations B.33 and B.34 are conditionally stable and bounded by the highest eigenvalue in the system (see [24,62] for analysis of integration operator stability). For an undamped system, this critical time increment, Δt , is defined as

$$\Delta t \leq \frac{2}{\omega_{\max}} \quad (\text{B.35})$$

where ω_{\max} is the highest natural frequency (eigenvalue) in the system.

In ABAQUS/Explicit, a small amount of controllable algorithmic damping is included to minimize high-frequency noise in the solution. Viscous pressure loads related to elemental volumetric strain-rates are included in the internal nodal forces, \tilde{f}^{int} . This type of damping is referred to as *bulk viscosity damping* (see [47,53] for further details). Since the solution utilizes a small amount of damping, the stable time increment is modified to (see Hughes [62])

$$\Delta t \leq \frac{2}{\omega_{\max}} \left(\sqrt{1 + \xi^2} - \xi \right) \quad (\text{B.36})$$

where ξ is the fraction of critical damping in the highest mode. As seen by Equation B.36, increasing the damping lowers the stable time increment.

For a discrete finite element model, the highest system natural frequency is always less than the highest individual element dilatational frequency in the model. Accurate bounds for dilatational frequencies of first order elements were developed by Flanagan and Belytschko [33] and are used to efficiently obtain the stable time increment for the mesh. The maximum undamped natural frequency is directly related to the dilatational wave speed, c_d , of the material by

$$\omega_{\max} = \frac{2 c_d}{l^{\text{eff}}} \quad (\text{B.37})$$

where l^{eff} is the effective or characteristic element length in the current (deformed) state. Equations for the calculation of these characteristic element lengths are found in [33,53]. The undamped dilatational wave speed of a material is defined as¹

$$c_d = \sqrt{\frac{\hat{\Lambda} + 2\hat{\mu}}{\rho}} \quad (\text{B.38})$$

where $\hat{\Lambda}$ and $\hat{\mu}$ are the effective Lamé constants and ρ is the current density.² For small deformations, the effective Lamé constants are related to Young's modulus, E , and Poisson ratio, ν , by

$$\hat{\Lambda} = \frac{E\nu}{(1+\nu)(1-2\nu)} \quad (\text{for small deformations}) \quad (\text{B.39})$$

$$\hat{\mu} = \frac{E}{2(1+\nu)} \quad (\text{for small deformations}) \quad (\text{B.40})$$

The stability limit can be written as

$$\Delta t = \min \left(\frac{l^{\text{eff}}}{c_d} (\sqrt{1 + \xi^2} - \xi) \right)_{\text{elem}} . \quad (\text{B.41})$$

Because of the possibility of large deformations and nonlinear constitutive relationships, all the quantities in Equation B.41 can change during the solution. Therefore the time increment must be adaptive; it is continuously updated during the solution (see Equations B.33 and B.34).

To update the dilatational wave speed, c_d , the material's constitutive law (regardless of the actual form used to relate strain to stress) is viewed as a hypoelastic law from which effective or tangent (current) hypoelastic moduli are computed. The effective Lamé constants are computed from incremental values of the mean pressure stress, $(\Delta\sigma_{kk})/3$, volumetric strain, $\Delta\varepsilon_{kk}$, deviatoric stress tensor, $\Delta\bar{\sigma}_{ij}$, and deviatoric strain tensor, $\Delta\bar{\varepsilon}_{ij}$, with the following equations

1. The dilatational wave speed is larger than the distortional wave speed as defined in [111]: $c_s = \sqrt{\hat{\mu}/\rho}$

2. The variable Λ is used instead of λ to avoid confusion with the stretch ratio which is denoted as λ .

$$\hat{K} = \frac{3\hat{\Lambda} + 2\hat{\mu}}{3} = \frac{(\Delta\sigma_{kk})/3}{\Delta\varepsilon_{ii}} \quad (\text{B.42})$$

$$2\hat{\mu} = \frac{\Delta\bar{\sigma}_{ij} \Delta\bar{\varepsilon}_{ij}}{\Delta\bar{\varepsilon}_{hk} \Delta\bar{\varepsilon}_{hk}} \quad (\text{B.43})$$

where \hat{K} is the effective bulk modulus and all indices range from one to three. This provides two equations and two unknowns ($\hat{\Lambda}$, $\hat{\mu}$). For cases when both the volumetric and deviatoric strains are not numerically significant, then the initial tangent values from the actual material law are used. For cases when only the deviatoric strains are not significant, then \hat{K} is computed based in Equation B.42 and $\hat{\mu}$ is determined by

$$2\hat{\mu} = \frac{3}{2} \left[\hat{\Lambda}_0 + 2\hat{\mu}_0 - \hat{K} \right] \quad (\text{B.44})$$

where $\hat{\Lambda}_0$ and $\hat{\mu}_0$ are initial tangent values. Further details can be found in [47].

The structure is then *marched* through time by repeated solution (without iteration) of Equations B.31, B.33, and B.34. Typical solutions using the explicit method require thousands of time increments because the stability limit restricts the time increment to be extremely small (less than twice that of the smallest natural period in the system). For typical structural mechanics problems, integrating at the stability limit provides excellent accuracy.

The book by Cook [24] provides good discussion regarding the accuracy of explicit solution methods. For explicit solution of a problem with only one degree of freedom, the accuracy of the solution (especially after thousands of time increments) is sensitive to the size of the time increment chosen for calculation. At a minimum, the time increment for an explicit method must be less than or equal to the critical value (Equation B.36) to assure stable solution. Decreasing the increment size below the critical value will increase the accuracy of the calculation. For typical structural mechanics problems (more than 20 D.O.F. and typically much greater than 100 D.O.F.) integrating at the stability limit provides excellent accuracy. The reason is that the analysis is interested in the structural response of the system which is a much lower-frequency, longer-time-scale behavior than

the *critical* element response which contains higher-frequency, shorter-time-scale behavior. In essence, the solution does not require highly accurate integration of high-frequency response; it only requires that they are integrated stably. The small time increments also allow for efficient, non-iterative contact logic to be employed.

Appendix C

Further Details on Ogden-Hill Hyperelasticity

This appendix provides a concise overview of Ogden-Hill strain-energy functions. Compressible and nearly/fully incompressible forms are discussed as well as issues related to Drucker stability. Additional information on some of the following equations are found in [49,51,54,59,86,87,88,109,114]. To compare these hyperelastic formulations with the more familiar small strain, Hookean material representations, we typically compute an *initial tangent* value of a given modulus (such as a shear or bulk modulus) for each of the material laws.

Please note that all forms of hyperelastic strain-energy densities presented have finite series representations. As such, the material parameters require indices in their definition. The index n (placed in the lower right side of the parameter) will be used to denote various finite terms for the material parameters.

C.1 Compressible Ogden-Hill

For materials that do not exhibit nearly incompressible or fully incompressible behavior, such as resilient foams, an Ogden-Hill strain-energy function, W , of the following form (as defined in [49]) is used:

$$W = \sum_{n=1}^N \frac{2\mu_n}{\alpha_n^2} \left[(\lambda_1^{\alpha_n} + \lambda_2^{\alpha_n} + \lambda_3^{\alpha_n} - 3) + \frac{1}{\beta_n} (J^{(-\alpha_n\beta_n)} - 1) \right] \quad (\text{C.1})$$

where μ_n , α_n and β_n represent material parameters, N is the number of finite terms in the series, and the principle stretch ratios and elastic volume ratio are defined by λ_i and J , respectively. The power terms α_n may be any real-valued number.

If material constants β_n are zero in Equation C.1, the strain-energy function appears to become indeterminate. Using the series expansion

$$a^x = 1 + x \ln(a) + \frac{[x \ln(a)]^2}{2!} + \frac{[x \ln(a)]^3}{3!} + \dots \text{H.O.T.} \quad (\text{C.2})$$

we find

$$\frac{1}{\beta_n} (J^{(-\alpha_n \beta_n)} - 1) = \frac{1}{\beta_n} [(1 - 1) - \alpha_n \beta_n \ln(J)] + \frac{1}{\beta_n} \sum_{h=2}^{\infty} \frac{[-\alpha_n \beta_n \ln(J)]^h}{h!} \quad (\text{C.3})$$

which simplifies to

$$\frac{1}{\beta_n} (J^{(-\alpha_n \beta_n)} - 1) = -\alpha_n \ln(J), \quad \text{if } \beta_n = 0. \quad (\text{C.4})$$

Writing Equation C.1 in terms of the *deviatoric* principal stretch ratios, $\bar{\lambda}_i$, demonstrates that the deviatoric and volumetric contributions are coupled:

$$W = \sum_{n=1}^N \frac{2\mu_n}{\alpha_n} \left[\underbrace{J^{(\alpha_n/3)} (\bar{\lambda}_1^{\alpha_n} + \bar{\lambda}_2^{\alpha_n} + \bar{\lambda}_3^{\alpha_n})}_{\text{volumetric and deviatoric coupling}} - 3 + \frac{1}{\beta_n} (J^{(-\alpha_n \beta_n)} - 1) \right]. \quad (\text{C.5})$$

To understand the physical significance of material parameters μ_n and β_n in Equation C.1 we compare these hyperelastic formulations with the more familiar small strain, Hookean material representations under common deformation modes. From Equation A.74 the principal nominal stresses for the Ogden-Hill form are computed as

$$\mathbb{T}_i^{\text{nom}} = \frac{\partial W}{\partial \lambda_i} = \frac{1}{\lambda_i} \sum_{n=1}^N \frac{2\mu_n}{\alpha_n} [\lambda_i^{\alpha_n} - J^{-\alpha_n \beta_n}] \quad (\text{no sum on } i). \quad (\text{C.6})$$

From Equation A.75 we find the principal Cauchy stresses as

$$\sigma_i = \frac{\lambda_i}{J} \frac{\partial W}{\partial \lambda_i} = \frac{1}{J} \sum_{n=1}^N \frac{2\mu_n}{\alpha_n} [\lambda_i^{\alpha_n} - J^{-\alpha_n \beta_n}] \quad (\text{no sum on } i) \quad (\text{C.7})$$

and from Equation A.76 the principal Kirchhoff stresses to be

$$\tau_i = \lambda_i \frac{\partial W}{\partial \lambda_i} = \sum_{n=1}^N \frac{2\mu_n}{\alpha_n} [\lambda_i^{\alpha_n} - J^{-\alpha_n \beta_n}] \quad (\text{no sum on } i). \quad (\text{C.8})$$

C.1.1 Uniaxial Deformation

The physical significance of β_n is seen by evaluating uniaxial deformation. The boundary conditions in this case are

$$\lambda_1 = \lambda_{\text{applied}}, \quad \sigma_k = 0, \quad k = 2, 3. \quad (\text{C.9})$$

Applying Equation C.9 to Equation C.7 yields

$$\frac{1}{J} \sum_{n=1}^N \frac{2\mu_n}{\alpha_n} [\lambda_k^{\alpha_n} - J^{-\alpha_n \beta_n}] = 0. \quad (\text{C.10})$$

If all β_n are equal to a constant value, β , then Equation C.10 can be satisfied if for every term n ,

$$\lambda_k^{\alpha_n} - J^{-\alpha_n \beta} = 0. \quad (\text{C.11})$$

Equation C.11 requires that $\lambda_2 = \lambda_3$ (which is expected since the material is isotropic). Using this fact and the definition of J (Equation A.35) yields, after some simplification, the following relationship

$$\lambda_2 = \lambda_1^{-\left(\frac{\beta}{1+2\beta}\right)}. \quad (\text{C.12})$$

Consider the definition of Poisson's ratio under large strains:

$$\varepsilon_2^{\text{ln}} = \varepsilon_3^{\text{ln}} = -\nu \varepsilon_1^{\text{ln}} \quad (\text{C.13})$$

where the principal logarithmic strains are defined as

$$\varepsilon_i^{\text{ln}} = \ln(\lambda_i). \quad (\text{C.14})$$

Rearranging Equation C.13 yields

$$\lambda_2 = \lambda_1^{-\nu}. \quad (\text{C.15})$$

Comparing Equation C.12 with C.15, we see that

$$\nu = \frac{\beta}{1+2\beta}. \quad (\text{C.16})$$

In the event that all β_n are not equal to a constant value, then the more complicated Equation C.10 must be utilized for uniaxial deformation. However, if we generalize Equation C.16 for non-equal β_n , this yields

$$v_n = \frac{\beta_n}{1 + 2\beta_n}. \quad (\text{C.17})$$

This equation can be rearranged into the form

$$\beta_n = \frac{v_n}{1 - 2v_n}. \quad (\text{C.18})$$

In the event that non-equal β_n are used, it should be noted that the generalized Poisson's ratio, v_n , become somewhat non-physical.

C.1.2 Simple-Shear Deformation

The physical significance of μ_n is seen by evaluating simple-shear deformation as shown in Figure C.1. The deformation for plane-strain simple-shear under idealized boundary conditions is described by

$$\mathbf{F} = \begin{bmatrix} 1 & \gamma & 0 \\ 0 & 1 & 0 \\ 0 & 0 & 1 \end{bmatrix} \quad (\text{C.19})$$

where the shear strain, γ , is defined as

$$\gamma = \frac{\Delta x}{H}. \quad (\text{C.20})$$

Equations A.22 – A.25 yield the following three principal stretch ratios for the deformation defined by Equation C.19:

$$\left\{ \begin{array}{c} \lambda_1 \\ \lambda_2 \\ \lambda_3 \end{array} \right\} = \left\{ \begin{array}{c} \sqrt{1 + \frac{1}{2}\gamma^2 + \frac{1}{2}\gamma\sqrt{4 + \gamma^2}} \\ \sqrt{1 + \frac{1}{2}\gamma^2 - \frac{1}{2}\gamma\sqrt{4 + \gamma^2}} \\ 1 \end{array} \right\}. \quad (\text{C.21})$$

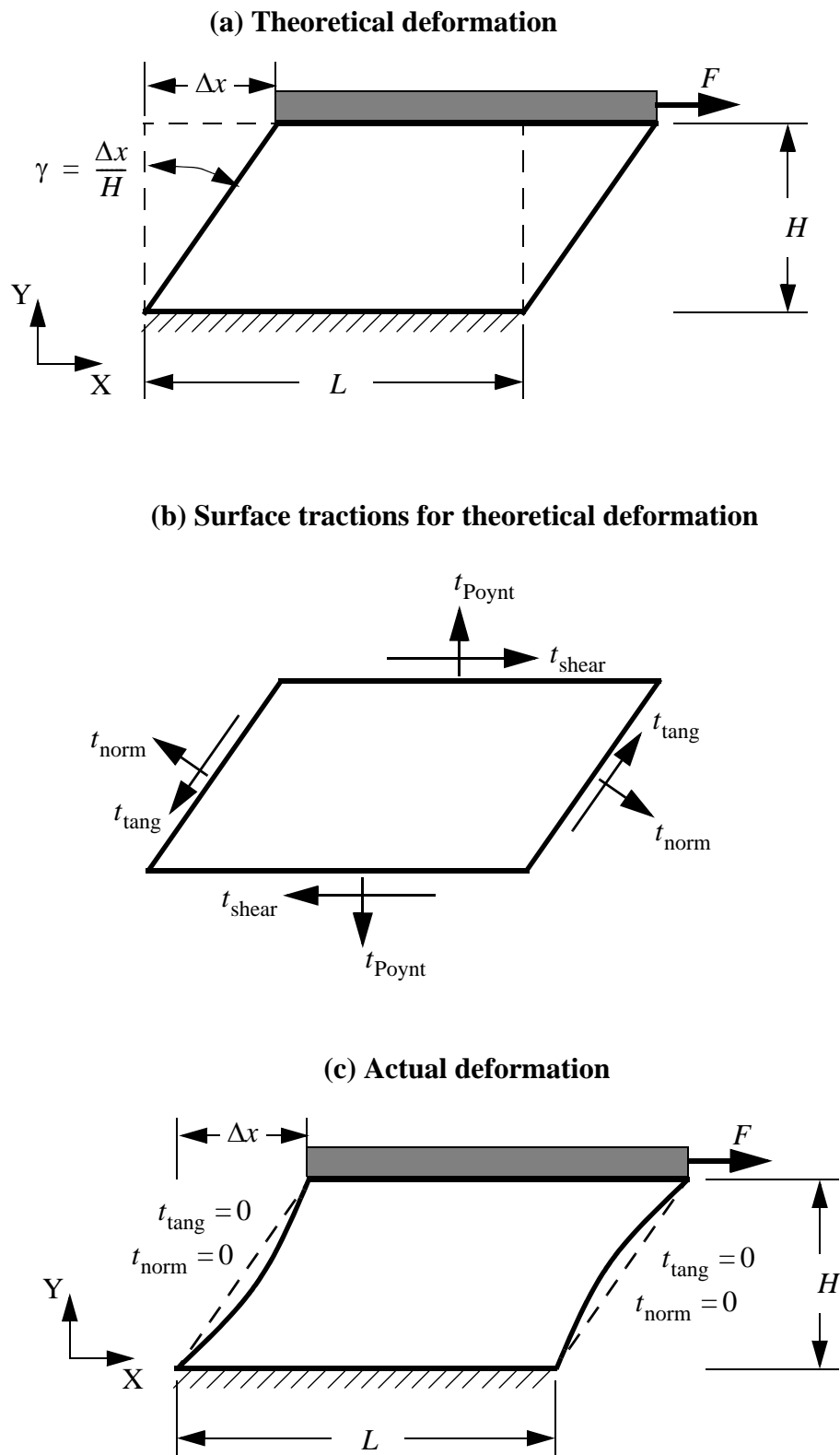


Figure C.1: Schematic of simple-shear.

These equations also yield the following principal directions of stretch in the unrotated and rotated configurations:

$$\tilde{\mathbf{N}}_{\text{I}} = \frac{\sqrt{\frac{\gamma^2 - \gamma\sqrt{4 + \gamma^2} + 2}{\gamma^2 - \gamma\sqrt{4 + \gamma^2} + 4}}}{\sqrt{\frac{\gamma^2 - \gamma\sqrt{4 + \gamma^2} + 2}{\gamma^2 - \gamma\sqrt{4 + \gamma^2} + 4}}} \left\{ \begin{array}{c} 1 \\ \frac{-2\gamma}{\gamma^2 - \gamma\sqrt{4 + \gamma^2}} \\ 0 \end{array} \right\}, \quad (\text{C.22})$$

$$\tilde{\mathbf{N}}_{\text{II}} = \frac{\sqrt{\frac{\gamma^2 + \gamma\sqrt{4 + \gamma^2} + 2}{\gamma^2 + \gamma\sqrt{4 + \gamma^2} + 4}}}{\sqrt{\frac{\gamma^2 + \gamma\sqrt{4 + \gamma^2} + 2}{\gamma^2 + \gamma\sqrt{4 + \gamma^2} + 4}}} \left\{ \begin{array}{c} 1 \\ \frac{-2\gamma}{\gamma^2 + \gamma\sqrt{4 + \gamma^2}} \\ 0 \end{array} \right\}, \quad (\text{C.23})$$

$$\tilde{\mathbf{N}}_{\text{III}} = \left\{ \begin{array}{c} 0 \\ 0 \\ -1 \end{array} \right\}, \quad (\text{C.24})$$

$$\tilde{\mathbf{n}}_{\text{I}} = \frac{\sqrt{\frac{\gamma^2 + \gamma\sqrt{4 + \gamma^2} + 2}{\gamma^2 + \gamma\sqrt{4 + \gamma^2} + 4}}}{\sqrt{\frac{\gamma^2 + \gamma\sqrt{4 + \gamma^2} + 2}{\gamma^2 + \gamma\sqrt{4 + \gamma^2} + 4}}} \left\{ \begin{array}{c} 1 \\ \frac{2\gamma}{\gamma^2 + \gamma\sqrt{4 + \gamma^2}} \\ 0 \end{array} \right\}, \quad (\text{C.25})$$

$$\tilde{\mathbf{n}}_{\text{II}} = \frac{\sqrt{\frac{\gamma^2 - \gamma\sqrt{4 + \gamma^2} + 2}{\gamma^2 - \gamma\sqrt{4 + \gamma^2} + 4}}}{\sqrt{\frac{\gamma^2 - \gamma\sqrt{4 + \gamma^2} + 2}{\gamma^2 - \gamma\sqrt{4 + \gamma^2} + 4}}} \left\{ \begin{array}{c} 1 \\ \frac{-2\gamma}{-\gamma^2 + \gamma\sqrt{4 + \gamma^2}} \\ 0 \end{array} \right\}, \quad (\text{C.26})$$

$$\tilde{\mathbf{n}}_{\text{III}} = \left\{ \begin{array}{c} 0 \\ 0 \\ -1 \end{array} \right\}. \quad (\text{C.27})$$

From Equation C.19 we see that the area-ratio in the X-Y plane is equal to unity and that the volume ratio, J , is also equal to unity;

$$J = |\mathbf{F}| = 1. \quad (\text{C.28})$$

Combining Equations C.7, C.21, C.27 and C.28 shows that the third principal Cauchy stress, which acts in the Z-direction, is zero under plane-strain conditions:¹

$$\sigma_3 = \sigma_{33} = 0. \quad (\text{C.29})$$

This results means that plane-stress simple-shear ($\sigma_3 = 0$ is specified and λ_3 is unknown) will yield the same result as plane-strain simple-shear for any material that is governed by Equation C.1.

Utilizing the general form of Equation A.37 and the result of Equation C.29, we compute the Cauchy stress tensor in the rotated configuration as

$${}^r\boldsymbol{\sigma} = \sigma_1 \tilde{\mathbf{n}}_I \tilde{\mathbf{n}}_I^T + \sigma_2 \tilde{\mathbf{n}}_{II} \tilde{\mathbf{n}}_{II}^T. \quad (\text{C.30})$$

The Piola-Kirchhoff stress tensor is then computed from Equation A.66 to be

$$\mathbf{T} = J {}^r\boldsymbol{\sigma} \mathbf{F}^{-T} = \begin{bmatrix} \sigma_{11} - \gamma\sigma_{12} & \sigma_{12} & 0 \\ \sigma_{12} - \gamma\sigma_{22} & \sigma_{22} & 0 \\ 0 & 0 & 0 \end{bmatrix}. \quad (\text{C.31})$$

From the discussion surrounding Equation A.68 we know that the Piola-Kirchhoff stresses are related to the nominal surface tractions. In particular we see that the unit outward surface-normal in the unrotated and rotated configurations on the Y-face of the block in Figure C.1 are simply defined by

$$\tilde{\mathbf{N}}^s = \begin{Bmatrix} 0 \\ 1 \\ 0 \end{Bmatrix}, \quad \tilde{\mathbf{n}}^s = \begin{Bmatrix} 0 \\ 1 \\ 0 \end{Bmatrix}. \quad (\text{C.32})$$

Thus, Equation A.68 yields

1. This fact is also true for Hooke's law when logarithmic strains are used. For the case of nearly/fully incompressible Ogden-Hill (Equation C.56), plane-strain and plane-stress simple-shear will produce slightly different answers.

$$\underset{\sim}{\mathbf{t}}^o = \begin{Bmatrix} \mathbf{T}_{12} \\ \mathbf{T}_{22} \\ 0 \end{Bmatrix} \quad (\text{C.33})$$

where $\underset{\sim}{\mathbf{t}}^o$ is the nominal surface traction (force per unit *original, undeformed*, surface area) directed in the *rotated* configuration. Since $\underset{\sim}{N}^s = \underset{\sim}{n}^s$, Equation C.33 defines the applied shear and Poynting (transverse) stresses;

$$t_{\text{shear}} = \mathbf{T}_{12}, \quad t_{\text{Poynt}} = \mathbf{T}_{22} . \quad (\text{C.34})$$

Combining Equations C.19, C.21, C.25, C.26, C.28, C.30, and C.31 we find, after some simplification, that

$$t_{\text{shear}} = \mathbf{T}_{12} = \sigma_{12} = \frac{1}{\sqrt{4 + \gamma^2}} \sigma_1 + \frac{-1}{\sqrt{4 + \gamma^2}} \sigma_2 . \quad (\text{C.35})$$

Utilizing the work conjugacy concepts of Section A.4.1, we can also compute the applied shear stress as

$$t_{\text{shear}} = \mathbf{T}_{12} = \frac{\partial W}{\partial \gamma} = \frac{\partial W}{\partial \lambda_i} \frac{\partial \lambda_i}{\partial \gamma} = \frac{\lambda_1}{\sqrt{4 + \gamma^2}} \frac{\partial W}{\partial \lambda_1} + \frac{-\lambda_2}{\sqrt{4 + \gamma^2}} \frac{\partial W}{\partial \lambda_2} . \quad (\text{C.36})$$

Substituting Equation C.8 into C.36 we find the applied shear stress simplifies to¹

$$t_{\text{shear}} = \frac{1}{\sqrt{4 + \gamma^2}} \left(\sum_{n=1}^N \frac{2\mu_n}{\alpha_n} [\lambda_1^{\alpha_n} - 1] - \sum_{n=1}^N \frac{2\mu_n}{\alpha_n} [\lambda_2^{\alpha_n} - 1] \right) . \quad (\text{C.37})$$

The applied Poynting stress is computed similarly to Equation C.35 as

$$t_{\text{Poynt}} = \mathbf{T}_{22} = \frac{1}{\sqrt{4 + \gamma^2}} \left(\frac{2}{\gamma + \sqrt{4 + \gamma^2}} \right) \sigma_1 + \frac{1}{\sqrt{4 + \gamma^2}} \left(\frac{2}{-\gamma + \sqrt{4 + \gamma^2}} \right) \sigma_2 . \quad (\text{C.38})$$

Evaluating the principle Cauchy stresses yields the final form for the Poynting stress:²

1. Equation C.37 is exactly equal to the relationship derived in [49, equation 4.5.6-3] for applied shear stress.

2. Equation C.39 is exactly equal to the relationship derived in [49, equation 4.5.6-4] for Poynting stress.

$$\begin{aligned}
t_{\text{Poynt}} = & \frac{1}{\sqrt{4 + \gamma^2}} \left(\frac{2}{\gamma + \sqrt{4 + \gamma^2}} \right) \sum_{n=1}^N \frac{2\mu_n}{\alpha_n} [\lambda_1^{\alpha_n} - 1] \\
& + \frac{1}{\sqrt{4 + \gamma^2}} \left(\frac{2}{-\gamma + \sqrt{4 + \gamma^2}} \right) \sum_{n=1}^N \frac{2\mu_n}{\alpha_n} [\lambda_2^{\alpha_n} - 1].
\end{aligned} \tag{C.39}$$

Since the volume ratio $J = 1$ from Equation C.28, we see that there is no Poisson influence in the simple-shear deformation mode; β_n does not appear in Equations C.37 or C.39.

From Figure C.1b we see that surface tractions must also exist on the inclined faces of the block for the theoretical (idealized) case. The unit surface normal and unit surface tangent of the inclined surface in the rotated configuration are

$$\tilde{\mathbf{n}}_{\text{norm}}^{\text{r,s}} = \frac{1}{\sqrt{\gamma^2 + 1}} \begin{Bmatrix} 1 \\ -\gamma \\ 0 \end{Bmatrix}, \quad \tilde{\mathbf{n}}_{\text{tang}}^{\text{r,s}} = \frac{1}{\sqrt{\gamma^2 + 1}} \begin{Bmatrix} \gamma \\ 1 \\ 0 \end{Bmatrix}. \tag{C.40}$$

The surface traction on the inclined surface, $\tilde{\mathbf{t}}^{\text{r}}$, is computed as

$$\tilde{\mathbf{t}}^{\text{r}} = \mathbf{\sigma}^{\text{r}} \tilde{\mathbf{n}}_{\text{norm}}^{\text{r,s}} = \frac{1}{\sqrt{\gamma^2 + 1}} \begin{Bmatrix} \sigma_{11} - \gamma \sigma_{12} \\ \sigma_{12} - \gamma \sigma_{22} \\ 0 \end{Bmatrix}. \tag{C.41}$$

This traction represents the loads per unit current (deformed) surface area acting in the direction of the rotated configuration with respect to the X-Y coordinate system. The surface tractions in the local *inclined* coordinate system are found to be

$$t_{\text{tang}} = \tilde{\mathbf{t}}^{\text{r}} \cdot \tilde{\mathbf{n}}_{\text{tang}}^{\text{r,s}} = \frac{\sigma_{12}}{\gamma^2 + 1}, \tag{C.42}$$

$$t_{\text{norm}} = \tilde{\mathbf{t}}^{\text{r}} \cdot \tilde{\mathbf{n}}_{\text{norm}}^{\text{r,s}} = \sigma_{22} - \gamma t_{\text{tang}} \tag{C.43}$$

where the following material-independent relationship for simple-shear (see [3]) has been used:

$$\sigma_{11} - \sigma_{22} = \gamma \sigma_{12}. \tag{C.44}$$

In an actual experiment, the application of the surface tractions defined by Equations C.42 and C.43 are difficult if not impossible to apply. As a result, the typical deformation of a block under simple-shear in reality will look something like the result depicted in Figure C.1c. As long as the length of the block, L , relative to the height of the block, h , is large, then this error will be negligibly small.

From linear elasticity (Hooke's law and small strains) we have

$$t_{\text{shear}} = \mu_0 \gamma \quad (\text{C.45})$$

where initial tangent shear modulus based on Hooke's law is μ_0 . From Equation C.45 we find for Hooke's law

$$\mu_0 = \frac{\partial t_{\text{shear}}}{\partial \gamma} . \quad (\text{C.46})$$

Computing the same derivative for Equation C.37 and evaluating the initial tangent value yields

$$\left. \frac{\partial t_{\text{shear}}}{\partial \gamma} \right|_{\gamma=0} = \mu_0 = \sum_{n=1}^N \mu_n . \quad (\text{C.47})$$

C.1.3 Volumetric Deformation

Volumetric deformation allows us to relate the initial tangent bulk modulus based on Hooke's law, K_0 , to the Ogden-Hill material constants. Volumetric deformation is defined such that all three principal stretch ratios are equal to an applied value, λ_v ,

$$\lambda_v = \lambda_i, \quad \Rightarrow \quad \lambda_v = J^{1/3} . \quad (\text{C.48})$$

The bulk modulus is related to the hydrostatic stress (also called the mean stress) σ^m which can be computed from the principal Cauchy stresses as

$$\sigma^m = \frac{1}{3} \sum_{i=1}^3 \sigma_i . \quad (\text{C.49})$$

Combining Equations C.7 and C.48 yields

$$\sigma^m = \frac{1}{J} \sum_{n=1}^N \frac{2\mu_n}{\alpha_n} [J^{\alpha_n/3} - J^{-\alpha_n\beta_n}]. \quad (\text{C.50})$$

From linear elasticity (Hooke's law and small strains) we have

$$\sigma^m = K_0 \varepsilon_{ii} \cong K_0(J-1) \quad (\text{C.51})$$

where ε_{ii} is the trace of the strain tensor.¹ From Equation C.51 we find for Hooke's law

$$K_0 = \frac{\partial \sigma^m}{\partial J}. \quad (\text{C.52})$$

Computing the same derivative for Equation C.50 yields

$$\frac{\partial \sigma^m}{\partial J} = \frac{1}{J^2} \sum_{n=1}^N \frac{2\mu_n}{\alpha_n} \left[J^{\alpha_n/3} \left(\frac{\alpha_n}{3} - 1 \right) + J^{-\alpha_n\beta_n} (\alpha_n\beta_n + 1) \right]. \quad (\text{C.53})$$

The initial tangent value is found when $J = 1$ (undeformed)

$$\left. \frac{\partial \sigma^m}{\partial J} \right|_{J=1} = K_0 = \sum_{n=1}^N 2\mu_n \left(\frac{1}{3} + \beta_n \right). \quad (\text{C.54})$$

Since the initial tangent bulk modulus should be positive for any realistic material, the following constraint is found

$$\sum_{n=1}^N \mu_n \left(\frac{1}{3} + \beta_n \right) > 0. \quad (\text{C.55})$$

C.2 Nearly/Fully Incompressible Ogden-Hill

For hyperelastic strain-energy functions in this section, the formulations are written as separable functions of *deviatoric* deformation and *volumetric* (dilatational) deformation. The functions are written in this manor because the material is expected to be nearly or fully incompressible.

The Ogden-Hill strain-energy function, W , as defined in [49] is

1. From Equation A.6 we know that all measures of strain are equivalent in the linear, small strain region.

$$W = \sum_{n=1}^N \left(\frac{2\mu_n}{\alpha_n} (\bar{\lambda}_1^{-\alpha_n} + \bar{\lambda}_2^{-\alpha_n} + \bar{\lambda}_3^{-\alpha_n} - 3) + \frac{1}{D_n} (J-1)^{2n} \right) \quad (\text{C.56})$$

where μ_n , α_n and D_n represent material parameters, N is the number of finite terms in the series, $\bar{\lambda}_i$ are the deviatoric principal stretch ratios (see Equation A.86), and J is the volume ratio. The material parameters μ_n and α_n have the same physical meanings as those described for the compressible version in Section C.1. The physical significance of D_n is seen by evaluating volumetric deformation (Section C.2.1).

From Equation C.56 we identify the *deviatoric* strain-energy density as

$$W^{\text{dev}} = \sum_{n=1}^N \frac{2\mu_n}{\alpha_n} (\bar{\lambda}_1^{-\alpha_n} + \bar{\lambda}_2^{-\alpha_n} + \bar{\lambda}_3^{-\alpha_n} - 3) \quad (\text{C.57})$$

and the *volumetric* strain-energy density as

$$W^{\text{vol}} = \sum_{n=1}^N \frac{1}{D_n} (J-1)^{2n} . \quad (\text{C.58})$$

Calculation of the various principal stresses for nearly/fully incompressible materials are described in Section A.4.2. To calculate stresses, partial derivatives of the deviatoric and volumetric portions of the strain-energy density are required.

Utilizing Equation A.97 we find for the deviatoric part that

$$\frac{\partial W^{\text{dev}}(\bar{\lambda})}{\partial \lambda_i} = \sum_{n=1}^N \left(\frac{2\mu_n}{3\alpha_n} J^{-\alpha_n/3} \right) \begin{bmatrix} \frac{2}{\lambda_1} & -\frac{1}{\lambda_1} & -\frac{1}{\lambda_1} \\ -\frac{1}{\lambda_2} & \frac{2}{\lambda_2} & -\frac{1}{\lambda_2} \\ -\frac{1}{\lambda_3} & -\frac{1}{\lambda_3} & \frac{2}{\lambda_3} \end{bmatrix} \left\{ \begin{array}{l} \lambda_1^{\alpha_n} \\ \lambda_2^{\alpha_n} \\ \lambda_3^{\alpha_n} \end{array} \right\} . \quad (\text{C.59})$$

The volumetric partial derivative is simply calculated as

$$\frac{\partial W^{\text{vol}}(J)}{\partial J} = \sum_{n=1}^N \frac{2n}{D_n} (J-1)^{2n-1} . \quad (\text{C.60})$$

Substitution of Equations C.59 and C.60 into the equations in Section A.4.2 allows one to calculate the various stress quantities required.

C.2.1 Volumetric Deformation

Volumetric deformation allows us to relate the initial tangent bulk modulus based on Hooke's law, K_0 , to the Ogden-Hill material constants D_n . Following the volumetric analysis of Section C.1.3 we have

$$K_0 = \left. \frac{\partial \sigma^m}{\partial J} \right|_{J=1} = \left[\sum_{n=1}^N \left(\frac{2n(2n-1)}{D_n} (J-1)^{2n-2} \right) \right]_{J=1} \quad (\text{C.61})$$

which simplifies to

$$K_0 = \frac{2}{D_1}. \quad (\text{C.62})$$

Hence, the material parameters D_n are related to the inverse of the bulk modulus. If $D_n = 0$ in Equation C.56, then the material is fully incompressible.

C.3 Drucker Stability

The hyperelastic material laws being used in the thesis are phenomenological models. In general, the material parameters (coefficients) are found by fitting a proposed strain-energy function to experimental data measured from a given material that was subjected to a variety of deformation modes. To be sure that the material parameters describe a stable material definition, Drucker stability should be verified (see [51] for more details). Drucker stability requires that the change in Kirchhoff stress, $d\tau_{ij}$, following an infinitesimal change in logarithmic (true) strain, $d\varepsilon_{ij}^{\ln}$, must satisfy¹

$$d\tau_{ij} d\varepsilon_{ij}^{\ln} > 0. \quad (\text{C.63})$$

The relationship between infinitesimal changes in Kirchhoff stress and logarithmic strain can be expressed in a hypoelastic form as

1. Logarithmic strain is the *true* measure of deformation. Kirchhoff stress is used here because it is conjugate to logarithmic strain.

$$d\tau_{ij} = E_{ijkl} d\varepsilon_{kl}^{\ln}. \quad (\text{C.64})$$

where E_{ijkl} is the current tangent material elasticity (also called tangent material stiffness) and all indices have values that range from 1 to 3. The stress-strain relationship can also be characterized using principal Kirchhoff stresses, τ_i , and principal logarithmic strains, ε_i^{\ln} , as

$$\begin{Bmatrix} d\tau_1 \\ d\tau_2 \\ d\tau_3 \end{Bmatrix} = \begin{bmatrix} E_{11} & E_{12} & E_{13} \\ E_{21} & E_{22} & E_{23} \\ E_{31} & E_{32} & E_{33} \end{bmatrix} \begin{Bmatrix} d\varepsilon_1^{\ln} \\ d\varepsilon_2^{\ln} \\ d\varepsilon_3^{\ln} \end{Bmatrix}. \quad (\text{C.65})$$

Combining Equation C.65 with Equations C.63 and C.64 yields the matrix form of Drucker stability

$$\{d\varepsilon^{\ln}\}^T [\mathbf{E}] \{d\varepsilon^{\ln}\} > 0. \quad (\text{C.66})$$

This form is also the definition of a positive-definite matrix. Hence, the tangent elasticity matrix, \mathbf{E} , must be positive definite for a stable material law. For the general three-dimensional case, a positive-definite matrix is guaranteed when all three tensor invariants of \mathbf{E} are positive:

$$I_1 = E_{ii} > 0, \quad (\text{C.67})$$

$$I_2 = \frac{1}{2}(I_1^2 - E_{ij} E_{ji}) > 0, \quad (\text{C.68})$$

$$I_3 = \det(\mathbf{E}) > 0. \quad (\text{C.69})$$

Another condition that comes from the positive definite requirement on \mathbf{E} are that all three eigenvalues of \mathbf{E} must be positive and that all diagonal terms of \mathbf{E} must be greater than zero.¹ An alternative check for positive definiteness is that all principal minors yield positive values; namely

$$E_{11} > 0, \quad (\text{C.70})$$

1. See [15,51,62,65,83,118] for further details on Drucker stability and positive-definite matrices.

$$\begin{vmatrix} E_{11} & E_{12} \\ E_{21} & E_{22} \end{vmatrix} > 0, \quad (\text{C.71})$$

$$\begin{vmatrix} E_{11} & E_{12} & E_{13} \\ E_{21} & E_{22} & E_{23} \\ E_{31} & E_{32} & E_{33} \end{vmatrix} > 0. \quad (\text{C.72})$$

Theoretically, these stability checks need to be made for every combination of the three principal stretch ratios over the range of deformation that may be encountered. This is generally not practical due to the computational expense required. A practical alternative is to check for several basic deformation modes, such as uniaxial, equibiaxial, planar, simple shear, and volumetric, throughout the deformation range of interest.

When Drucker stability is not satisfied, one can evaluate the instability to see how significant it is. Sometimes the instability may be small and localized; existing only over a short range of deformation. In this case, the material law may still be usable. In the event that the instability is severe (relative large negative values from one or more of Equations C.67 - C.69 that continue to become more negative as the deformation is increased), the material law will likely be unusable in the region of instability. More detailed understanding of the type of instability can be obtained by evaluating the eigenvalue and associated eigenvector for the deformation values at which the failure occurred.

Material stability is in general a physically reasonable expectation. However, when modeling highly foamed materials, some small amounts of *real* material instability may exist. This is due to the fact that we are modeling macroscopically a structure (material) that is microscopically made of components that resemble beams, plates, and shells. It is therefore possible in highly foamed materials that the local buckling of the material cells causes macroscopic buckling of the material. As the deformation of the material continues, densification typically arrests the macroscopic buckling. Hence, this type of behavior will show up as a small localized instability in the material data and in a Drucker stability check of a fitted hyperelastic material law. When a severe instability in a Drucker

stability check occurs, it often signifies that there was not sufficient data (enough deformation modes or large enough deformation range) to properly determine one or more of the material coefficients.

C.3.1 Drucker Stability for Compressible Ogden-Hill

This subsection derives the tangent elasticity matrix for the compressible form of the strain-energy. Computing the partial derivative of principal Kirchhoff stresses, τ_i , (Equation C.8) yields

$$d\tau_i = \sum_{n=1}^N \frac{2\mu_n}{\alpha_n} \left[\alpha_n \lambda_i^{\alpha_n} \left(\frac{d\lambda_i}{\lambda_i} \right) + \alpha_n \beta_n J^{-\alpha_n \beta_n} \left(\frac{dJ}{J} \right) \right] \quad (\text{no sum on } i) . \quad (\text{C.73})$$

Noting that $J = \lambda_1 \lambda_2 \lambda_3$, we can substitute

$$\frac{dJ}{J} = \frac{d\lambda_1}{\lambda_1} + \frac{d\lambda_2}{\lambda_2} + \frac{d\lambda_3}{\lambda_3} \quad (\text{C.74})$$

into Equation C.73 to obtain

$$d\tau_i = \sum_{n=1}^N 2\mu_n \left[\lambda_i^{\alpha_n} \left(\frac{d\lambda_i}{\lambda_i} \right) + \beta_n J^{-\alpha_n \beta_n} \left(\frac{d\lambda_1}{\lambda_1} + \frac{d\lambda_2}{\lambda_2} + \frac{d\lambda_3}{\lambda_3} \right) \right] \quad (\text{no sum on } i) . \quad (\text{C.75})$$

Since

$$d\varepsilon_i^{\ln} = \frac{1}{\lambda_i} d\lambda_i \quad (\text{no sum on } i) \quad (\text{C.76})$$

we see from Equation C.75 that

$$[E] = \sum_{n=1}^N 2\mu_n \begin{bmatrix} \lambda_1^{\alpha_n} + \beta_n J^{-\alpha_n \beta_n} & \beta_n J^{-\alpha_n \beta_n} & \beta_n J^{-\alpha_n \beta_n} \\ \beta_n J^{-\alpha_n \beta_n} & \lambda_2^{\alpha_n} + \beta_n J^{-\alpha_n \beta_n} & \beta_n J^{-\alpha_n \beta_n} \\ \beta_n J^{-\alpha_n \beta_n} & \beta_n J^{-\alpha_n \beta_n} & \lambda_3^{\alpha_n} + \beta_n J^{-\alpha_n \beta_n} \end{bmatrix} . \quad (\text{C.77})$$

Next, we show that Equation C.77 degenerates to the initial tangent elasticity matrix for Hooke's law. The stress-strain relationship for Hooke's law is

$$\tau_{ij}^{\text{con}} = \Lambda_0 \varepsilon_{kk}^{\text{con}} \delta_{ij} + 2\mu_0 \varepsilon_{ij}^{\text{con}} \quad (\text{C.78})$$

where all indices range from 1 to 3, τ_{ij}^{con} and $\varepsilon_{ij}^{\text{con}}$ are any work-conjugate pair of stress and strain in a common configuration, μ_0 is the shear modulus, and Λ_0 is a Lamé constant defined by

$$\Lambda_0 = \frac{2\mu_0\nu}{(1-2\nu)} \quad (\text{C.79})$$

where ν is Poisson's ratio. Since Hooke's law is valid for small elastic strains, we can choose any work-conjugate pair of stress and strain; say Kirchhoff stress and logarithmic strain. The strain-energy density for Hooke's law is

$$W = \frac{1}{2}\Lambda_0 (\varepsilon_{kk}^{\text{ln}})^2 + \mu_0 \varepsilon_{ij}^{\text{ln}} \varepsilon_{ij}^{\text{ln}} . \quad (\text{C.80})$$

This can equivalently be written in terms of principal strains as

$$W = \frac{1}{2}\Lambda_0 (\varepsilon_1^{\text{ln}} + \varepsilon_2^{\text{ln}} + \varepsilon_3^{\text{ln}})^2 + \mu_0 \left[(\varepsilon_1^{\text{ln}})^2 + (\varepsilon_2^{\text{ln}})^2 + (\varepsilon_3^{\text{ln}})^2 \right] . \quad (\text{C.81})$$

The principal Kirchhoff stresses are then computed using Equation A.78 as

$$\tau_i = \Lambda_0 (\varepsilon_1^{\text{ln}} + \varepsilon_2^{\text{ln}} + \varepsilon_3^{\text{ln}}) + 2\mu_0 \varepsilon_i^{\text{ln}} \quad (\text{C.82})$$

and the partial derivative of τ_i yields

$$d\tau_i = (\Lambda_0 + 2\mu_0) d\varepsilon_i^{\text{ln}} + \Lambda_0 (d\varepsilon_1^{\text{ln}} + d\varepsilon_2^{\text{ln}} + d\varepsilon_3^{\text{ln}} - d\varepsilon_i^{\text{ln}}) . \quad (\text{C.83})$$

Thus, the tangent elasticity matrix for Hooke's law is

$$[\mathbf{E}_0] = \begin{bmatrix} \Lambda_0 + 2\mu_0 & \Lambda_0 & \Lambda_0 \\ \Lambda_0 & \Lambda_0 + 2\mu_0 & \Lambda_0 \\ \Lambda_0 & \Lambda_0 & \Lambda_0 + 2\mu_0 \end{bmatrix} . \quad (\text{C.84})$$

To compare Equation C.84 to C.77, we evaluate Equation C.77 for linear, small deformations ($\lambda_i = 1, J = 1$) with $N = 1$. Substituting Equation C.18 and C.47 into C.77 we find for small deformations

$$\begin{aligned}
2\mu_1(\lambda_1^{\alpha_1} + \beta_1 J^{-\alpha_1 \beta_1}) &= 2\mu_0 + \frac{2\mu_0 \nu}{1-2\nu} \\
2\mu_1 \beta_1 J^{-\alpha_1 \beta_1} &= \frac{2\mu_0 \nu}{1-2\nu}
\end{aligned} \tag{C.85}$$

These values are equal to the terms found from Hooke's law (Equation C.84).

For a nearly/fully incompressible Ogden-Hill strain-energy function, a similar (but more lengthy) derivation of Drucker stability can be derived. Since the use of nearly/fully incompressible materials in this research is confined to small and moderate strain ranges, problems with material law stability are not expected for those materials.